PONTIFICIA UNIVERSIDAD CATÓLICA DEL PERÚ

ESCUELA DE POSGRADO

Título

APLICACIÓN DE LA FIBRA DE ACERO GALVANIZADO PARA EL REFORZAMIENTO ESTRUCTURAL DE MUROS DE ALBAÑILERÍA CONFINADA ANTE CARGAS CÍCLICAS EN SU PLANO

TESIS PARA OPTAR EL GRADO ACADÉMICO DE MAGÍSTER EN INGENIERÍA CIVIL

AUTORES

LUCIANO JHAIR YACILA ALVARADO

JHOSELYN JUNNY SALSAVILCA POMARCAHUA

ASESORES

SABINO NICOLA TARQUE RUIZ

GUIDO CAMATA

Julio, 2019

Agradecimientos

En primer lugar queremos agradecer a Dios por darnos salud, bienestar y sabiduría para poder afrontar este proyecto de investigación de la mejor forma. Asimismo, agradecemos a nuestros padres, hermanos y amistades por impulsarnos constantemente en la busqueda de ser cada día mejores personas y profesionales.

Por la orientación y el apoyo incondicional durante toda la investigación, queremos agradecer al Dr. Nicola Tarque, de la Pontificia Universidad Católica del Perú (PUCP), por ser un asesor comprometido con la investigación. De igual forma, agradecemos al Dr. Guido Camata de la Universidad Grabiel d'Anunzio (Chieti-Pescara), quien muy amablemente nos recibió y nos guió durante nuestra estancia en Italia. Al Dr. Paolo Casadei, representante de la compañía KERAKOLL, quien tuvo a bien donarnos los materiales necesarios para el reforzamiento de los muros que fueron objeto de este proyecto de investigación.

Finalmente, agradecemos a CONCYTEC por la beca de estudios que ahora nos permite lograr un nuevo título profesional y por el apoyo económico brindado a lo largo de este investigación. A la sección de Ingeniería civil por el apoyo económico brindado durante la campaña experimental conducida en el aboratorio de Estructuras Antisísmicas de la PUCP. Al personal del laboratorio por ser muy amables y estar siempre dispuestos a colaborar en que los ensayos requeridos sean realizados apropiadamente.

Índice

RESUMEN

La albañilería confinada se ha convertido en la tipología constructiva más empleada en el Perú a lo largo de las últimas décadas. No obstante, existe una elevada vulnerabilidad sísmica asociada a la informalidad y calidad de los materiales que son empleados durante su ejecución. Por ello, este trabajo pretende contribuir a la reducción de dicha vulnerabilidad mediante la aplicación de una novedosa técnica de reforzamiento estructural conocida como Steel Reinforced Grout (SRG). Una campaña experimental fue conducida para evaluar el desempeño cíclico de tres muros de albañilería confinada reforzados con SRG al ser sometidos a cargas cíclicas en sus planos. Los resultados mostraron las bondades del SRG al mejorar el desempeño cíclico de todos los muros ensayados en términos de ductilidad lateral, energía disipada, razón de amortiguamiento histerético y degradación de rigidez. Por otro lado, una contribución al estado del arte, en el conocimiento del comportamiento no lineal de la albañilería confinada y del SRG, fue hecha mediante la modelación numérica de muros de albañilería confinada y ensayos de adherencia entre el SRG y la albañilería. Dicha modelación fue hecha mediante el empleo del modelo de material Concrete Damage Plasticity del software ABAQUS, el cual es capaz de representar el comportamiento no lineal de materiales cuasi-frágiles como el concreto y la albañilería. Una comparación de resultados numéricos y experimentales permitieron corroborar la eficacia de los modelos numéricos al brindar respuestas muy cercanas a las obtenidas experimentalmente. Finalmente, cinco alternativas de refuerzo sísmico fueron comparadas en términos técnico-económicos para una sabia elección en el caso se requiera la aplicación masiva de un refuerzo sísmico. Dicha comparación dio a conocer que el FRP es la técnica con mayor aceptación técnico-económica seguido por el SRG.

Capítulo I

Aspectos generales

1.1. Introducción

La albañilería confinada (AC) es una de las técnicas de construcción que sigue siendo bastante empleada hasta el momento. Se caracteriza principalmente por la simplicidad con la que es construida. Otras características como la durabilidad, estética, bajo costo de mantenimiento, resistencia al fuego, entre otros, hacen que la AC sea una tipología de construcción interesante de profundizar. En esta tarea se observó que son construcciones que por sí solas no soportan adecuadamente las cargas laterales impuestas por un sismo. Es así que se ha venido estudiando diferentes técnicas de reforzamiento para mejorar su capacidad sísmica. Algunas de ellas son presentadas en este capítulo en la sección de antecedentes. Asimismo, se presenta y justifica la nueva técnica de reforzamiento que pretende competir con las anteriores. Finalmente, se detallan los objetivos, alcances y el plan de trabajo que se llevará a cabo.

1.1.1. Antecedentes y justificación

Códigos internacionales permiten la construcción de estructuras de albañilería confinada en zonas con baja sismicidad (FEMA, 2009). Sin embargo, décadas atrás fueron construidos incluso en áreas de alto peligro sísmico. Por ejemplo, desde finales del siglo XIX, Lima ha experimentado un crecimiento exponencial de la población. Por ello, una expansión acelerada de estructuras de albañilería confinada se dio paso (Salinas and Lazares, 2007). Actualmente, en Lima el 83% de las viviendas son construidas con albañilería confinada y cerca del 60% de estas son construcciones informales (INEI, 2008).

La informalidad de estas construcciones de albañilería confinada y características propias del material promueven una alta vulnerabilidad sísmica. La vulnerabilidad en conjunto con el peligro sísmico origina un alto riesgo. El riesgo sísmico plantea tres tipos de riesgo: a la vida humana, a la propiedad y a la pérdida de uso de la estructura (FEMA, 2009). La figura 1.1 muestra una casa de albañilería confinada devastada tras el terremoto del 2016 en Pescara del Tronto en Italia y viviendas dañadas después del sismo del 2007 en Pisco, Perú.

(a) Pescara del Tronto, Italia (b) Pisco, Perú

Figura 1.1: Viviendas de AC colapsadas por eventos sísmicos

Con la finalidad de mitigar estos tres tipos de riesgo, investigadores han estado estudiando la posibilidad de reparar y reforzar edificaciones de albañilería confinada con técnicas y/o sistemas que empleen compuestos adecuados. En un inicio, se estudió al acero como material de refuerzo en distintas formas como encamisado, malla electrosoldada, sistema de cables, malla de acero. Luego, desde inicios de los años 90?s los Polímeros Reforzados con Fibra (FRP) son tema de estudio para el reforzamiento externo de la albañilería. Este último se ha tornado popular mundialmente por las excelentes propiedades de los compuestos como la fibra de vidrio, carbono, basalto entre otros (Buchan and Chen, 2007). Actualmente, otras opciones de refuerzo como el sistema de Matriz Cementosa Reforzada con Fibra (FRCM), Mortero Reforzado con Fibra (FRM), Lechada Reforzada con Acero (SRG) han surgido para competir contra los anteriores, dado a las ventajas que ofrece la matriz inorgánica que las compone.

Las investigaciones que abarcaron las técnicas mencionadas han tratado de mejorar la capacidad sísmica de este tipo de construcciones en términos de resistencia, ductilidad y rigidez. En Australia, Chuang et al. (2004) investigaron el empleo de cables de

acero en forma de aspa anclados a los muros como sistema de reforzamiento. En Países Bajos, Zijl and Vries (2005) estudiaron el uso de fibra de carbono como refuerzo para el control de grietas en muros de albañilería. En China, Kaplan et al. (2008) evaluaron experimentalmente la posibilidad de emplear neumáticos usados. En EE.UU, Babaeidarabad et al. (2013) investigaron el comportamiento de muros reforzados con mallas de fibra de carbono envueltas en una matriz cementosa. En Italia, Gattesco and Boem (2017) estudiaron el refuerzo de muros con mortero reforzado con fibra de vidrio. En Perú, la Pontificia Universidad Católica del Perú (PUCP) ha estudiado el refuerzo de muros de AC con malla electrosoldada, polímero reforzado con fibra de carbono, con fibra de vidrio, malla de acero, malla de polímero y otros materiales (San Bartolomé and Castro (2002); San Bartolomé and Coronel (2009); Tumialán et al. (2004); San Bartolomé and Loayza (2004); Luján (2016); Torrealva (2007), entre otros).

Además de presentar los resultados en conferencias y que sean publicados, se han estado elaborando manuales e investigaciones técnicas como los siguientes: en Perú, “Construcción y mantenimiento de viviendas de albañilería" (Blondet, 2005), “Manual para la reparación y reforzamiento de viviendas de albañilería confinada dañadas por sismo" (Kuroiwa and Salas, 2009). En la India, “IITK-GSDMA Guidelines for structural use of reinforced masonry" (Rai et al., 2005). En EE.UU, El Departamento de Energía presentó en el artículo 1.3.2 del “Building Technologies Program: Recommended Approaches to the Retrofit of Masonry Wall Assemblies: Final Expert Report Meeting" (Ueno and Van Straaten, 2011), “Guides and specifications for the use of composites in concrete and masonry construction in North America" (Nanni, 2001). En Italia, el Comité Consultivo de Recomendaciones Técnicas para la Construcción- CNR publicó “Guide for the Design and Construction of Externally Bonded FRP Systems for Strengthening Existing Structures" (Aiello et al., 2014).

De este modo se evidencia que es necesario la implementación de métodos que empleen materiales adecuados para mejorar la capacidad sismorresistente de la AC, y así reducir todo tipo de riesgo. Por ello, esta investigación presenta a la fibra de acero galvanizado como una alternativa novedosa para el reforzamiento de muros de albañilería en una evaluación analítica- experimental y presenta una recopilación comparativa entre métodos empleados anteriormente con el propuesto.

1.2. Objetivos y alcances

1.2.1. Objetivo general

Contribuir con la reducción de la vulnerabilidad sísmica de muros de albañilería confinada mediante la aplicación de la fibra de acero galvanizado como material de reforzamiento estructural

1.2.2. Objetivos específicos

1. Validar las propiedades mecánicas de la fibra de acero galvanizado mediante ensayos experimentales
2. Desarrollar un modelo numérico que permita predecir el comportamiento de los muros reforzados con fibra de acero galvanizado
3. Ensayar tres muros de albañilería confinada a escala natural reforzados con fibra de acero galvanizado ante cargas cíclicas en su plano
4. Comparar el comportamiento sísmico y viabilidad técnica-económica de los sistemas de reforzamiento de la literatura con el propuesto, con y sin refuerzo

1.2.3. Alcances

Se estudiará la factibilidad técnica económica de emplear bandas de fibra de acero galvanizado para reforzar muros de albañilería confinada. Para evaluar la eficacia del refuerzo propuesto se ensayarán tres muros reforzados a escala natural bajo carga lateral cíclica.

1.3. Hipótesis

Se acepta que la fibra de acero galvanizado es un material ventajoso técnica y económicamente en comparación con los de la literatura para el reforzamiento estructural de muros de albañilería.

1.4. Metodología y plan de trabajo

Para alcanzar los objetivos específicos, se dividió el trabajo de investigación en 4 actividades de trabajo: Validación de propiedades mecánicas, modelamiento numérico, ensayo de muros reforzados a escala natural y comparación de alternativas de reforzamiento.

La primera actividad corresponde a la validación de las propiedades mecánicas de la fibra de acero galvanizado. Para ello, se llevará a cabo una recopilación de fichas técnicas de la malla a emplear para tener conocimientos previos de sus propiedades mecánicas. Luego, se realizarán seis ensayos de adherencia entre malla de acero galvanizado y la unidad de albañilería, y tres ensayos de tracción para la malla. Finalmente, se procesaron los resultados de laboratorio para validar las propiedades pre-escritas en las fichas técnicas.

La segunda actividad corresponde a la elaboración de un modelo numérico con elementos finitos de un muro de albañilería reforzado con fibra de acero galvanizado, a escala natural, ante cargas cíclicas en su plano. Para ello, se realizará una capacitación en el manejo del software ABAQUS FEA. Luego, se procederá con el modelado del muro, a la definición de los materiales que componen el modelo y a la elección del tipo de análisis a realizar. Finalmente, se procesarán los resultados obtenidos del modelo numérico para su posterior validación con los resultados experimentales de la tercera actividad.

La tercera actividad corresponde a la evaluación del comportamiento de tres muros de albañilería a escala natural reforzado con fibra de acero galvanizado ante cargas cíclicas en su plano. Para ello, se eligieron tres muros de seis que fueron ensayados en una tesis previa hasta un límite de reparabilidad (Manchego y Pari, 2016). Estos muros necesitarán una reparación previa al reforzamiento, lo cual será realizado en dos trabajos específicos. El primer trabajo consistirá en reparar la viga de cimentación de cada muro, ensanchándola de 300 mm a 800 mm y manteniendo el mismo peralte de 350 mm. El segundo trabajo consistirá en reparar los daños identificados en cada muro, para lo cual se picaron las fisuras existentes de tal forma que se abarque una franja de 50 mm de ancho que cubra cada fisura a reparar. Y en retirar los trozos de ladrillo triturados identificados para reemplazarlos por mortero de reparación. El tercer trabajo consistirá en rellenar las fisuras con mortero de reparación y en limpiar la superficie para la colocación de la malla de refuerzo. Posterior a la reparación de los muros, se procedió

a la colocación de las mallas de refuerzo y a la preparación de la superficie de acabado. Finalmente se ensayaron los tres muros reforzados ante desplazamiento cíclico lateral siguiendo un protocolo predeterminado y los lineamientos del FEMA 461, para pasar a procesar los resultados y comparar los obtenidos en el modelo numérico.

La cuarta y última actividad corresponde a la comparación de la capacidad sísmica y viabilidad técnica-económica de los sistemas de reforzamiento de la literatura con el propuesto. Para ello, se recolectará información técnica y literaria sobre ensayos experimentales acerca de sistemas de reforzamiento en muros de albañilería confinada. De los cuales se elegirán cuatro para ser comparados con la alternativa propuesta. Finalmente se generaran tablas y gráficos comparativos de las comparaciones realizadas.

Capítulo II

Marco teórico y estado del arte

Este capítulo abarca el marco teórico de la investigación, el cual tiene por objetivo describir las teorías y conceptos más importantes de la presente tesis. Se explican ciertos términos relacionados a sismos, albañilería confinada, reforzamiento sísmico, fibra de acero galvanizado, modelo numérico, etc. Por otro lado, un segundo punto que se abarca es el estado del arte relacionado al tema de investigación, el cual muestra una compilación de resultados sobre estudios anteriores y los esfuerzos que se ha venido elaborando para reducir la vulnerabilidad de las construcciones de albañilería confinada.

2.1. Marco teórico

Albañilería confinada

Es aquel sistema estructural compuesto por muros de ladrillos o unidades de arcilla cocida. Los muros son confinados lateralmente y superiormente por elementos de concreto: viga y columnas de confinamiento, ver figura 2.1 (a). Ambos elementos de confinamiento deben ser vaciados después de la construcción del muro y su conexión con los ladrillos puede ser dentada o al ras. Ambas razones justifican que los elementos de confinamiento y el muro respondan monolíticamente antes cargas laterales (Okail et al., 2014). La columna y viga de confinamiento otorgan ductilidad al sistema; asimismo, el pórtico de concreto funciona como arriostres cuando el sistema está sujeto a cargas perpendiculares al plano (San Bartolomé et al., 2011). Este es un sistema predominante en el Perú tal como muestra la figura 2.1 (b).

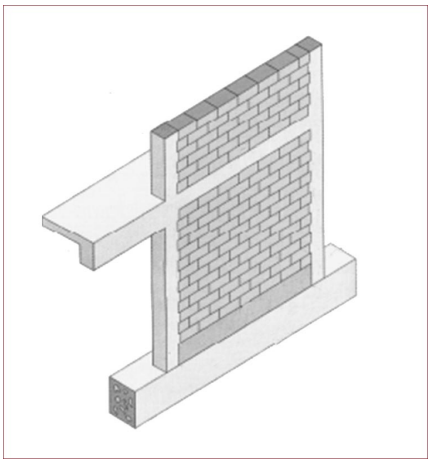

(a) muro de AC

(b) viviendas de AC

Figura 2.1: Tipología constructiva de albañilería confinada

Vulnerabilidad, peligro y riesgo sísmico

La vulnerabilidad es el daño que puede ocurrir en una estructura solo en función de sus características propias (Muñoz, 2011). El tipo de construcción, la formalidad y orden en la obra, acatarse a las normativas son algunos parámetros que definen las características propias de resistencia, rigidez y ductilidad de la estructura. Mientras mejores características propias posea la estructura, su vulnerabilidad será menor. Por otro lado, el peligro está relacionado directamente con la ubicación de las edificaciones. Ello debido a que la severidad de los sismos depende de las características del suelo, panorama sismotectónico y topografía local (Muñoz, 2011). Finalmente, el riesgo sísmico es el daño posible en una estructura originado por el peligro que la amenaza y su vulnerabilidad (Muñoz, 2011). El riesgo puede ser controlado reduciendo la vulnerabilidad y no el peligro que es una amenaza natural.

Fibra de acero galvanizado (FAG)

Es un tejido unidireccional o bidireccional formado por micro-filamentos de alta resistencia de acero galvanizado, fijado en un micro-red de fibra de vidrio que facilita las fases de instalación (Fig. 2.2). Esta fibra es instalada con una matriz inorgánica, la cual puede variar en función de los requisitos de diseño y construcción.

El tejido de refuerzo estructural es fácil de manejo, ya que combina en sí mismo excelentes propiedades mecánicas, de instalación y alta durabilidad gracias al galvanizado

de alambres individuales. El tejido de fibras de acero galvanizado tiene recursos estructurales y mecánicos únicos, muy superior a los tejidos tradicionales de fibra de vidrio, arámida y carbono. De este modo, particularmente, es eficaz en las diferentes aplicaciones para el refuerzo estructural o reforzamiento sísmico.

Figura 2.2: Rollo de fibra de acero galvanizado

Modelación numérica

Es una herramienta útil para predecir el comportamiento de las estructuras mediante su representación en distintos programas de cómputo. El comportamiento generalmente abarca desde la etapa lineal, a través de la fisuración y degradación hasta la pérdida total de la resistencia (Lourenço, 1997). Prediciendo el comportamiento es posible poder controlar los estados límites de servicio, comprender los mecanismos de falla, y evaluar la seguridad estructural según Lourenço (1997). Adicionalmente, es empleado para la validación de resultados experimentales. Para asegurar los beneficios mencionados es necesario que leyes constitutivas estén correctamente definidas de la mano de procesos de solución avanzada que provienen de la discretización de un elemento tras adoptar el método de elementos finitos (MEF) para simular el comportamiento estructural. La figura 2.3 muestra como un muro de albañilería confinada es dividido en varios elementos para su análisis. En ella se ha evaluado el desplazamiento del nodo superior derecho ante una carga lateral de 110 [kN].

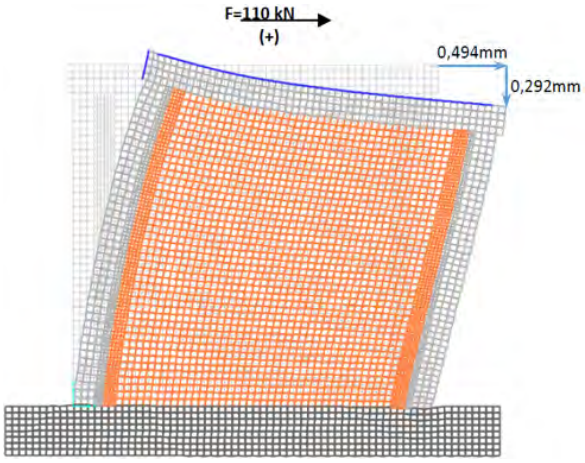

Figura 2.3: Análisis de un muro de AC mediante elementos finitos

El enfoque numérico puede ser clasificado en tres grupos de acuerdo al nivel de precisión que se requiera: micro modelamiento detallado, micro modelamiento simplificado y macro modelamiento. El primero considera tanto al mortero como a la unidad de albañilería como elementos continuos, mientras que a la interfaz unidad/mortero como un elemento discontinuo como se detalla en la figura 2.4 (a). El segundo grupo, como señala la figura 2.4 (b), aumenta ligeramente la sección del ladrillo que es representado por elementos continuos, y combina el comportamiento del mortero y la interfaz en elementos discontinuos llamados “joints". Finalmente, la figura 2.4 (c) muestra que el macro-modelo unifica la unidad de albañilería, mortero e interfaz unidad/mortero en un compuesto continuo.

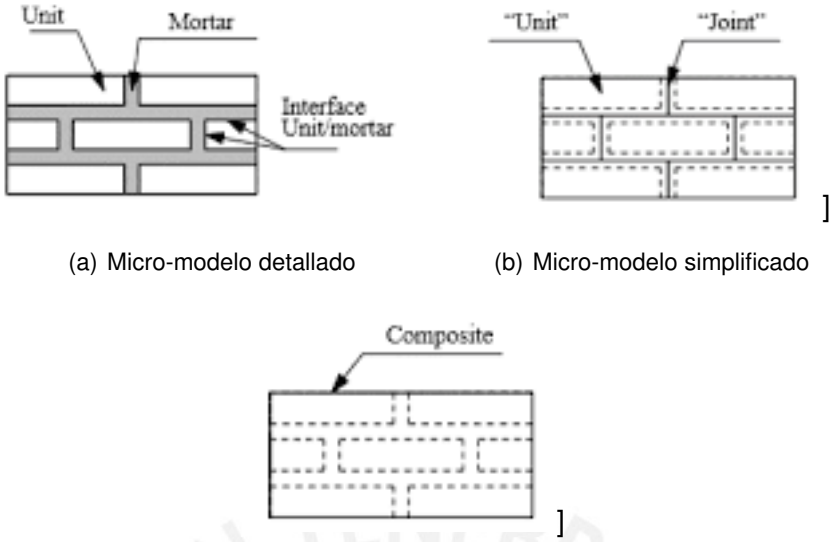

(a) Micro-modelo detallado (b) Micro-modelo simplificado

(c) Macro-modelo

Figura 2.4: Tipos de modelamiento numérico

Macro-modelo

Este enfoque asume al material como homogéneo y no hace diferencia entre unidad de albañilería, mortero e interfaz. En esta estrategia, las propiedades de los elementos se engloban en uno solo y se pierde la precisión. Estas propiedades que engloban se obtienen de ensayos experimentales en el que se tiene como muestra pilas y muretes de albañilería. La simplificación que presenta este enfoque hace posible un menor esfuerzo computacional que involucra menor tiempo requerido de cálculo y memoria, así como la generación de un mejor y rápido mallado (Lourenço, 1997).

La aplicación del macro modelo generalmente son para estructuras que están compuestas por muros con el suficiente largo para asumir que los esfuerzos en ellos sean uniformes.

Micro-modelo

Es un enfoque heterogéneo que permite un análisis detallado de estructuras como la de albañilería confinada. En esta estrategia se representa necesariamente las propiedades de cada elemento por separado, y con ello se alcanza el principal objetivo de representar de cerca la albañilería. Por lo mencionado, la precisión del micro-modelo es mayor; sin embargo, esto trae consigo un mayor coste computacional.

Según Lourenço (1997), los estudios del presente enfoque son necesarios para una

mejor entendimiento del comportamiento local de las estructuras de albañilería. Este enfoque se divide del siguiente modo: micro-modelo detallado y simplificado. Ambos fueron descritos en párrafos anteriores. Se puede agregar que mientras las lineas potenciales de fractura para el micro-modelo detallado se ubican en la interfaz, para el micro.modelo simplificado se ubican en los “joints". Asimismo, el modelo simplificado pierde cierta precisión al omitir los efectos de poisson del mortero (Lourenço, 1997).

Reforzamiento sísmico

Algunos sistemas estructurales no son capaces de resistir cargas laterales impuestas por un terremoto (e.g. albañilería confinada), y frecuentemente fallan en forma frágil. La técnica que busca mejorar este comportamiento mediante el aumento de la capacidad sísmica y retraso del colapso es el reforzamiento sísmico (Bhattacharya et al., 2013). Es así que es un proceso que modifica las estructuras para lograr los objetivos mencionados. Por ello, el reforzamiento sísmico es un proyecto de construcción importante que puede impactar en los propietarios, ocupantes y comunidad en general. Se ha planteado estrategias para el reforzamiento sísmicos, algunas de ellas son:

- El aumento de la capacidad global, lo cual se realiza comúnmente mediante la adición de refuerzos transversales o nuevas paredes estructurales.
- La reducción de la demanda sísmica a través de amortiguación y/o el uso de los sistemas de aislamiento de la base.
- El aumento de la capacidad local de los elementos estructurales. Esta estrategia adopta un enfoque más rentable para actualizar de forma selectiva la capacidad local de los componentes estructurales individuales.

Cargas dentro del plano

Son aquellas que actúan de forma paralela al plano conformado por la superficie mayor del elemento. Ante estas surgen patrones de daño típicos en estructuras de albañilería como se muestra en la figura 2.5. El primer tipo es uno de los principales tipos de falla por esfuerzos de tracción diagonal. Este puede ser controlado mediante la mejora de la adherencia entre la unidad de albañilería y mortero. El segundo tipo de falla es por cizallamiento, y ocurre cuando las conexiones entre paredes continuas son de resistencia adecuada. Ello hace que la resistencia al corte se movilice en el plano de la pared,

después se desarrollan grietas por cizallamiento (Bhattacharya et al., 2013). La falla por volteo es el tercer tipo, el cual tiene por origen posibles conexiones pobres entre muro y suelo/pared. Finalmente, la última imagen muestra el fallo por flexión en el plano cuyas grietas se muestran en la parte inferior derecha.

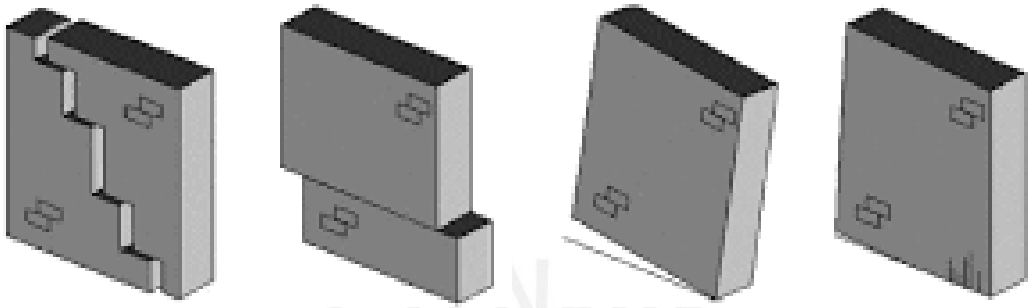

(a) Tracción diagonal (b) Cizallamiento (c) Volcamiento (d) Flexión

Figura 2.5: Fallas típicas por cargas en el plano

Cargas fuera del plano

Son aquellas cargas perpendiculares al plano de elementos estructurales como muros de albañilería. Estas actúan tanto hacia dentro como hacia fuera del muro causando principalmente tensiones de flexión (FEMA, 2009).

En construcciones de albañilería se generan algunos modos de falla repetitivos. Uno de los principales tipos son los generados por el fallo de la unión angular que conduce el colapso fuera del plano. Asimismo, otro modo de falla es el caracterizado por la expansión de grietas de cizallamiento en las paredes que tienen inicio en las esquinas de las aberturas en la pared.

También se ha visto que ocurre la falla fuera del plano en largos tramos y se derrumba el muro como resultado de una mala conexión entre las paredes y el techo como se ve en la figura 2.6. Este es un tipo de falla bastante peligroso, ya que al derrumbarse las paredes puede producirse el colapso de los pisos superiores y por ende de toda la estructura.

Figura 2.6: Falla fuera del plano en una estructura de albañilería

Según Bhattacharya et al. (2013), los modos de falla mencionados pueden ser controlados con la mejora de ciertas características de la albañilería. Por ejemplo, mientras mejor sea la conexión entre las paredes de ladrillo, el derribo fuera del plano podrá ser controlado. Asimismo, si se mejora la conexión de en las esquinas de las paredes, se evitará la desintegración en las uniones de las esquinas. Finalmente, se debe asegurar una adecuada conexión entre el muro o pared y suelo/techo para tratar de contrarrestar el último modo de falla presentado.

2.2. Estado del arte

Las construcciones de albañilería confinada son consideradas una de las más populares a nivel mundial por su fácil y rápida construcción, y por su bajo costo (Alcocer et al., 2003). Específicamente, su uso es común en el centro y sur de América, sureste de Europa, India y otras partes de Asia (Bhattacharya et al., 2013). Sin embargo, eventos telúricos alrededor del mundo han mostrado el pobre desempeño sísmico de las estructuras existentes de albañilería y la alta vulnerabilidad sísmica asociada a este tipo de construcciones (Marcari et al., 2016). La figura 2.7 (a) muestra la distribución geográfica de los sismos en el mundo. Como se observa esta distribución coincide con la ubicación de los lugares donde hay más presencia de construcciones de AC señalado por la figura 2.7 (b).

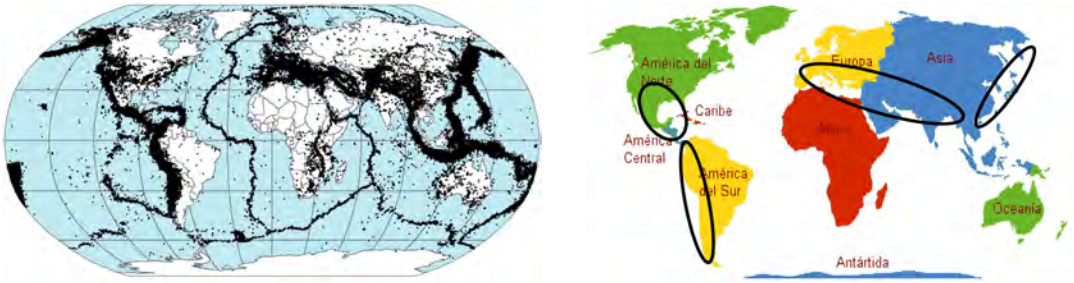

(a) (b)

Figura 2.7: (a) Distribución de epicentros de todos los terremotos ocurridos entre 1963 y 1998 (Lowman y Montgomery, 1998) (b) Señalización de construcciones de AC

Este tipo de construcciones han sido practicados en Chile y Colombia desde 1930´s y en México desde 1940´s (Brzev and Perez, 2014). Según Alcocer et al. (2003), en México hasta el año 2003, más del 70% de sus construcciones eran de albañilería. En Punjab, una de las provincias más pobladas de Pakistan, el 63% del total de edificaciones son de albañilería (Rafi et al., 2012). En Perú, el porcentaje de personas que viven en casas de AC se redujo de un 83% a un casi 60% según las estadísticas hechas por el INEI entre los años 2007 y 2014.

En respuesta al uso masivo de la AC alrededor del mundo y a su alta vulnerabilidad sísmica, numerosas investigaciones fueron llevadas a cabo para reforzar estas estructuras y así mejorar su resistencia, ductilidad y rigidez como se mencionó en el capítulo 1. A continuación se realiza una revisión literaria de ensayos experimentales de muros de albañilería reforzados para comprender mejor su comportamiento sísmico. Además una revisión literaria de modelos numéricos para muros reforzados es presentada con la finalidad de reconocer distintas técnicas que se han venido desarrollando.

2.2.1. Revisión literaria sobre ensayos experimentales de albañilería reforzada

El tipo de carga aplicada y la técnica de reforzamiento empleada influyen en la respuesta sísmica de muros de albañilería reforzada. Especímenes de muros con refuerzo pueden estar sujetos a cargas fuera y dentro del plano. Asimismo, en el tiempo aparecieron distintas técnicas y materiales para el reforzamiento como el acero, Polímeros Reforzado con Fibra (FRP), Matriz Cementosa Reforzada con Fibra (FRCM), Mortero reforzado con Fibra (FRP), entre otros. Esta sección recopila las investigaciones realiza-

das alrededor del mundo sobre muros de albañilería reforzados ante carga cíclica en su plano.

Sistemas de reforzamiento basados en acero estructural

Los esfuerzos que se realizaron empleando varillas de acero como material de refuerzo se muestran en la figura 2.8.

La primera alternativa consiste en el reforzamiento con malla electrosoldada (San Bartolomé and Castro, 2002) realizado en la PUCP. La campaña consistió en el ensayo de un muro de AC a escala natural ante carga cíclica controlado por desplazamiento antes y después del reforzamiento. Durante el experimento se notó que el muro original falló por corte, mientras que el muro reforzado falló por flexión. Asimismo, se concluyó que la rigidez lateral elástica del muro reparado alcanzó el 85% del muro original y la resistencia del muro con refuerzo fue 40% más que el muro sin refuerzo, mientras que la ductilidad aumentó 35%.

La segunda alternativa consiste en el reforzamiento con malla de acero (Luján, 2016) también hecho en la PUCP. En esta ocasión se ensayaron tres muros de AC a escala natural ante carga cíclica controlado por desplazamientos antes y después del reforzamiento. Los resultados arrojaron que la ductilidad aumentó en un 36% y la resistencia máxima en un 32% en relación a los muros sin reforzar; sin embargo, la rigidez no se recuperó, sino está en el orden de 7.8% por debajo del muro original.

Finalmente, la tercera alternativa consiste en el reforzamiento con un sistema de cables en forma de aspa anclados en los muros. En Australia, Chuang et al. (2004) ensayaron tres muros de albañilería reforzados con el sistema de cables y un muro no reforzado ante carga cíclica controlada por desplazamiento y carga axial de compresión. Los cables poseen una gran resistencia a la tensión y corrosión. Por ello, pueden absorber esfuerzos de tensión, además de incrementar la rigidez y ductilidad del sistema. Se puede mencionar que los cables se llevaron el 50% de la carga aplicada al muro. Por lo tanto, la resistencia última del muro reforzado es dos veces la del no reforzado. Finalmente, los lazos histeréticos del ensayo para el muro con y sin reforzamiento muestran que el primero disipa mayor cantidad de energía que el segundo.

(a) (b) (c)

Figura 2.8: Sistemas de reforzamiento con (a) malla electrosoldada (San Bartolomé and Castro, 2002) (b) malla de acero (Luján, 2016) y (c) cables de acero (Chuang et al., 2004)

Polímeros reforzados con fibra (FRPs)

A pesar del excelente comportamiento post refuerzo de los sistemas de refuerzo con malla electrosoldada, malla de acero y sistemas de cables, se notó ciertas desventajas. Las desventajas están asociadas al costo y tiempo requerido para la instalación, y la cantidad de masa que es añadida a la estructura. Por ello, a finales de la década del siglo XX, el estudio y uso de polímeros como material de refuerzo empezó a expandirse. Los FRPs consisten en fibras de alta resistencia impregnadas en una resina polimérica. Presentan una solución conveniente pues prácticamente no añaden masa a la estructura, son manejables, flexibles, de rápida instalación, y tienen un excelente desempeño en términos de resistencia a la tracción y durabilidad (Quagliarini et al. (2016); Gattesco and Boem (2017)). Asimismo, los FRPs son métodos cuyo empleo en el reforzamiento de patrimonios culturales es bastante adecuado. Características como el no ser invasivo permite aplicaciones como la anterior.

Esta técnica de reforzamiento varía de acuerdo al tipo de fibra que las componga. Entre los principales tipos destacan los siguientes: Carbon Fiber Reinforced Polymer (CFRP), Glass Fiber Reinforced Polymer (GFRP) y Aramid Fiber Reinforced Polymer (AFRP).

La aplicación de CFRP en albañilería es un método muy eficaz para mejorar la capacidad e integridad de la mampostería de ladrillo sometida a carga lateral. En la PUCP, los investigadores San Bartolomé and Coronel (2009) analizaron la efectividad del CFRPcomo refuerzo estructural (Fig. 2.9). Durante la campaña experimental, se ensayó un muro de AC ante carga cíclica en su plano controlada por desplazamientos antes y después

de reforzamiento. Se observó que el muro original falló por fuerza cortante y se presentó delaminación de las bandas de FRP en el muro reforzado. Entre los resultados cuantitativos, se nota que la rigidez inicial del muro reforzado fue el 50 % del original. Asimismo, la resistencia del muro reforzado fue mayor al original en 22 % y la ductilidad del muro reforzado es mayor al original, pues admite una capacidad de deformación del 73 % mayor. Finalmente, se puede destacar que el reforzamiento ayudó a controlar el ancho de grietas.

Figura 2.9: Muro de AC reforzado con CFRP, extraída de San Bartolomé y Coronel, 2009

La distribución de las bandas de CFRP es un parámetro que influye en la respuesta sísmica de los muros de albañilería. La configuración horizontal y diagonal son las más empleadas. Santa María et al. (2004) realizaron una investigación experimental que permite comparar el comportamiento post refuerzo de muros de albañilería con configuración diagonal y horizontal (Fig. 2.10). Los resultados mostraron que el arreglo diagonal es más efectivo que el horizontal en términos de resistencia al corte, ya que puede incrementar la resistencia de los muros no reforzados hasta un 70 %. La rigidez también aumentó con la configuración diagonal; sin embargo, la configuración horizontal de las láminas FRCP no tuvo mayor efecto en la rigidez. Asimismo, ambas configuraciones logran disminuir el grosor y extensión de las fisuras; por ende, las fallas frágiles por corte decrecen (técnicas). Se debe tener especial cuidado con esta técnica, ya que ante cargas altas de compresión, las láminas de FRCP tienden a desprenderse del muro, pues su resistencia a esfuerzos de compresión es nula.

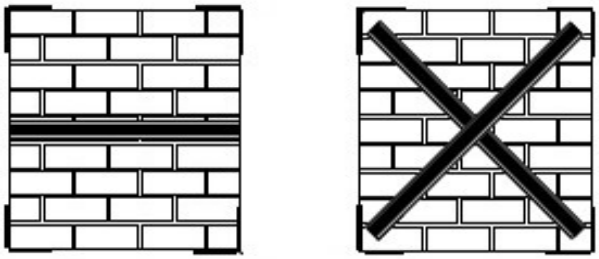

Figura 2.10: Configuración horizontal y diagonal de CFRP, extraída de Santa María et al., 2004

La adherencia parcial o completa de las bandas de CFRP también influye en el comportamiento. Kassem et al. (2016) ensayaron especímenes reforzados con configuraciones adheridas y no adheridas de la fibra de carbono como señala la figura 2.11 (a) y (b) respectivamente.

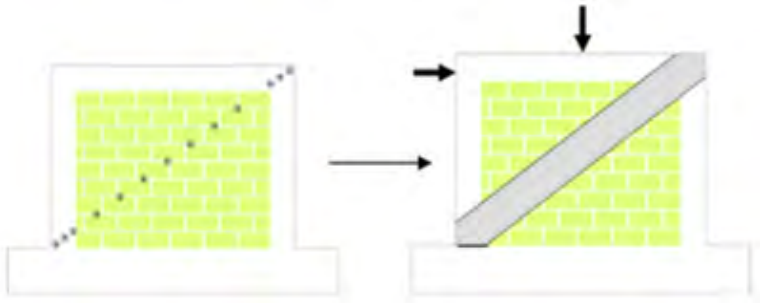

(a) Sistema adherido

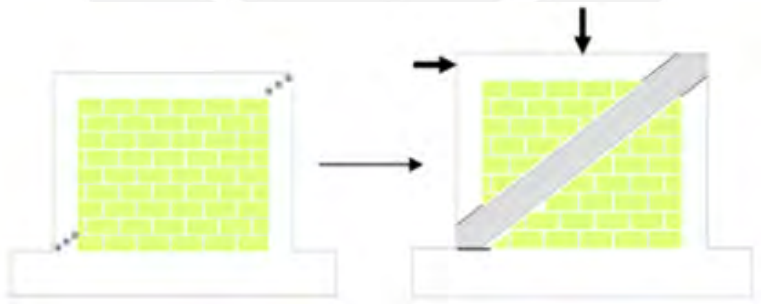

(b) Sistema no adherido

Figura 2.11: Configuración de CFRP, extraída de Kassem et al. (2016)

Se concluyó que ambas configuraciones aumentan la capacidad final lateral del muro de AC en una proporción comprendida entre 34% y 95%. La ductilidad también se incrementa en una proporción de 64% a 104%. Sin embargo, entre las dos técnicas, la

más dúctil es el sistema no adherido debido al efecto de la longitud no adherida entre puntos de anclaje.

Otra técnica bastante difundida, es la GFRP. En el año 2009, San Bartolomé and Coronel (2009) analizaron la efectividad de la técnica de reforzamiento con varillas de fibra de vidrio en la PUCP como lo muestra la figura 2.12 (a). Para ello, ensayaron un muro de AC a escala natural a carga cíclica en el plano pre y post refuerzo. El muro original falló por corte. Durante la rehabilitación se colocaron varillas de fibra de vidrio de forma horizontal cada dos hiladas. Los resultados arrojaron que rigidez inicial del muro reforzado es el 73% del original y la resistencia no se incrementó en más de 3%.

Del mismo modo, El-Diasity et al. (2015) investigaron el comportamiento de muros de AC reforzados con fibra de vidrio. El sistema de reforzamiento se muestra en la figura 2.12 (b) cuya configuración es diagonal. Estos muros estaban a una escala de 0.8. Resultados de la investigación mostraron que la técnica mejora la resistencia lateral en un porcentaje que oscila entre 25% y 32%. Asimismo, se señala que hay una mejora en el total de la energía de disipación en un porcentaje que oscila entre 25% y 32%. El arreglo diagonal permitió prevenir una falla de corte por tracción diagonal.

Cabe mencionar que esta técnica es fácil de aplicación pues personas sin mucha experiencia lo pueden realizar con algunas capacitaciones previas.

(a) (b)

Figura 2.12: Muro de AC reforzado con (a) Varillas de vidrio, extraída de San Bartolomé and Coronel (2009) (b) GFRP, extraída de El-Diasity et al. (2015)

Matriz Cementosa Reforzada con Fibra (FRCM)

A pesar de las ventajas del sistema FRP, este presenta algunas limitaciones ligadas a su aplicación en superficies húmedas. Además, dado que los FRPs necesitan resina epóxica como material aglutinante, el conjunto no resiste temperaturas más allá de la

vítrea, tiene pobre comportamiento en ambientes alcalinos y carece de permeabilidad al vapor (Triantafillou and Papanicolaou, 2006).

Con la finalidad de combatir estas desventajas inducidas por el aglutinante orgánico, surge una nueva opción. Esta consiste en un sistema de reforzamiento llamado Fiber Reinforced Cementitious Matrix (FRCM), el cual reemplaza la resina epóxica por una matriz cementosa. Asimismo, esta técnica de reforzamiento consta de una o varias capas de fibras secas. Estas fibras están embebidas en una matriz típicamente hecha de la combinación de cemento portland, humo de sílice y cenizas volantes que actúan como aglutinante inorgánico. Del mismo modo que los FRPs, pueden utilizar distintos tipos de fibra como el carbono, fibra de vidrio, entre otros.

Investigaciones previas como Prota et al. (2006) y Parisi et al. (2013) mostraron un mejoramiento significativo en la resistencia y ductilidad de muros de albañilería reforzados con diferentes capas de FRCM ensayadas bajo cargas de compresión diagonal. Asimismo, (Papanicolau et al., 2008) estudió el reforzamiento de muros reforzados con FRCM bajo cargas cíclicas dentro y fuera del plano, y también mostró ganancia de resistencia y ductilidad. A pesar de los esfuerzos previos, aún falta realizar más estudios para caracterizar completamente los FRCM y cuantificar su contribución con la resistencia y ductilidad. Por ello, Babaeidarabad et al. (2013) emprendió una campaña experimental que estuvo conformada por ensayos de nueve muros bajo compresión diagonal. Dos esquemas de refuerzo se aplicaron: el tejido de refuerzo estaba compuesto por una red de fibra de carbono en una o cuatro capas en sentido horizontal y vertical con un espaciamiento de 10mm. Resultados mostraron que el aumento de la resistencia es de 2.4 a 4.7 veces de los de sin refuerzo usando una o cuatro capas respectivamente. Asimismo, en base al diagrama esfuerzo cortante- deformación, puede observarse que este tipo de refuerzo es efectivo para aumentar la ductilidad y rigidez. Sin embargo, debe notarse que el aplicar solo una capa de refuerzo brinda mayor rigidez que con cuatro capas.

En el año 2013, Babaeidarabad et al. (2013) estudiaron el comportamiento de muros de albañilería reforzados con fibra de carbono en una matriz cementosa (CFRCM) ante cargas fuera del plano. Para ello, como se observa en la figura 2.13, durante la campaña experimental se ensayaron nueve muros con dimensiones de 142 x 122 x 9.2 [cm^2], y dos esquemas de refuerzo fueron implementados. En uno de ellos el tejido de refuerzo estaba compuesto por una red de fibra de carbono en una capa y la otra en cuatro capas. Las capas podrían figurar en sentido horizontal y vertical con un espaciamiento

de 10 [mm].

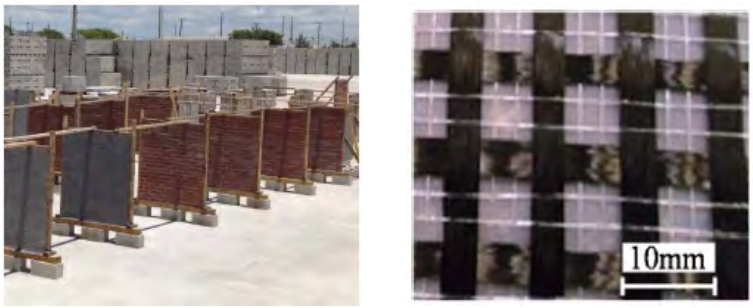

(a) (b)

Figura 2.13: Campaña experimental (a) Disposición de nueve muros (b) Configuración de la malla de fibras, extraída de Babaeidarabad et al. (2013)

Resultados mostraron que el aumento de la resistencia a la flexión es de 2.8 a 7.5 más que de los de sin refuerzo usando una o cuatro capas respectivamente. Asimismo, en base a los resultados del diagrama momento–deflexión puede observarse que este tipo de refuerzo es efectivo para aumentar la ductilidad y rigidez. Sin embargo, debe notarse que el aplicar solo una capa de refuerzo brinda mayor rigidez que con cuatro capas. Finalmente, los investigadores definen w_f como el ratio de refuerzo calibrado:

$$w_f = \left(\frac{\rho E_{fm}}{f_m}\right)\frac{h_{eff}}{t_m} \tag{2.1}$$

Si este valor excede 0.6, la falla por corte será la que controle. Entonces, cantidad de refuerzo FRCM más allá de ese valor es improductivo.

Morteros reforzados con textiles o fibra

El reforzamiento para muros de albañilería también puede ser embebido en un revestimiento de mortero inorgánico. Es así que aparece el sistema Fiber Reinforced Mortars (FRM) o Textile Reinforced Mortars (TRM). Este resulta ser adecuado pues también prescinde de la resina epóxica orgánica. Ello conduce a una alta resistencia al fuego, protección contra rayos UV. Además, el empleo de morteros inorgánicos permite una mejor adherencia a una superficie no uniforme como el de la albañilería (Gattesco and Boem, 2017). Consecuentemente, FRMs llaman la atención por su aplicación a estructuras históricas (Ghiassi et al., 2016). En contraste a FRCMs cuyo aglutinante es el cemento, el mortero de los FRMs puede estar hecho de materiales naturales, lo cual presenta un

menor impacto ambiental (Marcari et al. (2016); Gattesco and Boem (2017)).

Entre los materiales que pueden acompañar a los FRMs destacan la fibra de vidrio, fibra de carbono, fibra de basalto y acero. Esta variedad hace posible la existencia de FRMs con propiedades físicas y mecánicas diferentes. En consecuencia, un diseño y aplicación unificada es una tarea difícil (Ghiassi et al., 2016). Las investigaciones que buscan comprender mejor el comportamiento de la técnica TRM se enfocaron en ensayos bajo cargas de compresión axial y diagonal de muros de albañilería. Por ello, los estudios que se presentarán incluyen estos dos tipos de ensayos.

Marcari et al. (2016) investigaron el comportamiento de paneles reforzados con Mortero Reforzado con Fibra de Basalto (BTRM). Para ello, se ensayaron tres paneles no reforzados bajo compresión axial y dos especímenes no reforzados bajo compresión diagonal, tres especímenes reforzados en una sola cara y dos reforzadas en ambas caras. Los resultados muestran que hay un buen incremento del esfuerzo cortante alrededor de 40 % con BTRM en una sola cara y 60 % en ambas caras. Asimismo, la rigidez inicial aumentó en un 13 % para el reforzamiento en un sola cara y de 39 % para ambas caras. La ductilidad incrementó en un factor de 2.3 y 1.5 para el reforzamiento en una y dos caras respectivamente. Por otro lado, Yardim and Lalaj (2016) también estudio el comportamiento de muros de albañilería reforzados con la técnica TRM. En este caso, su estudio se basó en una comparación entre materiales que pueden conformar los TRM´s. Se comparó el desempeño del TRM enlucido que fue aplicado en una y dos caras de los muros, TRM con polipropileno enlucido y el ferro cemento como muestra la figura 2.14. Se construyeron 10 muros a escalada de 0.5 y 2 muros a escala natural. Todos los especímenes se sometieron al ensayo de corte diagonal bajo los lineamientos del ASTM 519. En el ensayo, se observó que varias fisuras delgadas aparecieron antes que el muro fallará. Los muros que se reforzaron en solo una cara son los que peor comportamiento exhibieron. La rigidez al corte se incrementó en mayor porcentaje cuando se reforzó con polipropileno (278 %) y ferro cemento (2240 %), a diferencia con TRM enlucido en ambas caras que solo aumentó 76 %. También se evaluó el incremento de la resistencia al corte. El polipropileno, ferro cemento y TRM enlucido en ambas caras lograron un incremento de 401 %, 412 % y el 300 %, respectivamente. En conclusión, la técnica TRM con los materiales ensayados es eficiente para reforzar muros de albañilería. Sin embargo, entre los tres materiales, se resalta los resultados obtenidos con el ferro cemento como técnica TRM.

(a) (b) (c)

Figura 2.14: Aplicación de materiales. (a) TRM enlucido en ambas caras, (b) Ferro cemento, (c) Polipropileno

De los diferentes sistemas de reforzamiento mencionados, algunos destacan en aspectos de economía, tecnicidad o capacidad sísmica. Difícilmente se encuentra una solución que englobe los tres aspectos. Por ello, los estudios continúan en búsqueda de la mejor solución.

2.2.2. Revisión literaria sobre ensayos de caracterización para el sistema TRM

Los sistemas TRM están ganando popularidad como refuerzo estructural. Su facilidad de instalación y efectividad son algunas ventajas que han fomentado su aplicación en albañilería. A pesar de la buena solución que puede ser, aún falta información en el conocimiento de sus propiedades fundamentales. Las propiedades fundamentales pueden obtenerse a través de ensayos de control como ensayos de tracción de la fibra, ensayos de adherencia entre fibra y unidad de albañilería y ensayos de compresión del mortero. Hasta el momento todavía hay una brecha en las normas que controlan estos ensayos. Por ello, ha elaborado una revisión bibliográfica de estudios experimentales que incluyan los tres tipos de ensayos de caracterización mencionados. En cada investigación se resalta aspectos importantes que se deben de tener en cuenta en el diseño de las pruebas de caracterización. Estos parámetros son el sistema de sujeción, la longitud de anclaje, protocolo de ensayo y las dimensiones de las muestras.

Gattesco and Boem (2017) realizaron ensayos de caracterización para el sistema de reforzamiento Mortero Reforzado con Fibra de Vidrio (GFRM). Durante la campaña experimental se realizaron ensayos de tracción en la fibra de vidrio como se muestra en la figura 2.15. Estos ensayos fueron ejecutados acorde a la guía de diseño CNR DT 203.

Debido a que esta fibra no actúa sola, sino que está embebida en un mortero inorgánico, se ejecutaron otros ensayos como de tracción de fibra reforzada con mortero, ensayos de adherencia entre GFRM y albañilería, extracción y empalme acorde a la figura 2.16.

El ensayo de tracción de la fibra sola se hizo con fibra GFRM de 500 [mm] de largo libre. El sistema de sujeción se basó en la inserción de ambas partes finales de la fibra en un cilindro de aluminio relleno de resina epóxica que sirvió como anclaje. El ensayo a tracción de la fibra con el mortero se realizó en una muestra de 132 x 900 x 30 [mm^3]. Para el sistema de sujeción fue necesario emplear fibra de carbono en los extremos de la muestra para evitar concentraciones de esfuerzos y daños locales. La longitud de agarre fue de 180 [mm] en los extremos; esta distancia resultó ser el largo necesario obtenido de las pruebas de adherencia para prevenir el deslizamiento entre fibra y mortero.

(a) (b)

Figura 2.15: Ensayos de tracción (a) en la fibra (b) en el conjunto fibra-mortero, extraída de Gattesco and Boem (2017)

En el ensayo de adherencia, las muestras variaban la longitud de contacto entre el mortero–fibra y la albañilería: 120 [mm], 180 [mm] y 240 [mm], con un ancho constante de 132 [mm]. En el primer caso, el desprendimiento del mortero ocurrió. En el último caso, la falla longitudinal de la fibra ocurrió. Mientras que una longitud de adherencia de 180 [mm], resultó ser la mejor opción ya que aprovecha la máxima resistencia de las fibras a tracción. Por otro lado, en el ensayo de extracción o pull–out se observó que para una carga de 2.2 [kN] hay una separación gradual entre la fibra y mortero. Finalmente para el ensayo de empalme, se solaparon las fibras y fueron colocadas a la mitad del espesor del mortero. Resultados señalan que 180 [mm] de traslape permite la explotación total de la resistencia de la malla.

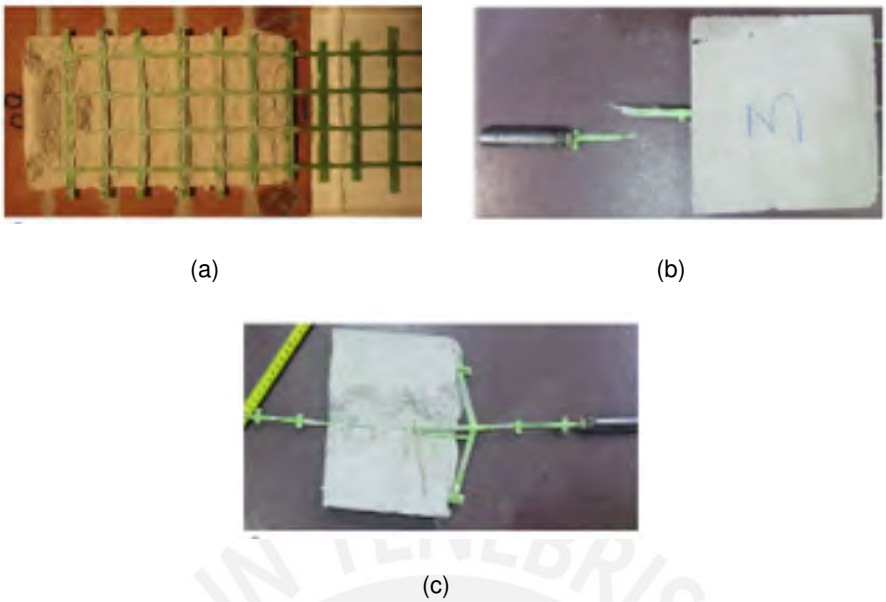

(a) (b)

(c)

Figura 2.16: Ensayo en el conjunto. (a) Ensayo de adherencia (b) Ensayo de extracción (c) Ensayo de empalme, extraída de Gattesco and Boem (2017)

Información y lineamientos para ensayos de adherencia aún falta. Por ello, Martins et al. (2015) realizaron cinco ensayos de adherencia entre TRM y albañilería, pull-out, entre otros. El TRM que empleó fue una malla compuesta por filamentos trenzados (BCRs). Una de las características más importantes de este ensayo es la longitud de adherencia. En este caso, esta longitud fue de 200 [mm] con un ancho de 100 [mm] y un espesor del mortero de 20 [mm]. El estudio resaltó que el esfuerzo de adherencia es mejor con la malla trenzada que con alguna otra malla TRM, ya que la trenza rugosa mejora el agarre entre el mortero y fibra.

Otra interesante investigación realizada en el 2016 fue realizada por Ghiassi et al. (2016). Durante la campaña experimental, se ejecutaron ensayos en el material compuesto y fibra o mortero solo. Los ensayos son de adherencia entre TRM y albañilería, tracción de TRM, pull–off. El ensayo de tensión directa se realizó en una franja de fibra de 50 x 450 mm para obtener el esfuerzo de tensión y módulo de elasticidad (Fig. 2.17). Para el sistema de sujeción se colocaron pestañas de aluminio pegadas en los extremos de la fibra para asegurar una distribución de esfuerzos uniformes y evitar deslizamientos en zonas de agarre. Asimismo, se realizaron cinco ensayos de adherencia y los autores proponen para el ensayo de adherencia considerar una longitud de adherencia de 150 [mm] y un ancho constante de 50 [mm] a lo largo de la zona de adherencia. También

señalan que previo a la colocación del mortero de refuerzo y la malla, se debe dejar reposando el ladrillo sobre agua durante 24 [hrs] para evitar la absorción del agua del mortero que se colocará encima. Luego, se colocaron 5 [mm] de capa de mortero, para después presionar ligeramente la malla de refuerzo, y luego se colocó otros 5 [mm] de mortero sobre este. Al final quedó 10 [mm] de capa de mortero y se quedó 3 [$meses$] en el laboratorio hasta la fecha de ensayo. El sistema de sujeción para el ensayo se muestra en la figura 2.17, se observa como con ángulos de acero se restringe el movimiento del espécimen y cómo se aplica la carga.

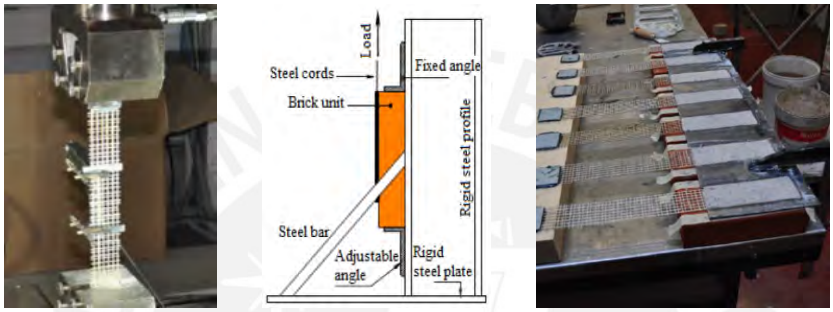

(a) (b) (c)

Figura 2.17: Ensayos (a) tracción de la fibra, (b) esquema de ensayo de adherencia y (c) espécimen de ensayo

En el 2017, De Santis et al. (2017) emprendieron una campaña experimental para caracterizar el sistema TRM hechos de acero, basalto, carbono, vidrio, PBO y arámida. Para ello, llevaron a cabo ensayos de tracción en el compuesto y fibra sola, y ensayos de adherencia TRM–albañilería. El ensayo que presentó mayor detalles fue el de adherencia. Entre los aspectos más detallados resaltan la rugosidad de la superficie de albañilería, la longitud de adherencia, dimensiones y características del espécimen. La rugosidad debe presentarse en la albañilería para una mejor adhrencia con el TRM. La longitud de adherencia debe considerarse al menos 250 [mm]. Finalmente, entre las características se nota una distancia entre el borde lateral y el lado del ladrillo de al menos 20 [mm] y una distancia no adherida de 30 [mm] para minimizar efectos de borde. Los apectos de longitud de adherencia y dimensiones del espécimen se observa en la figura 2.18.

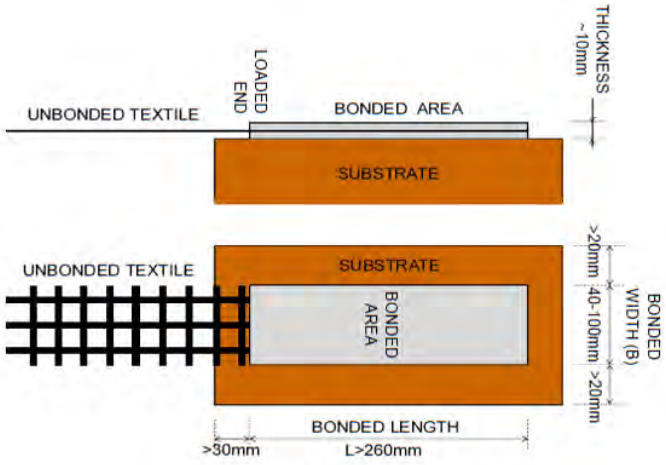

Figura 2.18: Características del espécimen para ensayo de adherencia extraída de De Santis et al. (2017)

Durante el desarrollo de la campaña experimental hecha por De Santis et al. (2017), también se realizaron ensayos de tensión y adherencia para conocer las propiedades mecánicas del sistema TRM basado en fibra de acero y mortero de cal natural. Se discutieron otros aspectos como la influencia de la longitud de adherencia, propiedades mecánicas del mortero, condiciones de preparación y curado de especímenes, protocolo de ensayo e instrumentación para contribuir con la optimización del uso de TRMs y en el desarrollo de recomendaciones para ensayos en laboratorio. Para el ensayo de tracción se emplearon pestañas de aluminio adheridas en los extremos con una resina epóxica con dimensiones de 90 x 55 x 3 [mm^3]. La malla de refuerzo fue pegada correctamente a las pestañas y las esquinas de las pestañas se redondearon cuidadosamente para evitar una falla prematura causada por esfuerzos concentrados. Los resultados a través de la curva esfuerzo–deformación mostraron que el rango elástico es hasta 60-80 % del esfuerzo máximo.

Para el ensayo de adherencia se construyeron arreglos de ladrillo con dimensiones de 250 x 120 x 55 [mm^3] y el mortero del TRM tuvo una resistencia a la compresión de aproximadamente 5 [N/mm^2]. Asimismo, la longitud de adherencia fue de 260 [mm] y se consideraron otras distancias como se muestra en la figura 2.182.18. Previo a la instalación del mortero y fibra, la superficie fue limpiada con una espátula metálica y se removió el polvo con aire comprimido. Finalmente se mojó la superficie para que no sea absorbida el agua del mortero de refuerzo. Para colocar el sistema TRM, primero se esparció una capa de mortero de 5 [mm] de espesor, luego se colocó la malla a

presión manual, y finalmente se esparció otros 5 [mm] de mortero. Los especímenes fueron curados por 28 días. Las condiciones de borde para el espécimen consistieron en bloquear el movimiento en la dirección de la carga aplicada y evitar la rotación en su plano. Para ello, colocaron cuñas de acero arriba y abajo como muestra la figura 2.19.

(a) Tensión de la fibra (b) Adherencia TRM–Albañilería

Figura 2.19: Ensayos de control

La caracterización de cualquier material en general hace posible un procedimiento de diseño correcto. Asimismo da paso a la posibilidad de realizar un modelamiento numérico. En este caso, con las propiedades del sistema TRM establecidas (mortero y fibra), es posible realizar un análisis de elementos finitos de un muro, vivienda o estructura de albañilería reforzada con esta técnica.

2.2.3. Revisión literaria sobre modelamientos numéricos de albañilería reforzada

Los modelos numéricos son herramientas esenciales para predecir el comportamiento de estructuras de albañilería reforzada. Su empleo antes de ensayos experimentales permitirá poder tomar mejores decisiones sobre las condiciones de ensayo como la cantidad de refuerzo. En esta sección se revisarán las investigaciones hechas sobre modelos numéricos de albañilería reforzada.

Wang et al. (2016) estudió el comportamiento no lineal de muros de albañilería reforzados con el sistema TRM. La investigación discute la validación del modelo para simular el comportamiento no lineal del sistema TRM. Asimismo, presenta el efecto que tiene el compuesto TRM en la respuesta inelástica de los muros y los modos de falla de los mismos.

Por un lado, el proceso de validación que consiste en comparar resultados numéricos

con experimentales utilizó resultados de ensayos de tracción del TRM de la investigación hecha por Carozzi and Poggi (2015). El propósito del proceso de validación fue encontrar la técnica de modelaje del TRM (tamaño del mesh) y la ley constitutiva de tracción del mortero.

Para el modelo de validación se empleó el programa *DIANA 10* y se hizo un macro modelo que representó el comportamiento no lineal del mortero adoptando el modelo *total strain rotating crack model* el cual también fue usado en las investigaciones hechas por Basili et al. (2015) y Garofano et al. (2015). El mortero se asumió homogéneo con refuerzo distribuido. La malla de refuerzo se modeló como embebida en el mortero, y por eso las deformaciones son iguales tanto del mortero como fibra. Esto último se puede asemejar a la hipótesis de adherencia perfecta entre el concreto y acero. Las condiciones de borde fueron acorde al ensayo experimental y se hizo un análisis estático no lineal aplicando una historia de desplazamientos verticales incrementales en el extremo superior del espécimen como señala la figura 2.20. Las propiedades mecánicas se extrajeron de ensayos experimentales y fichas técnicas. Se recomienda un tamaño menor a 5 [mm] de acuerdo a su análisis de sensibilidad de malla.

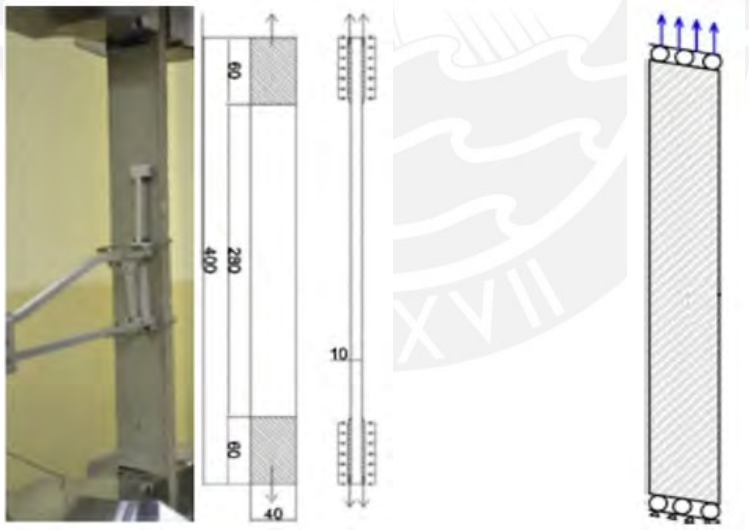

(a) (b)

Figura 2.20: (a) Ensayo de tracción hecho por Carozzi and Poggi (2015) (b) Condiciones de borde y aplicación de carga extraida de Wang et al. (2016)

La variedad de fibra y mortero en el mercado origina que la caracterización sea una tarea complicada. Por ello, durante el proceso de validación también se escogió el modelo parabólico de compresión y se discutieron dos modelos de leyes constitutivas de

tracción para el mortero que se muestran en la figura 2.21. Ambos modelos arrojaron resultados que se ajustan correctamente a los resultados experimentales en cuestión de resistencia máxima, deformación última, rigidez y comportamiento después del agrietamiento. Sin embargo, el segundo modelo fue escogido para los siguientes modelos por su comportamiento más realista en la fase del desarrollo de patrones de grietas.

(a) Compresión (b) Tracción I (c) Tracción II

Figura 2.21: Leyes constitutivas para el mortero, extraída de Wang et al. (2016)

Posteriormente, Wang et al. (2016) creó un modelo numérico para evaluar el comportamiento de paneles de albañilería reforzados con TRM ante cargas verticales y laterales en un análisis estático no lineal (pushover). Los paneles tuvieron dimensiones de 1000 x 1000 x 100 [mm^3] y ambas caras fueron reforzadas con 5 [mm] de espesor de TRM. El modelo de elementos finitos de dos dimensiones fue hecho en el software *DIANA*. Tanto el muro de albañilería como la capa de TRM fueron modelados con elementos shell perfectamente adheridos. El tamaño de malla fue de 5 [mm] como se recomendó. Por un lado, la albañilería fue modelada como un modelo continuo elasto-plástico y anisotrópico siguiendo el modelo *rotating smeared crack*. Las propiedades mecánicas de la albañilería fueron tomadas de la investigación hecha por Grande et al. (2008) y modificadas de acuerdo a ensayos experimentales de caracterización (Tabla 2.1).

Por otro lado, el TRM fue modelado como modelo continuo isotrópico siguiendo el modelo ?rotating smeared crack?. Se escogió un modelo parabólico de compresión y un modelo de tracción 2 cuya elección se discutió anteriormente. Las propiedades del mortero y fibra se basaron en fichas técnicas y ensayos pasados. Las fibras se asumen embebidas en el mortero con perfecta adherencia y un comportamiento lineal hasta la falla.

La parte inferior (base) del panel de albañilería se considera fija y la parte superior se sujeta con una viga de acero rígida con restricciones rotacionales. Finamente para

resolver las ecuaciones no lineales se emplea el método iterativo modificado de Newton-Raphson junto con el método de búsqueda de línea.

La albañilería reforzada con TRM puede presentar tipos de fallas complejos, tres de ellos son: deslizamiento entre mortero- albañilería, deslizamiento entre fibra- mortero y ruptura por tracción de la fibra. Durante el modelo que se hizo, se tuvo en cuenta la ruptura por tracción de la fibra al momento de ingresar las propiedades mecánicas y leyes constitutivas. El comportamiento adherente entre fibra y mortero se considera teniendo en cuenta un buen comportamiento a tensión del mortero. Si se desea simular el deslizamiento del mortero se puede optar por modelos específicos de daño o por factores de reducción al esfuerzo de tensión del mortero. Por otro lado si no se evita el posible deslizamiento de la fibra en bordes o conexiones con otros elementos, debe ser considerado en el modelo. Para ello, también se puede aplicar un factor de reducción en el esfuerzo de tensión y en la rigidez de las fibras. Algunos programas como DIANA permiten definir una ley constitutiva para el deslizamiento para las fibras embebidas.

Tabla 2.1: Parámetros mecánicos de la albañilería adaptada de Wang et al. (2016)

Parámetros	Símbolo	Valor
Módulo de Young [MPa]	E	8000
Módulo de Poisson	ν	0,15
Esfuerzo de tensión en x [MPa]	σ_{tx}	0,25
Esfuerzo de tensión en y [MPa]	σ_{ty}	0,35
Esfuerzo de compresión en x [MPa]	σ_{cx}	7,80
Esfuerzo de compresión en y [MPa]	σ_{cy}	8,50
Energía de fractura en tensión en x [Nmm/mm^2]	G_{fx}	0,018
Energía de fractura en tensión en y [Nmm/mm^2]	G_{fy}	0,054
Energía de fractura en compresión en x [Nmm/mm^2]	G_{fcx}	15,00
Energía de fractura en compresión en y [Nmm/mm^2]	G_{fcy}	20,00
Factor que determina la contribución del esfuerzo cortante en la falla por tensión	α	1,00
Factor que une el esfuerzo de compresión	β	$-1,00$
Factor que controla la contribución del esfuerzo cortante a la falla por compresión	γ	3,00
Factor que especifica la deformación plástica equivalente correspondiente al esfuerzo de compresión pico	K_p	0,0012

Zhang et al. (2017) desarrolló un modelo numérico de muros de albañilería reforzados con FRP de basalto ante carga sísmica en el plano. A diferencia del trabajo anterior, Zhang et al. realizaron un meso–modelo o también llamado micro–modelo simplificado, y no uno macro. El modelaje a meso escala permite ver la evolución del daño en la albañilería. Estos modelos pueden o no tomar en cuenta el posible deslizamiento entre ladrillos y mortero. Para tomarlo en cuenta se debe unir los nodos del ladrillo y mortero en todos los grados de libertad y si no se desea tomar en cuenta se puede emplear contacto o elementos como resortes, interfaz, etc. para reemplazar el mortero. El programa que emplearon fue *ABAQUS*, ya que este brinda una variedad de interfaces que incluyen elementos cohesivos que son bastante usados para simular el deslizamiento y simulan el comportamiento de las juntas de mortero. Es así que se modeló el ladrillo como sólido y el mortero como elemento cohesivo de espesor cero. El elemento cohesivo se creó con

el método de *Share node* que es descrita por la guía de *Abaqus*, la cual requiere que el elemento cohesivo y los elementos vecinos tenga el mismo tamaño de malla. Dado que el refuerzo tiene entre 0.15 y 0.30 [mm] de espesor, se modelo el FRP como un elemento shell asumiendo una adherencia perfecta con la albañilería, y para ello se usó la opción *tie* en *ABAQUS*.

Por otro lado, se definieron leyes constitutivas para el elemento cohesivo (mortero), unidad de ladrillo y refuerzo FRP. Para reproducir la fractura por tensión y corte en el mortero, el comportamiento del elemento cohesivo se define con la ley de tracción–separación que comúnmente se usa para definir comportamiento de deslizamiento o delaminación en las interfaces. Esta ley comprende tres criterios según *ABAQUS*: comportamiento elástico lineal, criterio de iniciación de daño y criterio de evolución de daño. La ley de tracción–separación consiste en que hay un comportamiento lineal hasta que la deformación y/o esfuerzo del material en estudio satisfaga el criterio de iniciación de daño. Así la degradación empieza y el comportamiento del material satisface la ley de evolución de daño. Para las unidades de albañilería se selecciona el modelo *Concrete Damage Plasticity* (CDP) para simular el comportamiento no lineal. Este modelo permite evaluar dos tipos de mecanismo de falla: por tensión y compresión; además de capturar la degradación del material. Finalmente, el FRP es modelado como un material ortotrópico y que permanece en el rango elástico.

Capítulo III

Evaluación experimental

3.1. Experimental and Analytical Bond Behavior of Masonry Strengthened with Steel Reinforced Grout (SRG)

Experimental and Analytical Bond Behaviour of Masonry Strengthened with Steel Reinforced Grout (SRG)

Jhoselyn Salsavilca[1*], Jhair Yacila[2], Nicola Tarque[3], and Guido Camata[4]

[1]Pontifical Catholic University of Peru. Department of Civil Engineering. San Miguel 15088, Lima, Peru. Email: jsalsavilcap@pucp.pe
[2]Pontifical Catholic University of Peru. Department of Civil Engineering. San Miguel 15088, Lima, Peru. Email: jhair.yacila@pucp.edu.pe
[3]Pontifical Catholic University of Peru. Department of Civil Engineering. San Miguel 15088, Lima, Peru. Email: sntarque@pucp.edu.pe
[4]University "G.d'Annunzio" of Chieti and Pescara. Department of Engineering and Geology. Pescara 65127, Italy. Email: g.camata@unich.it
[*]Corresponding author. T: +51 975583794. Email: jhoselyn.salsavilca@pucp.pe

ABSTRACT

Steel Reinforced Grout (SRG) is gaining popularity as a retrofitting system for structural elements due to advantages such as its effectiveness and ease of installation. The good performance of SRG system has turned out to be substantially dependent on the behaviour of the bond between the composite layer and the substrate. This paper presents an experimental study of the bond behaviour of Peruvian masonry strengthened with SRG, along with a characterization of the materials by means of direct tensile tests on the fiber and compression tests on the mortar. The criteria of the sample's geometry, construction and test procedure are discussed for each trial since up to now there has been a gap in the standards that control them. In addition, an analytical model is employed in order to obtain design bond parameters to define a Cohesive Material Law (CML). The strain profile, slip profile, force profile and shear stress profile along the length of the bond are presented for each bond test. Finally, an optimal bond length is proposed for SRG material and a fracture energy value at the matrix–fiber interface.

INTRODUCTION

Confined Masonry (CM) is a type of construction widely diffused in Peru since it is easy and quick to install. According to INEI (2014), masonry dwellings constitute 74% of the total buildings in Peru and 60% of them are informal (i.e. constructions that are built without technical or professional control). In the case of informal dwellings, seismic events have evidenced their high vulnerability, which leads to human and material losses. Therefore, it is necessary to reinforce informal CM with strengthening techniques to develop a better seismic performance.

There are several methods of strengthening. One of the most appealing is external reinforcement with composite materials. Composite materials are regarded as an efficient method because of their advantages, such as ease of application, high strength/weight ratio, and versatility (i.e. they are applicable to different types of substrate).

Composite materials can consist of fibers or high strength textiles embedded in an organic matrix, such as epoxy resin, a technique known as fiber reinforced polymer (FRP), or in inorganic matrices, such as cementitious or mortar (FRCM). These techniques are a convenient solution since they do not add mass to the structure, they are easy to handle, are flexible, and can be installed quickly. However, there has arisen the idea of replacing epoxy resin with an inorganic matrix, so as to overcome some of the disadvantages related to its inapplicability on wet surfaces, its poor performance at high temperatures and in alkaline environments,

possible hazards for workers, the incompatibility of the resin with the substrate materials, and lack of water vapor permeability (Triantafillou and Papanicolaou, 2005; Papanicolaou et al., 2008; Razavizadeh et al., 2014). In this regard, TRM seems to be one of the most convenient and in addition is reversible (i.e. it can be removed from the surface without major damage) and has a competitive performance in terms of tensile strength and durability (Quagliarini et al., 2017; Gattesco and Boem, 2017).

A TRM system can comprise different types of fiber: basalt, glass, carbon, polyparaphenylene benzobisoxazole (PBO), and aramid, among others. When high strength steel fibers are embedded in a mortar based matrix, the system is known more as steel reinforced grout (SRG), which has already been studied as a strengthening technique for concrete and masonry structures (Borri et al., 2009, 2011; Wobbe et al., 2004; Huang et al., 2005; Barton et al., 2005).

Although previous investigations have focused on evaluating properties such as its shear and flexural capacity, the performance of the bond between the composite layer and the substrate is another property that determines its effectiveness as a strengthening technique. Past studies that have addressed this include (Razavizadeh, 2013; Razavizadeh et al., 2014; Ghiassi et al., 2016; Grande et al., 2013; De Santis et al., 017a,b; De Felice et al., 2018). The bond is a key mechanism in transferring the stresses from the structural elements to the SRG, so a comprehensive understanding of its governing mechanism is crucial for strengthening and design purposes (Razavizadeh et al., 2014). In this way, there is a need to continue investigating the behaviour of the bond between the composite layer and the substrate.

Standards such as CNR-DT200 (2013) contain sections governing the design process that consider the evaluation of the debonding strength. However, that analysis is only focused on the FRP between concrete and masonry, and not for SRG. Although it is common to apply FRP formulations to SRG, it would be better to calibrate parameters for these formulations based on experimental tests. Hence, the need to carry out SRG bond tests in order to get more information about its behaviour is totally justified.

For this purpose, the present paper shows and discusses the results of 5 experimental bond tests for Peruvian masonry strengthened with SRG in terms of bond strength, slip at peak load, and the failure mode, among others. The experimental campaign, carried out at the Structural Laboratory of the Pontifical Catholic University of Peru, also includes direct tensile tests on the steel fiber and compressive tests on lime-based mortar, with the aim of characterizing the materials.

In addition, different trilinear cohesive material laws for the behaviour of SRG-Peruvian masonry have been calibrated, starting from the experimental load response, by means of analytical formulations (Carozzi et al., 2016; D'Antino et al., 2018). Employing these CMLs and the provided analytical formulations within a fracture mechanics approach, an average value for the optimal bond length and fracture energy is proposed.

MECHANICAL CHARACTERIZATION OF MATERIALS

To perform and analyse the shear bond tests, it is recommended to get a better knowledge about each component, such as the lime mortar, the steel galvanized textile, the joint mortar, and the bricks. Therefore, additional tests were also carried out for such a characterization. In particular, single fiber tensile tests were performed on the steel textile specimens and compressive tests were performed on cubic mortar specimens. In case of the employed bricks and joint mortar, a previous study characterized them and provided their mechanical properties, which are mentioned below.

Description of materials

SRG system

The galvanized steel textile is an ultra high tensile strength steel (UHTSS) and is coated with zinc. This textile is unidirectional and comprises cords, which are obtained by twisting two wires around three rectilinear ones. Each dry cord has a cross-sectional area equal to 0.538 mm^2.

The SRG system makes use of lime-based mortar also. This mortar, also called the matrix, functions as a binder and is made of lime of strength type M15 in accordance with EN 998-2 and type R1 in accordance

with EN 1504-3. Its low Portland cement content allows reducing the need to add organic compounds to prevent shrinkage. In addition, lime-based mortar is an eco-friendly product since it contains raw materials of natural origin and recycled minerals. The CO_2 emissions involved are low, and there are very low emissions of volatile organic substances (Kerakoll, 2017a). Lime-based mortars are suitable for application to historic substrates because they meet the compatibility requirements due to their relatively low Young's modulus (De Santis et al., 017a,b) and breathability with existing material.
The mechanical properties of the steel textile, based on technical data sheets, are collected in Table 1, which lists the tensile strength (f_{ts}), Young's modulus (E_s) and failure deformation (ε). In addition, it shows the cord density (c), spacing (i) and equivalent (design) thickness (t^*). For the lime mortar, the compressive strength (f_{cm}), Young's modulus (E_{cm}) and the tensile strength (f_{tm}) are provided by technical data sheets and listed in Table 1 as well.

Table 1. Properties of steel textile and mortar (SRG system) provided by manufacturer (Kerakoll, 2017a,b)

Material				
Galvanized Steel	Tensile Strength	f_{ts}	[MPa]	> 2800
	Young's Modulus	E_s	[GPa]	> 190
	Failure deformation	ε	[%]	> 1.5
	Cord density (low)	c	[cord/mm]	0.157
	Cord spacing	i	[mm]	6.35
	Equivalent thickness	t^*	[mm]	0.084
Mortar	Compressive strength	f_{cm}	[MPa]	> 15
	Tensile strength	f_{tm}	[MPa]	> 5
	Young's Modulus	E_{cm}	[GPa]	9

Bricks and joint mortar

The joint mortar of the masonry is a mixture of fine aggregate, cement, and enough water to provide a workable mixture. Its purpose is to bond and correct the imperfections of the masonry units in the construction process. A previous study (Manchego and Pari, 2016) carried out compressive tests on mortar specimens for which the geometry was $50 \times 50 \times 50$ mm (Fig. 1(a)). The mortar was used in a volumetric ratio of 1: 4 (cement: sand); the cement used was Portland Type I and the sand was thick, natural, and free of organic material and salts. For the masonry, hollow clay brick with dimensions of $230 \times 130 \times 90$ mm was tested by the aforementioned study, complying with Peruvian standard Ministerio de Vivienda (2006) (Fig. 1(b)). The compressive strength of the mortar and bricks were 14.40 MPa and 11.00 MPa, respectively.

Tensile behaviour of steel textiles: Tests and results

The fiber tensile test is an effective means for providing information about mechanical properties, such as the tensile strength and elastic modulus. Previous studies (De Santis et al., 017a,b; Ghiassi et al., 2016) have performed fiber tensile tests and provided recommendations for the procedure and geometry. The present study followed those indications.
A series of tensile tests were carried out at the Pontifical Catholic University of Peru on 5 specimens composed of galvanized steel fiber and aluminium tabs. The latter ($190 \times 55 \times 6$ mm) were glued by means of a strong adhesive (epoxy resin) on the ends of the specimens to assure a uniform stress distribution and prevent slips in the gripping areas that could affect the global strain response. The 5 samples shared the same geometry, with free length and width equal to 400 mm and 50 mm, respectively (Fig.2(a)). In addition, an extra length of 90 mm on each side was used with the aim of distributing the local stresses in the gripping

(a) (b)

Fig. 1. Specimens and experimental set-up for masonry materials: (a) compressive test on joint mortar; (b) compressive test on brick.

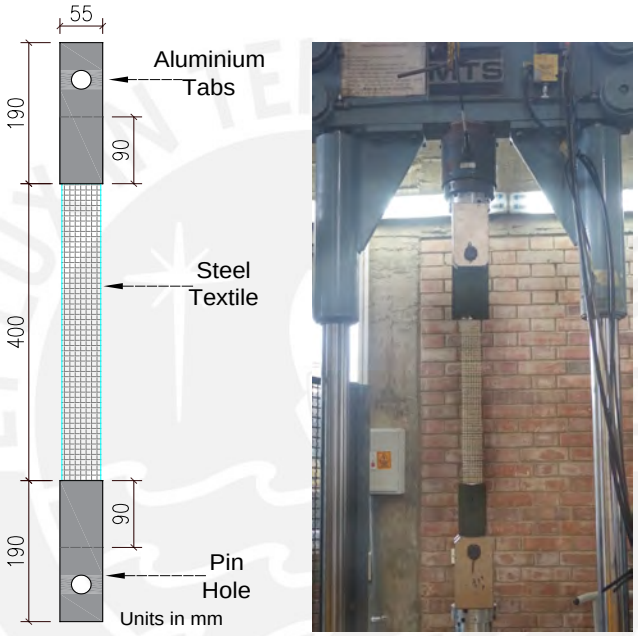

(a) (b)

Fig. 2. Mechanical characterization for steel textile: (a) sample's geometry; (b) tensile test.

areas. Therefore, with this minimum length, it is hoped to avoid local failures and succeed with the stress distribution.

The testing speed was selected based on ASTM (2017b), which specifies a speed of 2 mm/min for the FRP composite. Although the standard speed is not for single fiber, it is considered appropriate for steel galvanized textile since its elongation at failure is nearly equal to that of CFRP (1.67%). In this way, the velocity was 2 mm/min for this study.

The load was applied under displacement control at a rate of 2 mm/min and recorded by the load cell integrated in the universal testing machine. The stresses were computed by dividing the registered load by the cross-sectional area of the dry textile. This latter was obtained by multiplying the design thickness of the textile by the number of cords and by the cord spacing, or by multiplying the area of one cord by the number of cords (De Santis et al., 017a). The global displacements were recorded by a linear variable differential transformer (LVDT) integrated in the testing machine. The strains were evaluated as the displacements divided by the distance between the gripping wedges. Although the displacements registered by the machine

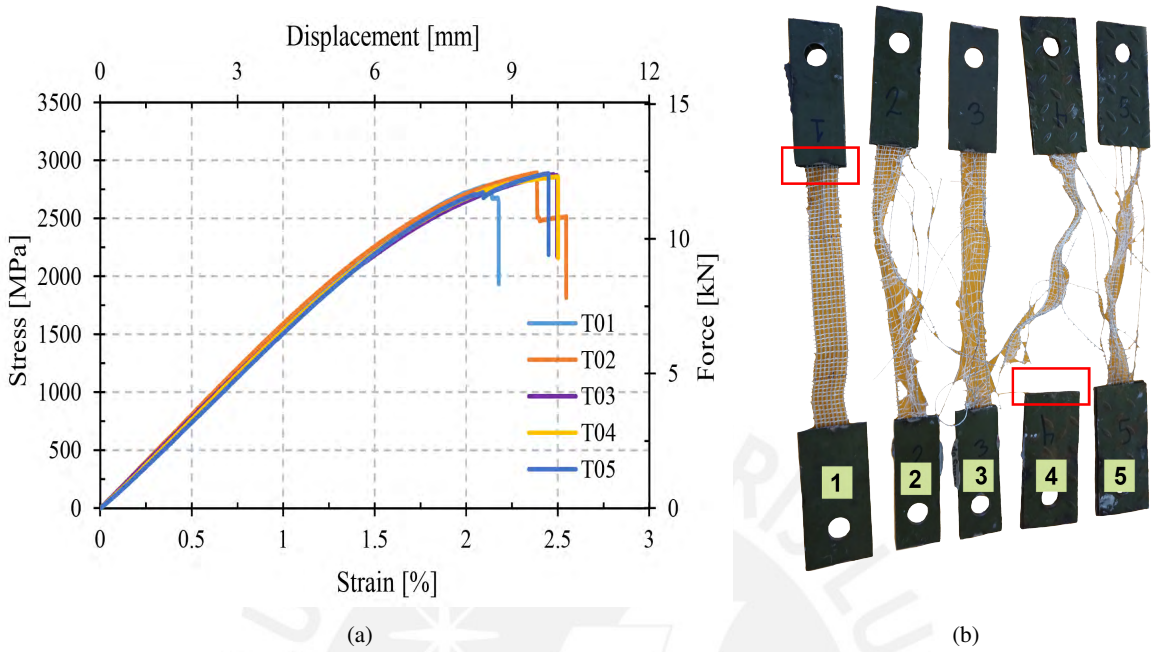

Fig. 3. Tensile behaviour of steel galvanized fiber: (a) strain–stress curves; (b) failure modes.

lead to a global response, which includes the gripping areas, it could be said that it is a local behaviour due to the strong adhesive used that does not allow an extra displacement.

The stress–strain curves (Fig. 3(a)) display an initial elastic behaviour up to about 60%–65% of the tensile maximum strength, followed by a non-linear phase before the peak. The readjustment of the equipment should be taken into account at the beginning of the test as it may cause a non-linear behaviour at the beginning of the stress–strain curves that must be corrected.

In this study, two failure modes (FM) were identified: (A) the nearly simultaneous failure of the cords along the free length of the textile, and (B) the rupture of the cords around the gripping areas. The first mechanism of failure (A) is a global one that indicates that the gripping systems succeeded in distributing the load uniformly over the width (De Santis et al., 017a). The second mechanism of failure (B) is a local one that indicates a stress concentration.

All specimens experienced the first mode, but, as an exception, the T01 and T04 failed to concentrate the stresses in the gripping areas, as is shown in Fig. 3(b).

The main results, such as peak stress (f_s) and corresponding load per unit width (F_s), secant Young's modulus (E_s) analysed between 10% and 50% of f_s, and strain (ε_s) regarding to peak stress are collected in Table 2.

Compressive behaviour of lime mortar: test and results

The lime mortar test was carried out according to American standard ASTM (2017a), which specifies that the dimension of the specimens is should be 50 mm (2 in) on each side of the cubic specimens, as shown in Fig.4(a).

For the test, 6 cubic mortar specimens were prepared and immersed in water for the curing process for 28 days to be tested by axial compression (Fig. 4(b)). The test protocol was defined with a universal machine with a loading speed of 100 kN/min, in accordance with the literature.

Table 2. Results of tensile test on steel textile

Specimen	E_s [GPa]	f_s [MPa]	F_s [kN/m]	ε_s [%]	FM
T01	160	2786	240	2.18	B
T02	161	2893	249	2.55	A
T03	155	2879	248	2.50	A
T04	155	2859	246	2.50	B
T05	153	2886	249	2.45	A
Average	157	2861	246	2.44	
COV	2.2%	1.5%	1.5%	6.1%	

(a) (b) (c)

Fig. 4. Mechanical characterization of mortar: (a) specimens; (b) compressive test; (c) typical failure mode.

The average compressive load and strength of the lime-based mortar were obtained as 60 kN and 22 MPa with a COV equal to 3.30% and 2.80%, respectively. Fig. 4(c) depicts the failure mode of the mortar under compression axial load. All specimens failed conically, which means that due to Poisson effects, the lateral sides tend to widen and since there is no confinement, these parts explode, leaving an intact core.

SHEAR BOND TESTS

The effectiveness of the SRG system lies in the performance of the bond between the substrate and the composite since the bond is a key mechanism in transferring stresses between the structural element and the strengthening system (Razavizadeh, 2013). Due to the critical importance of the bond for the overall performance of the composite system, a shear bond test is widely used as an effective means for the characterization of the behaviour of the bond between the externally bonded reinforcement and the masonry substrates (Ghiassi et al., 2012).

Specimens and test set-up

The presented single-lap shear bond tests followed the indications proposed by De Santis et al. (017a,b), whose investigations were the basis for developing the test recommendations by Rilem TC 250-CSM (Composites for the Sustainable strengthening of Masonry)(De Felice et al., 2018).
The shear bond test was carried out on 5 specimens comprising lime mortar, steel galvanized textile, and masonry prisms. The lime mortar and steel textile that make up the SRG system, and the bricks and joint mortar that make up the masonry prisms, were described in Section 2. For the masonry prisms, the arrangement was *running bond*, which is quite wide-spread in Peru (Fig. 5(a)).

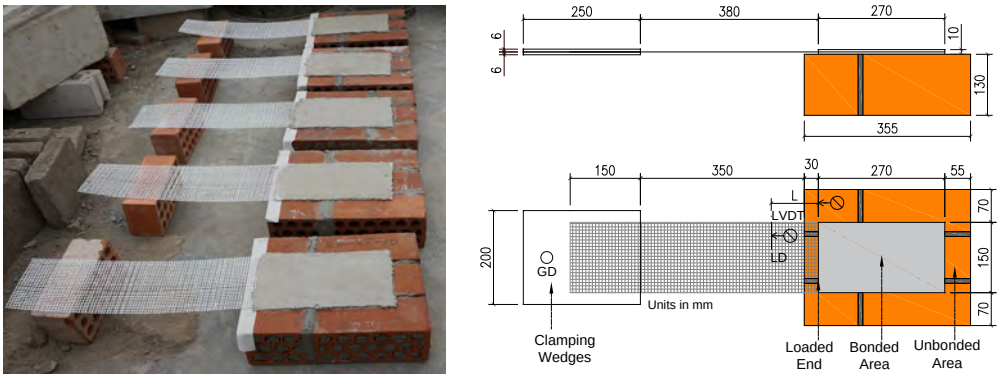

(a) (b)

Fig. 5. Geometry of SRG strengthened masonry samples: (a) specimens in laboratory; (b) scheme.

The SRG system applied on the substrate prisms ($290 \times 355 \times 130$ mm) has a bond length of 270 mm, leaving an unbonded length of 30 mm from the extremity of the masonry on the side of the application of the load, with the aim of minimizing edge effects (De Santis et al., 017a,b). The width was 150 mm and the length between the free lateral side of the prism and the end of the bonded area was 70 mm for all tests. The textile free length was 350 mm and an extra length of 150 mm was embedded in the clamping wedges to guarantee a correct distribution of the stresses. These specimens were characterized by placing the reinforcing strips parallel to the greater side of the brick as for masonry arrangements, which allows having more representative results. The final scheme is observed in Fig. 5(b).

The tests were carried out by blocking the masonry prism by rigid steel plates either at the back and at the front, and applying a vertical load (10 kN) to the substrate in the vertical direction, with the aim of avoiding rotations of the prisms. The vertical load was applied by means of two wood blocks located in unbonded lateral zones. These wood blocks function as a support for a metal bridge dividing the vertical load into two, as shown in section A-A in Fig.6.

Moreover, the alignment between the applied load (P) and the middle plane of the reinforcement was guaranteed by preparing clamping wedges with a hole (located in the middle) which, along with a pin, transmit the load to the whole system (Fig.6). In this way, the intensity of the normal stresses at the substrate–mortar interface, which are always present in single-lap tests due to the eccentricity between the push and pull forces, is limited. Two LVDTs were used to record the local (LD) and global (GD) displacements (Fig. 5(b)). For the GD, one end of the device was fixed to the substrate and the other one was fixed close to the pin hole (i.e. where the load is applied). For the LD, one end of the device was fixed to the substrate and the other one to the textile (making use of the wood plates), outside the bonded area, at a certain distance (L) from the first bonded section (Fig. 5(b)). Using the clamping wedges, the fiber is pulled out from the bottom by controlled displacements at a machine stroke speed of 0.3 mm/min. The clamping wedges were two metal tabs ($250 \times 200 \times 6$ mm) glued to the fiber with epoxy resin so that they adhered well and caused a uniform distribution of stress on the composite.

Results

The results of the shear bond tests (Table 3) were the maximum stress (or bond strength, f_b), the corresponding load per unit width (F_b), the shear strength regarding the bonded area (τ) and the slip (s); the exploitation ratios of the tensile strength (n_s), referred to dry textiles ($n_s = f_b/f_s$), and the failure mode (FM), also called the detachment mechanism.

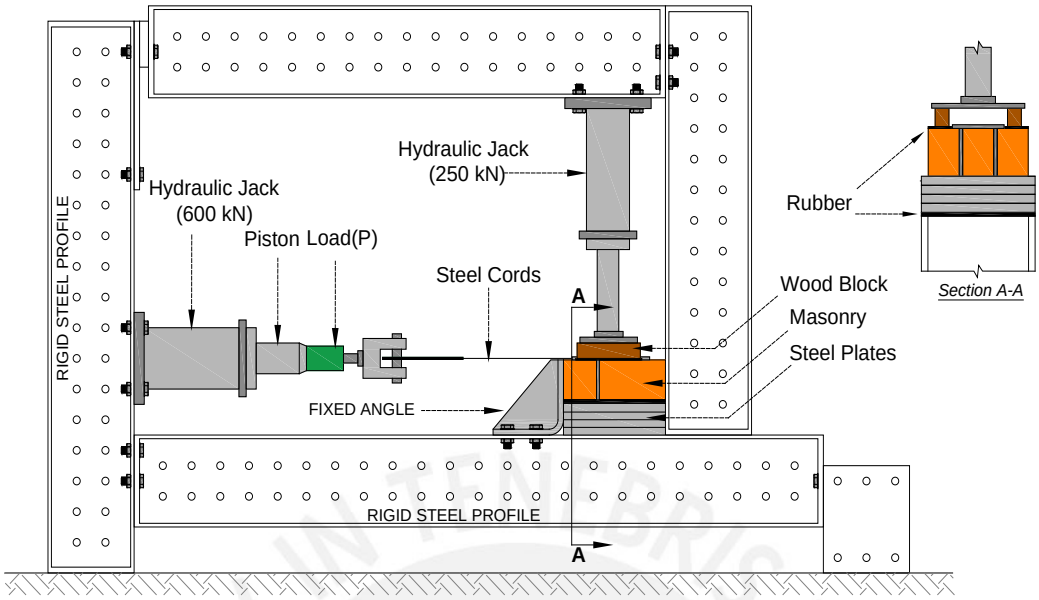

Fig. 6. Shear bond test set-up

For calculating the stress f_b, the load F was recorded by the load cell integrated in the testing machine and divided by the cross-sectional area of the textile. The slip (s) or relative displacement between the textile and the substrate at the loaded end of the reinforcement was calculated as

$$s = LD - \varepsilon\, L \tag{1}$$

where LD is the local displacement, ε is evaluated as the applied load divided by the sectional area and the Young's modulus E_s of the textile derived from tests on dry textile specimens, and L is the distance from the first bonded section (Fig. 5(b)). In this way, $\varepsilon\, L$ is the elastic elongation of the unbonded textile. This computation is possible by assuming that all the cords were equally loaded due to the gripping system.

The failure mode, indicated in Table 3, is according to the following classification proposed in Ghiassi et al. (2016); De Santis et al. (017a) : (A) debonding with cohesive failure of the substrate, (B) debonding at the mortar-to-substrate or (C) at the textile-to-mortar interface, (D) textile slippage within the matrix without or (E) with cracking of the outer layer of mortar, and, finally, (F) tensile rupture of the textile outside of the bonded area (Fig. 7). Failure modes D and E are very similar to each other; both are governed by the sliding of the cords.

The 5 specimens were named ADH0X, where X is the number of the specimen. After each test, it was observed that sample ADH01 experienced a localized debonding occurring at the textile-to-mortar and mortar-to-substrate interface with a premature cracking of the outer mortar layer and the rupture of the fibers (Fig. 8(a)). Moreover, during the testing of ADH02 there occurred a debonding with cohesive failure of the masonry (Fig. 8(b)). The specimen ADH03 presented a good bond strength at the mortar-to-substrate interface but not for the textile-to-mortar interface, causing a debonding at that interface (Fig. 8(c)). Exactly the same occurred for specimen ADH04. Finally, ADH05 presented a debonding at the textile-to-mortar interface combined with a premature cracking of the outer mortar layer without any rupture of the fibers (Fig. 8(d)). It is observed that only for ADH01 and ADH05 was premature cracking present along almost the entire bonded length, which may entail having similar results for both.

The applied stress f_b–slip s response curves (Fig. 9) display a good agreement at the lineal-elastic stage with the exception of ADH02, which is higher than the others from the beginning, associated to the test in

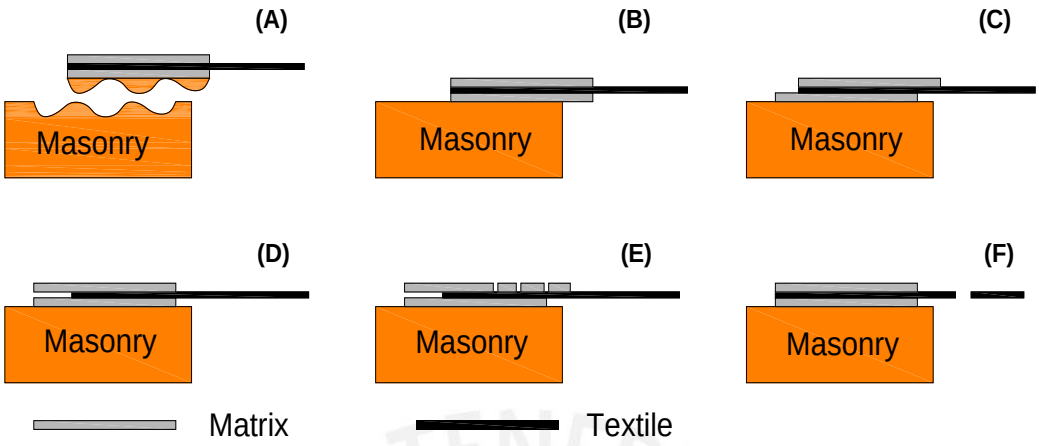

Fig. 7. Sketches of failure modes in shear bond tests (adapted from Ghiassi et al. (2016).

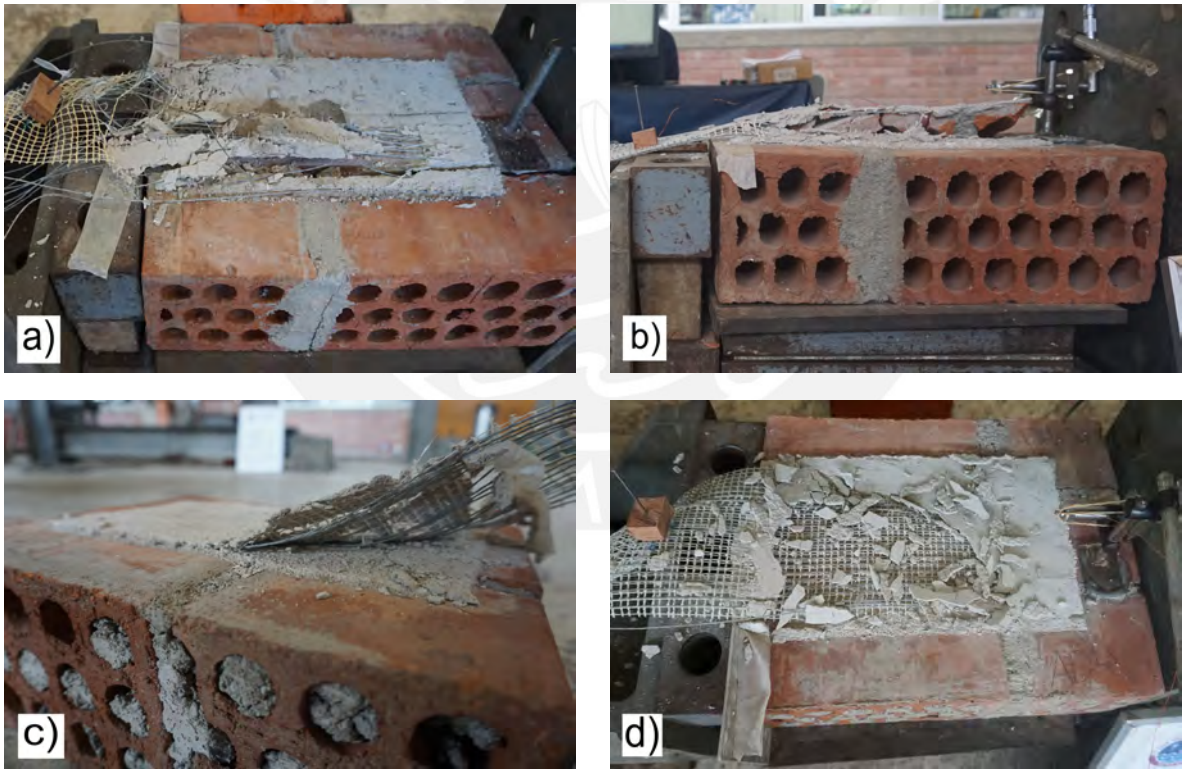

Fig. 8. Failure modes of shear bond tests: (a) debonding at the the mortar-to-substrate and textile-to-mortar interface, premature cracking of the outer mortar layer and rupture of fibers: ADH01; (b) cohesive failure of the masonry: ADH02; (c) debonding at textile-to-mortar interface: ADH03-04; (d) debonding at the textile-to-mortar interface and premature cracking of the outer mortar layer: ADH05.

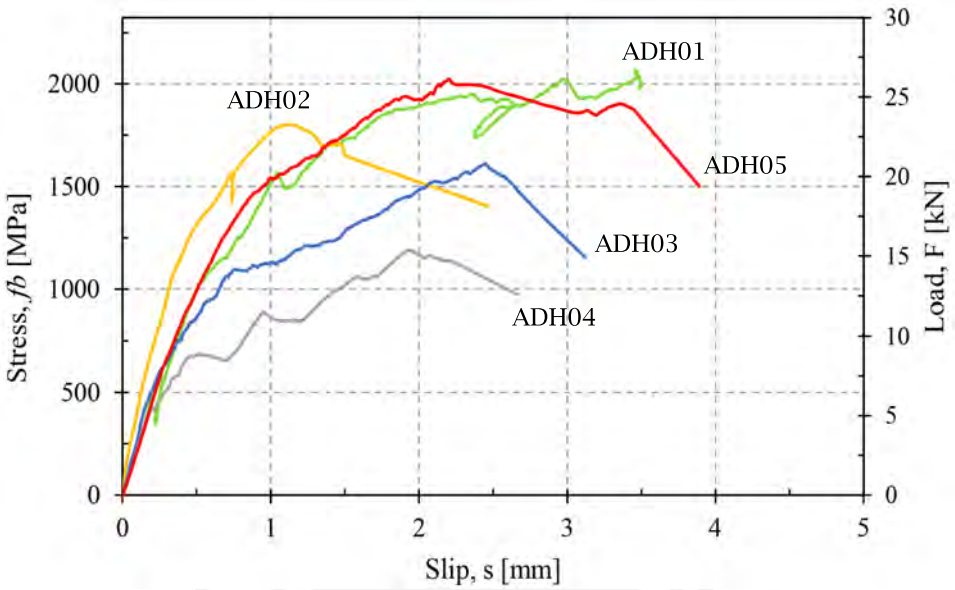

Fig. 9. Stress–slip curves of shear bond tests.

which the failure mode A occurred. It could be said then that ADH02 failed with a better bond strength at the mortar-to-substrate interface and textile-to-mortar interface. The similar detachment mechanisms of ADH01 and ADH05 leads to almost equal curves up to 3 mm, and then the response for ADH05 decreases but not that of ADH01. The latter can be explained by the additional failure mode presented in ADH01, which is a localized failure at the mortar-to-substrate interface. A localized failure at that interface means the whole system is able to support high applied loads, and that is why the rupture of the fibers occurred. In the case of ADH03 and ADH04 which are associated to a single failure mode C, the maximum applied stress is lower than the other specimens.

Table 3. Results of shear bond tests on SRG strengthened masonry

Specimen	f_b [MPa]	F_b [kN/m]	τ [MPa]	s [mm]	$n_s = f_b/f_s$ [%]	FM
ADH01	2068	178	0.66	3.5	72	B,C,E,F
ADH02	1793	155	0.57	1.2	63	A
ADH03	1612	139	0.51	2.4	56	C
ADH04	1191	103	0.38	1.9	42	C
ADH05	2023	175	0.64	2.2	71	C,E
Average	1738	150	0.55	2.2	61%	
COV	21%	20%	21%	37%	21%	

ESTIMATION OF CML AND DESIGN PARAMETERS THROUGH AN ANALYTICAL MODEL

There is a lack of theoretical formulations regarding design purposes exclusively for SRG on masonry substrate (Razavizadeh, 2013). It has been common to adopt formulas provided by standards documents and design guidelines for FRP so as to estimate the design parameters regarding an SRG system (Grande et al., 2013). However, these two strengthening systems develop different detachment mechanisms. While the

failure mode for FRP is debonding at the substrate-matrix interface (B in Fig. 7) with a partial detachment of the substrate, in most of the cases SRG debonds at the matrix–fiber interface (C in Fig. 7). Hence, it should be noted that the theoretical formulations for the FRP technique might not be applicable to the SRG system due to this difference. For this reason, an analytical model for the evaluation of the bond strength when using SRG, which belongs to FRCM materials, has been developed (Carozzi et al., 2016; D'Antino et al., 2018). This model is capable of predicting the entire matrix–fiber debonding process, and therefore it will be possible to estimate the cohesive material laws (CML) and design parameters, such as the fracture energy and optimal bonded length.

Relationship between F–s response curve and CML

The applied load F–slip s response curve behaviour is directly related to the shear stress τ–displacement u behaviour at the matrix–fiber interface. The shear stress τ–displacement u is modelled by means of a trilinear law (CML), as shown in Fig. 10(a). In the first stage (I) the shear stress at the matrix–fiber interface increases proportionally to the fiber displacement, that is, $\tau = k_1 u$ and the slip u lies between 0 and u_{max}. During this phase, the fiber is totally bonded to the matrix due to the elastic behaviour at the interface. Once τ_{max} is attained, microcracking at the matrix–fiber interface and the softening stage (II) begins, where the shear stress decreases proportionally to the fiber displacement until the onset of debonding at the mentioned interface. In this softening branch, the slip lies between u_{max} and u_0 and the shear stress at the interface can be computed as

$$\tau = -k_2 u + \tau_{max} \left(\frac{k_1 + k_2}{k_1} \right) \tag{2}$$

where k_1 and k_2 are the slopes of the ascending and descending branch, respectively. Finally, the displacement reached at the end of the softening phase is

$$u_o = -\frac{\tau_0}{k_2} + \tau_{max} \left(\frac{k_1 + k_2}{k_1 k_2} \right) \tag{3}$$

With reference to the last stage (III) of the CML, with a fiber displacement greater than u_0, it is characterized by the onset of the debonding process and by a constant shear stress τ_0 in order to account for the friction phenomena between the matrix and the textile (Carozzi et al., 2016).
The load response depicted in Fig. 10(b) shows an elastic behaviour up to the point A, which is associated to the linear ascending branch of the CML. After point A, a non-linear behaviour starts due to the beginning of micro-cracking at the matrix–fiber interface (Carozzi et al., 2016), while the shear stress starts decreasing. The value of the applied load F increases until the onset of debonding at the matrix–fiber interface ($\tau = \tau_0$ and $u = u_0$), which corresponds to point B in Fig. 10(b). After point B, the applied load F continues increasing until point C, due to the presence of friction between the single fiber filaments and between the fibers and the matrix (Banholzer, 2004; Hartig et al., 2008; D'Antino et al., 2014). The load at point B is also referred to as the debonding load F_{deb}, i.e. the load carrying capacity of the steel–mortar interface. At point C, the applied load reaches the peak load F_{max}. After the peak load, the applied load decreases with increasing displacement until a constant applied load F_f, which is provided by friction only, is attained (D'Antino et al., 2014). At point D, the fibers are fully debonded from the matrix.

Analytical model

This section presents the theoretical formulations developed by Carozzi et al. (2016) which are arranged with the aim of a comprehensive understanding of the behaviour of the bond at the steel–mortar interface until a portion of the bonded area enters the friction stage (III) and the remaining part is in the elastic-softening phase (segment BC in Fig. 10(b)).
The proposed analytical expressions for the load displacement response consider the effect of the friction phenomena. The main hypotheses of the model are: (i) rigid substrate and matrix, i.e. only the fiber

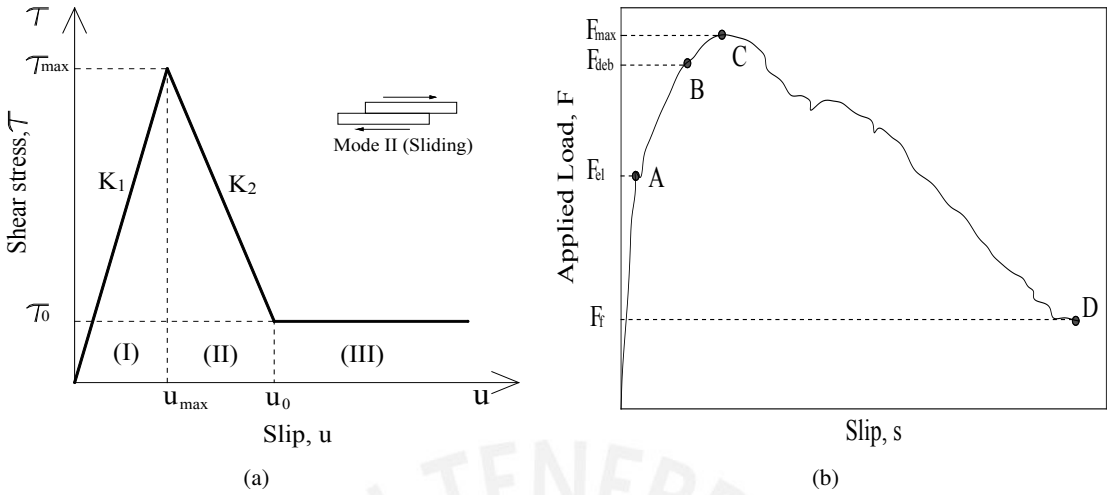

Fig. 10. (a) Shear stress–displacement law at matrix–fiber interface; CML (b) Typical load response.

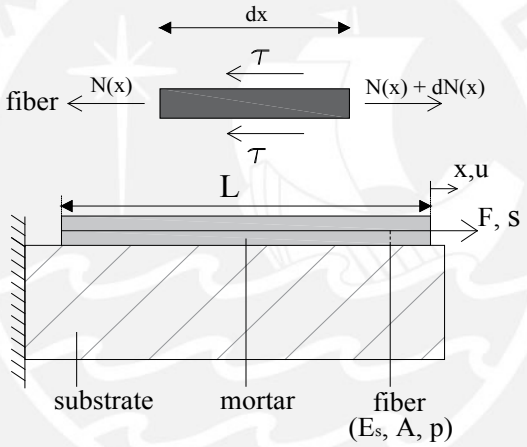

Fig. 11. Loading scheme and equilibrium of a single filament (adapted from Carozzi et al. (2016).

displacement u is taken account; (ii) it is assumed that each filament of the grid has the same displacement and then the external applied load is considered to be equally distributed between the filaments of the textile; (iii) pure Mode-II failure at the matrix–fiber interface (Fig. 10(a), sliding due to shear stresses); (iv) no width effect across the width of the composite; (v) linear elastic behaviour of the fiber until the failure. It should be noted that assumption (iv) is supported by the literature (D'Antino et al., 2014), which states that in FRCM composite materials there is no width effect.

The loading configuration employed in Carozzi et al. (2016) was similar to the one considered in the experimental campaign and is shown in Fig. 11. With this configuration and according to the assumptions stated above, the behaviour of a single filament of the textile was investigated. The fiber bundles or filaments were assumed to have a rectangular cross-section with width b^* and thickness t^*. The effective area of the fiber is denoted by A, the elastic modulus of the fiber is E_s, and p denotes the wet perimeter of the filament equal to $2b^*$ since the thickness of the fiber bundle is negligible compared to its width. The fiber displacement, s, at the loaded end is equal to $u(0)$ and the applied force, F, is given by $N(0)$ (see Fig. 11).

Fig. 11 also shows an infinitesimal segment of the fiber. The equilibrium of this small length dx of the

filament yields

$$\tau(x) = \frac{1}{p}\frac{dN}{dx} \tag{4}$$

$$or\ \tau(x) = \frac{1}{2}\, E_s\, t^* \frac{\varepsilon}{dx} \tag{5}$$

where τ is the shear stress at the matrix–fiber interface and N is the axial force of the filament. Then, the compatibility and constitutive relationships for the fiber bundle provide

$$\varepsilon(x) = \frac{du}{dx} \tag{6}$$

$$\frac{dN}{dx} = E_s A \frac{du^2}{dx^2} \tag{7}$$

Inserting Eq. 4 into Eq. 7 or Eq. 6 into Eq. 5 one has

$$\frac{du^2}{dx^2} - \frac{p}{E_s A}\tau = 0 \tag{8}$$

Eq. 8 was solved by Carozzi et al. (2016) by adopting the described trilinear CML to evaluate the filament displacement, u, and the shear stress at the matrix–fiber interface, τ. The solution is presented in the following with reference to the different phases of the matrix–fiber interface (elastic, softening and friction). As was mentioned, the solution is detailed for an applied load up to peak load (C in Fig. 10(b) since the load response between F_{max} and F_f could not be completely obtained experimentally because of the duration of the testing time.

Elastic Phase

This first stage is for applied loads between O and A in Fig. 10(b). In the first phase, $\tau = k_1 u$ and Eq. 8 becomes

$$\frac{du^2}{dx^2} - \lambda^2 u = 0 \tag{9}$$

where $\lambda = \sqrt{\frac{pk_1}{E_s A}}$ and with the following boundary conditions:
$N = 0 \quad$ at $x = -L$
$N = F \quad$ at $x = 0$
The solution of Eq. 9 is:

$$u(x) = \frac{F}{\lambda E_s A}\frac{cosh\,[\lambda(L+x)]}{sinh(\lambda L)} \tag{10}$$

At the end of the elastic phase, when the shear stress reaches the maximum stress τ_{max} at $x = 0$, the displacement, u, in the fiber with a total bonded length L is

$$u(x) = \frac{\tau_{max}}{k_1}\frac{cosh\,[\lambda(L+x)]}{cosh(\lambda L)} \tag{11}$$

Eqs. 5–7 provide the interfacial shear stress $\tau_{(x)}$, fiber strain $\varepsilon_{(x)}$ and fiber axial force $N_{(x)}$, respectively for each point of the resulting load response.

$$\tau(x) = \tau_{max}\frac{cosh\,[\lambda(L+x)]}{cosh(\lambda L)} \tag{12}$$

$$\varepsilon(x) = \frac{\tau_{max}}{k_1}\,\lambda\,\frac{sinh\,[\lambda(L+x)]}{cosh(\lambda L)} \tag{13}$$

$$N(x) = \frac{p\,\tau_{max}}{\lambda}\frac{sinh\,[\lambda(L+x)]}{cosh(\lambda L)} \tag{14}$$

Elastic-softening phase

This stage is for applied loads between A and B in Fig. 10(b). When the shear stress τ_{max} is reached at the loaded end, softening starts, so a portion of the interface enters the softening state, while the other remains in the elastic state. The length of the softening part is denoted by l and the load continues to increase as l increases.

For the elastic phase, Eqs. 11–14 can be used but with a bonded length equal to $(L - l)$ instead of just (L), which means that the elastic part concludes at $(x = -l)$. Hence the displacement for $-L < x < -l$ is

$$u(x) = \frac{\tau_{max}}{k_1} \frac{cosh\,[\lambda(L + x)]}{cosh\,[\lambda(L - l)]} \tag{15}$$

In the elastic- softening phase, for $-l < x < 0$, the shear stress τ is given by Eq. 2, so Eq. 8 becomes

$$\frac{du^2}{dx^2} + \omega^2 u = \frac{p\ \tau_{max}}{E_s\ A} \left(\frac{k_1 + k_2}{k_1} \right) \tag{16}$$

where $\omega = \sqrt{\dfrac{pk_2}{E_s A}}$ and with the following boundary conditions which comply with the continuity conditions at $x = -l$:

$u = \dfrac{\tau_{max}}{k_1}$ at $x = -l$

$N = \dfrac{p\ \tau_{max}}{\lambda}\ tanh[\lambda(L - l)]$ at $x = -l$

The solution of Eq. 16 is

$$u(x) = \frac{\tau_{max}}{k_2} \frac{sin(\omega x + \varphi)}{sin(\omega l - \varphi)} + \left(\frac{k_1 + k_2}{k_1} \right) \tau_{max} \tag{17}$$

where $\varphi = \omega l - arctg \dfrac{\lambda}{\omega\ tanh\,[\lambda(L - l)]}$ and with Eqs. 5–7 the interfacial shear stress $\tau_{(x)}$, fiber strain $\varepsilon_{(x)}$ and fiber axial force $N_{(x)}$ can be computed as

$$\tau(x) = -\tau_{max} \frac{sin(\omega x + \varphi)}{sin(\omega l - \varphi)} \tag{18}$$

$$\varepsilon(x) = \frac{\tau_{max}\ \omega}{k_2} \frac{cos(\omega x + \varphi)}{sin(\omega l - \varphi)} \tag{19}$$

$$N(x) = \frac{\tau_{max}\ p}{\omega} \frac{cos(\omega x + \varphi)}{sin(\omega l - \varphi)} \tag{20}$$

Elastic-softening-friction phase

This stage is for applied loads between B and C in Fig. 10(b). When the shear stress attains τ_0 at the loaded end, the load at the matrix–fiber interface can not decrease due to the friction phenomena in the debonded part (Carozzi et al., 2016). In this phase, the bonded length is divided into three parts: elastic, softening and friction. The length of the debonded part (friction) is denoted by d while l denotes the length of the softening part.

During the elastic phase, for $-L < x < -l - d$, Eqs. 11–14 can be used but with a bonded length equal to $(L - l - d)$, which means that the elastic part concludes at $(x = -l - d)$. In this way, the displacement in the elastic phase for a load between B and C is

$$u(x) = \frac{\tau_{max}}{k_1} \frac{cosh\,[\lambda(L + x)]}{cosh\,[\lambda(L - l - d)]} \tag{21}$$

For the elastic-softening phase ($-l - d < x < -d$), Eqs. 17–20 are still valid, but should take into account the following friction phenomena. In the friction phase the axial force per unit length is equal to $p\ \tau_0$ and then the axial force in the filaments at $x = -d$ is equal to $F - p\ \tau_0\ d$. Therefore, considering Eq. 21 at the end of the softening phase ($x = 0$) and replacing L with $(L - d)$, the axial force at $x = -d$ should also satisfy

$$F - p\ \tau_0\ d = \frac{\tau_{max} p}{\omega} \frac{cos(\varphi)}{sin(\omega l - \varphi)} \tag{22}$$

where $\varphi = \omega l - arctg \dfrac{\lambda}{\omega\ tanh\left[\lambda(L - d - l)\right]}$

In addition, the fiber displacement at $x = -d$ is equal to u_0. With the conditions in terms of load and displacement at $x = -d$, the displacement at the interface $u_{(x)}$, the interfacial shear stress $\tau_{(x)}$, fiber strain $\varepsilon_{(x)}$ and fiber axial force $N_{(x)}$ are

$$u(x) = \frac{\tau_{max}}{k_2} \frac{sin\left[\omega(x + d) + \varphi\right]}{sin(\omega l - \varphi)} + \left(\frac{k_1 + k_2}{k_1\ k_2}\right) \tau_{max} \tag{23}$$

$$\tau(x) = -\tau_{max} \frac{sin\left[\omega(x + d) + \varphi\right]}{sin(\omega l - \varphi)} \tag{24}$$

$$\varepsilon(x) = \frac{\tau_{max}\ \omega}{k_2} \frac{cos\left[\omega(x + d) + \varphi\right]}{sin(\omega l - \varphi)} \tag{25}$$

$$N(x) = \frac{\tau_{max}\ p}{\omega} \frac{cos\left[\omega(x + d) + \varphi\right]}{sin(\omega l - \varphi)} \tag{26}$$

Finally, in the elastic-softening-friction phase, i.e. $-d < x < 0$, the shear stress τ is constant due to friction, so Eq. 8 becomes

$$\frac{du^2}{dx^2} + \frac{p\ \tau_0}{E_s\ A} = 0 \tag{27}$$

and boundary conditions which comply with the continuity conditions at $x = -d$ are

$u = u_0 \quad$ at $x = -d$

$N = F - p\ \tau_0\ d \quad$ at $x = -d$

The solution of Eq. 27 is $u(x)$ and the interfacial shear stress $\tau(x)$, fiber strain $\varepsilon(x)$ and fiber axial force $N(x)$ can be evaluated with Eqs. 29–31, respectively:

$$u(x) = u_0 + \frac{F\ (x + d)}{E_s\ A} + \frac{\tau_0\ p(x^2 - d^2)}{2\ E_s\ A} \tag{28}$$

$$\tau(x) = \tau_0 \tag{29}$$

$$\varepsilon(x) = \frac{\tau_0\ p}{E_s\ A} + \frac{F}{E_s\ A} \tag{30}$$

$$N(x) = \frac{\tau_0\ p\ x}{F} \tag{31}$$

Proposed CML

The bond parameters k_1, k_2, τ_{max} and τ_0 have been experimentally calibrated using data of certain key points of the experimental load–displacement response (Fig. 10(b)). These key points are related to the end of the elastic phase (point A) and the end of the elastic-softening phase (point B). In order to obtain the parameters that define the CML, it is assumed that the bonded length (L) is greater than the elastic effective bond length $L_{eff,e}$ for the elastic phase, and also greater than the optimal bonded length L_{opt} for the elastic-softening phase. These assumptions will be verified later and for the sake of a better understanding, both meanings will be explained in the following section, Section `Results`.

Since the parameters k_1 and τ_{max} are associated to the ascending linear part of CML, these can be obtained from the limit elastic part by means of the displacement, u_A, and the load for a single filament, F_A, from the experimental load–displacement (Fig. 9). From Eq. 14 there can be obtained the load at the load end and for $L > L_{eff,e}$ that load at the elastic limit becomes

$$F = \frac{p\,\tau_{max}}{\lambda}\cancel{tanh(\lambda\,L)}^{1} = \frac{p\,k_1\,u_A}{\sqrt{p\,k_1/E_f\,A}} \tag{32}$$

Solving Eq. 32, the slope of the elastic ascending branch of the bond–displacement relationship is given in Eq. 33 and, finally, $\tau_{max} = k_1\,u_A$:

$$k_1 = \frac{F_A^2}{u_A^2\,p\,E_f\,A} \tag{33}$$

To calibrate the slope k_2 of the softening branch of the bond–displacement relationship, point B should be determined in the experimental load response. For $L > L_{opt}$, the load level at the end of elastic-softening phase converges to (Carozzi et al., 2016)

$$F = \frac{p\,\tau_{max}}{\omega}\sqrt{1 + \frac{\omega^2}{\lambda^2}} \tag{34}$$

Eq. 34 can be rewritten as follows, which should be solved numerically to get k_2.

$$F_B = \frac{p\,\tau_{max}}{\sqrt{p\,k_2/E_f\,A}}\sqrt{1 + \frac{k_2}{k_1}} \tag{35}$$

Finally, the estimation of the friction shear stress τ_0 is straightforward by using Eq. 2 and determining the corresponding displacement u_0 from the experimental load–displacement curve (Point B). One has then:

$$\tau_0 = -k_2\,u_B + \tau_{max}\left(\frac{k_1 + k_2}{k_1}\right) \tag{36}$$

The values of the bond parameters for SRG materials are presented in Table 4 by means of Eq. 33, 35 and 36, and using an effective area approximately equal to 75% of the dry filament area ($b* = 5$ mm) as Carozzi et al. (2016) recommends. It is worth pointing out that the numerical solution for k_2 entails an approximation with a difference of no more than 5%. As an exception, when theoretical formulations were applied to ADH04, it was realized that this sample does not comply with $L > L_{opt}$, and the evaluation using the approach with $L < L_{opt}$ is outside the scope of this study. CML_ADH01-03,05 are shown in Fig. 12 as a continuous line, whereas the average CML (without considering ADH04) is the dashed line.

Table 4. Proposed bond parameters

Sample	k_1 [N/mm^3]	k_2 [N/mm^3]	τ_{max} [MPa]	τ_0 [MPa]
ADH01	1.82	1.2	0.75	0.18
ADH02	5.77	3.2	1.59	0.07
ADH03	2.30	1.0	0.62	0.09
ADH04	1.94	1.0	0.78	0.25
Average	2.96	1.6	0.935	0.15

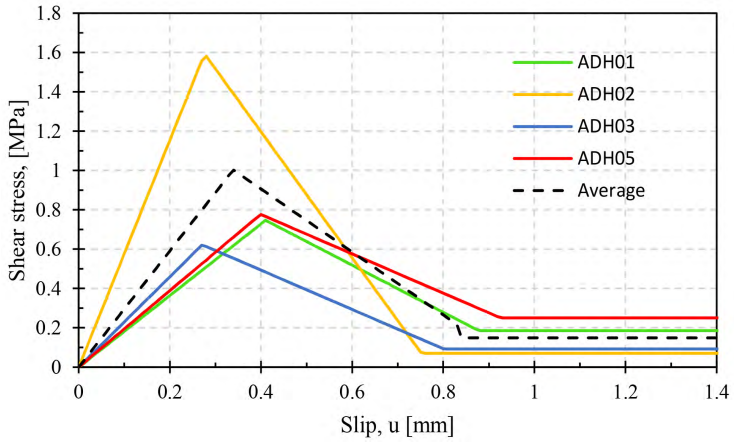

Fig. 12. Comparison between the proposed CMLs.

Results

The main results of the analytical model will now be discussed in terms of the elastic and elastic softening effective bond length as well as the optimal bond length. In addition, the displacement at the interface $u(x)$, the interfacial shear stress $\tau(x)$, fiber strain $\varepsilon(x)$ and fiber axial force $N(x)$ across the entire bonded length will be presented.

The elastic effective bond length, $L_{eff,e}$, is defined as the bond length required to transfer 97% of the maximum transferable load (Carozzi et al., 2015). One has then from Eq. 14 evaluated at $x = 0$, $tanh\left(\lambda\, L_{eff,e}\right) = 0.97$ and finally

$$L_{eff,e} = \frac{2}{\lambda} \tag{37}$$

The elastic-softening effective bond length, $L_{eff,es}$, is obtained by evaluating Eq. 17 at the loaded end ($x = 0$) with $l = L$ and $u(x = 0) = u_0$. Then the solution obtained by (Carozzi et al., 2016) gives

$$L_{eff,es} = \frac{arcsin\left(-\dfrac{\tau_0}{\tau_{max}}\right) + \dfrac{\pi}{2}}{\omega} \tag{38}$$

The optimal bond length is the minimal length able to carry the maximum anchorage force or to fully develop the stress transfer mechanism at the matrix–fiber interface (D'Antino et al., 2018). In other words, it is the length required to complete the elastic-softening phase (Carozzi et al., 2016). It is computed by combining Eqs. 37 and 38:

$$L_{opt} = \frac{2}{\lambda} + \frac{arcsin\left(-\dfrac{\tau_0}{\tau_{max}}\right) + \dfrac{\pi}{2}}{\omega} \tag{39}$$

As L_{opt} is the length required to fully establish the stress transfer zone, this should be computed as the distance between the point of the strain distribution along the direction of the fiber where the strain is zero and the point where its derivative reaches a constant value (D'Antino et al., 2018). The optimal bond length L_{opt} obtained by Eqs. 39 and from the strain profiles ε (depicted in Fig. 13) are presented in Table 5 for each CML. As was mentioned in the previous section, Section `Proposed CML`, it is verified that L is greater than the optimal bond length. The elastic effective bond length, $L_{eff,e}$, and the elastic-softening effective bond length, $L_{eff,es}$, are listed as well in Table 5.

The fracture energy G_F is another parameter that defines the CML. It is defined as the amount of energy

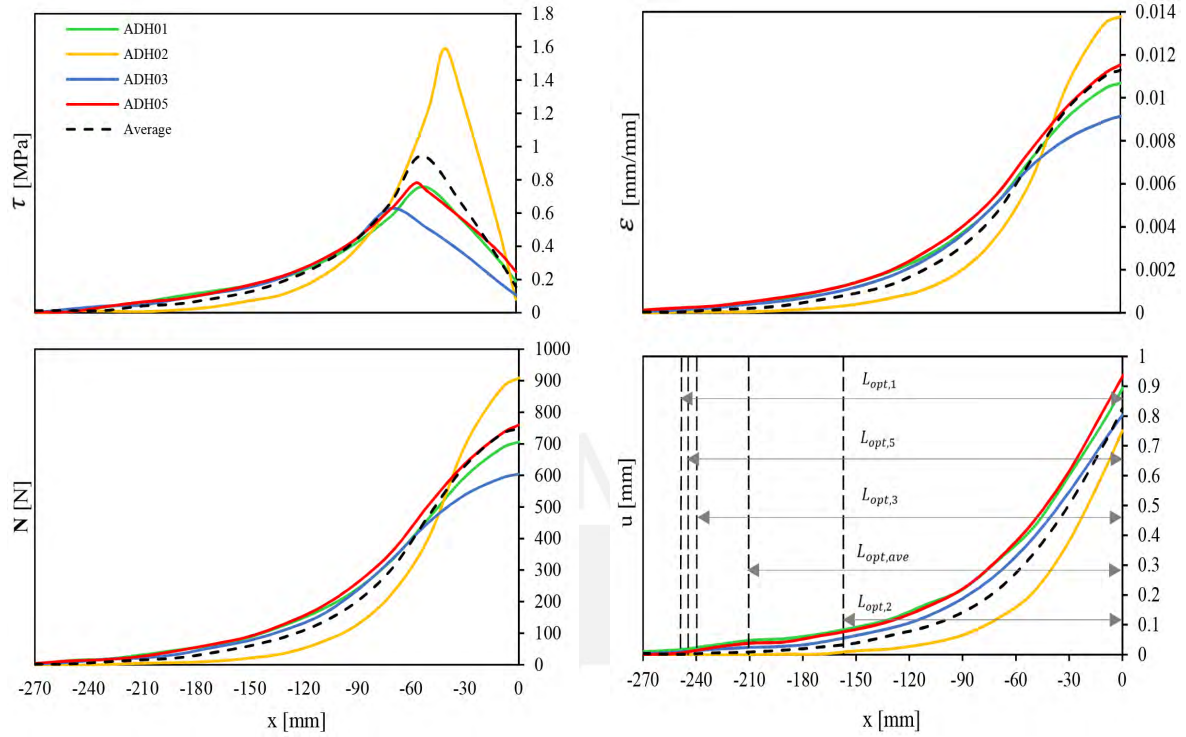

Fig. 13. Slip $s(x)$, force(x), strain ε(x), and shear stress τ(x) along the bonded length at the debonding stress F_{deb}.

needed to create a unit area of a crack along the matrix–fiber interface. Fracture energy is the area underneath the bond stress–slip curve in the range of $0 \leq u \leq u_0$, without including friction (D'Antino et al., 2014). With the proposed CMLs, it is possible to compute the fracture energy:

$$G_F = \int_0^{u_0} \tau \, du \tag{40}$$

In addition, the fracture energy is associated with the load-carrying capacity associated with the initiation of the debonding F_{deb} (point B) according to Eq. (41) (D'Antino et al., 2014, 2018):

$$G_F = \frac{1}{4 \, E_f \, t^*} \left(\frac{P_{deb}}{n \, b^*} \right)^2 \tag{41}$$

The values of the fracture energy G_F obtained by Eqs. 40 and 41 are quite similar, and are presented in Table 5 for each CML.

CONCLUSIONS

The behaviour of the bond between steel reinforced grout (SRG) and clay masonry was investigated due its importance as a key mechanism in transferring stresses between the composite material and the substrate. In addition, a characterization of the materials that make up the SRG system was carried out by means of direct tensile tests on galvanized steel fiber and compressive test on lime-based mortar. The compressive tests complied with the ASTM C141 standard, while the tensile and shear bond tests were performed based on the previous literature for the sample's geometry, construction and test procedure.

Table 5. Results in terms of key bond lengths and fracture energy

Sample	$l_{eff,e}$	$l_{eff,es}$	l_{opt} [mm]		G_F [N/mm]	
	[mm]	[mm]	Eq. 39	profile	Eq. 40	Eq. 41
ADH01	120	116	237	251	0.37	0.40
ADH02	68	71	140	157	0.62	0.54
ADH03	107	128	235	240	0.27	0.26
ADH04	117	128	244	247	0.43	0.48
Average	94	101	195	210	0.43	0.41

The results for the tensile tests on the fibers show that there is no great difference between the studies despite the criteria used. Based on the studies, the appropriate width and free length of the fiber samples are 50 mm and 400–450 mm, respectively; and a speed test of 2 mm/min. During the test, two failure modes were identified: the nearly simultaneous failure of the cords along the free length of the textile and the rupture of the cords in or around the gripping areas. Finally, the average tensile strength and failure elongation obtained in this study is 2861 MPa and 2.44%.

In the case of the shear bond tests, the average maximum strength is 1738 MPa and the associated slip is 2.2 mm. The failure modes observed indicate that the debonding mainly occurs at the matrix–fiber interface rather than at the substrate–fiber interface, as occurs with FRP. This leads to the inapplicability to the SRG technique of the theoretical formulations for FRP materials. As a consequence, this paper has employed an analytical model developed by Carozzi et al. (2016) and D'Antino et al. (2018) in order to obtain and propose a trilinear cohesive material law (CML) which describes the shear stress τ–displacement u behaviour at the steel–mortar interface. The average k_1, k_2, τ_{max}, and τ_0 was estimated to be 2.96 N/mm^3, 1.6 N/mm^3, 0.935 MPa and 0.15 MPa, respectively. In addition, a fracture energy G_F at the matrix–fiber interface has been proposed equal to 0.43 N/mm or 0.41 N/mm.

Finally, an optimal bond length L_{opt} could be determined from the strain profiles at the onset of debonding and from the formulations of the analytical model. Hence, this paper provides some parameter values for computing the bond length when reinforcing masonry constructions. A minimal optimal bond length of 210 mm is suggested.

ACKNOWLEDGMENTS

This project was partially funded by CONCYTEC within the framework of the N° 232-2015-FONDECYT Agreement. Finally, the authors would like to express their gratitude for the important collaboration of the industrial company Kerakoll S.p.A., and especially to Dr. Paolo Casadei, for providing the materials for the experimental part of this work.

REFERENCES

ASTM (2017a). "Standard specification for hydrated hydraulic lime for structural purposes." *ASTM C141/C14M*, ASTM International, 4.

ASTM (2017b). "Standard test method for tensile properties of polymer matrix composite materials." *D3039/D3039M*, ASTM International, 13.

Banholzer, B. (2004). "Bond behavior of multi-filament yarn embedded in a cementitious matrix." Ph.D. thesis, RETH Aachen University, United Kingdom.

Barton, B., Wobbe, E., Dharani, L., Silva, P., Birman, V., Nanni, A., Alkhrdaji, T., Thomas, J., and Tunis, G. (2005). "Characterization of reinforced concrete beams strengthened by steel reinforced polymer and grout (SRP and SRG) composites." *Materials Science and Engineering: A*, 412(1), 129–136 International Conference on Recent Advances in Composite Materials.

Borri, A., Casadei, P., Castori, G., and Hammond, J. (2009). "Strengthening of brick masonry arches with externally bonded steel reinforced composites." *Journal of Composites for Construction*, 13(6), 468–475.

Borri, A., Castori, G., and Corradi, M. (2011). "Shear behavior of masonry panels strengthened by high strength steel cords." *Construction and Building Materials*, 25(2), 494–503 Composite Materials and Adhesive Bonding Technology.

Carozzi, F. G., Colombi, P., Fava, G., and Poggi, C. (2016). "A cohesive interface crack model for the matrix–textile debonding in FRCM composites." *Composite Structures*, 143, 230–241.

Carozzi, F. G., Colombi, P., and Poggi, C. (2015). "Calibration of end-debonding strength model for FRP-reinforced masonry." *Composite Structures*, 120, 366–377.

CNR-DT200 (2013). "Guide for the design and construction of externally bonded frp systems for strengthening existing structures-materials, RC and PC structures, masonry structures." Italian National Research Council, Rome, Italy.

D'Antino, T., Carloni, C., Sneed, L., and Pellegrino, C. (2014). "Matrix–fiber bond behavior in PBO FRCM composites: A fracture mechanics approach." *Engineering Fracture Mechanics*, 117, 94–111.

D'Antino, T., Colombi, P., Carloni, C., and Sneed, L. H. (2018). "Estimation of a matrix–fiber interface cohesive material law in FRCM-concrete joints." *Composite Structures*, 193, 103–112.

De Felice, G., Aiello, M. A., Caggegi, C., Ceroni, F., De Santis, S., Garbin, E., Gattesco, N., Hojdys, Ł., Krajewski, P., Kwiecień, A., Leone, M., Lignola, G. P., Mazzotti, C., Oliveira, D., Papanicolaou, C., Poggi, C., Triantafillou, T., Valluzzi, M. R., and Viskovic, A. (2018). "Recommendation of RILEM technical committee 250-CSM: Test method for Textile Reinforced Mortar to substrate bond characterization." *Materials and Structures*, 51(4), 95.

De Santis, S., Carozzi, F., De Felice, G., and Poggi, C. (2017b). "Test methods for textile reinforced mortar systems." *Composites Part B: Engineering*, 127, 121–132.

De Santis, S., Ceroni, F., De Felice, G., Fagone, M., Ghiassi, B., Kwiecie, A., Lignola, G., Morganti, M., Santandrea, M., Valluzzi, M., and Viskovic, A. (2017a). "Round robin test on tensile and bond behaviour of steel reinforced grout systems." *Composites Part B: Engineering*, 127, 100–120.

Gattesco, N. and Boem, I. (2017). "Characterization tests of GFRM coating as a strengthening technique for masonry buildings." *Composite Structures*, 165, 209–222.

Ghiassi, B., Marcari, G., Oliveira, D. V., and Lourenço, P. B. (2012). "Numerical analysis of bond behavior between masonry bricks and composite materials." *Engineering Structures*, 43, 210–220.

Ghiassi, B., Oliveira, D. V., Marques, V., Soares, E., and Maljaee, H. (2016). "Multi-level characterization of steel reinforced mortars for strengthening of masonry structures." *Materials & Design*, 110, 903–913.

Grande, E., Imbimbo, M., and Sacco, E. (2013). "Modeling and numerical analysis of the bond behavior of masonry elements strengthened with SRP/SRG." *Composites Part B: Engineering*, 55, 128–138.

Hartig, J., Häußler-Combe, U., and Schicktanz, K. (2008). "Influence of bond properties on the tensile behaviour of textile reinforced concrete." *Cement and Concrete Composites*, 30(10), 898–906.

Huang, X., Birman, V., Nanni, A., and Tunis, G. (2005). "Properties and potential for application of steel reinforced polymer and steel reinforced grout composites." *Composites Part B: Engineering*, 36(1), 73–82.

INEI (2014). "Una mirada a Lima Metropolitana." Instituto nacional de Estadística e Informática, Lima, Peru.

Kerakoll (2017a). "Technical data sheet: Geocalce® f antisismico.

Kerakoll (2017b). "Technical data sheet: Geosteel g600.

Manchego, A. and Pari, S. (2016). "Análisis experimental de muros de albañilería confinada en viviendas de baja altura en lima, perú." M.S. thesis, Pontificia Universidad Católica del Perú, Lima, Peru.

Ministerio de Vivienda, C. y. S. S. (2006). "E.070: Reglamento nacional de edificaciones: Albañilería." Ministerio de Vivienda, Construcción y Saneamiento (SENCICO), Lima, Peru.

Papanicolaou, C. G., Triantafillou, T. C., Papathanasiou, M., and Karlos, K. (2008). "Textile reinforced mortar (TRM) versus FRP as strengthening material of URM walls: Out-of-plane cyclic loading." *Materials and Structures*, 41(1), 143–157.

Quagliarini, E., Monni, F., Greco, F., and Lenci, S. (2017). "Flexible repointing of historical facing-masonry column-type specimens with basalt fibers: A first insight." *Journal of Cultural Heritage*, 24, 165–170.

Razavizadeh, A. (2013). "Numerical modeling of bond in SRG-strengthened masonry." M.S. thesis, University of Minho, University of Minho.

Razavizadeh, A., Ghiassi, B., and Oliveira, D. V. (2014). "Bond behavior of SRG-strengthened masonry units: Testing and numerical modeling." *Construction and Building Materials*, 64, 387–397.

Triantafillou, T. and Papanicolaou, C. (2005). "Textile reinforced mortars (TRM) versus fiber reinforced polymers (FRP) as strengthening materials of concrete structures." *International Concrete Abstracts Portal*, 230, 99–118.

Wobbe, E., Silva, P., Barton, B., Dhanari, L., Birman, V., Nanni, A., Alkhrdaji, T., Thomas, J., and Tunis, G. (2004). "Flexural capacity of RC beams externally bonded with SRP and SRG." *Soc. Adv. Mater. Process. Eng.*

3.2. Experimental assessment of confined masonry walls retrofitted with SRG under lateral cyclic loads

Experimental assessment of confined masonry walls retrofitted with SRG under lateral cyclic loads

Jhair Yacila, Jhoselyn Salsavilca, Nicola Tarque, and Guido Camata

***Abstract*—Around the world, many informal masonry buildings have collapsed due to the failure of their bearing walls under lateral seismic loads. This is related to the many involved factors, such the quality of the materials, the quality of workmanship, the lack of technical intervention, and the high seismicity of the zone, among others. However, the fact is that these constructions need to be retrofitted in order to upgrade their ultimate strength and allow them to properly absorb inelastic deformations. Currenly, fiber reinforced polymer (FRP) has been widely studied as a retrofitting technique. However, it has some technical and economic disadvantages that are remedied by fiber reinforced mortar (FRM). In this paper, a variant of FRM known as steel reinforced grout (SRG) is studied as a seismic retrofitting technique for cracked confined masonry walls (CMW). For this purpose, three full-scale cracked walls were repaired, retrofitted with SRG strips, and tested under in-plane cyclic loads at the Pontifical Catholic University of Peru (PUCP). The experimental results show the benefits of SRG in improving the lateral displacement ductility, energy dissipation, and stiffness degradation of CMWs.**

***Index Terms*—Confined masonry wall, SRG, seismic vulnerability, seismic retrofit**

I. Introduction

Confined masonry is a type of construction widely diffused in Peru due to its easy and fast construction. According to [1], masonry dwellings represent 84% of the total buildings in Peru and 60% of them were built informally. In the case of informal dwellings, seismic events have evidenced their high vulnerability, which has led to human and material loss (i.e. Lima, 1746; Arequipa, 2001; Pisco, 2007). Therefore, there is a necessity to reinforce a huge quantity of confined masonry buildings in order to improve their seismic performance.

The main aim of seismic retrofitting is to upgrade the ultimate strength of the building by improving the structure's ability to absorb inelastic deformations [2]. In this way, external reinforcement by using composite materials has arisen as an efficient method due to its advantages, such as its facility of application, high stress/weight ratio, and versatility, which means it is applicable to different types of substrates.

One of the most commercial composites is the well-known fiber reinforced polymer (FRP). This composite consists of different kinds of fibers (e.g. carbon, glass, basalt, and others), or high strength textiles and an organic binder (e.g. epoxy resin). In general, FRPs are a convenient solution because they do not add mass to the structure, they are easy to handle, flexible, quick to install, and have an excellent performance in terms of tensile strength and durability [3], [4]. However, their application on wet surfaces is not feasible and has a poor performance at high temperatures and in alkaline environments. In contrast, reinforcement systems based on cement (fiber reinforced cementitious matrix, FRCM) and mortar (fiber reinforced mortar, FRM), have arisen to overcome these drawbacks. In addition, they are reversible (i.e. they can be removed from the surface without major damage) and are not architecturally invasive since the thickness of the intervention can be 10 mm or less.

A particular case of FRM is when the steel fiber or textile is used for composite, when it is more commonly known as steel reinforced grout (SRG). This composite is of great interest due to its mechanical properties and bond efficiency. For instance, steel fibers have a high tensile strength, a higher stiffness than basalt or glass, and less thickness than carbon and aramid. These particular fibers are less fragile than the others because a ductile behaviour is exhibited before tensile failure. Furthermore, due to the zinc coating, steel textiles do not get rusty and are protected from sulphate attacks [5]. However, their application is recent compared to other fibers. Hence, knowledge about their design, construction and modeling has been limited.

This paper presents a criterion for designing, as well as the application process for retrofitting, confined masonry walls with SRG to support in-plane shear loads. Hopefully this will contribute to the formation of guidelines for their design and application. For the design process, the CNR and AC434 guidelines have been taken into account [6], [7]. Although the CNR guideline is focused on FRP, it has been assumed that it is also applicable to SRG since similar design concepts were applied. The construction process for retrofitting confined masonry walls with SRG, as well as the considerations to be taken into account during the experimental campaign, will also be discussed. The experimental results will presented and discussed in terms of lateral deformation, energy dissipation, hysteresis damping, and stiffness degradation.

II. Previous Work

A. Description of the tested walls

In [8], [9], a total of 9 full-scale confined masonry walls were built and tested under cyclic lateral loads at the PUCP. These walls were built with *king kong* bricks of 18 holes with a net area less than 60% of the gross area. These are industrial bricks, with dimensions 230 x 130 x 90 mm, and are commonly used for bearing walls in Peru, although prohibited by the Peruvian Seismic Code in the coastal area [10]. The construction process of a typical confined masonry wall implies that steel reinforcing is located in its final position before constructing the masonry panel. It is not recommended to lay the bricks more than 1.3 m high per working day,

in order to avoid crushing the mortar in the lower part of the panel. The typical mortar thickness, either horizontal or vertical, varies between 10 and 15 mm and has a typical volumetric ratio cement/sand of 1/4. Moreover, an intentional toothed finish is left for a subsequent concrete casting. In this way, it is intended to guarantee a monolithic union between concrete and masonry. The dimensions of a typical confined masonry wall as well as the reinforcing detail are shown in Fig. 1.

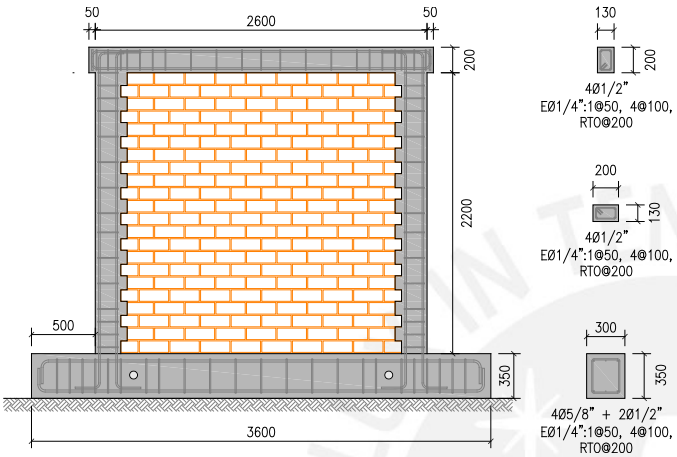

Figure 1. Geometry and reinforcement detail of a typical wall (dimensions in millimeters)

Regarding the experiments, three walls were tested under only lateral loads, until a repairable limit state was reached, i.e. equivalent to a drift of 0.125% according to the Peruvian Code [10]. The next three, unlike the previous ones, were tested until a collapsed state was reached, which had a drift of 0.833%. Finally, the last three had a constant vertical load of 170 kN, which represents the vertical load on a first floor wall from a total of three, and were tested also until reaching a collapsed state, with an associated drift of 0.625%. In this research, three collapsed walls were selected from the previous research to be repaired and tested under lateral cyclic loads again (Fig. 2).

B. Characterization of the materials

In order to characterize the properties of the materials involved in the walls, control tests were carried out at the PUCP [8], [9]. To characterize the mortar employed for the masonry panel, 12 cubic samples with dimensions 50 x 50 x 50 mm were extracted and tested under uni-axial compression. To assess the compressive behaviour of the masonry, 4 masonry piles with dimensions 230 x 130 x 600 mm were made and tested under uni-axial compression parallel to the largest dimension. In the case of a tensile behaviour of the masonry, 4 masonry walls with dimensions of 600 x 600 x 130 mm were made and tested under uni-axial compression parallel to the diagonal of each square sample (diagonal compression test). The concrete compressive strength of the foundation and confining elements was evaluated through compression tests of cylindrical specimens 150 mm wide and 300 mm high. For this job, 4 samples were extracted from each concrete element. All specimens were properly cured for 28 days before testing.

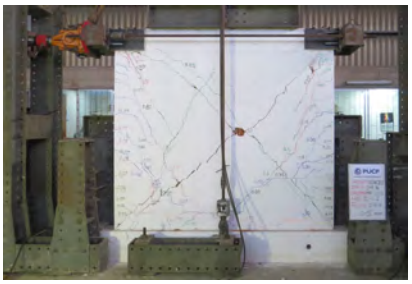

(a) With vertical load W-01

(b) without vertical load W-02

(c) without vertical load W-03

Figure 2. Selected walls for retrofitting

Table I shows the average results obtained from this control campaign. It is worth commenting that the concrete tensile strength and Young's modulus were computed in accordance with the CEB-FIP model code [11].

Table I
MATERIAL PROPERTIES INVOLVED IN THE WALLS

Material	Compressive strength [MPa]	Tensile strength [MPa]	Elastic modulus [MPa]
Mortar	17.50	-	-
Concrete foundation	27.50	2.18	25900
Concrete columns	19.00	1.49	22500
Concrete beam	28.00	2.22	26200
Masonry	10.00	1.40	5700

III. STEEL REINFORCED GROUT (SRG)

In this paper, the performance of the confined masonry walls under shear loads are intended to be improved by means of a novel retrofitting technique called SRG. SRG is composed of ultra-high tensile strength steel fibers 100 mm wide, 0.084 mm thick, and a natural lime mortar 100 mm wide and 10

mm thick. These fibers are uni-directional since the they result from twisting two wires around three straight wires. However, they are connected by perpendicular glass fiber filaments, therefore they can also be considered as textiles. As a previous step, the steel wires were coated with zinc before twisting, to protect them against corrosion [12]. The natural lime mortar employed had a M15 resistance class according to EN 998-2 and R1 according to EN 1504-3, as technical specification [13]. Furthermore, it is highly breathable, it is made strictly from natural and recycled minerals, and its manufacture produces very low emissions of CO_2 and other volatile organic substances. All these properties make it part of the innovative *GreenBuilding* technology.

A. Control tests

In order to characterize the material properties involved in SRG, control tests were carried out. For instance, to characterize the natural lime mortar which serve as a blinder for the steel galvanized fiber, 6 samples of 50 x 50 x 50 mm were made and tested under uni-axial compression (Fig. 3a). Table II shows the experimental results from these tests, where the length and width resulted from averaging parallel dimensions from the face subjected to an axial load.

In the case of the galvanized steel fiber, 5 samples were made and tested, as shown in Fig. 3b. In these tests, two main failure modes were recognized: one was related to the failure at the union between the textile and steel plates (U), whereas the other one was related to the middle part of the textile (M). It is worth noting that in these tests, the second failure mode is expected, in order to obtain a representative strength of the textile, since the first mode is linked to the participation of the steel plates in the failure. Table III shows the experimental results related to these tests, where E_f is the Young's modulus, f_f is the maximum strength, and ε_{fu} is the maximum strain of the steel mesh.

Finally, the interaction between SRG and masonry substrate under shear loads was explored through 5 debonding tests, as shown in Fig. 3c. In these tests, 5 main failure modes were recognized: (1) rupture of the masonry substrate (2) debonding at the mortar-to-substrate interface, (3) debonding at the textile-to-mortar interface, (4) premature cracking of the outer mortar layer, and (5) rupture of the textile. Table IV shows the experimental results related to these tests, where f_b is the maximum tensile stress developed by the steel mesh, τ is the stress computed as the relation between the maximum force and the cross sectional area of the SRG, and *Slip* is the relative displacement between two control points (one located in the masonry substrate and the other one in the steel mesh). These two control points were intended to capture the deformation of the SRG prior to total failure.

B. Design of SRG reinforcement for shear behaviour enhancement

Before retrofitting, it is necessary to properly design the reinforcement in order to minimize the costs in materials and workmanship. For this purpose, some design concepts were

Table II
EXPERIMENTAL RESULTS FROM COMPRESSIVE TESTS

Specimen	Length [mm]	Width [mm]	Maximum Load [kN]	Stress [MPa]
M-01	50.55	50.90	57.75	22.44
M-02	51.35	50.97	60.79	23.22
M-03	51.22	50.95	58.98	22.60
M-04	51.40	51.07	62.62	23.85
M-05	51.32	50.75	57.59	22.11
M-06	51.22	50.80	60.71	23.33
Average	51.18	50.91	59.74	22.93
CV [%]	0.62	0.23	3.31	2.83

Table III
EXPERIMENTAL RESULTS FROM TENSILE TESTS

Specimen	E_f [GPa]	f_f [MPa]	ε_{fu} [%]	Failure mode
F-01	160	2786	2.18	U
F-02	161	2893	2.55	M
F-03	155	2879	2.50	M
F-04	155	2859	2.50	U
F-05	153	2886	2.45	M
Average	157	2861	2.44	-
CV [%]	2.23	1.52	6.05	-

extracted from the Peruvian Code, CNR-DT and AC434 [10], [6], [7], as explained below.

Regarding the adopted reinforcement scheme, CNR-DT recommends horizontal strips when a shear reinforcement is required. The nominal shear resistance of a retrofitted confined masonry wall can be evaluated as the sum of the contributions from the masonry wall and the reinforcement:

$$\phi_v V_n = \phi_v (V_m + V_f) \tag{1}$$

where ϕ_v is the strength reduction factor for Load and Resistance Factor Design method (LRFD), taken as 0.75 for shear loads; V_m is the shear contribution of the masonry; and V_f is the shear contribution of the reinforcement. Regarding V_m, it should be evaluated according to local code. For instance, in this work it was evaluated according to the Peruvian Code:

$$V_m = 0.5 \cdot v'_m \cdot \alpha \cdot t \cdot L + 0.23 \cdot \cancelto{0}{P_g} \tag{2}$$

where v'_m is the characteristic shear strength of the masonry, α is a wall slenderness factor correction, t is the wall's thickness, L is the wall's length, and P_g is the contribution of the vertical load to the shear resistance, which is neglected for design purposes. It is worth noting that Eq. 2 refers to the shear resistance of a new wall, therefore, an appropriate reduction

Table IV
EXPERIMENTAL RESULTS FROM DEBONDING TESTS

Specimen	f_b [MPa]	τ [MPa]	*Slip* [mm]	Failure mode
D-01	2068	0.66	3.50	2,4,5
D-02	1793	0.57	1.20	1
D-03	1612	0.51	2.40	3
D-04	1191	0.38	1.90	3
D-05	2023	0.64	2.20	3,4
Average	1737	0.55	2.24	-
CV [%]	20.52	20.47	37.43	-

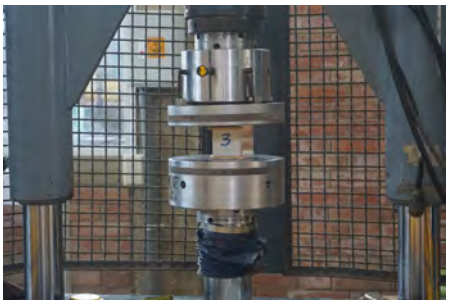

(a) Compressive test

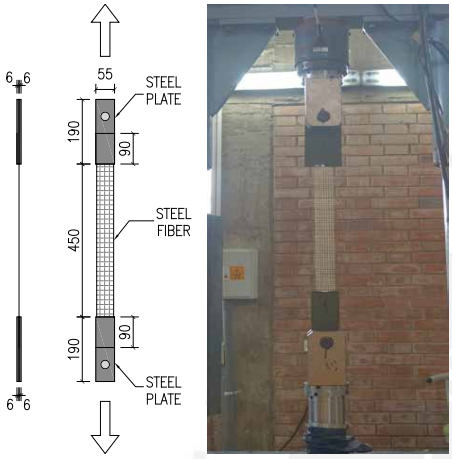

(b) Tensile test

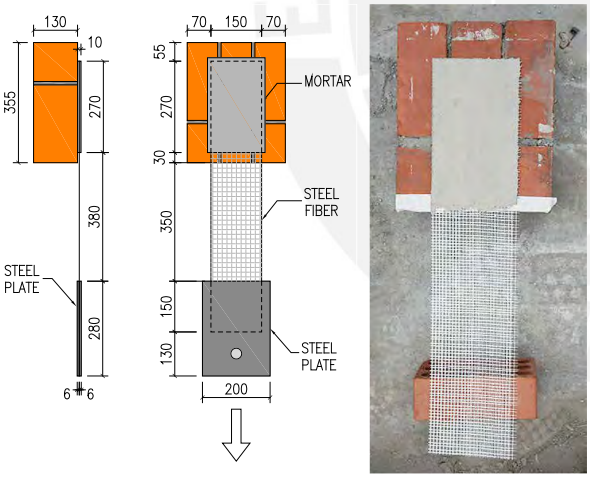

(c) Debonding test

Figure 3. Testing setup for control specimens (dimensions in millimeters)

factor must be employed to take into account the reduced contribution of a damaged wall.

Regarding the shear contribution of one reinforcing strip, it can be evaluated as

$$V_f = \frac{1}{\gamma} \cdot 0.6 \cdot d \cdot f_{fv} \cdot 2 \cdot \frac{A_{fv}}{p_{fv}} \tag{3}$$

where γ is a partial factor, taken as 1.2 for shear loads, d is the distance between the end of the fiber in compression and the centroid of the opposite confinement column, f_{fv} is the SRG design tensile strength, which can be calculated as $f_{fv} = E_f \varepsilon_{fv}$, E_f is the tensile modulus of elasticity of the cracked SRG, ε_{fv} is the SRG tensile design strain, which can be taken equal to the ultimate strain of steel textile but not greater than 0.004, $\varepsilon_{fv} = \varepsilon_{fu} \leq 0.004$, A_{fv} is the area of one steel textile branch, and p_{fv} is the separation between strips. Finally, the amount of strips required can be calculated as

$$n = \frac{1}{V_f} \left(\frac{V_u}{\phi_v} - V_m \right) \tag{4}$$

The cracked walls treated in the present work were designed with a shear resistance of $V_m = 211$ kN. However, taking into account their damaged state as well as the hysteretic behaviour showed in the cyclic tests, 75% of V_m was taken as the shear contribution of the masonry for design purposes. From the geometry of a typical wall (Fig. 1), it was possible to deduce $d = 2500$ mm. Hence, it was assumed that once the SRG is cracked, the tensile behaviour is governed by the steel textile. For this reason, E_f was taken to be the Young's modulus of the steel mesh: $E_f = 150$ GPa (Table III). Due to the fact that ε_{fu} was greater than 0.004 in all tests (Table III), $\varepsilon_{fv} = 0.004$ was adopted. Regarding A_{fv}, it was assumed that the strips were 100 mm wide and that there were 16 steel cords, which resulted in $A_{fv} = 8.6$ mm^2 according to the manufacturer's data sheet [12]. Finally, 450 mm was assumed as the separation between strips for design purposes. Fig. 4 shows the reinforcing scheme adopted for the present work.

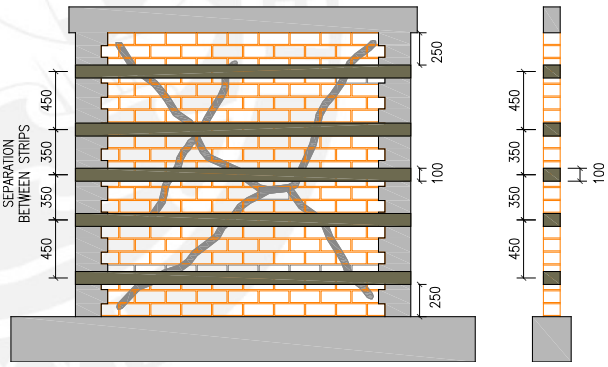

Figure 4. Details of the reinforcement for the repaired walls (dimensions in millimeters)

It should be noted that in Fig. 4, less separation between the strips was assumed at the mid-height of the walls. This assumption was related to the fact that the largest number of cracks were concentrated in the mid-height of the walls.

C. Procedure for retrofitting confined masonry walls with SRG

Before retrofitting, it is necessary to make a proper repair of the cracks since a good repair improves the recovery of the initial stiffness. In this study, cracks greater than 8 mm were opened using hand tools in order to avoid excessive out-of-plane effects. In the case of crushed bricks, it is recommended to replace them by new ones (Fig. 5b). Thereafter, the openings were filled with reparation mortar based on Portland cement with a volumetric ratio cement/sand = 1/3. After being repaired, the walls should be properly cured for at least 28 days. However, taking into account what would be done in a

massive application, they were moistened three times a day for seven days. In this way, it was hoped to guarantee a reasonable resistance of the reparation mortar. Fig. 5 shows the main steps involved in repairing CMW.

Regarding retrofitting, there are two previous jobs needed for the proper preparation of the zone of intervention. The first one is related to the fact that additional roughness can be provided by punching the bricks lightly by means of pointed tools. The second one consists in delimiting the intervention zone by means of Scotch tape. Although these jobs are not obligatory, they allow providing better adhesion between the SRG and the masonry substrate, as well as saving on material by using only what is necessary.

The retrofitting process started by moistening the intervention zone in order to avoid the absorption of the SRG's water by the masonry. Then, a first layer of mortar, 5 mm thick, was laid upon the masonry within the area delimited by the Scotch tape. Subsequently, the steel mesh was embedded lightly inside the first layer of mortar. Thereafter, a second layer of mortar 5 mm thick was laid in order to finish covering the embedded steel mesh. Finally, once all the SRG strips were finished, the Scotch tape was removed to start the curing process. Fig. 6 shows the main stages of the retrofitting process as explained above. It is worth noting that, in this work, it was possible to anchor the steel mesh by overlapping them 250 mm interspersed at each column's ending, because it only had to reinforce isolated walls. However, for other applications, a proper anchor for the steel mesh must be previously studied or applied according to the manufacturer's recommendations, in order to guarantee a good transmission of the stresses from the masonry to the SRG. Like reparation mortar, an SRG composite needs a proper curing process of at least 28 days. However, again taking into account what would be done in a massive application, the SRG composite was moistened for 14 days to guarantee a good mortar strength before testing.

D. Boundary conditions and instrumentation for the cyclic tests

Before testing, each foundation end was fixed to a reaction slab by means of hydraulic jacks to restrict them vertically. Another hydraulic jack and a reaction frame were used as rigid horizontal stops also for the foundation ends. A vertical load of 170 kN was applied by another hydraulic jack through two rigid steel beams in order to distribute the vertical load along the confinement beam. Regarding the horizontal cyclic loads, they were applied at the top of the wall by means of a dynamic actuator which was controlled by a computer.

Regarding the instrumentation, linear variable differential transformers (LVDTs) were placed, as shown in Fig. 7. Two LVDTs (LVDT 1 and 2) were placed along the diagonals of the masonry panel to measure their deformations and thus to have enough data in case an idealized strut-and-tie model is carried out. Another two LVDTs (LVDT 3 and 4) were placed at the confinement columns to measure their deformations due to vertical loads and bending effects during the cyclic test. One LVDT (LVDT 5) was placed between the geometric centre of the confinement beam and a reaction frame, which was assumed to be static. Fig. 7 shows the general testing setup as well as the instrumentation scheme for each cyclic test.

The cyclic loading was controlled by displacements, which means that the dynamic actuators applied displacements instead of forces. However, this had an internal load cell that allowed registering the load related to each displacement, thus it was possible to plot the corresponding hysteretic behaviour. In order to avoid kinematic effects, a quasi-static test was intended to be carried out by applying an average velocity of 0.25 cycles/minute. Regarding the applied history of displacements, it was defined according to FEMA 461 [14]. Thereby, each level of displacement resulted from increasing the previous level of displacement by a factor of 1.4. In addition, two cycles were also defined for each displacement level. It is worth highlighting that in the previous work [8], [9], only 11 displacement phases were considered, with a maximum displacement level of 20 mm, whereas in this work, 12 displacement phases have been taken into account, with a maximum displacement level of 30 mm, as shown in Fig. 8.

IV. Discussion of the Results

A. Cracking pattern

Within the category of confined masonry buildings, masonry walls act as bearing elements. Therefore, a premature failure of these walls would result in the building's collapse. In performance design, it is intended that the building has a specific performance level, which in turn is related to the post-earthquake disposition of the building. These performance levels can be roughly classified and assigned to certain levels of drift: (1) Immediate Occupancy (IO) – drift = 0.3%, (2) Life Safety (LS) – drift = 0.6%, and (3) Collapse Prevention (CP) – drift = 1.0% [15]. Fig. 9 shows the final cracking pattern for all the tested walls. However, in this work, each tested wall was evaluated separately by analysing its cracking patterns associated to each performance level, as well as its evolution along incremental displacements.

In general, all the retrofitted walls showed bending cracks at the columns' feet prior to a drift of 0.12%, which corresponds to the fifth loading phase. Subsequently, the cracks that were previously repaired started opening. However, it should be noted that not only the repaired cracks were opened during the tests, on the contrary, additional cracks took place. Fig. 9 and Table VI show the final cracking pattern and the evolution of cracking according to the different performance levels of the tested walls, respectively. It is worth noting that the tested walls had a mixed failure mode, namely, they started having cracks due to bending effects but finished having cracks also due to shear effects.

1) RW-01: During the fifth loading phase (drift = 0.12%), the first visible cracks occurred at the columns' feet because of bending effects. Thereafter, progressive bending cracks began to appear along the column's height. The first diagonal crack produced by shear effects took place at the seventh loading phase (drift = 0.23%). It should be noted that as the displacements increased, additional cracks due to shear effects occurred. Instead of RW-02 and 03, in this wall it was possible to explode all the tensile strength of the SRG composite. This

(a) Cracks opening (b) Filling of openings (c) Curing process

Figure 5. Main steps for repairing CMW (W-01)

(a) First layer of mortar (b) Placement of steel fiber mesh

(c) Second layer of mortar (d) Retrofitted wall

Figure 6. Stages for strengthening CMW with SRG (W-02)

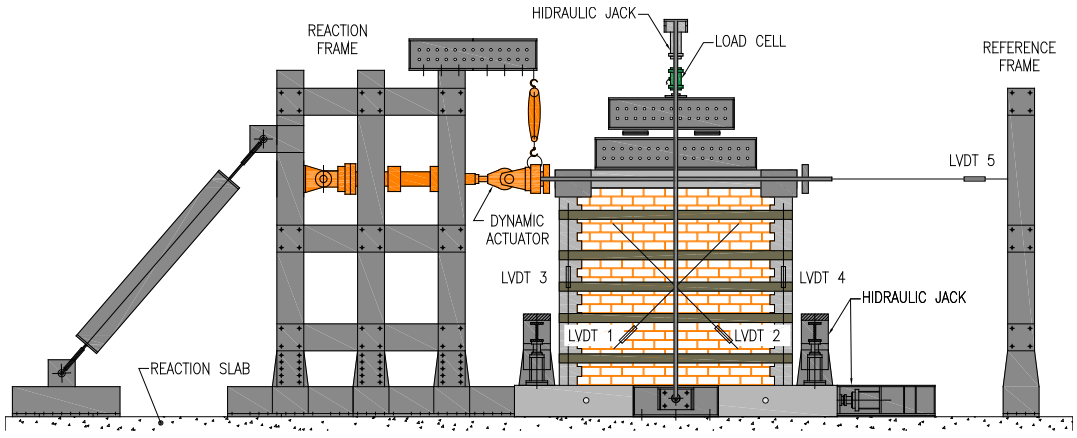

Figure 7. Setup and instrumentation for cycling test

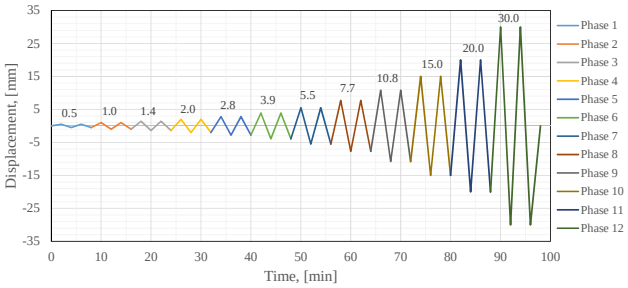

Figure 8. History of displacements

(a) RW-01

(b) RW-02

(c) RW-03

Figure 9. Cracking pattern of tested walls

could be seen by the rupture of the two SRG strips at the mid-height of the wall. However, it is worth noting that the ruptures were characterized by the breakage of the steel meshes and not by debonding failure, which in turn demonstrates the perfect adhesion developed among the SRG's mortar and masonry substrate. Similarly, other SRG strips showed elongations of the steel mesh, which could be observed because of the rupture of the external layer of mortar.

2) RW-02 & RW-03: Like RW-01, the first visible cracks in these walls occurred at the columns' feet due to bending effects. However, unlike RW-01, they took place at the fourth loading phase (drift = 0.083%). The first diagonal crack produced by shear effects took place at the eleventh (drift = 0.833%) and ninth (drift = 0.45%) loading phase, respectively. In addition, it should be noted that as the displacements increased, additional cracks due to shear effects took place. Unfortunately, in these walls it was not possible to explode the total tensile strength of the SRG strips. Nevertheless, it should be highlighted that this means they were prepared to withstand more tensile stress than they were subjected to. In addition, it is worth noting that a horizontal crack took place in both cases at the base of the wall, to have a sort of rocking effect, as is shown by the shape of the hysteresis loops in Fig. 10. The results associated to the first cracking and maximum load capacity are summarized in Table V.

In all cases, the collapse state was governed by the instability of the walls or the abrupt loss in load capacity either within the first or second loading phase. For instance, Fig. 10 (a) and (b) show only one cycle in the last loading phase, which was associated to the instability of the walls. Whereas Fig. 10 (c) shows an abrupt loading loss in the second cycle of the last loading phase.

Regarding the performance of the retrofitted walls, it is worth highlighting that only the retrofitted walls managed to prevent a collapse. Namely, the original walls were not able to withstand the drift level associated with collapse prevention (drift = 1.00%), whereas once repaired and retrofitted with SRG they were able to attain that level of performance. In fact, this helps to reduce the risk of life-threatening injury, which is of great interest in seismic areas.

B. Lateral displacement ductility

As mentioned above, the original walls were not able to reach the performance level of collapse prevention, which means they did not have enough ductility to resist lateral forces while maintaining their integrity. Taking into account the final lateral displacement reached by each wall, δ_u, and the displacement related to the change from linear to non-linear behaviour of the walls, δ_y, the ductility was evaluated as follows.

$$\mu = \frac{\delta_u}{\delta_y} \tag{5}$$

Fig. 11 and Table VIII compare the envelope curves of the un-retrofitted and the retrofitted walls, and a summary of the calculation of the ductility for the original and the retrofitted walls. The envelope curves resulted from averaging both the pushing and pulling envelope curves, which were extracted

Table V
EXPERIMENTAL RESULTS OF TESTED WALLS

Specimen	Direction	First cracking		Maximum load	
		Load [kN]	Drift [%]	Load [kN]	Drift [%]
RW-01	Push	195	0.116	340	0.833
	Pull	−180	−0.116	−340	−0.833
RW-02	Push	90	0.083	235	0.833
	Pull	−110	−0.116	−285	−0.833
RW-03	Push	95	0.083	255	0.625
	Pull	−125	−0.116	−205	−0.625

Table VI
CRACKING EVOLUTION OF TESTED WALLS

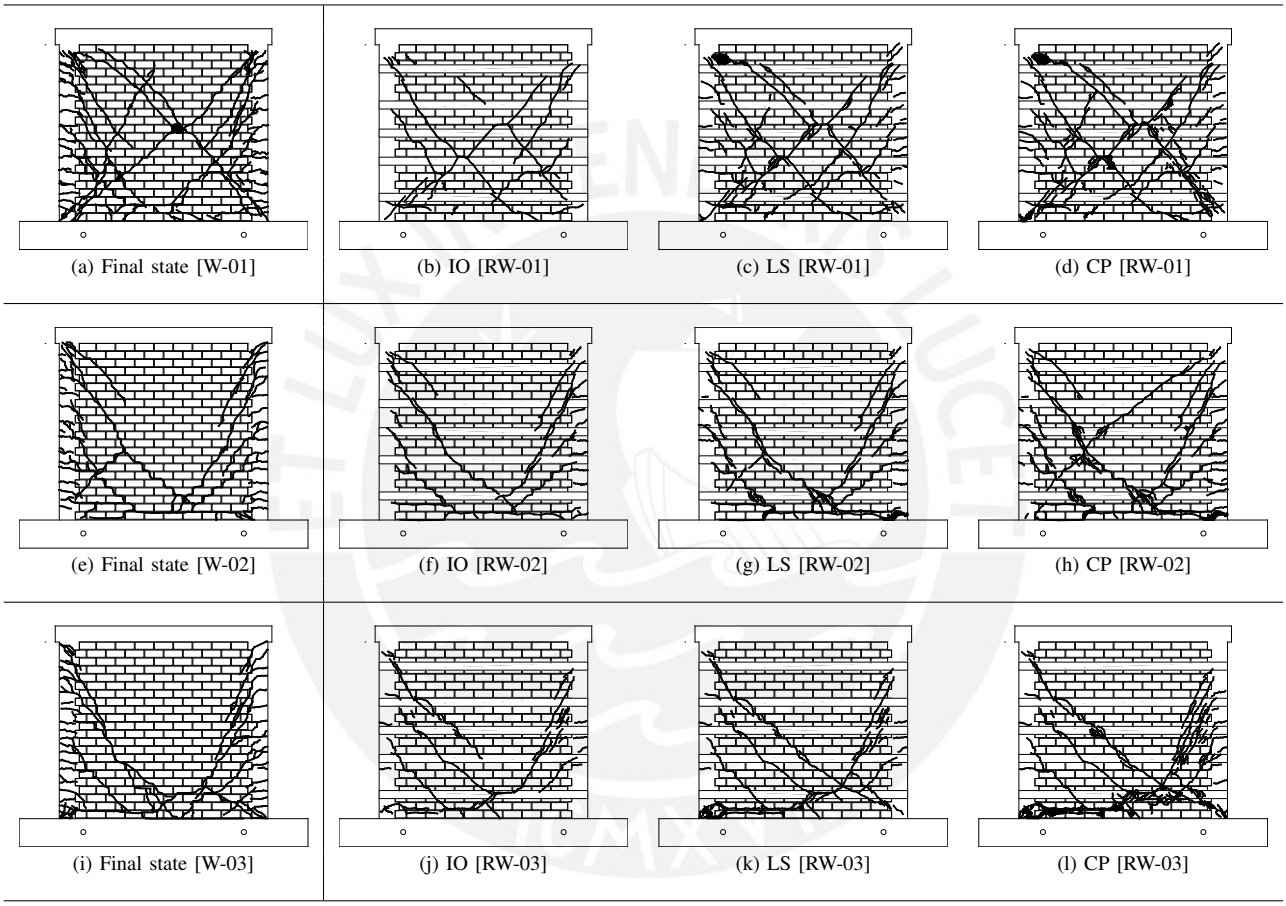

(a) Final state [W-01] (b) IO [RW-01] (c) LS [RW-01] (d) CP [RW-01]

(e) Final state [W-02] (f) IO [RW-02] (g) LS [RW-02] (h) CP [RW-02]

(i) Final state [W-03] (j) IO [RW-03] (k) LS [RW-03] (l) CP [RW-03]

from the first and third quadrants of the hysteresis curves (Fig. 10). It has to be noted that in the case of RW-01 the increment in ductility was about 100%, whereas in the rest it was about 50%. It also has to be pointed out that the original walls withstood higher forces than the retrofitted ones in the first performance level (IO). However, for the second performance level (LS), both the original and retrofitted walls showed almost the same performance level in terms of lateral forces. Finally, the retrofitted walls, besides being the only ones which could reach the last desired performance level (PC), were able to withstand almost the same level of lateral forces as the LS. This means that after the LS performance level, the retrofitted walls could continue withstanding forces by maintaining their integrity.

Table VII
IMPROVED DUCTILITY CALCULATION OF TESTED WALLS

Specimen W / RW	δ_y [mm]	W		RW		Increment [%]
		δ_u [mm]	μ	δ_u [mm]	μ	
01	2.8	15.0	5.35	30.0	10.7	100
02	2.0	20.0	10.0	30.0	15.0	50
03	2.0	20.0	10.0	30.0	15.0	50

C. Energy dissipation and damping ratio

The Ultimate Limit State (ULS) design approach considers the maximum strength that could be withstood by the structural elements. This is considering both linear and non-linear behaviour of the elements, either due to material or geometric non-linearity. Whenever non-linear behaviour takes

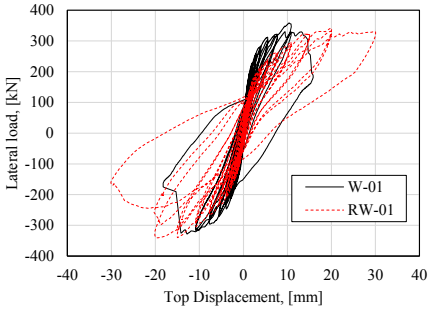

(a)

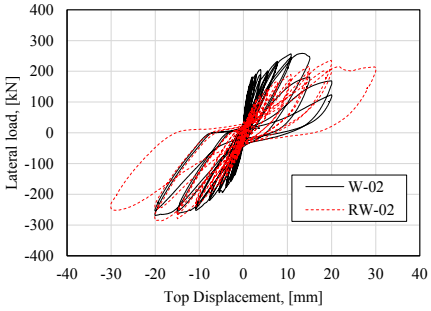

(b)

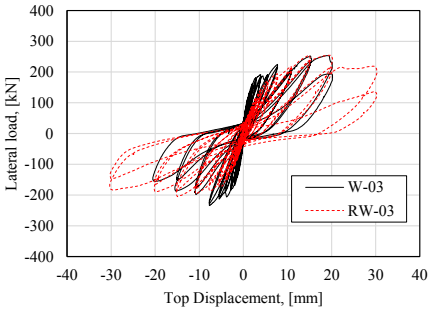

(c)

Figure 10. Hysteresis curves for tested walls

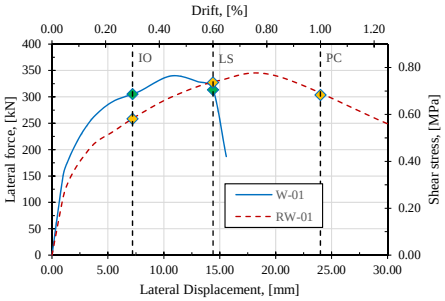

(a)

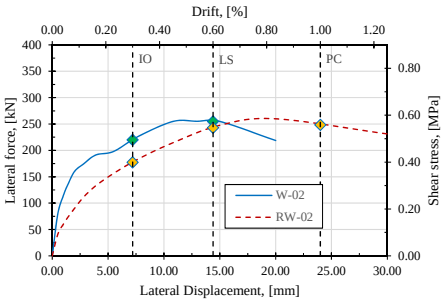

(b)

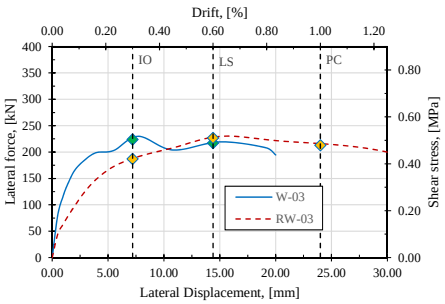

(c)

Figure 11. Envelope curves for tested walls

place, inelastic strains are experienced, which in turn can produce damage. It should be noted that the more inelastic strains there are, the more structural damage will take place. During this process, a certain amount of energy absorption and dissipation is involved. In this section, the energy dissipation, E_d, will be evaluated by the area within each hysteretic loop, as shown in Fig. 12. Additionally, the equivalent hysteretic viscous damping, ξ_{hyst}, is evaluated as the ratio between the dissipated energy and the elastic strain energy, as shown in Fig. 12.

Fig. 13 shows the cumulative energy dissipated for each loading phase. It has to be noted that the SRG gave the original walls the ability to dissipate more energy by means of greater inelastic displacements. In general terms, both the original and retrofitted walls had almost the same cumulative energy dissipation until the maximum displacement of the original walls. However, a freak tendency could be observed in the

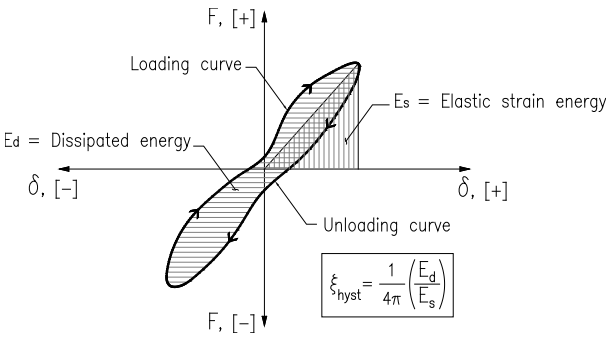

Figure 12. Calculation of energy dissipation and damping ratio

last loading phase of W-01, where an abrupt increment of energy dissipated was captured, as is shown in Fig. 13. This is related to the fact that in this loading phase an abrupt loss of capacity load (Fig. 10a) was registered, which in turn resulted in a quite large hysteretic loop. A similar phenomenon was registered for RW-01. However, this took place for a displacement that corresponded to the double of its original wall and this occurred only in the pulling branch of the hysteresis loops (Fig. 10a).

It is well-known that pushing-and-pulling equipment needs certain small displacements to be properly calibrated before measuring reasonable forces. This usually causes unreal loops at small displacements, which can be understood as an unrealistic non-linear behaviour since they are expected to have a linear-elastic behaviour. This assumption was taken into account by excluding the first two loading phases from the calculation of the average hysteresis damping. Fig. 14 shows the variation of the hysteresis damping along the incremental loading phases for each tested wall. It is worth noting that the retrofitted walls had greater values of hysteresis damping throughout the tests. Nevertheless, the freak energy dissipation just mentioned also affected the calculation of the hysteresis damping in the last loading phase of W-01. For this reason, this value was also excluded from the computation of the average hysteresis damping. Once this assumption is made, it is possible to note that RW-01 showed an average hysteresis damping of 9.65% against the 7.90% of W-01, which means an increment of 20%. RW-02 showed an average hysteresis damping of 12.00% against the 10.50% of W-02, which means an increment of 14%. Finally, RW-03 showed an average hysteresis damping of 12.45% against the 9.90% of W-03, which mean an increment of 26%.

D. Initial stiffness and stiffness degradation

Fig. 15 shows the stiffness degradation of tested walls. The same effect of the first two loops is shown when computing the initial stiffness. Therefore, the initial stiffness was considered as that related to the third loop. It should be noted that each point in Fig. 15 was obtained from averaging the stiffness related to the push-and-pull directions for each loading phase. Additionally, it is also important to highlight that the recovery of the initial stiffness will be as good as the goodness of the repair. Since one aim of this work is to show that repairing and retrofitting with SRG can be done in an easy and massive way, this work tried to reproduce an effective and economic repair job, as explained above. This resulted in a recovery of 75% of the original wall's initial stiffness for RW-01 and 50% for RW-02 and 03.

Regarding stiffness degradation, it is known that it can be the result of cracking, crushing, rebar buckling, cracks opening and closing, among other factors. Likewise, the level of stiffness degradation is related to the features of the structure (e.g. material properties, geometry, connection types), as well as to the loading history (e.g. displacement level for each loading phase, number of cycles per phase, increment ratio of displacements) [16]. The stiffness degradation is very helpful for design codes since it allows them to define the drifts according to the expected performance levels. In this case, following the three main desired performance levels (IO, LS and CP), the stiffness decay of the initial stiffness of the retrofitted walls was evaluated for each of these states, as described in Table VIII.

Table VIII
PERCENTAGES OF STIFFNESS AT PERFORMANCE LEVELS REGARDING INITIAL STIFFNESS

Wall	Immediate Occupancy (IO)	Life Safety (LS)	Collapse Prevention (CP)
W-01	35%	12%	-
RW-01	40%	25%	15%
W-02	32%	16%	-
RW-02	47%	32%	20%
W-03	32%	16%	-
RW-03	48%	30%	16%

The vertical load applied to W/RW-01 gives them more stiffness which is clearly evidenced in the first loading phases. However, at the same time, this makes them more brittle, which means they lose stiffness more quickly than W/RW-02 and 03, as new cracks take place or existing cracks become enlarged. Moreover, taking into account the fact that before the retrofitting, the walls were totally failed, one can be sure that the SRG had an impact on reducing the brittle behaviour of confined masonry walls. Indeed, Fig. 15 shows that regardless of the walls, the retrofitted ones showed a lesser stiffness degradation than the original walls, which in turn was related to the integrity and stability of the walls.

V. CONCLUSIONS

The suitability of SRG as a seismic retrofitting technique was evaluated by applying it externally to three confined masonry walls and testing them under cyclic in-plane loads. Prior to the retrofitting, the walls were subjected to cyclic loads and were led to their ultimate limit state. It should be noted that of the three tested walls, one had a vertical load of 170 kN during the testing and the rest were only subjected to lateral loads.

A design procedure was developed by taking some concepts from the Peruvian Code, CNR-DT and AC434. Subsequently, the retrofitting system consisted of 5 SRG strips, each one with a thickness of 10 mm and a width of 100 mm. Within each strip, there was embedded a mesh of 0.084-mm thick galvanized steel fiber. The retrofitting process was also given in detail, showing its easy maneuverability and applicability of the materials involved.

The experimental results showed that there was a considerable improvement of the seismic performance of the retrofitted confined masonry walls in comparison with the originals. In terms of ductility, SRG could increase the lateral deformation capacity by 100% in one wall and 50% in the rest. This allowed the walls to reach the performance level of collapse prevention, according to FEMA-356. In terms of energy dissipation, the retrofitted walls showed they were able to dissipated more energy than the original walls. Likewise, greater average values of hysteresis viscous damping were registered during the incremental loading phases. Finally, taking

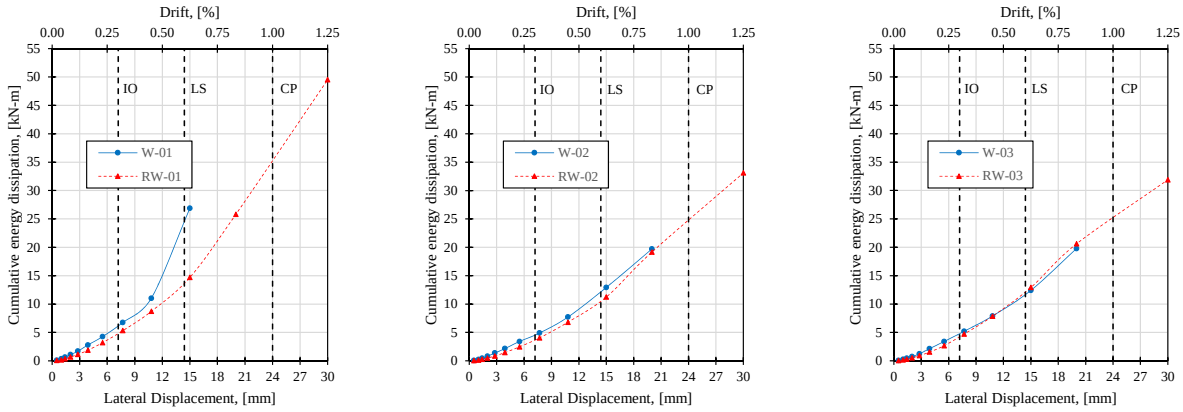

(a) (b) (c)

Figure 13. Cumulative energy dissipation for tested walls

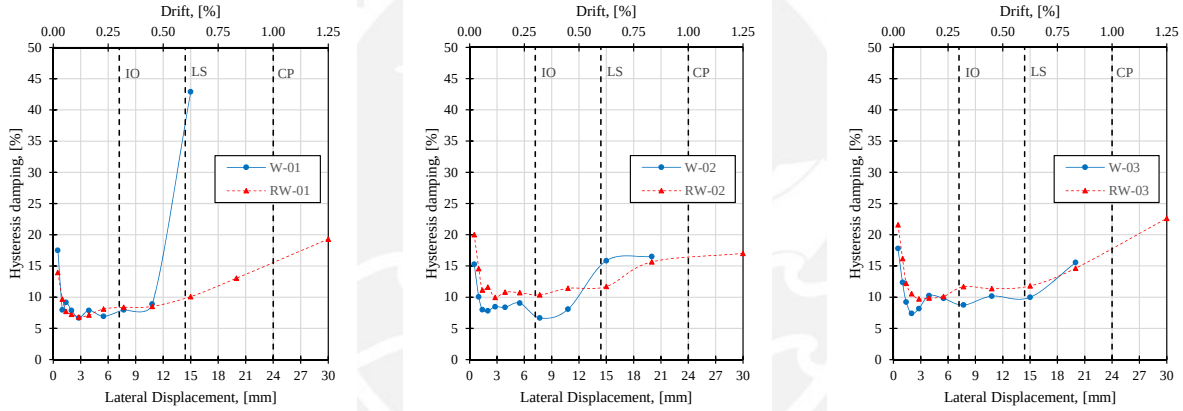

(a) (b) (c)

Figure 14. Hysteretic damping ratio for tested walls

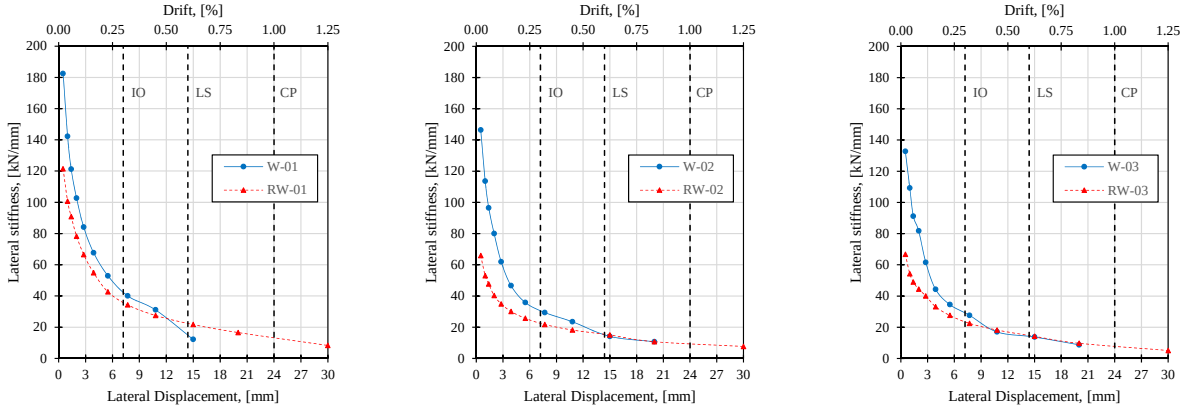

(a) (b) (c)

Figure 15. Stiffness degradation for tested walls

into account that the retrofitting was applied to failed walls, it was possible to observe that the SRG allowed the walls to enjoy a slighter degradation of their stiffness than the original walls. In this way, the brittle behaviour was improved and also the integrity and stability of the walls were guaranteed.

ACKNOWLEDGMENT

The authors are grateful for the financial support provided by CONCYTEC within the framework of the N° 232-2015-FONDECYT Agreement, as well as to the industrial company KERAKOLL for providing the necessary materials for the retrofitting.

REFERENCES

[1] Instituto nacional de estadística e informática (INEI), *Censos nacionales 2014: población y vivienda*, 2014.
[2] N. Kassem, A. Atta, and E. Etman, "Structural Behavior of Strengthening Masonry In-filled Frames Subjected to Lateral Load using Bonded and Un-bonded CFRP," *KSCE Journal of Civil Engineering*, vol. 21, no. 3, pp. 818–828, 2016.
[3] E. Quagliarini, F. Monni, F. Greco, and S. Lenci, "Flexible repointing of historical facing-masonry column-type specimens with basalt fibers: A first insight," *Journal of Cultural Heritage*, 2016.
[4] N. Gattesco and I. Boem, "Characterization tests of GFRM coating as a strengthening technique for masonry buildings," *Composite Structures*, vol. 165, pp. 209–222, 2017.
[5] S. De Santis, F. Ceroni, G. De Felice, M. Fagone, B. Ghiassi, A. Kwiecie, G. Lignola, M. Morganti, M. Santandrea, M. Valluzzi, and A. Viskovic, "Round robin test on tensile and bond behaviour of steel reinforced grout systems," *Composites Part B*, 2017.
[6] Advisory Committee on Technical Recommendations for Construction, *CNR-DT-200-R1, Guide for the design and construction of externally bonded FRP systems for strengthening existing structures*, 2013.
[7] International Code Council – Evaluation Service, *AC-434, Acceptance criteria for masonry and concrete strengthening using Fabric-Reinforced Cementitious Matrix (FRCM) and Steel Reinforced Grout (SRG) composite systems*, 2017.
[8] J. Manchego and S. Pari, "Análisis experimental de muros de albañilería confinada en viviendas de baja altura en Lima, Perú," Master's thesis, Pontificia Universidad Católica del Perú, Lima, Peru, 2016.
[9] M. Luján, *Refuerzo de muros de albañilería confinada con mallas de acero*, Lima, Peru: Fondo Editorial PUCP, 2016.
[10] Ministerio de Vivienda, Construcción y Seneamiento (SENCICO), *E070, Reglamento nacional de edificaciones: Albañilería*, 2006.
[11] CEB-FIP, *Model code 2010*, London: Thomas Telford, 2010.
[12] Kerakoll, "GeoSteel G600," Kerakoll - The GreenBuilding Company, Tech. Rep., 2013.
[13] ——, "GeoCalce F Antisismico," Kerakoll - The GreenBuilding Company, Tech. Rep., 2017.
[14] Applied Technology Council, Mid-America Earthquake Center, Multidisciplinary Center for Earthquake Engineering Research, Pacific Earthquake Engineering Research Center, and National Earthquake Hazards Reduction Program, *Interim Testing Protocols for Determining the Seismic Performance Characteristics of Structural and Nonstructural Components*. Washington, DC: Federal Emergency Management Agency, 2007.
[15] Federal Emergency Management Agency, "FEMA-356, Commentary for the seismic rehabilitation of buildings," Washington, DC: Federal Emergency Management Agency, 2000.
[16] Applied Technology Council of the FEMA, *P440A: Effects of strength and stiffness degradation on seismic response*, Washington, DC: Federal Emergency Management Agency, 2009.

Capítulo IV

Evaluación numérica

4.1. Numerical analysis of bond behavior between masonry and SRG strengthening technique

Numerical Analysis of Bonding between Masonry and Steel Reinforced Grout

Jhoselyn Salsavilca[a,*], Jhair Yacila[a], Nicola Tarque[a], Guido Camata[b]

[a] *Pontifical Catholic University of Peru. Department of Civil Engineering. San Miguel 15088, Lima, Peru.*
[b] *University G.d'Annunzio of Chieti and Pescara. Department of Engineering and Geology. Pescara 65127, Italy*

Abstract

The behaviour of the bonds between masonry and composite materials such as steel reinforced grout (SRG) applied as an externally bonded reinforcement is critical in transferring stresses from the structural elements to the SRG. An experimental and numerical investigation with single-lap shear bond tests between Peruvian masonry and an SRG system is presented. The experimental part shows that the main failure mechanism is the slippage of the fibers from the mortar with a premature cracking of the outer mortar layer, showing that the mortar has a significant influence, along with the properties of the fiber–mortar interface, on the behaviour of the bond. The numerical model, validated against experimental results, takes the non-linearity of the mortar into consideration so as to analyse its effect on the bond when compared to assuming a rigid and linear mortar. This shows that modelling a non-linear mortar leads to more accurate results. The load–slip response considering a non-linear mortar is put forward after evaluating different values of the fracture energy of the mortar.

Keywords: bond behaviour, SRG, masonry, numerical model, non-linear mortar

1. Introduction

In Peru, confined masonry (CM) is a type of construction that is quite widespread: dwellings made of CM constitute 74% of all buildings, and 60% of them are informal [1]. Earthquakes have evidenced the high vulnerability associated to informal dwellings, which leads to human and material losses. Therefore, reinforcing structures with composite materials has arisen as an innovative solution to improve their seismic performance.

Fiber Reinforced Polymer (FRP) has shown its effectiveness as a strengthening technique for structures, whether concrete or masonry. However, some drawbacks related to its organic matrix have fostered the development of new materials for this technique: epoxy resin has been replaced by an inorganic matrix (mortar) to overcome problems such as its inapplicability to wet surfaces, poor performance at high temperatures and in alkaline environments, possible hazards for workers, some incompatibilities of the resin with substrate materials, and lack of permeability to water vapour [2, 3, 4]. This newly developed alternative to FRP is called Fiber Reinforced Mortar (FRM), and if it comprises high strength steel cords, it is known as Steel Reinforced Grout (SRG).

The effectiveness of SRG depends on the bonding between the composite material and the substrate [5]. Several researchers [6, 7, 8, 9] have studied the bond experimentally by means of shear bond tests. The main debonding mechanism observed was the detachment of the fibers from the matrix (i.e. at the fiber–mortar interface), and not at the matrix–substrate interface as is the case with FRP. This has led to the belief that in most cases the bonding with masonry strengthened with SRG is more dependent on factors such as the characteristics of the matrix and fiber. Due to this difference between the two techniques, the formulations derived for FRP can turn out to be inaccurate for design purposes in the case of SRG reinforcing systems, for which specific formulations are certainly required [10]. Hence a comprehensive understanding of the behaviour of the whole of the bond between SRG and masonry is crucial for design and strengthening purposes. Due to the development of reliable numerical modelling methods, it is now

*Corresponding author at: Pontifical Catholic University of Peru. Department of Civil Engineering. San Miguel 15088, Lima, Peru
Email addresses: jsalsavilcap@pucp.pe (Jhoselyn Salsavilca), jhair.yacila@pucp.edu.pe (Jhair Yacila), sntarque@pucp.edu.pe (Nicola Tarque), g.camata@unich.it (Guido Camata)

possible to investigate the required aspects with much less expense in terms of time and money (i.e. experimental tests) [11].

Previous research has studied the bond analytically [12, 13], where the main assumption is to consider the mortar as a rigid material, i.e. only the displacement of the fiber is taken account. Other studies [5, 4, 14] have considered the mortar in terms of linear-elastic continuum elements during the numerical modelling of shear bond tests. In both cases, (rigid and linear-elastic), the non-linearities of the system are concentrated at the fiber–mortar and substrate–mortar interfaces. According to [5], this approach is attractive since it can capture critical aspects related to the initiation and propagation of the bond by using suitable bond interface slip laws. However, according to the failure modes observed in past studies [6, 7, 8, 15], a premature cracking of the outer mortar layer has been observed. Hence, it turns out to be interesting to model lime-based mortar as a plastic damaged material in order to evaluate the effect of its non-linearity on the whole of the response of the bond; the present paper addresses this issue.

This paper presents the results of experiments that were carried out to evaluate the bond between SRG and Peruvian masonry by means of single-lap shear bond tests at the Structural Laboratory of the PUCP. The tests followed the indications proposed by [6, 7], whose investigations were the basis for developing the test recommendations of Rilem TC 250-CSM (Composites for the Sustainable strengthening of Masonry) [9]. It was observed that the main failure mechanism was the detachment of the fiber from the matrix with a premature cracking of the outer mortar. A three-dimensional (3D) numerical model is used to describe the behaviour of the bond between SRG and masonry. The bond consists of one layer of a galvanized steel fiber net embedded within two layers of a lime-based mortar. The bond slip law at the fiber–mortar interface was calibrated assuming the mortar to be rigid. It was observed that it is not necessary to implement a bond slip law at the mortar–substrate interface and it is correct to assume a perfect bond at that interface. This is supported by experimental results, where the main failure was at the fiber–mortar interface and not at the mortar–substrate interface.

With the aim of evaluating the influence of the mortar on the behaviour as a whole, linear-elastic and plastic-damaged behaviour were considered in the model. The validity of the constitutive behaviour considered for each material and interfaces was assessed through a comparison with experimental data and it is shown that the FE simulations are in satisfactory agreement with the experimental results. However, the numerical curves with a non-linear mortar have a better fit to the experimental curves, which is in accordance with the experimental results where the cracking of the outer mortar occurred. Therefore, the authors conclude that a modelling that takes into consideration the non-linearity of the matrix should be encouraged. Finally, it is evaluated how the fracture energy in traction for the mortar affects the whole behaviour and its failure pattern. Based on this, the present paper also describes the relation between the constitutive law of the mortar and the F–s (force–slip) curve of the behaviour of the SRG–masonry bond.

2. Discussion of the experiments

The single-lap shear bond test is widely used as an effective means for the characterization of the behaviour of a bond between externally bonded reinforcement and concrete as well as masonry substrates [5]. It has been adopted in the work presented here. Five shear bond tests were performed on specimens composed of Peruvian masonry as the substrate and galvanized steel fiber net embedded in lime-based mortar as the SRG system. The tests are explained in the following.

2.1. Materials and specimens

A masonry arrangement was used as the substrate for the shear bond test. The compressive strength (σ_c) and the elastic modulus (E) of the masonry were characterized through compressive tests in accordance with NTP E.070 [16] on four specimens with dimensions of $230 \times 600 \times 130$ mm (Fig. 1(a)). The lime-based mortar was characterized with compressive tests on six 50-mm cubic specimens according to American Standard ASTM C141 [17] (Fig. 1(b)) in order to know their strength. These lime-based mortar samples were taken from the same batch of the mortar as for the shear bond tests.

A series of tensile tests on five specimens composed of galvanized steel fiber and aluminum tabs were tested to evaluate the elastic modulus and maximum strength. The aluminum tabs ($190 \times 55 \times 6$ mm) were glued by means of a strong adhesive (epoxy resin) on the ends of the galvanized steel fiber net to assure a uniform stress distribution and prevent slips in the gripping areas. The five samples shared the same geometry, with free length and width equal to 400 mm and 50 mm, respectively (see Fig. 1(c)). A summary of the material mechanical properties is presented in Table 1.

(a) (b) (c)

Fig. 1. Characterization tests for: (a) masonry; (b) lime-based mortar; (c) steel fiber.

Table 1. Material properties, CoV in round brackets.

Material	E [GPa]	σ_c [MPa]	σ_t [MPa]
Masonry	5.72 (12%)	10.16 (7%)	1.39 (10%)
Mortar	9.1*	22.93 (2.83%)	2.92*
Steel Mesh	157 (2.2%)	–	2861 (1.5%)

*Reported by [18]

2.2. *Debonding testing*

The shear bond test was carried out on five specimens (ADH01-05) with brick arrangements (masonry prism) of $290 \times 355 \times 130$ mm. The SRG system applied on the arrangement had a bond length of 270 mm and a width of 150 mm. The steel cord strip was embedded in the middle of the 10-mm thick mortar. The length between the free lateral side of the prism and the end of the bonded area was 70 mm. These specimens were characterized by placing the reinforcing strips parallel to the largest side of the brick, which allows having more representative results. The final scheme is presented in Fig. 2.

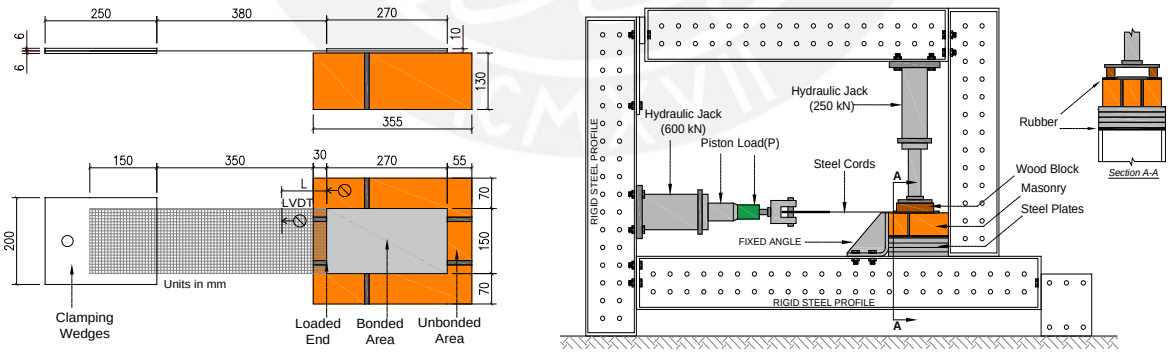

(a) (b)

Fig. 2. (a) Geometry of SRG strengthened masonry specimens and (b) shear debonding test set-up.

The tests were performed while blocking the masonry prism by rigid steel plates both at the back and at the front and applying a vertical load (10 kN) to the substrate, with the aim of avoiding rotation. Moreover, the alignment between the applied load and the middle plane of the reinforcement was guaranteed by preparing clamping wedges with a hole (located in the middle) which along with a pin transmit the load to the whole system (Fig. 2(a)). With the

clamping wedges, the fiber is pulled out from the bottom by controlled displacements at a constant rate of 0.3 mm/min until failure and the resulting load was measured by means of a load cell.
The measurement system consisted of a linear variable differential transformer (LVDT) placed at a certain distance (l) from the loaded end of the composite allowing the measurement of a local displacement (LD) Fig. 2(a). In order to evaluate the displacement of the steel cords relative to the masonry support, a simple formula was employed:

$$s = LD - \varepsilon\, L \tag{1}$$

where $\varepsilon\, L$ is the elastic elongation of the unbonded textile, ε being evaluated as the applied load divided by the sectional area, and with Young's modulus E of the textile derived from tests on dry textile specimens. It is adequate to assume that all the cords are equally loaded, due to the gripping system that consists of steel textile embedded with a strong epoxy in the aluminum tabs, as in this case.

2.3. Experimental results

The main modality of failure consists in the detachment of the fibers from the lime-based mortar with a premature cracking of the outer mortar layer. For instance, the ADH01 specimen presented a localized debonding at the mortar–substrate and steel–mortar interfaces with a premature cracking of the outer mortar layer and a rupture of the fibers (Fig. 3(a)). During the testing of ADH02, a debonding with cohesive failure of the masonry occurred, which may indicate a higher initial stiffness at the steel–mortar and mortar–substrate interfaces than for the other samples that failed at either of these interfaces (Fig. 3(b)). Samples ADH03 and ADH04 presented a good bond strength at the mortar–substrate interface but not at the textile-to-mortar interface, causing a debonding at that interface (Fig. 3(c)). The last specimen, ADH05, presented a debonding at the steel–mortar interface also but combined with a premature cracking of the outer mortar layer without any rupture of the fibers (Fig. 3(d)).

The load–slip (F–s) response curves are illustrated in Fig. 4 and display a good agreement at the linear-elastic stage with the exception of ADH02, which presents a high initial stiffness associated to its totally different failure mode described above. The similar detachment mechanisms of ADH01 and ADH05 lead to almost equal curves for both. The samples associated to a failure at the steel–mortar interface (ADH03 and ADH04) developed a lower maximum applied load than the others. The response appears more scattered beyond 0.35 mm slip, i.e. the elastic phase, due to the different ways in which the debonding process took place. The average debonding force of the specimens is 22.44 kN (CoV=21%) and the average slip at the maximum force is 2.2 mm (CoV=37%).

3. Numerical calibration of bond slip laws at the interfaces

The approach consists of modelling the bond using a zero-thickness interface element between the substrate and the mortar. Additionally, another non-linear interface was considered, between the steel and mortar, due to the failure modes occurring during the experiments. The masonry and fiber are modelled as linear-elastic continuum elements. The assumption of material linear elasticity for these elements was verified through the stress observed in the numerical model, which was always lower than the maximum stresses given in Table 1. The mortar is modelled as a rigid material, which means that only the displacement of the steel textile is considered [12].
The bond–slip law (BSL) at the substrate–mortar interface can be evaluated with formulations proposed for FRP [19, 20, 21] since its type of failure is generally at that interface. However, the BSL at the steel–mortar interface, which is the most important as it is the weakest interface in this model, is evaluated following the formulations extracted from the analytical model develop by [12].

3.1. Numerical Formulation

The numerical analysis has been developed with a 3D finite element model using the FE code of ABAQUS. It is useful to think of each interface as a cohesive zone that joins two surfaces. These surfaces belong to certain materials, which develop a relative displacement between them, such as substrate–mortar or steel–mortar. The cohesive zone is described by means of cohesive zone models, which can be trilinear, parabolic, exponential, etc., and are represented by a traction–separation (i.e. force–displacement) law (TSL). In this way, cohesive zones are implemented to investigate the initiation and propagation of a crack in a solid [22].
The cohesive behaviour of each interface was element-based, which is modelled with the cohesive elements labeled as

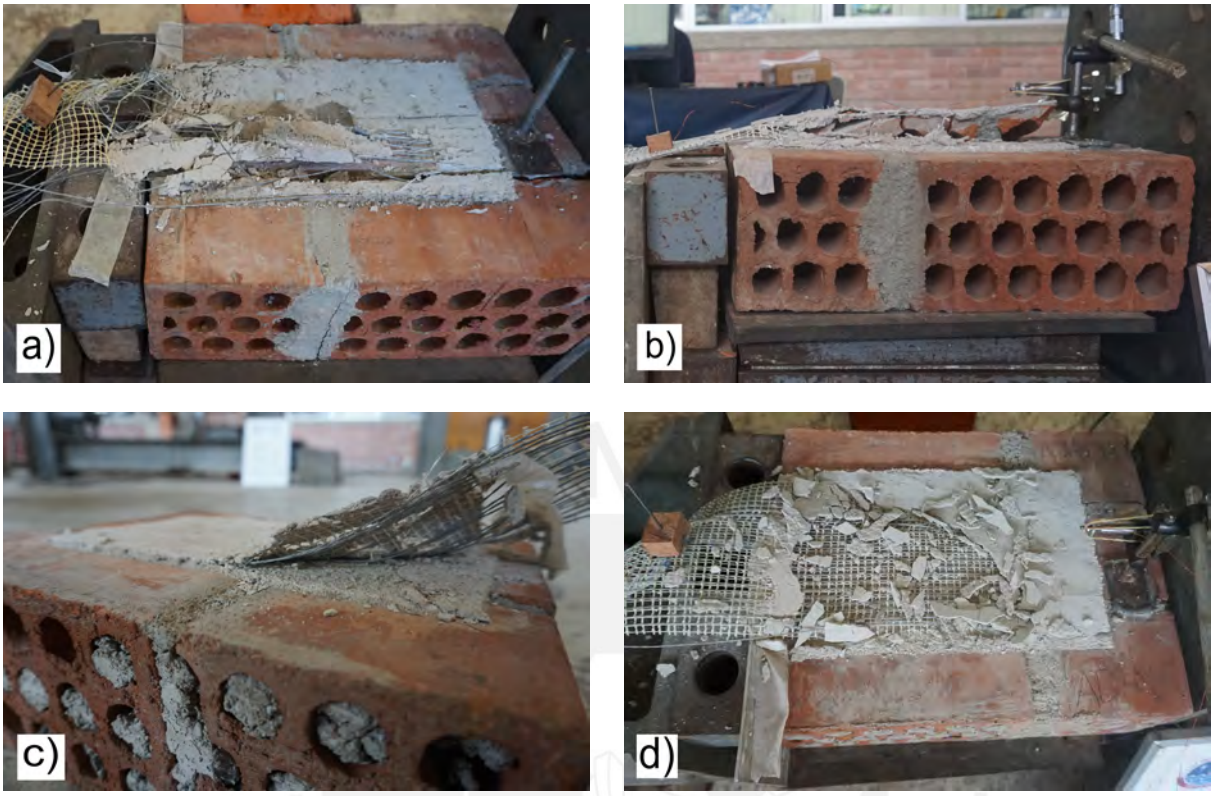

Fig. 3. Failure modes during shear bond tests: (a) debonding at the the mortar–substrate and steel–mortar interfaces, premature cracking of the outer mortar layer and rupture of fibers: ADH01, (b) cohesive failure of the masonry: ADH02, (c) debonding at steel–mortar interface: ADH03-04, (d) debonding at the steel– mortar interface and premature cracking of the outer mortar layer: ADH05.

COH3D8 in ABAQUS if they are eight-node ones. The constitutive response assumes an initial linear elastic behaviour followed by the initiation and evolution of damage when a damage criterion is satisfied. The linear ascending branch is defined by a traction separation model which is written in terms of an elastic constitutive matrix that relates the stresses to the displacements across the interface:

$$t = \left\{ \begin{array}{c} t_n \\ t_s \\ t_t \end{array} \right\} = \begin{bmatrix} K_{nn} & K_{ns} & K_{nt} \\ K_{sn} & K_{ss} & K_{st} \\ K_{tn} & K_{ts} & K_{tt} \end{bmatrix} \left\{ \begin{array}{c} \delta_n \\ \delta_s \\ \delta_t \end{array} \right\} = K\ \delta \tag{2}$$

where t is the nominal traction vector with normal component t_n and shear components t_s and t_t; the corresponding separations are denoted by δ_n, δ_s, and δ_t.
The cohesive behaviour follows Eq. 2 until a specific damage criterion is reached. Damage initiation refers to the onset of a degradation of the response of a material point. Damage initiates when a quadratic interaction function involving the nominal stress ratios reaches a value of one. This criterion can be represented by

$$\left(\frac{\langle t_n \rangle}{t_n^0}\right)^2 + \left(\frac{t_s}{t_s^0}\right)^2 + \left(\frac{t_t}{t_t^0}\right)^2 = 1 \tag{3}$$

where $\langle . \rangle$ denotes the Macaulay bracket function which implies no damage initiation under pure compression. The superscript 0 indicates the peak values of the nominal traction vector.
Once the corresponding initiation criterion is met, the damage evolution law describes the rate at which the stiffness

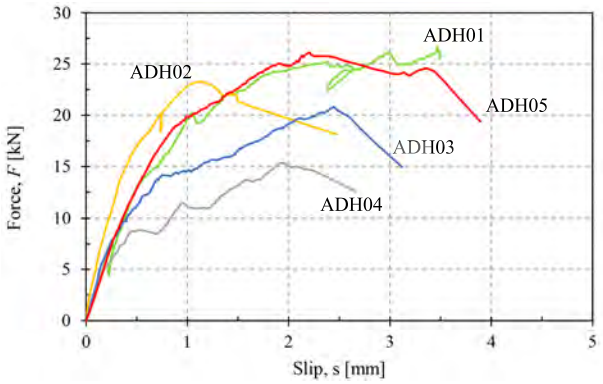

Fig. 4. Load–slip curves from shear bond tests.

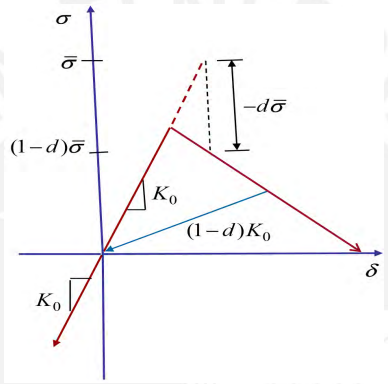

Fig. 5. Typical damage response for cohesive zone (taken from [22]).

is degraded. The stress components of the traction–separation model are affected by the damage variable D:

$$t_n = \begin{cases} (1-D).\overline{t_n} & \text{if } \overline{t_n} > t_n^0 \\ \overline{t_n} & \text{otherwise} \end{cases} \tag{4a}$$

$$t_i = \begin{cases} (1-D).\overline{t_i} & \text{if } \overline{t_i} > t_i^0 \\ \overline{t_i} & \text{otherwise} \quad i = s,t \end{cases} \tag{4b}$$

where $\overline{t_n}$, $\overline{t_s}$, and $\overline{t_t}$ are the stress components predicted by the elastic traction–separation behaviour for the current strains without damage, and t_n is the normal component of the traction damage vector while t_s and t_t= are its shear components. A typical damage response is plotted in Fig. 5. Different damage evolution laws were assigned to each interface. In the case of the substrate–mortar interface, the damage variable D, which varies between 0 (damage initiates) and 1 (when complete delamination has occurred in the interface element), was defined by means of the linear damage evolution law.

$$D = \frac{\overline{\delta}_f \left(\overline{\delta}_{max} - \overline{\delta}_0\right)}{\overline{\delta}_{max} \left(\overline{\delta}_f - \overline{\delta}_0\right)} \tag{5}$$

Here, $\overline{\delta}_{max}$ denotes the maximum value of the effective displacement attained during the loading history, while $\overline{\delta}_0$ is the effective separation ($\overline{\delta}$) at the onset of damage and $\overline{\delta}_f$ is that at complete failure. According to [23], an effective displacement is the one which combines normal and shear deformation across the interface defined by

$$\overline{\delta} = \sqrt{\langle \delta_n \rangle^2 + \delta_s^2 + \delta_t^2} \tag{6}$$

The damage evolution law associated with the steelâmortar interfaces was defined in a tabular form by specifying the damage variable D and each component of the displacement $\overline{\delta}_p$.

$$\overline{\delta}_p = \overline{\delta} - \overline{\delta}_0 \tag{7}$$

With the aim of quantifying the relative proportions of normal and shear deformation for a coupled behaviour between Mode-I and Mode-II at the substrate–mortar interface, the Benzeggagh and Kenane [24] (B–K) mixed mode fracture criterion was adopted.

$$\begin{aligned} G^C &= G_n^C + \left(G_s^C - G_n^C\right)\left\{\frac{G_{shear}}{G_T}\right\}^\eta \\ G_T &= G_n + G_{shear} \end{aligned} \tag{8}$$

Here, G_n^C and G_s^C are the critical energy release rates for pure Mode-I and Mode-II loading conditions, respectively; G_n, G_s and G_t are the Mode-I, Mode-II and Mode-III energy release rates, respectively; $G_{shear} = G_s + G_t$; η is a material parameter that takes values from 1.45 to 2. For isotropic failure ($G_n^C = G_s^C$), the response is insensitive to the value of η [25]. According to the BK criterion [24], debonding occurs when the total energy release rate G_T is equal to or greater than the critical energy release rate G^C [26, 14]. G^C is also defined by Eq. 9 [23].

$$G^C = \int_0^{\overline{\delta}_f} \overline{T}\, d\overline{\delta} \tag{9}$$

Here, $\overline{T}$ and $\overline{\delta}$ are the effective traction and displacement.
For the steel–mortar interface, Mode-I and Mode-II were assumed to be uncoupled, i.e. mode independent. This assumption is justified by the considerations deriving from the test [15], that indicates there is little influence of Mode-I on the whole responOse.

3.2. The finite element (FE) model

The adopted mesh comprises eight-node continuum elements with reduced integration (labeled C3D8R in ABAQUS) for representing the masonry, mortar, and steel textile, and eight-node cohesive elements (labeled COH3D8 in ABAQUS) at the substrateâmortar and steel–mortar interfaces (Fig. 6).
As [20] mentions, the cohesive interface elements consist of two surfaces (top and bottom) separated by a thickness. The relative motion of the top and bottom parts of the cohesive elements along the direction of the thickness represents the opening or closing of the interface, which leads to normal failure. However, what is important to measure in this study is the in-plane relative motion of these parts, representing the transverse shear behaviour of the cohesive element, which leads to a shear bond failure.
The constraints and loading conditions were applied to the model following the test conditions as shown in Fig. 2(b). An incremental monotonic displacement load was applied to the free end of the steel textile. Finally, the non-linear equations were solved using a modified NewtonâRaphson iterative scheme together with the line search method.

3.3. Constitutive material laws

As mentioned before, isotropic linear elastic material models are used for masonry and steel cords. The mechanical properties selected for these elements are those obtained from the tests, see Table 1. The mortar is modelled as a rigid element in this section in order to capture the displacement that comes only from the steel textile. In this way, the non-linearities observed during the shear bond tests are only due to the blond–slip laws at the interfaces.
In the case of the interfaces, if the failure occurred at the substrate–mortar interface, its bond–slip law (BSL) could be evaluated following theoretical formulations provided for FRP. Much research has been focussed on developing formulas and also comparing their effectiveness. [27] studied many bond–slip laws for FRP [20, 28, 19, 21] and concluded that the [19] bondâslip law provided a good prediction of the structural behaviour of beams externally strengthened with SRG. Hence, the present paper carries out an analysis using the aforementioned formulations for the bond–slip law at the substrate–mortar interface. It is worth mentioning that in no case is a geometrical corrective factor is considered, since the absence of a global width effect is a characteristic of FRCM composites as SRG when

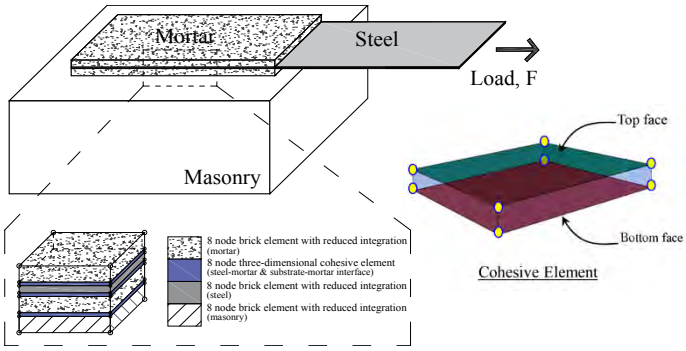

Fig. 6. Finite element model

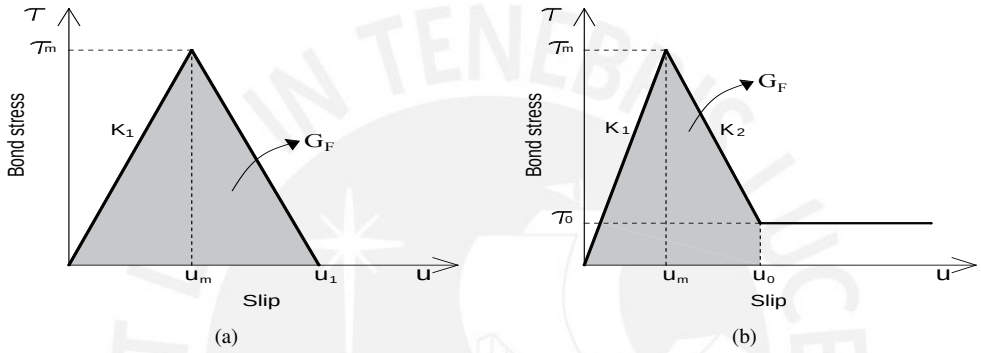

Fig. 7. Adopted bond stressâslip laws: (a) substrate–mortar interface and (b) steel–mortar interface

compared to FRP composites; this was proved by experimental results [29]. The parameters are listed in Table 2 and follow a bilinear BSL, as shown in Fig. 7(a), where τ_m is the bond strength, u_m is the slip corresponding to τ_m, and u_1 is the ultimate slip.

The conveyance of stresses from the steel fibers to the lime-based mortar is one of the mechanisms that governs the overall shear behaviour of the bond. Analytical models have been proposed to evaluate the behaviour at the steel–mortar interface [12, 13]. The analytical solution for the problem was obtained adopting a trilinear BSL at the steel–mortar interface, as shown in Fig. 7(b). Basically, it comprises (i) an elastic phase with a stiffness K_1, (ii) a softening phase with a stiffness K_2 where the interface experiences some micro-damage until the onset of debonding, and (iii) a friction phase where the fibers have debonded, τ_0 is the residual bond stress or friction stress and u_0 is the slip at the end of the softening branch where the cohesion is lost and only friction resists. The parameters for the bond–slip law at this interface were studied [15] under the aforementioned analytical approach and the average results are listed in Table 2. These values were taken as reference during the calibration process.

Table 2. Bond parameters at SM and BM interface.

Interface	K_1 [N/mm^3]	G_F [N/mm]	τ_m [MPa]	τ_0 [MPa]
Substrate–Mortar	76.92	0.356	2.06	-
Steel–Mortar	2.96	0.43	0.935	0.15

3.4. Calibration process

Since the main failure mode was at the steel–mortar interface, in order to gain a comprehensive understanding of its effect on the whole behaviour, the model only considers the steel–mortar interface, assuming a perfectly bonded

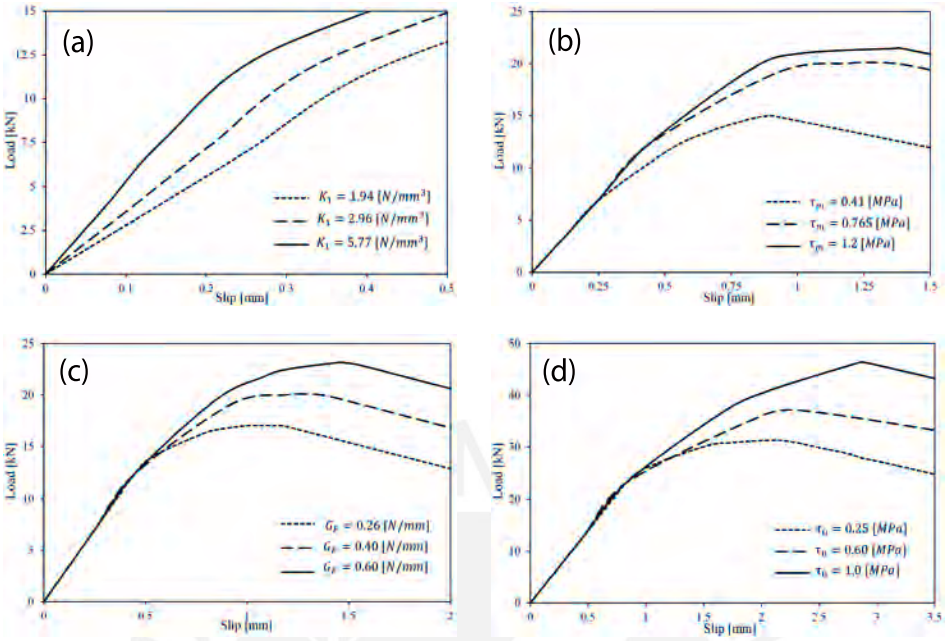

Fig. 8. Results of the sensitivity analysis of the bond parameters at the steel–mortar interface: (a) stiffness; (b) peak bond stress; (c) fracture energy and (d) residual stress.

behaviour at the substrate–mortar interface. Then, to complete the understanding of the interfaces, a bond–slip law at the substrate–mortar interface which complies with the parameters in Table 2 was implemented in the model.

With the aim of deterining the accuracy of the values of the steel–mortar BSL parameters, a sensitivity analysis for each parameter was carried out to determine its influence on the global load response. The ascending branch stiffness K_1 was the first parameter calibrated. Three values were selected (taking as reference values in Table 2) to see its effect on the entire response (Fig. 8(a)). It is evident that the effect of K_1 is directly proportional to the elastic branch of the load response, and thus the behaviour is different from the beginning. The appropriate value of K_1 is around 1.94 N/mm^3 and 2.96 N/mm^3, which results in the same initial stiffness of the whole response average for almost all experimental curves, with the exception of ADH02.

The influence of the peak shear stress steel–mortar interface τ_m is shown in Fig. 8(b). The load response is equal until the onset of micro-cracking at the interface, i.e. when non-linearity starts, and τ_m influences the bond resistance of the overall load response. In addition, the fracture energy G_F directly affects the load response from the hardening branch due to the initiation of micro-cracking at the interface, as shown in Fig. 8(c). Lastly, the effect of the residual bond stress τ_0 (i.e. mechanical interlocking between steel and mortar) on the load response is related to the hardening branch due to the friction phenomena. The greater is the residual stress at the steel–mortar interface, the more difficult will be the debonding and, consequently, a higher resistance in the load response will be attained (Fig. 8(d)).

Then, four substrate–mortar bond–slip laws (Table 2) were taken into account in the numerical model. The results for each case of BSL were exactly the same as when considering a perfect bond behaviour at that interface, which leads to the conclusion that the deformation is concentrated at the steel–mortar interface. While the steel–mortar interface enters a damage evolution process, the substrate–mortar interface remains almost undamaged [4]. Hence, it is concluded that it makes no difference whether one uses a bond stress–slip law at the substrate–mortar interface or assumes it to be perfectly bonded, since what finally governs the whole behaviour is the steel–mortar bond–slip law.

Summarizing all the results obtained through the sensitivity analysis, five bond stress–slip laws for the steel–mortar interface were obtained and are listed in Table 3. These values confront the analytical ones (Table 2) and are very similar, which means the calibration process makes sense. The values in Table 3 provide well fitted load responses within the experimental envelope, as depicted in Fig. 9.

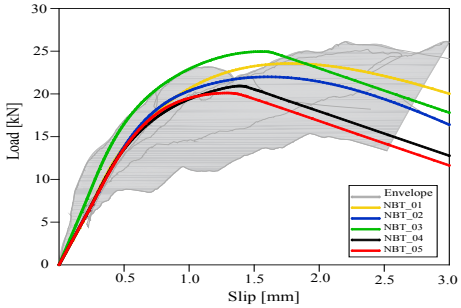

Fig. 9. Comparison of applied force–slip curves of numerical models and experimental curve envelopes of specimens.

Table 3. Calibrated parameters for steel–mortar CML.

Numerical Model	K_1 [N/mm^3]	G_F [N/mm]	τ_m [MPa]	τ_0 [MPa]
NBT_01	1.96	0.42	0.93	0.20
NBT_02	1.96	0.43	0.80	0.20
NBT_03	2.96	0.42	0.94	0.30
NBT_04	1.94	0.30	0.80	0.30
NBT_05	1.94	0.40	0.765	0.10

4. Numerical model of the single-lap shear bond test

The main failure mechanism observed was debonding at the steel–mortar interface with cracking of the outer mortar layer, as was mentioned before. Hence, it can be concluded that the mortar plays an important role in the load response. Although considering the mortar as a rigid material (analytical model approach) leads to good results, a sophisticated analysis for design and strengthening purposes may consider the non-linearity of the mortar. This section presents the numerical model of the shear bond tests considering the real behaviour of the lime-based mortar (i.e. as a non-linear material) and these results are discussed and compared with the assumption of a rigid and a linear elastic mortar.

4.1. Concrete Damage Plasticity model for the lime-based mortar

Concrete Damage Plasticity (CDP) is a constitutive model for modelling failure and fracture with the recognition of crack patterns [30]. A damage plasticity model is displayed in Fig. 10 for uniaxial compression and tension. It is shown that the damage generates a degradation of the stiffness because the slope of the unloading–reloading branch is $(1 - d)E_0$, where d is a damage variable between 0 (no damage) and 1 (destruction).
The plastic damage concrete model in ABAQUS makes use of the yield function proposed by [31] and incorporates the modifications proposed by [32] to account for different evolutions of the strength under tension and compression. The yield function represents a surface in effective stress space which determines the states of failure or damage. The plastic flow in CDP is governed by a flow potential function (Drucker–Praguer hyperbolic function) according to a non-associative flow rule [30]. In the CDP model, four constitutive parameters identify the shape of the flow potential surface and yield surface. The dilatation angle ψ and eccentricity ϵ are responsible for the shape of the flow potential function, while the ratio of the biaxial compressive strength to the uniaxial compressive strength f_{b0}/f_c, and the ratio of the second stress invariants on the tensile and compressive meridians K_c are used to describe the shape of the yield function. Table 4 presents the values used in this study.

A parabolic compression curve has been selected for modelling the lime-based mortar material. It assumes a hardening–softening behaviour in compression, where the fracture energy is represented by G_{fc} (Fig. 10(a)). The model used to characterize the mortar material in traction is based on an exponential softening (Fig. 10(b)). The softening behaviour in a tensile constitutive law is represented by the fracture energy G_{ft}. The values for the

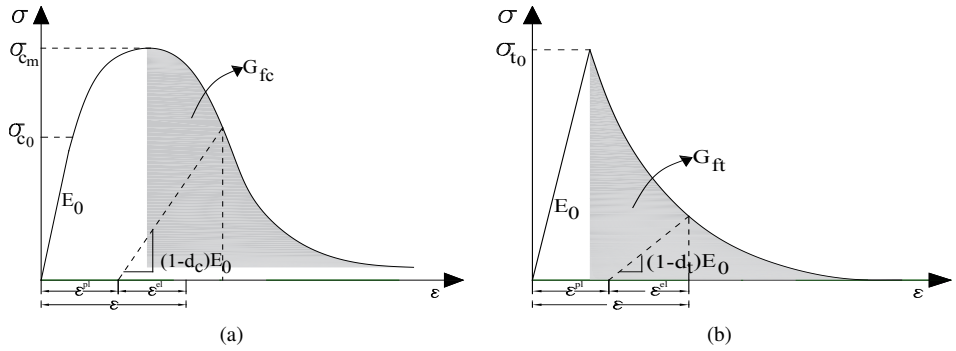

Fig. 10. Constitutive Law for: (a) Compression ; (b) Tension

Table 4. Parameters of CDP model [33].

$\psi(^\circ)$	ϵ	f_{b0}/f_c	K_c
13	0.1	1.16	0.7

parameters that define each law are taken from Table 1, where the elastic modulus, compressive and tensile strength are totally defined experimentally. Although the fracture energy was not measured by testing, G_{fc} was taken to be 11.5 N/mm, and G_{ft} equal to 0.045 N/mm, which are tentative values and are reasonable for this kind of material. This fracture energy is defined as the amount of energy needed to create a unit area of crack in the element.
For a complete definition of the CDP model, ABAQUS requires the uniaxial damage variables in traction and compression (i.e. damage evolution), which are provided by the user and in this study the model proposed by [33] is used. This method for calculating the damage variables starts from the definition of the compressive and tensile variables as the portion of normalized energy dissipated by the damage. The inputs for the damage model are the compressive strength and characteristic length. The latter depends on the mesh size, the type of finite element, and the direction of the crack [33].

4.2. Influence of the mortar on the load response

The effect of considering a linear–elastic and plastic-damaged mortar when compared to a rigid mortar is illustrated in Fig. 11 for each NBT [1]–[5].
In all cases, it is evident that assuming a linear elastic mortar leads to a small decrease of the maximum applied load compared to assuming a rigid element for the mortar. However, when a plastic-damaged model for mortar is adopted, there is a big difference, which is reflected by a greater decrease of the maximum applied load from that of the rigid model. In case of the slip associated to the maximum applied load, there is no difference between the assumptions of a rigid and a deformable mortar. However, the non-linear mortar model results in a greater value of slip corresponding to the maximum applied load.
This decrease of the load and increase of the slip for a response with a non-linear mortar can be explained with Fig. 12, which compares the tensile behaviour of dry textile and the SRG system. In Fig. 12, for a specific stress, the SRG system has a greater value of the slip than does the dry textile, and for a specific slip, the SRG system has a lower value of stress than does the dry textile. The tensile behaviour of the dry textile can be attributed to the load–slip response curve assuming a linear-elastic mortar, while the SRG system can be related to the load–slip response curve when a non-linear mortar is considered.
It is possible to conclude that CML is the one which totally governs the final load response when linear-elastic mortar is adopted, since there is no big difference from the rigid model in most cases (Fig. 11). However, when the non-linearity of the mortar is considered, it takes on importance and causes a decrease of the maximum applied load and an increase of its associated slip, and these curves fit better the experimental ones. For a deep analysis with design and strengthening purposes, it is recommended to model the mortar as a non-linear element, given its great influence on

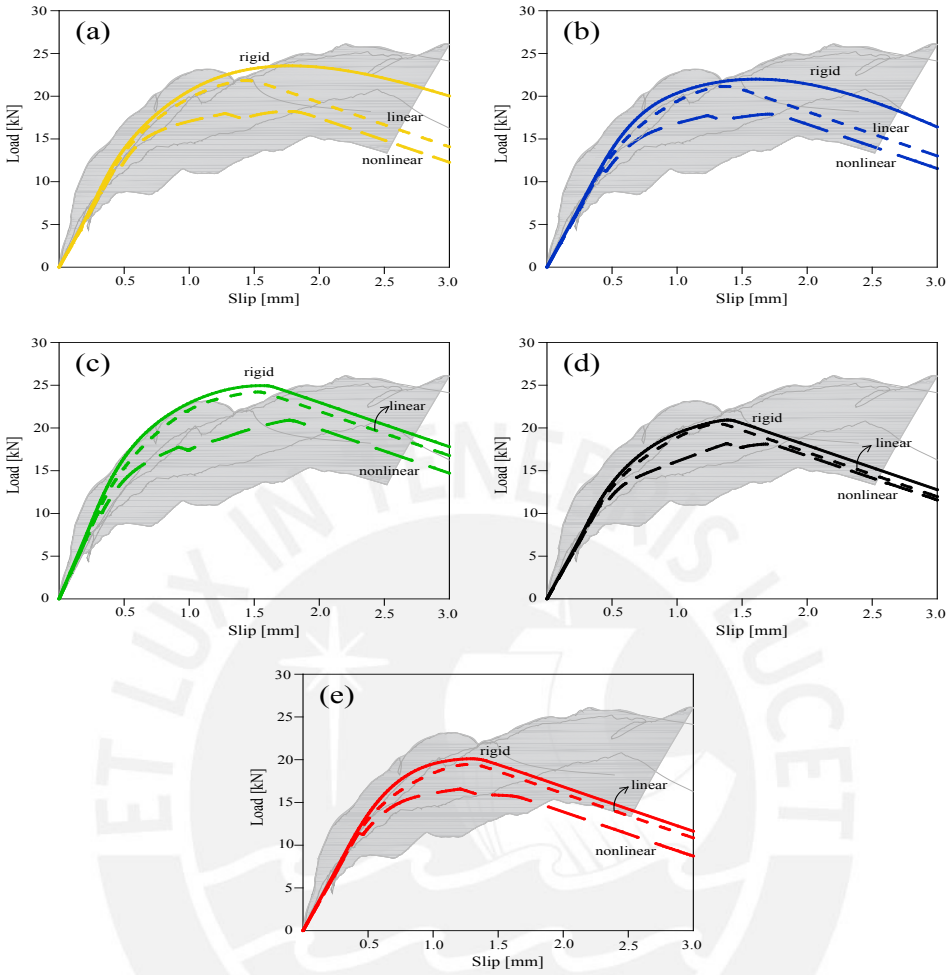

Fig. 11. Influence of the behaviour of the mortar on the load–slip curves for: (a) NBT_01 (b) NBT_02 (c) NBT_03 (d) NBT_04 (e) NBT_05

the final response. Besides, this could yield information about the failure pattern of the mortar which is totally related to the premature cracking of the mortar observed in the experimental results. The latter is addressed in the following.

4.3. Influence of the mortar on the failure pattern

When non-linearity is taken into account in the model, information about the failure pattern can be obtained, as shown in Fig. 13(a) for NBT_04. Fig. 13(a) depicts the progressive damage that the mortar develops during the shear bond test through the red lines, which show the mortar is completely damaged in traction. The failure mechanism of the mortar, the quantity of these totally damaged cracks, and how they take place in the load–slip curve from the shear bond test, is explained below.

As mentioned before, the numerical results have shown that the lime-based mortar experienced damage in traction and not in compression. This means that during the shear bond tests, the fiber leads the mortar to the traction and that is why between compressive and tensile behaviour of the mortar, which controls the entire response along with the BSL at mortar-fiber interface is the tensile behaviour. Hence, the traction parameters, such as the fracture energy, which is not experimentally defined in Table 1, has a dominating effect on the failure pattern and final load–slip response.

The bond–slip law (BSL) of NBT_04 was selected to study the failure mechanism of the mortar during the shear bond test. Three different values of G_{ft} were selected: 0.045, 0.08 and 0.45 N/mm, to achieve a clear understanding of the effect of the properties of the mortar on the behaviour of the bond. A significant change should be noted in the

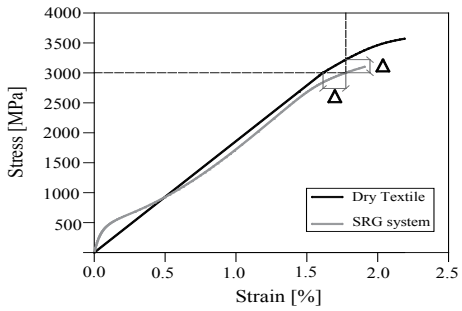

Fig. 12. Stress–Strain curves of dry textile and SRG system under uniaxial tension.

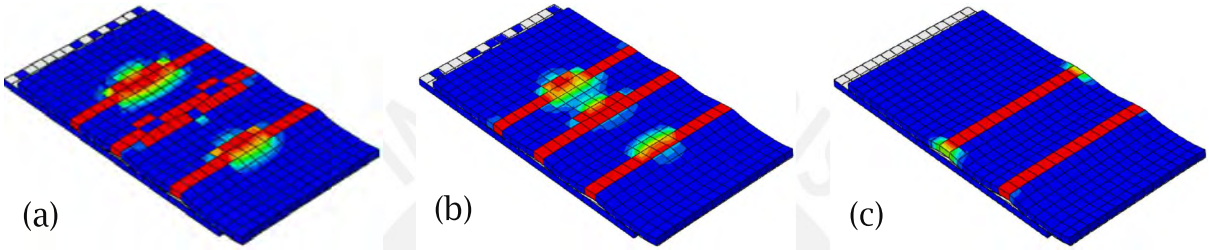

Fig. 13. Failure pattern of the mortar with tensile fracture energies of (a) 0.045 N/mm (b) 0.08 N/mm (c) 0.45 N/mm

overall failure pattern presented along the bonded length, as shown in Fig. 13. While with a G_{ft} equal to 0.045 or 0.08 N/mm the outer mortar layer presents three remarkable totally damaged lines, with G_{ft} equal to 0.45 N/mm the outer mortar layer presents only two totally damaged lines. These totally damaged lines represent the progressive damage of the matrix and their quantity is attributed to the characteristics of the mortar, such as the tensile fracture energy. The cracking spread with a lower value of G_{ft} is more brittle than with a higher value of G_{ft}. The more brittle is the cracking spread, the more damage will be experienced by the mortar (i.e. there will be more totally damaged lines).
On the other hand, changing the tensile fracture energy G_{ft} does not affect the load–slip response, which is evidence that the whole behaviour is mainly governed by the bond–slip law at the steel–mortar interface instead of by the non-linearity of the mortar. Thus, it turns out to be complicated to calibrate a value of the fracture energy just based on numerical results, so the ideal would be to obtain this parameter experimentally. This study recommends G_{ft}=0.045 N/mm for lime-based mortar (the expected value for this type of material), as mentioned in Section 4.1, whose results were optimal.
Regarding how totally damaged cracks in the mortar take place in the F–s curve, in all cases, cracking in the mortar starts in the elastic phase of the load–slip response (black point in Fig. 14), and the first critical mortar line is totally damaged when non-linearities in the load–slip response have already started. The second and third damaged lines are reached just before and after attaining the maximum applied load.

5. Applied load–slip response considering a non-linear mortar

Fig. 15(a) shows an idealized load–slip response put forward by taking into account the presented numerical results. This final response of bond tests has a direct relation with the Bond Slip Law (BSL) at the steel–mortar interface and the mortar constitutive law.
The BSL at the steel–mortar interface is depicted in Fig. 15(b) by a grey line along with the constitutive law for a non-linear mortar (black line). The stresses are plotted versus time in order to compare them consistently. It can be seen that when a linear elasticity is adopted for the matrix, it does not influence the final response since at any point in time the predominant law is that of the steel–mortar interface. However, the non-linearity of the matrix does influence the final response since, at a certain point âIpâ which belongs to the ascending elastic branch of BSL, the black line

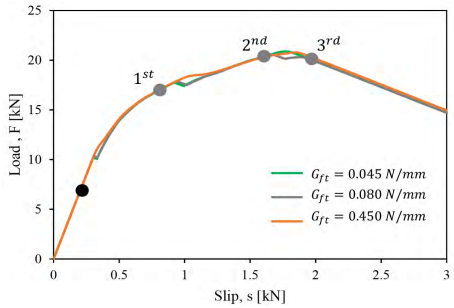

Fig. 14. Load–Slip curve response of NBT_04 for different values of fracture energy of the mortar in traction.

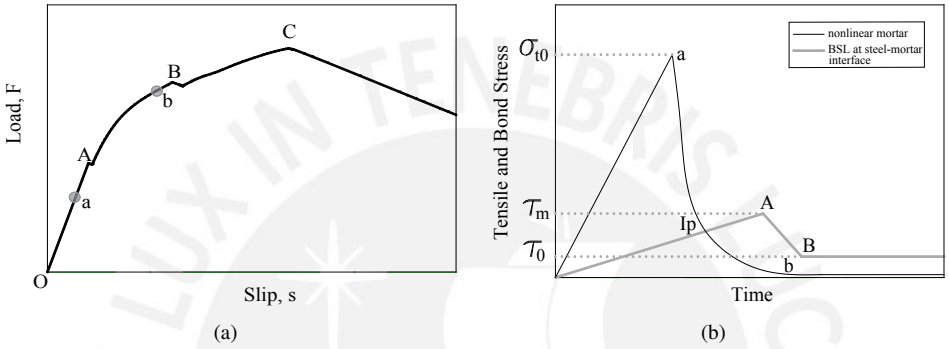

Fig. 15. (a) Idealized load–slip response; (b) Constitutive law for non-linear mortar and BSL at steel–mortar interface

intersects the grey line. Therefore, the final load response is controlled by the BSL alone, until point âIpâ (i.e. at the linear branch of the final response). After point âIpâ, the non-linearity of the mortar begins to strongly influence the load response and the response starts to be controlled by the BSL at the steel–mortar interface and the non-linearity of the matrix.

The first part of the load–slip response is depicted by a linear branch (OA) associated with the elastic behaviour between the steel and the mortar (up to A in Fig. 15(b)) and within the OA portion, the initiation of mortar cracking takes place (a in Fig. 15). After point A, the response starts being non-linear, corresponding to the softening phase of BSL where the applied load increases until the beginning of debonding (point B). The spread of mortar cracks continues during the AB portion and its first failure occurs just before the onset of friction phenomena. After point B, the load continues increasing due to friction phenomena between the steel and the mortar and the remaining unloaded mortar starts to experience damage until it fails, which generally occurs around the maximum applied load. After point C in Fig. 15(a), the load decreases because the bond mechanism is no longer fully established (i.e. the residual bonded length (l_r) is lower than the optimal bonded length (l_{eff}) [29].

For each of the labelled points in Fig. 15(a), the bond mechanism and mortar cracking are summarized in Table 5. At point A, the interface is undamaged (initial bonded length, l_0=270 mm, is equal to the residual bonded length, l_r) and the mortar starts to experience some damage. By point B, the interface has already entered a softening phase (i.e. some micro-damage occurs at the steel–mortar interface) before a first line of mortar totally fails. The residual bonded length l_r continues being 270 mm. During the BC portion, the interface evidences the friction mechanism through a constant colour red near the loaded end section. The fibers have debonded due to the friction mechanism and that is why $l_r < l$. At point C, a greater part of l_0 is loaded and l_r becomes shorter. Additionally, a second line of mortar fails. Just after point C, a third line of mortar is totally damaged and the residual bonded length l_r becomes even shorter until it is equal to zero (l_r =0) and only the friction mechanism is acting (interface totally red).

6. Conclusions

With the aim of a comprehensive understanding of the behaviour of the bond between SRG and Peruvian masonry (substrate), experiments were carried out and a three-dimensional numerical model capable of simulating the bond mechanism and the premature cracking of mortar observed in the experimental results was presented in this paper.
The experiments consisted of single-lap shear bond tests on SRG-strengthened Peruvian masonry. It was found that the main failure mechanism was the slippage of the steel fibers from the lime-based mortar with a premature cracking of the outer mortar layer. Hence, if a sophisticated analysis for design and strengthening purposes is desired, it is usefule to model the non-linearity of the lime-based mortar. This has been addressed in the present paper.
The numerical approach consisted of linear-elastic materials for the masonry and steel cords, but a non-linear behaviour was considered for the mortar. The bond behaviour was modelled using a zero-thickness interface between the masonry and the mortar. Another interface between the substrate and the mortar was taken into account; however, the results showed that the interlock at the substrate–mortar interface is enough to assume a perfect bond behaviour. Therefore, the weaker interface and the one which controls the whole behaviour is that between the steel and the mortar. The numerical results showed a good agreement with the experimental ones.
The results of the bond behaviour considering a non-linear mortar have been discussed in comparison with the assumption, as proposed by previous studies, of a rigid and a linear elastic mortar. The influence of the linearity of the mortar regarding adopting a rigid model is not so evident as when a plastic-damaged model was used. It was shown that assuming a non-linear mortar entails a decrease of the maximum applied load and an increase of its associated slip in the load–slip response. This paper indicates the desirability of modelling the mortar as a non-linear material in order to capture the progressive damage that occurs in the matrix during the experiments and to obtain an accurate final load response. Based on the importance of the non-linearity of the mortar in the model, an applied load–slip response was put forward and described taking into account the cohesive material law at the steel–mortar interface and the mortar constitutive law. The bond mechanism and mortar cracking for the idealized load–slip response was also described.

Acknowledgements

This project was partially funded by CONCYTEC within the framework of the $N°232 - 2015-$FONDECYT Agreement. The authors would like to acknowledge the important collaboration of the industrial company Kerakoll S.p.A., especially Dr Paolo Casadei, for providing the materials for the experimental part of this work.

References

[1] INEI, Una mirada a Lima metropolitana, Instituto nacional de Estadística e Informática, Lima, Perú, 2014.
[2] T. Triantafillou, C. Papanicolaou, Textile reinforced mortars (TRM) versus fiber reinforced polymers (FRP) as strengthening materials of concrete structures, International Concrete Abstracts Portal 230 (2005) 99–118.
[3] C. G. Papanicolaou, T. C. Triantafillou, M. Papathanasiou, K. Karlos, Textile reinforced mortar (TRM) versus FRP as strengthening material of URM walls: Out-of-plane cyclic loading, Materials and Structures 41 (1) (2008) 143–157. doi:10.1617/s11527-007-9226-0.
[4] A. Razavizadeh, B. Ghiassi, D. V. Oliveira, Bond behavior of SRG-strengthened masonry units: Testing and numerical modeling, Construction and Building Materials 64 (2014) 387–397. doi:https://doi.org/10.1016/j.conbuildmat.2014.04.070.
[5] B. Ghiassi, G. Marcari, D. V. Oliveira, P. B. Lourenço, Numerical analysis of bond behavior between masonry bricks and composite materials, Engineering Structures 43 (2012) 210–220. doi:https://doi.org/10.1016/j.engstruct.2012.05.022.
[6] S. De Santis, F. Ceroni, G. De Felice, M. Fagone, B. Ghiassi, A. Kwiecie, G. Lignola, M. Morganti, M. Santandrea, M. Valluzzi, A. Viskovic, Round robin test on tensile and bond behaviour of steel reinforced grout systems, Composites Part B: Engineering 127 (2017a) 100–120. doi:https://doi.org/10.1016/j.compositesb.2017.03.052.
[7] S. De Santis, F. Carozzi, G. De Felice, C. Poggi, Test methods for textile reinforced mortar systems, Composites Part B: Engineering 127 (2017b) 121–132. doi:https://doi.org/10.1016/j.compositesb.2017.03.016.
[8] B. Ghiassi, D. V. Oliveira, V. Marques, E. Soares, H. Maljaee, Multi-level characterization of steel reinforced mortars for strengthening of masonry structures, Materials & Design 110 (2016) 903–913. doi:https://doi.org/10.1016/j.matdes.2016.08.034.
[9] G. de Felice, M. A. Aiello, C. Caggegi, F. Ceroni, S. De Santis, E. Garbin, N. Gattesco, Ł. Hojdys, P. Krajewski, A. Kwiecień, M. Leone, G. P. Lignola, C. Mazzotti, D. Oliveira, C. Papanicolaou, C. Poggi, T. Triantafillou, M. R. Valluzzi, A. Viskovic, Recommendation of RILEM Technical Committee 250-CSM: Test method for textile reinforced mortar to substrate bond characterization, Materials and Structures 51 (4) (2018) 95. doi:10.1617/s11527-018-1216-x.
[10] E. Grande, M. Imbimbo, E. Sacco, Modeling and numerical analysis of the bond behavior of masonry elements strengthened with SRP/SRG, Composites Part B: Engineering 55 (2013) 128–138. doi:https://doi.org/10.1016/j.compositesb.2013.06.003.

[11] A. Razavizadeh, Numerical modeling of bond in SRG-strengthened masonry, M.S. thesis, University of Minho (2013).
[12] F. G. Carozzi, P. Colombi, G. Fava, C. Poggi, A cohesive interface crack model for the matrix–textile debonding in FRCM composites, Composite Structures 143 (2016) 230–241. doi:https://doi.org/10.1016/j.compstruct.2016.02.019.
[13] T. D'Antino, P. Colombi, C. Carloni, L. H. Sneed, Estimation of a matrix–fiber interface cohesive material law in FRCM–concrete joints, Composite Structures 193 (2018) 103–112. doi:https://doi.org/10.1016/j.compstruct.2018.03.005.
[14] C. Carloni, T. D?Antino, L. H. Sneed, C. Pellegrino, Three-dimensional numerical modeling of single-lap direct shear tests of FRCM–concrete joints using a cohesive damaged contact approach, Journal of Composites for Construction 22 (1) (2018) 04017048. doi:10.1061/(ASCE)CC.1943-5614.0000827.
[15] J. Salsavilca, J. Yacila, N. Tarque, G. Camata, Experimental and analytical bond behavior of masonry strengthened with steel reinforced grout (SRG), submitted manuscript.
[16] E.070, Reglamento nacional de edificaciones: Albañilería, Ministerio de Vivienda, Construcción y Saneamiento-SENCICO, Lima, Perú, 2006.
[17] ASTM, Standard specification for hydrated hydraulic lime for structural purposes, in: ASTM C141/C14M, ASTM International, 2017, p. 4.
[18] C. Carloni, Prove di compressione diagonale per la valutazione dell'efficacia di rinforzi strutturali applicati su pannelli murari di laterizio e malta di calce. convenzione di ricerca con kerakoll spa rapporto di prova, Tech. rep., Universita di Bologna (2017).
[19] X. Lu, J. Teng, L. Ye, J. Jiang, Bond–slip models for FRP sheets/plates bonded to concrete, Engineering Structures 27 (6) (2005) 920–937. doi:https://doi.org/10.1016/j.engstruct.2005.01.014.
[20] Y. T. Obaidat, S. Heyden, O. Dahlblom, Evaluation of parameters of bond action between FRP and concrete, Journal of Composites for Construction 17 (5) (2013) 626–635. doi:10.1061/(ASCE)CC.1943-5614.0000378.
[21] CNR-DT200, Guide for the design and construction of externally bonded FRP systems for strengthening existing structures-materials, RC and PC structures, masonry structures, Italian National Research Council, Rome, Italy, 2013.
[22] A. Salve, S. Narayan, Implementation of cohesive zone in ABAQUS to investigate fracture problems, in: National Conference for Engineering Post Graduates RIT NConP-15.
[23] P. P. Camanho, C. G. Davila, Mixed-mode decohesion finite elements for the simulation of delamination in composite materials, NASA/TM-2002-211737, National Aeronautics and Space Administration, Langley Research Center, Hampton, VA, USA (2002) 1–37doi:https://doi.org/10.1016/0266-3538(96)00005-X.
[24] M. Benzeggagh, M. Kenane, Measurement of mixed-mode delamination fracture toughness of unidirectional glass/epoxy composites with mixed-mode bending apparatus, Composites Science and Technology 56 (4) (1996) 439–449. doi:https://doi.org/10.1016/0266-3538(96)00005-X.
[25] ABAQUS theory manual, user manual, example manual, version 6.14, Providence, RI, USA, 2008.
[26] R. Krueger, An approach to assess delamination propagation simulation capabilities in commercial finite element codes, NASA TM/2008-215123, National Aeronautics and Space Administration, Langley Research Center, Hampton, VA, USA.
[27] F. Bencardino, A. Condello, SRG/SRP–concrete bond–slip laws for externally strengthened RC beams, Composite Structures 132 (2015) 804–815. doi:https://doi.org/10.1016/j.compstruct.2015.06.068.
[28] M. Monti, M. Renzelli, P. Luciani, FRP adhesion in uncracked and cracked concrete zones, in: Proceedings of the 6th international Symposium on Fiber Reinforced Polymer Reinforcement for Concrete Structures.
[29] T. D'Antino, C. Carloni, L. Sneed, C. Pellegrino, Matrix–fiber bond behavior in PBO FRCM composites: A fracture mechanics approach, Engineering Fracture Mechanics 117 (2014) 94–111. doi:https://doi.org/10.1016/j.engfracmech.2014.01.011.
[30] T. Jankowiak, T. Lodygowski, Identification of parameters of concrete damage plasticity constitutive model, Foundations of Civil and Environmental Engineering 6 (2012) 53–69.
[31] A plastic-damage model for concrete, International Journal of Solids and Structures 25 (3) (1989) 299–326. doi:https://doi.org/10.1016/0020-7683(89)90050-4.
[32] J. Lee, G. L. Fenves, Plastic-damage model for cyclic loading of concrete structures, Journal of Engineering Mechanics 124 (8) (1998) 892–900. doi:10.1061/(ASCE)0733-9399(1998)124:8(892).
[33] B. Alfarah, F. López-Almansa, S. Oller, New methodology for calculating damage variables evolution in plastic damage model for RC structures, Engineering Structures 132 (2017) 70–86. doi:https://doi.org/10.1016/j.engstruct.2016.11.022.

Table 5. Bond mechanism (interface) and mortar cracking.

Stage	Interface	Mortar
A	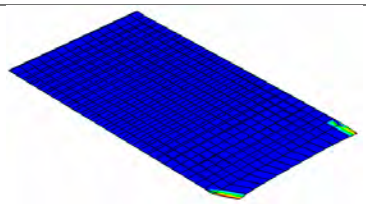	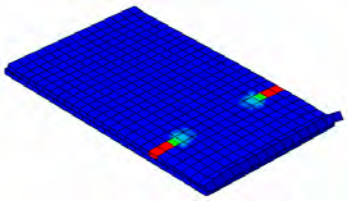
B	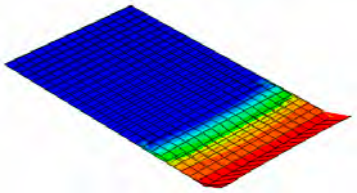	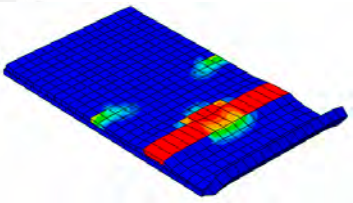
B-C	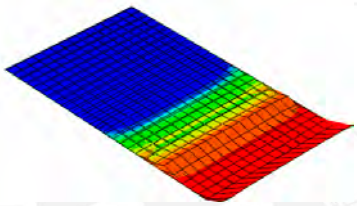	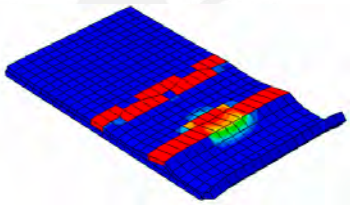
C	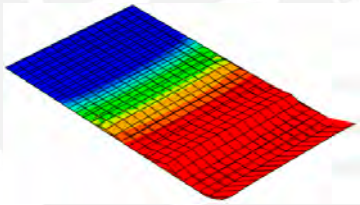	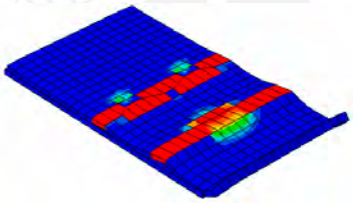
After C	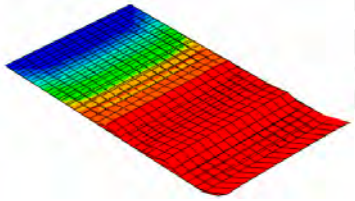	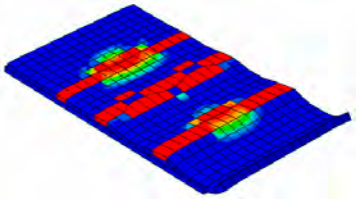
Fail	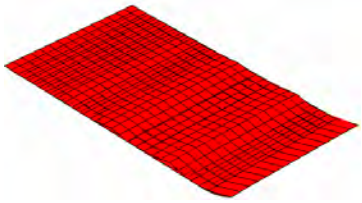	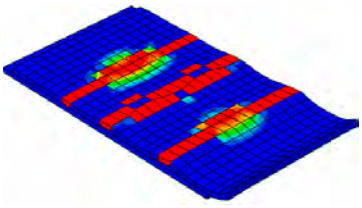

4.2. Pushover analysis of confined masonry walls throughout 3D macro-modeling approach

Pushover analysis of confined masonry walls using a 3D macro-modelling approach

Jhair Yacila, Guido Camata, Jhoselyn Salsavilca, and Nicola Tarque

***Abstract*—This paper shows the suitability of a 3D macro-modelling technique to simulate the nonlinear behaviour of confined masonry walls subjected to in-plane lateral loading. For this purpose, the finite elements method implemented in ABAQUS software was used. All the 3D solid finite elements have been modelled as a single part, which allows avoiding modelling the contact interfaces between concrete and masonry elements. The nonlinear behaviour of the concrete and masonry is governed by two main types of failures: crushing and cracking, which were properly captured by the Concrete Damage Plasticity (CDP) model. Steel rebars were modelled as elastic-plastic with hardening and were assumed to have a perfect adhesion with the surrounding concrete by means of the embedded constraint. Prior to the modelling process, experiments were carried out whose results were used to validate the proposed model. Subsequently, a parametric study was conducted by varying the elastic modulus, tensile strength and fracture energy of the masonry to fit the experimental results. There is good agreement between the numerical and experimental outcomes in terms of capacity curves and cracking patterns.**

***Index Terms*—Macro-modelling, confined masonry, pushover, dynamic explicit analysis**

I. Introduction

Confined masonry buildings are the most common type of construction for dwellings in Peru and other South American countries. The major issue with many of these constructions is their informality: According to [1], masonry dwellings constitute 84% of the total buildings in Peru and 60% of them did not have any engineering participation. Additionally, just in Lima, 9 out of 10 masonry dwellings were built by using bricks with a percentage of voids between 40% and 50%, which mean bricks with a density lower than that required by the Peruvian seismic code [2]. Fig. 1 shows a common case of masonry dwellings in Lima of up to five stories.

Figure 1. Masonry dwellings in Lima [2]

Peruvian seismic events have revealed the poor quality of these informal masonry dwellings, which has been responsible for human and material losses. However, this is not only related to the informality of the masonry constructions, but also to the lack of knowledge of the nonlinear behaviour of the masonry. For this reason, much research around the world has been devoted to experimental studies of the nonlinear behaviour of masonry walls, either for in-plane or out-plane loads [3]–[6]. However, such studies need economic resources, which are often scarce. To overcome this issue, numerical modelling is an alternative way to study this topic, since it allows replacing economic resources by computational resources.

Regarding modelling techniques, there are three main modelling approaches. The first one is known as macro-modelling, which means assuming all the materials are homogeneous and not distinguishing between the bricks, the mortar, and the interfaces, as shown in Fig. 2(a). The second one is known as micro-modelling, which means that all the components are modelled separately, as shown in Figure 2(b). The last one is a combination of the previous two, and is known as simplified micro-modelling. It consists of increasing the size of the bricks to absorb the mortar, but maintaining the modelling of the interfaces, as shown in Figure 2(c). The main differences between these approaches are the computational cost and the accuracy of the results that can be obtained [7].

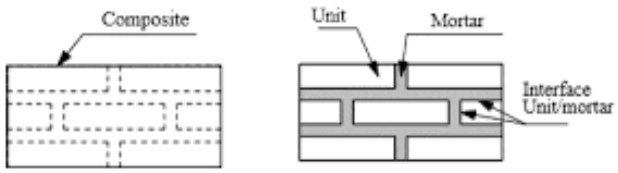

(a) Macro-modelling (b) Micro-modelling

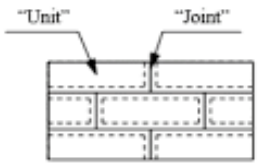

(c) Simplified micro-modelling

Figure 2. Modelling approaches for masonry [7]

Different numerical studies have been conducted to assess the behaviour of masonry walls subjected to in-plane lateral loads. For instance, [8]–[10] used the macro-modelling

technique to perform pushover analyses of confined masonry walls with different arrangements. In this case, the contact surface between the masonry and the concrete was considered as *Hard-Contact* for the normal direction and *frictional* for the shear direction. On the other hand, [9], [11] used the micro-modelling approach for masonry walls without confinement, for which the bricks, mortar and contact surfaces were modelled separately by taking into account their nonlinear behaviour. The nonlinear behaviour of the bricks and mortar were modelled by the well-known Concrete Damage Plasticity (CDP), whereas the contact between the blocks was modelled by cohesive elements with a thickness of 0 mm. Basically, the behaviour of the cohesive elements is governed by a linear-elastic behaviour until its maximum tensile or shear strength is reached. Subsequently, its nonlinear behaviour is governed by a softening part characterized by progressive damage. Once the maximum damage is reached, the cohesive elements are deleted and contact properties begin to be dominant. For this purpose, *hard-contact* and *frictional* properties were defined to be the normal and shear contact properties, respectively. Finally, [12]–[14] used the simplified micro-modelling approach for modelling the in-plane behaviour of in-fill masonry walls, and diagonal compression tests, respectively. Like micro-modelling, cohesive elements were used for contact between blocks, and a frictional behaviour was defined to be activated once cohesive elements exhausted their strength.

Regardless of the modelling approach adopted, these papers have evaluated these aproaches in terms of their accuracy, computational cost, and complexity. In the present paper, the macro-modelling technique was selected, with the aim of reproducing the experimental results obtained in previous work [15].

II. Previous Work

The previous work was carried out by Manchego and Pari [15], with colaboration of the current research group, and consisted in testing 6 full-scale confined masonry walls subjected to in-plane lateral cyclic loading at the Pontifical Catholic University of Peru. Three of these walls had were subjected to a vertical load of 170 kN, which was intended to represent the weight of a three-floor building over a wall located on the first floor. This vertical load was applied prior to the application of lateral loads. The other three walls were only subjected to lateral cyclic loads. In addition, all of these walls were built by common workmanship in order to get the usual features of confined masonry walls in Peruvian dwellings.

A. Geometry and steel reinforcement of the tested walls

Fig. 3 shows the typical assemblage of the tested walls. Note the toothed connection between the confining columns and the masonry panel. This mechanical connection is intended to guarantee a monolithic join, as much as possible. Since the main aim of the confining elements is to avoid the quick disintegration of the masonry panel, as well as providing more ductility, typical practice is to provide corrugated steel reinforcement with a diameter of $\phi 1/2$” as longitudinal reinforcement and with a diameter of $\phi 1/4$” as transverse stirrups. It should be mentioned that in a real confined masonry dwelling, beam foundations are not built. In this case, they were built only for hoisting the walls and to fix them to a reaction slab prior to testing.

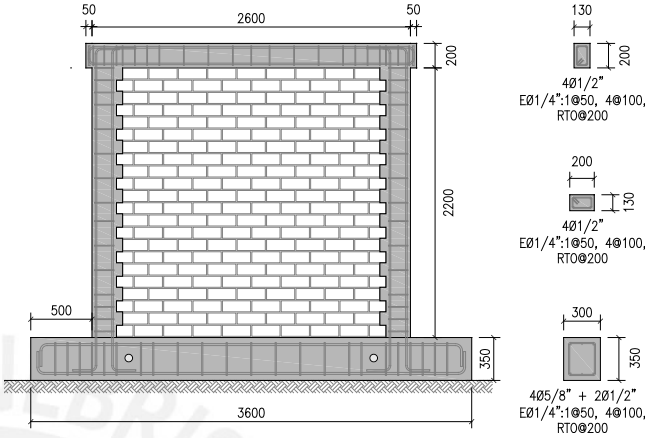

Figure 3. Geometry and details of reinforcement of the walls

B. Testing setup

Fig. 4 shows the typical assemblage that was used to carry out the cyclic tests. The lateral displacements were imposed by means of a dynamic actuator, which was controlled by displacements on a computer. This actuator was intended to be fixed to a reaction frame rigid enough to avoid distorted lateral displacements. On the other hand, one hydraulic jack was located at each end of the foundation to prevent its being overturned. In addition, one hydraulic jack was located at one of the ends of the foundation to prevent its sliding horizontally in one direction. In the other direction, the foundation was intended to react against the rigid reaction frame. The vertical load, where it was applied, was imposed by an additional hydraulic jack, which in turn was connected to two rigid steel beams, in order to distribute as much as possible the vertical load over the wall's confinement beam.

C. Experimental results

In order to compare the pushover analysis conducted in this paper with the cyclic experimental test conducted by [15], only the envelope curve in the pushing direction was taken into account. Fig. 5 shows these envelope curves for both walls with and without vertical load. Note that the shear stresses shown on the secondary vertical axis do not correspond to the real stresses, but to normalized stresses computed as the ratio between the lateral forces and the cross-sectional area of the walls.

Experimental tests on small samples were also carried out in order to characterize the material properties involved in the confined masonry walls with and without vertical load. For instance, uniaxial compressive tests of piles of 5 bricks were conducted to get the compressive strength and Young's modulus of the masonry. In addition, uniaxial diagonal compressive tests were conducted over small square masonry walls

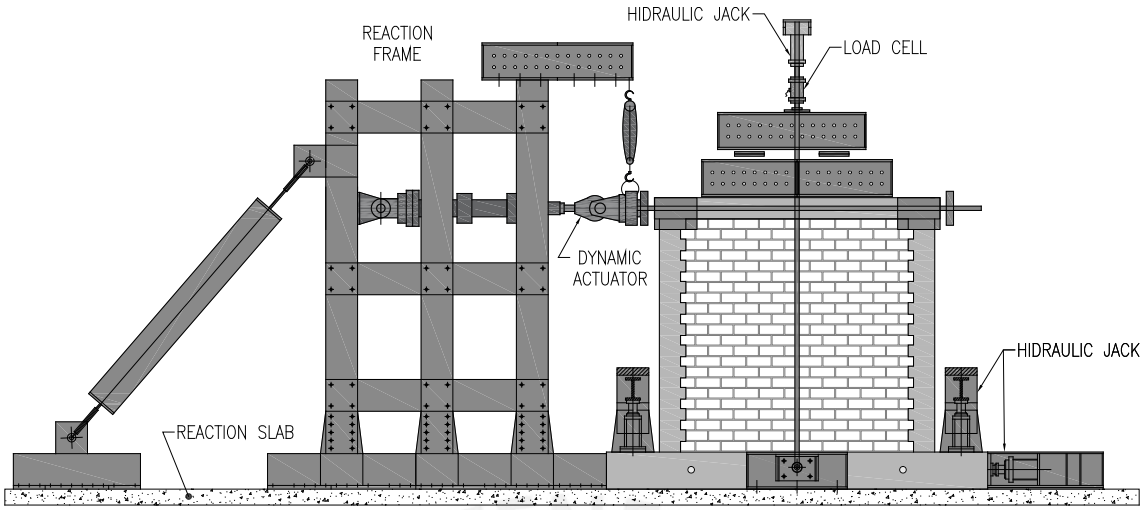

Figure 4. Testing setup

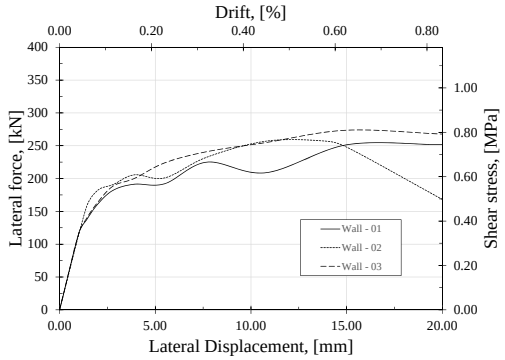

(a) without vertical load

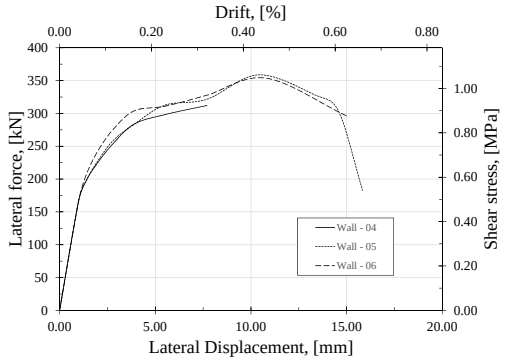

(b) with vertical load

Figure 5. Experimental envelope curves of the walls

in order to get their tensile strength. Typical compressive tests of cylindrical specimens were carried out for each concrete element (foundation, column and beam), in order to get their compressive strength. It should be noted that every small sample was taken from each kind of tested wall (with and without vertical load) by considering they were built on different dates. The experimental results of these tests are shown in Table I.

III. Finite Element Model

In this research, the macro-modelling approach has been adopted. In this way, the bricks, mortar, concrete, and their contact interfaces were not modelled separately. Rather, all components were treated as homogeneous and isotropic materials. The modelling process was carried out in the commercial software package ABAQUS. The foundation and wall were intended to be a single part, which meant that each contact between different materials was assumed to be monolithic. This assumption was made because no relative slip was observed in either the concrete-to-concrete interface or the concrete-to-masonry interface during the tests.

Except for the steel reinforcement, all the components were modelled as continuum three-dimensional elements with 8 nodes with reduced integration (C3D8R). The steel rebars were modelled as truss three-dimensional elements with two nodes (T3D2). The interaction between the steel rebars and the surrounding concrete was considered to be one of perfect adhesion, implemented by means of an embedded constraint. This means that no slip was taken into account between these two materials.

As boundary conditions, each wall was assumed to be over an analytical rigid surface which represents the reaction slab shown in Fig. 4. The hydraulic jack and reaction frame intended to prevent the horizontal sliding of the foundation, as well as the dynamic actuator, were also modelled as analytical rigid surfaces. The hydraulic jacks which were intended to prevent the foundation from overturning were modelled as pin supports where only the vertical component was restricted. However, these hydraulic jacks had an unknown initial pressure prior to the cyclic testing, which in turn was increasing while the lateral displacements were increasing. This fact was intended to be modelled by assuming that a certain area below the foundation did not suffer vertical displacements like its corresponding restricted top area. For this purpose, it was assumed that the transmission of pressure between these

hydraulic jacks and the reaction slab had a slope of 1:2, as shown in Fig. 6.

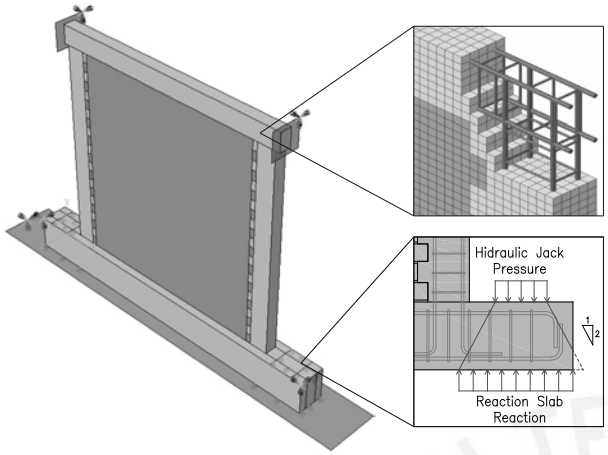

Figure 6. Typical numerical scheme

A variant of classical plasticity theory with the introduction of damage concepts is commonly used with *Concrete Damage Plasticity* to simulate the nonlinear behaviour of quasi-brittle materials. However, its accuracy is questionable, due to its tensile behaviour formulation [16]. Even when the tensile stiffness degradation is properly simulated, as is shown by some experimental tensile cyclic tests [17], this may fail when strong incursions between the tensile and compressive strains take place. Since the main objective of the present work is to get the capacity curve of the walls, pushover analyses were carried out. In this way, severe changes between the tensile and compressive strains were intended to be avoided.

A. Concrete Damage Plasticity

Concrete Damage Plasticity (CDP) is a continuum plasticity-based damage model for concrete and other quasi-brittle materials in any type of structure. It is assumed that the failure of a material is governed by two main mechanisms: tensile cracking and compressive crushing. The evolution of its yield surface, which is defined by Equation 1, is controlled by two hardening variables, $\tilde{\varepsilon}_t^{pl}$ and $\tilde{\varepsilon}_c^{pl}$, which are the tensile and compressive equivalent plastic strain, respectively.

$$F = \frac{1}{1-\alpha}\left(\bar{q} - 3\alpha\bar{p} + \beta(\tilde{\varepsilon}^{pl})\langle\hat{\bar{\sigma}}_{max}\rangle - \gamma\langle-\hat{\bar{\sigma}}_{max}\rangle\right) - \bar{\sigma}_c(\tilde{\varepsilon}_c^{pl}) \leq 0 \tag{1}$$

where $\bar{p}$ is the effective hydrostatic pressure, $\bar{q}$ is the von Mises equivalent effective stress, $\hat{\bar{\sigma}}_{max}$ is the maximum eigenvalue of $\bar{\sigma}$, and $\beta(\tilde{\varepsilon}^{pl})$ is the function defined by

$$\beta(\tilde{\varepsilon}^{pl}) = \frac{\bar{\sigma}_c(\tilde{\varepsilon}_c^{pl})}{\bar{\sigma}_t(\tilde{\varepsilon}_t^{pl})}(1-\alpha) - (1+\alpha) \tag{2}$$

where $\bar{\sigma}_t$ and $\bar{\sigma}_c$ are the tensile and compression effective stress, respectively. The parameter α can be obtained experimentally with the following expression:

$$\alpha = \frac{\sigma_{b0} - \sigma_{c0}}{2\sigma_{b0} - \sigma_{c0}} \tag{3}$$

where σ_{b0} and σ_{c0} are the failure stress for biaxial and uniaxial conditions, respectively. The parameter γ is defined as

$$\gamma = \frac{3(1-K_c)}{2K_c - 1} \tag{4}$$

where K_c is a constant that can be obtained experimentally through triaxial tests [18]. Finally, CDP uses a potential flow, G, which is governed by the Drucker–Prager hyperbolic function

$$G = \sqrt{(e\sigma_{t0}\tan\psi)^2 + \bar{q}^2} - \bar{p}\tan\psi \tag{5}$$

where ψ is the dilation angle measured in the $p-q$ plane with a high level of confinement pressure, σ_{t0} is the uniaxial tensile strength, and e is an eccentricity that defines the rate at which the function reaches the asymptote. A typical yield surface for plane stress conditions is shown in Fig. 6. The intersection between the yield boundary and principal axes represents both the compressive and tensile uniaxial strength of the material. As is characteristic of quasi-brittle materials, a reduced biaxial tension and increased biaxial compression are also illustrated in Fig. 7 [12].

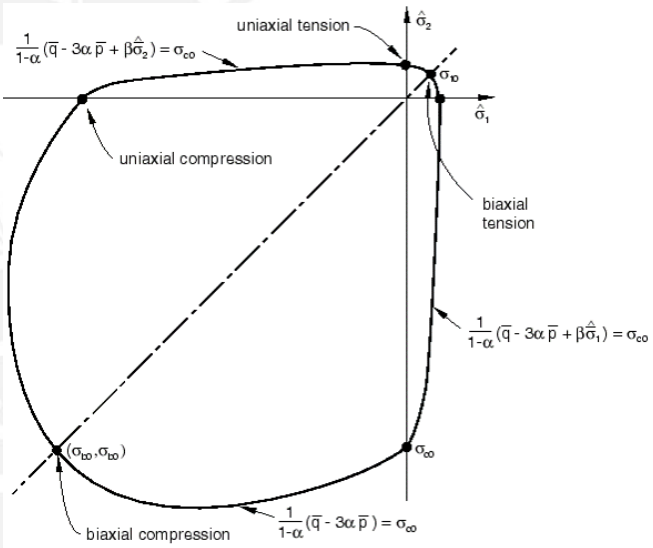

Figure 7. Yield surface of CDP for plane stress conditions [19]

All the parameters involved in CDP can be obtained from uniaxial, biaxial and triaxial tests, as described by Jankowiak and Lodygowski [18]. Regarding the dilation angle, values of 30° and 35° were used for concrete and masonry, respectively, as were correctly used by [6]. Regarding the other parameters, in the absence of experimental results, the eccentricity, σ_{b0}/σ_{c0} and K_c were taken with their default values from ABAQUS to be 0.1, 1.16 and 0.667, respectively [19]. Regarding the parameter of viscosity, it was taken to be 0.0001, following the recommendations of [20].

B. Material models

According to the configuration of the tested walls [15], 5 different materials were considered for modelling: (1) the foundation's concrete, (2) the column's concrete, (3) the

beam's concrete, (4) the masonry, and (5) the rebar's steel. Table I shows their mechanical properties, which were used for modelling purposes, where E is Young's modulus, ν is Poisson's ratio, f_c' is the compressive strength, f_t is the tensile strength, f_y is the yield strength, G_{ch} is the crushing energy, and G_f is the fracture energy of the materials.

Regarding the constitutive laws of concrete and masonry, it is known that their behaviour lies between ideal brittle and ductile. In fact, they are closer to a brittle behaviour than ductile, therefore, both are considered as quasi-brittle materials [21]. In the following subsections, the constitutive models adopted for the concrete, masonry and steel reinforcement will be discussed.

1) Concrete: The compressive behaviour of concrete was represented by three main parts: (1) lineal, (2) hardening and (3) softening. The linear part was taken to last up to a compressive stress equivalent of $0.4f'_{cm}$. The second part was characterized by a parabolic hardening, in compliance with CEB-FIP [22], up to the peak strength f'_{cm} and its associated strain ε_{cm}. The last part was taken as a hyperbolic softening, according to the recommendations of Krätzig and Pölling [23]. Eq. 6 represents this formulation.

$$\sigma_{c(1)} = E_0\varepsilon_c \tag{6a}$$

$$\sigma_{c(2)} = \frac{E_{ci}\dfrac{\varepsilon_c}{f_{cm}} - \left(\dfrac{\varepsilon_c}{\varepsilon_{cm}}\right)^2}{1+\left(E_{ci}\dfrac{\varepsilon_{cm}}{f_{cm}}-2\right)\dfrac{\varepsilon_c}{\varepsilon_{cm}}} f_{cm} \tag{6b}$$

$$\sigma_{c(3)} = \left(\frac{2+\gamma_c f_{cm}\varepsilon_{cm}}{2f_{cm}} - \gamma_c\varepsilon_c + \frac{\varepsilon_c^2\gamma_c}{2\varepsilon_{cm}}\right)^{-1} \tag{6c}$$

where

$$\gamma_c = \frac{\pi^2 f_{cm}\varepsilon_{cm}}{2\left[\dfrac{G_{ch}}{l_{eq}} - 0.5f_{cm}\left(\varepsilon_{cm}(1-b)+b\dfrac{f_{cm}}{E_0}\right)\right]^2}$$

According to CEB-FIP [22], these parameters can be expressed as $\varepsilon_{cm} = 0.0022$, $f_{cm} = f_{ck}+8$, where f_{ck} is the characteristic compression strength. $E_{ci} = 10000 f_{cm}^{1/3}$ and $E_0 = (0.8+0.2f_{cm}/88)E_{ci}$, where E_0 is the modulus of the secant corresponding to a stress of $0.4f_{cm}$. The moduli of the stresses and elasticity are expressed in [MPa]. G_{ch} is the crushing energy per unit area [Nmm/mm^2]. l_{eq} is the characteristic length, which depends on the mesh size, type of element, and cracking direction [24]. In this paper, l_{eq} is taken equal to the chosen mesh size. This is so as to take into account the direction of the expected cracks on the concrete. Finally, b results from averaging the ratio $\varepsilon_c^{pl}/\varepsilon_c^{ch}$ over the relevant strain range. In this work, $b = 0.70$ was initially assumed, however, this value was later iterated until convergence was reached. Fig. 8 shows the stress–strain curves considered for concrete in compression.

Regarding the tensile behaviour, it was assumed to be governed by a first linear elastic part up to its tensile strength,

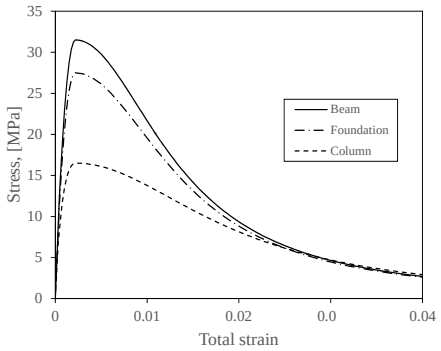

(a) without vertical load

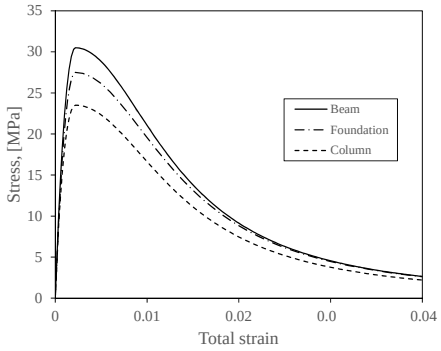

(b) with vertical load

Figure 8. Stress–strain relations for concrete in compression

at which point tensile failure begins. Thereafter, a post-failure behaviour of cracked concrete was intended to be defined in strain-softening terms. For this purpose, the formulation given by Hordijk [26] was selected. It is given by

$$\sigma_{t(1)} = E_0\varepsilon_t \tag{7a}$$

$$\frac{\sigma_{t(2)}}{f_{tm}} = \left[1+\left(c_1\frac{w}{w_c}\right)^3\right]e^{-c_2\frac{w}{w_c}} - \frac{w}{w_c}(1+c_1^3)e^{-c_2} \tag{7b}$$

where $c_1 = 3$, $c_2 = 6.93$ [26], w_c is a critical crack opening, for which $\sigma_{t(2)}$ becomes zero, which can be calculated as $w_c = 5.14G_f/f_{tm}$. In addition, in the absence of experimental data, G_f may be estimated as $G_f = 0.073f_{cm}^{0.18}$ [22]. Likewise, G_{ch} may be estimated as $G_{ch} = (f_{cm}/f_{tm})^2 G_f$ [27]. It should be noted that Eq. (7b) defines the post-failure tensile behaviour in terms of the crack opening w [mm]. However, in the case of reinforced concrete, the post-failure relation is usually expressed in terms of strains. In this way, it is intended to avoid any dependence of the results on the mesh size. For this purpose, the cracking strain was expressed as $\varepsilon_{ck} = w/l_{eq}$. Fig. 9 shows the adopted post-failure stress–strain curves for the tensile behaviour of the concrete. It should be noted that a residual stress $\sigma_r = f_{tm}/50$ was used to avoid kinetic instabilities.

2) Masonry: The compressive behaviour of the masonry was represented by three main parts: (1) parabolic hardening,

Table I
MECHANICAL PROPERTIES OF MATERIALS

Material	E_0 [MPa]	ν [-]	f'_{cm} [MPa]	$f_{tm}(f_y)$ [MPa]	G_{ch} [N/mm]	G_f [N/mm]
Wall without vertical load						
Foundation's concrete	25900	0.15	27.50	2.75	13.70	0.137
Column's concrete	21300	0.15	16.50	1.95	8.60	0.120
Beam's concrete	27500	0.15	31.50	3.00	14.90	0.136
Masonry	5700	0.15	10.00	1.40	-	0.12
Steel rebars	200000	0.30	-	(420)	-	-
Wall with vertical load						
Foundation's concrete	25900	0.15	27.50	2.75	13.70	0.137
Column's concrete	24400	0.15	23.50	2.47	11.60	0.129
Beam's concrete	27100	0.15	30.50	2.94	14.50	0.135
Masonry	5700	0.15	10.00	1.40	-	0.12
Steel rebars	200000	0.30	-	(420)	-	-

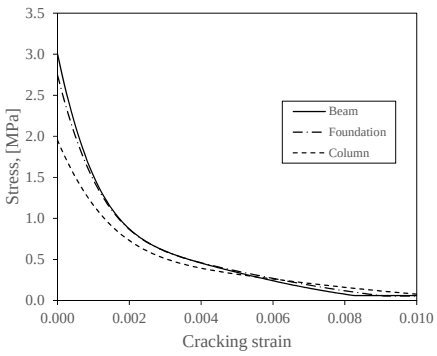

(a) without vertical load

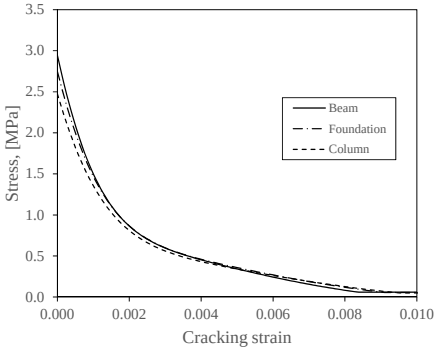

(b) with vertical load

Figure 9. Stress–strain relations for concrete in traction

(2) linear softening and (3) residual, according to the constitutive model proposed by [28], as is shown in Fig. 10. It is worth highlighting that, a residual stress of $0.1 f_{cm}$, unlike Fig. 10, was taken into account to avoid kinetic instabilities [7].

As with the concrete, the tensile behaviour was assumed to be governed at first by a linear-elastic part followed by nonlinear behaviour. In this case, a post-failure exponential softening was assumed [7]. However, it is worth noting that, unlike the reinforced concrete, the masonry panel does not have reinforcement, which would introduce an unreasonable mesh sensitivity into the results when a post-failure stress–strain curve is defined [19]. To address this problem, Hillerborg's fracture energy proposal was employed to define a post-

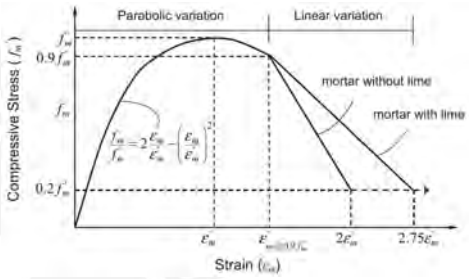

Figure 10. Stress–strain formulation for masonry in compression [25]

failure stress–displacement curve (Eq. 8) [29]. Fig. 11 shows the adopted curves for the masonry.

$$\sigma_{t(1)} = E_0 \varepsilon_t \tag{8a}$$

$$\sigma_{t(2)} = f_{tm} \exp\left(-\frac{f_{tm} w}{G_f}\right) \tag{8b}$$

3) Steel reinforcement: In cases where the behaviour of the reinforced concrete is what dominates (e.g. infill walls and structures with nothing but reinforced concrete), it is important to consider the *bond slip* effect between the steel reinforcement and the concrete. This effect is related to the fact that given a particular deformation of an RC element, the steel reinforcement and the concrete have different strains due to the difference in their material properties (e.g. the Young and Poisson moduli). This effect can be taken into account by modifying the constitutive law of the steel reinforcement [30]. Nevertheless, in the case of confined masonry walls, where the behaviour of the masonry is what dominates, no considerable differences result from considering the *bond slip* effect. For this reason, this paper does not take this effect into consideration.

On the other hand, the steel reinforcement was modelled as elastic-plastic with a hardening of $2\%E$ slope between the strains related to the yield and the ultimate stresses, ε_y and ε_u, respectively. Fig. 12 compares a typical experimental curve for the steel reinforcement and the numerical curve adopted as the constitutive law.

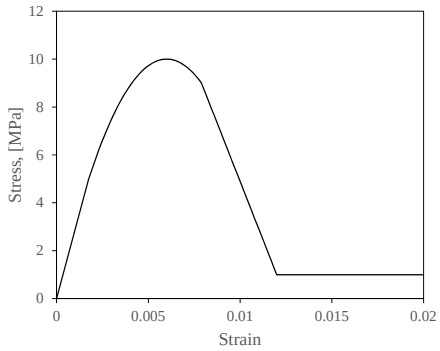

(a) Compression

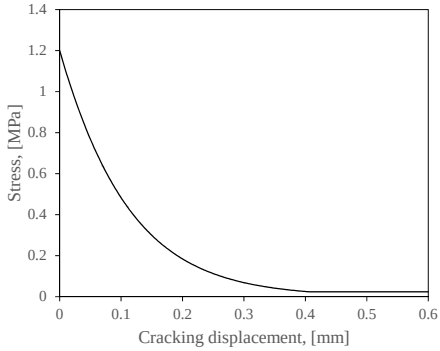

(b) Traction

Figure 11. Constitutive laws for masonry

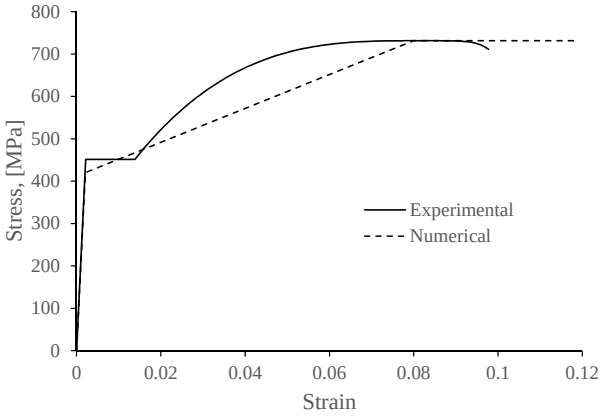

Figure 12. Stress–strain curve for the steel reinforcement

C. Damage models

The damage parameters for both the compressive and tensile behaviour of the concrete were extracted from Alfarah et al. [24], which is an update of the formulation of Lee and Fenves [17]. On the other hand, the pivot rule formulation proposed by Park et al. [31] was used for both the compressive and the tensile behaviour of the masonry.

It is worth mentioning that even when a unit value of a damage parameter means a total failure of the material, which in turn means that the material can not carry more stress, this could not be applied to the model. This is related to the formulation of CDP [19], which states that a unit value of damage parameter would lead to an infinite value of the plastic strain. For this reason, in the present paper, all the damage parameters are fixed to have a maximum value of 0.98.

D. Quasi-static modelling

Experimentally, the cyclic tests of the walls were carried out slowly, as a quasi-static event, in order to avoid kinematic effects. For modelling quasi-static phenomena, ABAQUS offers two powerful solvers: implicit and explicit. The implicit solver involves the solution of static equilibrium equations by enforcing an equilibrium between the internal and external forces. If the implicit solver does not find a convergence between these forces in a specific time increment, it adds certain corrections through the Newton–Raphson method. The process continues until the difference between the internal and external forces is less than a small value, called the convergence criterion. However, to solve the equilibrium equations, the implicit solver needs to invert the stiffness matrix, which involves a high computational cost, depending on the number of degrees of freedom.

On the other hand, the explicit solver involves the solution of dynamic equilibrium equations. Unlike the implicit solver, the explicit solver does not enforce an equilibrium between the internal and external forces, which means that there is no convergence criterion. Moreover, the explicit solver needs to invert the mass matrix instead of the stiffness matrix, which turns out to be much cheaper computationally. Indeed, inverting an uncoupled diagonal mass matrix is less expensive than inverting a fully coupled stiffness matrix. Once the mass matrix has been inverted, the acceleration in a specific time increment is calculated. Thereupon, the velocity and displacements are calculated by means of the central difference method.

In general terms, an explicit solution moves away from the real solution if each time step is divided into only a few time increments. That is why the ABAQUS Explicit Solver efficiently implements a large number of time increments in order to obtain reliable results [19]. In this work, the explicit solver was used to model the quasi-static phenomena involved in the pushover analysis. Nevertheless, to avoid considerable kinematic effects, the kinetic energy was intended to kept less than 1% of the internal energy during the largest part of the test [32], [33].

IV. Validation of the Proposed Model

A. Walls without vertical load

Taking into account that each wall was assumed to be a single part, a single mesh size would affect the entire part. Therefore, in order to find an appropriate mesh size, one that would require less computational cost without losing accuracy, a sensitivity analysis was carried out.

The Young's modulus of the masonry shown in Table I was computed experimentally by uniaxial compressive tests conducted perpendicularly to the bed joints. However, this value can not be used directly for modelling since it would lead

to stiffer responses, as has also been observed by others [34]. This is related to the fact that the macro-modelling approach tries to simulate even totally anisotropic materials as isotropic. As with Young's modulus, all the material properties obtained experimentally from small specimen tests were expected to be calibrated for the macro-modelling. For this reason, many iterations were carried out by varying the material properties of the masonry and the concrete. It was noted that the properties related to the tensile behaviour of the masonry controlled the overall response of the confined masonry wall. Therefore, a subsequent parametric study was conducted by varying three main parameters of masonry: Young's modulus, tensile strength, and fracture energy. This had the aim of getting average values that would allow properly fitting the experimental curves. The parametric study began considering the material properties shown in Tab. I.

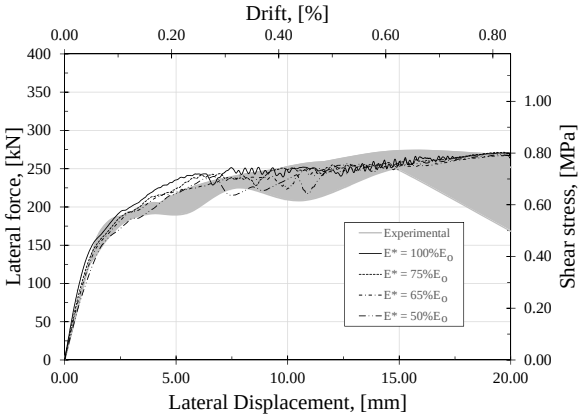

Figure 13. Numerical responses to changes in Young's modulus

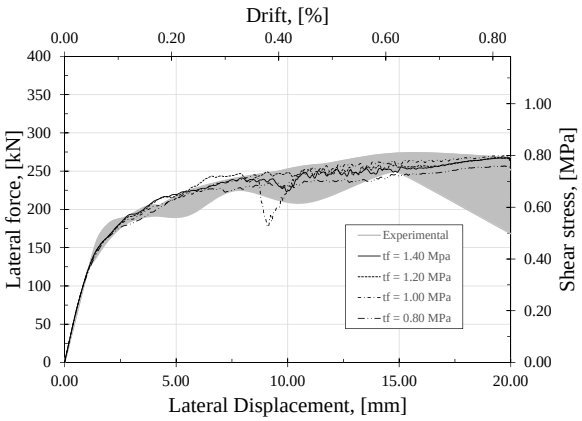

Figure 14. Numerical responses to changes in the tensile strength

Fig. 13 shows the numerical curves obtained from iterating the Young's modulus, where it was possible to note that an equivalent Young's modulus $E^* = 65\%E_0$ allowed to properly fit the initial stiffness of the experimental results. Anyway, it has to be noted that regardless the percentage of the experimental Young's modulus, the variation of the initial stiffness of the entire wall is not quite and it also does not affect

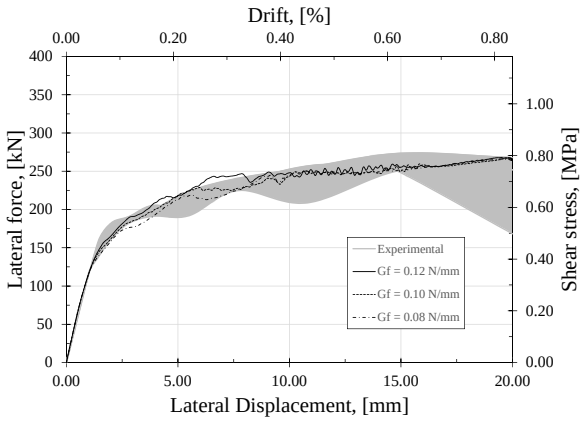

Figure 15. Numerical responses to changes in the tensile strength

too much the nonlinear behaviour of the wall. In addition, it is worth mentioning that the experimental zone showed in Fig. 13 and thereafter turned out from the area enclosed by the experimental curves showed in Fig. 5. Once calibrated the Young's modulus, masonry's tensile strength was the next parameter to be iterated, as is shown in Fig. 14.

In terms of fitting the nonlinear part of the experimental capacity zone (Fig. 14), it has to be noted the effect of decreasing the tensile strength of masonry, which is related to an earlier cracking of the masonry panel which in turns results in a quicker decreasing of the wall elastic modulus. According to Fig. 14, a value of $t_f = 1.20$ MPa was taken into account for the iteration of the next parameter. Regarding the fracture energy, Fig. 15 shows the numerical curves obtained from iterating this parameter. Like tensile strength, the effect of decreasing this parameter is associated to a quicker cracking process and indeed to a quicker stiffness degradation. These results allowed to conclude that both parameters are linked and govern the nonlinear behaviour of the wall. According to the experimental zone, the value $G_f = 0.10N/mm$ was chosen for showing the best fitting.

Once calibrated all the material parameters, it turned out important to compare the cracking pattern of both experimental cyclic test and numerical pushover analysis. Fig. 16 shows the cracking pattern for both experimental and numerical tests, according to different performance levels related to: (1) end of linear behaviour, (2) yielding beginning and (3) maximum load capacity. It has to be noted that there was a good agreement in terms of cracking pattern between half an experimental wall and numerical results by showing bending cracks due to the fact that there was no vertical constraint in the top part of the walls. It should also be noted that the experimental cracking pattern shows additional cracks that can not be captured by a pushover analysis since they are related to the cyclic behaviour of materials. Namely, additional cracks are intended to appear when there are incursions among compressive and tensile states.

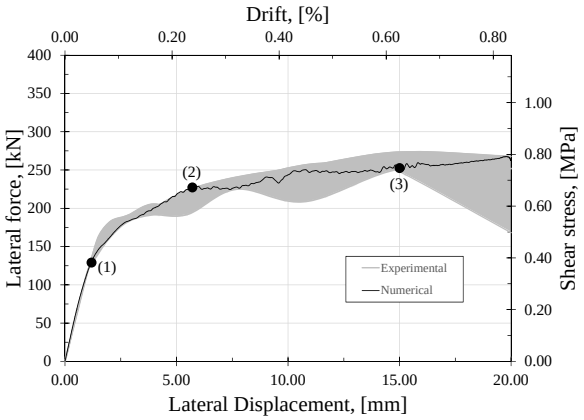

(a) Final numerical curve

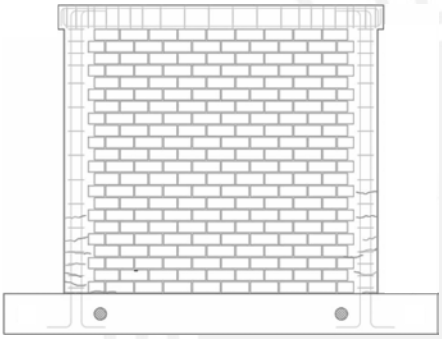

(b) (1) Experimental cyclic test

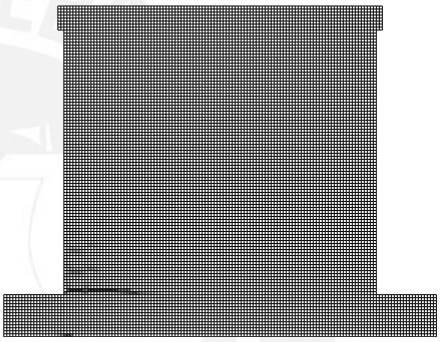

(c) (1) Numerical pushover

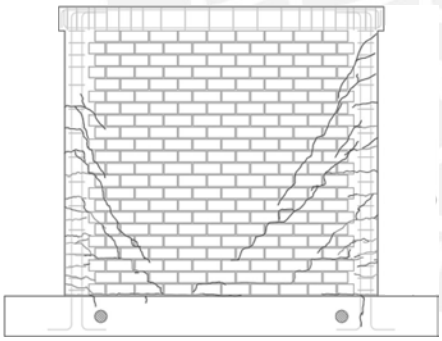

(d) (2) Experimental cyclic test

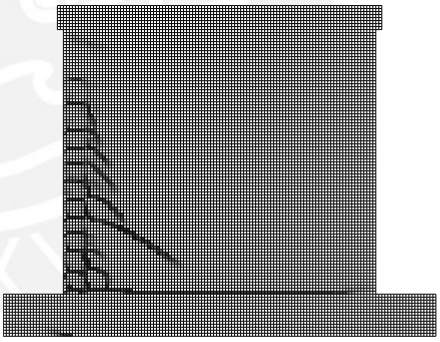

(e) (2) Numerical pushover

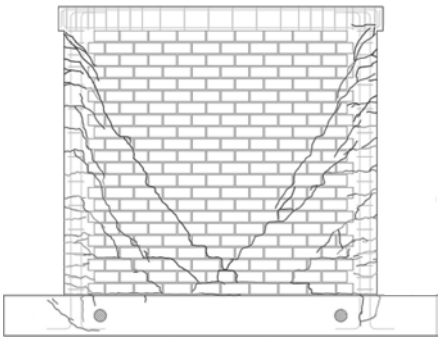

(f) (3) Experimental cyclic test

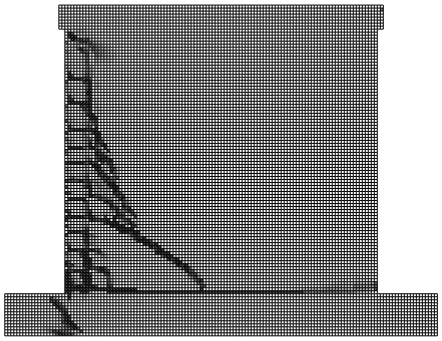

(g) (3) Numerical pushover

Figure 16. Experimental and numerical cracking patterns for walls without vertical load

B. Walls with vertical load

The calibrated material properties for the case of walls without vertical load, were intended to be used for showing the reliability of the proposed model for fitting the experimental results of another testing setup, which corresponded to consider a vertical load prior the application of lateral loading. This vertical load had a value of 170 kN which tried to represent the weight of 3 stories over a wall located at the first floor. In addition, it is worth mentioning that this vertical load was controlled manually by an operator who noted an oscillating variation of the vertical load conforming the lateral displacements were increasing. In fact, this variation became significant from a displacement level of 7.70 mm onwards. That was why the first test with vertical load was stopped for this displacement level (Fig. 5). For the next tests, this vertical load was intended to keep close to the 170 kN as much as possible. However, it was not possible to control which meant a complication for the modelling process to capture the nonlinear behaviour of the walls from the displacement level aforementioned. This oscillating effect of the vertical load caused an increment in the load capacity of the walls which was considered as unreal because it was caused by an uncontrollable boundary condition during their tests.

As it was mentioned before, the calibrated material properties from walls without vertical load were used here. However, it was noted that an equivalent Young's modulus of $E^* = 65\%E_0$ did not capture the initial stiffness showed by the experimental results. On contrary, it had to be used a value of $E^* = 100\%E_0$ to properly fit the initial stiffness of the experimental results (Fig. 17). This variation in percentage is attributed to the fact that each wall, from its construction up to its test, has enough time to develop some micro-cracks which are related to the shrinkage of concrete and mortar, or to the fact that some high stresses can take place during the lifting of the walls. It is known that the presence of cracks is linked to the reduction of the Young's modulus of the materials. However, the presence of vertical load helps to the closing of these cracks which is related to a recovery of this parameter. Anyway, within the showed range $65\% - 100\%$, it can be highlighted that the variation of Young's modulus does not affect too much the nonlinear response of the wall, as it was noted in Fig. 13 and can also be seen in Fig. 17.

It is important to mention that a proper application of the vertical load should have lead to a behaviour more close to the numerical curve. In fact, a constant vertical load would be more appropriate to represent the load condition of a wall located on the first floor in a real house. To support this idea, it can be seen the results of the experimental tests conducted by Perez et al. [35], where it can clearly seen the tendency of the capacity curves.

Fig. 18 shows the cracking pattern for both experimental and numerical tests, according to different performance levels related to: (1) end of linear behaviour, (2) maximum load capacity and (3) ultimate state. It should be noted there was a good agreement between experimental and numerical cracking pattern until the second analyzed performance level. In the ultimate state, differences are evidence by the presence of additional cracks, which in fact were produced by the effect of the experimental cyclic loading and the uncontrollable vertical load from second point onwards.

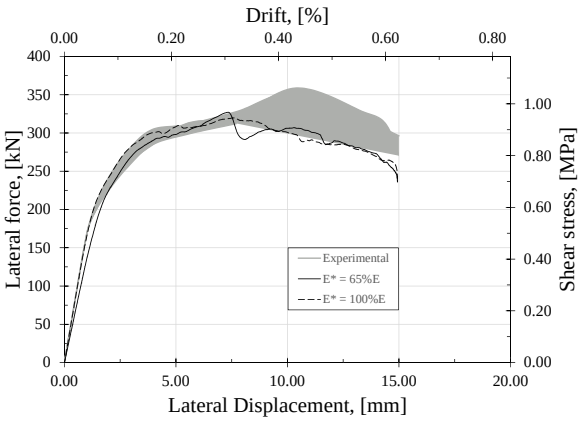

Figure 17. Young's modulus calibration for the effect of the vertical load

As mentioned before, the quasi-static problem was intended to be solved by means of a purely dynamic explicit solver. For this purpose, the loads were applied by defining smooth step amplitudes, which has the advantage of having zero velocity in the application of the loading at the beginning and ending of the load step. In addition, these smooth steps allow gradually increasing the application of the loading, which in turns helps to minimize kinematic effects. Subsequently, in order to be sure that the numerical results resulted mainly from quasi-static effects, i.e. that kinematic effects were not dominant, the kinetic and internal energy of the whole model (ALLKE and ALLIE, respectively) were compared over the entire time step. Fig. 19 shows this comparison. Note that the kinetic energy is less than 1% of the internal energy over the largest part of the time step.

V. Conclusion

A 3D finite element model based on the macro-modelling technique was presented to simulate the nonlinear behaviour of confined masonry walls subjected to in-plane lateral loading. For this purpose, all the solid elements were modelled as single parts, which means that no contact surfaces between the different materials were physically modelled. In addition, due to the assumptions made by Concrete Damage Plasticity (CDP) of treating quasi-brittle materials as isotropic, it was not possible to use the material properties directly obtained from small sample tests. On the contrary, these materials properties needed to be calibrated. After many iterations, varying the material properties of the concrete and masonry, it was concluded that the main parameters that controlled the nonlinear behaviour of the walls were the Young's modulus, tensile strength and fracture energy of the masonry. Therefore, in a parametric study, these parameters were iteratively varied until reaching a good fit to the experimental results.

Recalling that Young's modulus, E_0, of masonry was obtained experimentally by means of the well-known compressive tests of brick piles, it could be seen that values of $65\%E_0$

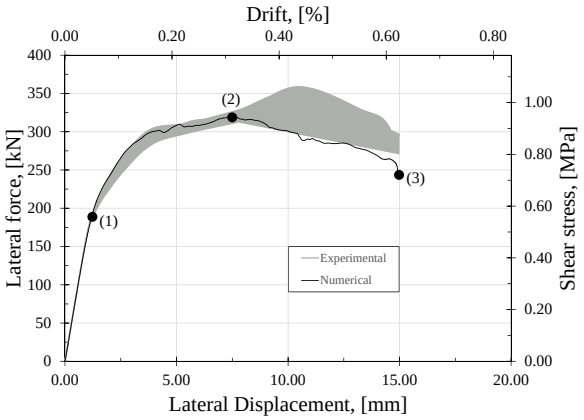

(a) Final numerical curve

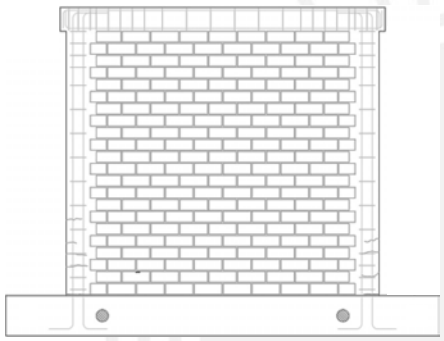

(b) (1) Experimental cyclic test

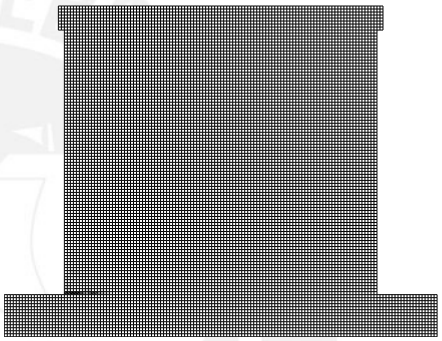

(c) (1) Numerical pushover

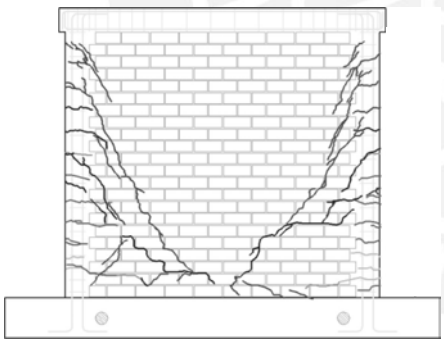

(d) (2) Experimental cyclic test

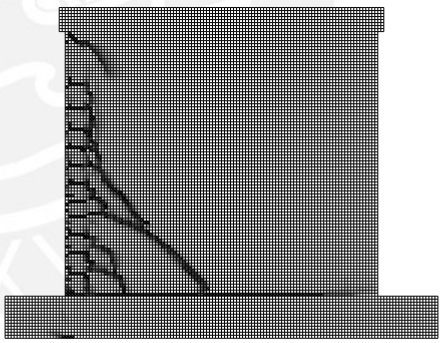

(e) (2) Numerical pushover

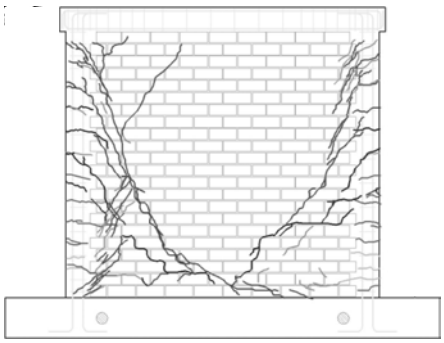

(f) (3) Experimental cyclic test

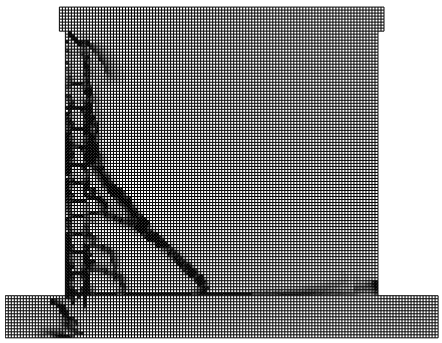

(g) (3) Numerical pushover

Figure 18. Experimental and numerical cracking patterns for walls with vertical load

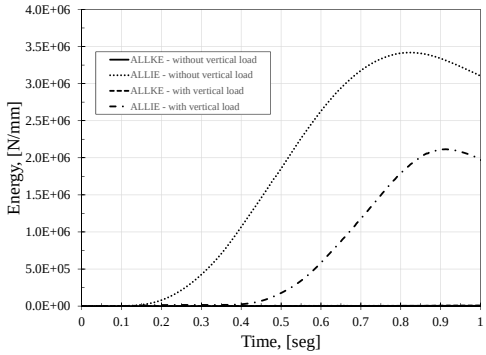

Figure 19. Comparison of kinetic and internal energies

and $100\%E_0$ properly fit the initial stiffness of walls without and with vertical load, respectively. In fact, Young's modulus is related to the presence of cracks prior to testing, but anyway the impact of fitting the initial stiffness with a more or a little less precision does not affect too much the nonlinear response of the confined masonry walls.

Regarding the tensile strength and fracture energy of the masonry, it is worth mentioning that both parameters controlled the cracking pattern and the nonlinear behaviour of the confined masonry walls. Therefore, they were iterated together so as to obtain a reduced value of $t_f = 1.20$ MPa, instead of the $t_f = 1.40$ MPa obtained from the well-known diagonal compressive test of square masonry samples, and a fracture energy of $G_f = 0.10$ N/mm, which allowed properly fitting both the cracking pattern and the nonlinear part of the capacity curves.

Finally, the proposed model acheived good precision in capturing the nonlinear response of confined masonry walls as well as their cracking pattern. Therefore, taking into account the efficiency and the simplicity of the application of the model herein proposed, it can be concluded that it can be used to help laboratory tests and designing codes in case it is important to predict the cracking patterns, maximum load capacity, and the ultimate displacements of confined masonry walls.

ACKNOWLEDGMENT

The authors wish to acknowledge the economic support provided by CONCYTEC within the framework of the N° 232-2015-FONDECYT Agreement.

REFERENCES

[1] INEI, "Censos nacionales 2014: población y vivienda," *Instituto nacional de estadística e informática*, 2014.

[2] J. Lara and J. León. (2017) https://elcomercio.pe/lima/sucesos/viviendas-construidas-ladrillos-pandereta-riesgo-sismos-lima-noticia-464070?foto=1.

[3] M. El-Diasity, H. Okail, O. Kamal, and M. Said, "Structural performance of confined masonry walls retrofitted using ferrocement and GFRP under in-plane cyclic loading," pp. 54–69, 2015.

[4] W. Wijaya, D. Kusumastuti, M. Suarjana, K. Pribadi *et al.*, "Experimental study on wall-frame connection of confined masonry wall," *Procedia Engineering*, vol. 14, pp. 2094–2102, 2011.

[5] N. Kassem, A. Atta, and E. Etman, "Structural behavior of strengthening masonry in-filled frames subjected to lateral load using bonded and unbonded CFRP," *KSCE Journal of Civil Engineering*, vol. 21, no. 3, pp. 818–828, 2016.

[6] M. Breveglieri, G. Camata, and E. Spacone, "Strengthened infilled RC frames: Continuum and macro modeling in nonlinear finite element analysis," *Composites Part B: Engineering*, 2018.

[7] P. J. B. B. Lourenço, "Computational strategies for masonry structures." 1997.

[8] O. Hussein, A. Arm, A. Arm, and M. Mostafa, "Experimental and analytical investigation of the lateral load response of confined masonry walls," *HBRC*, vol. 12, pp. 33–46, 2016.

[9] M. Annecchiarico, F. Portioli, and R. Landolfo, "Micro and macro finite element modeling of brick masonry panels subject to lateral loadings," in *Proc., COST C26 Action Final Conf*, 2010, pp. 315–320.

[10] C. Gatta, D. Addessi, and F. Vestroni, "Static and dynamic nonlinear response of masonry walls," *International Journal of Solids and Structures*, vol. 155, pp. 291–303, 2018.

[11] A. M. D'Altri, S. de Miranda, G. Castellazzi, and V. Sarhosis, "A 3d detailed micro-model for the in-plane and out-of-plane numerical analysis of masonry panels," *Computers & Structures*, vol. 206, pp. 18–30, 2018.

[12] E. Nasiri and Y. Liu, "Deveolpment of a detailed 3D FE model for analysis of the in-plane behavior of masonry infilled concrete frames," *Engineering Structures*, vol. 143, pp. 603–616, 2017.

[13] A. J. Aref and K. M. Dolatshahi, "A three-dimensional cyclic meso-scale numerical procedure for simulation of unreinforced masonry structures," *Computers & Structures*, vol. 120, pp. 9–23, 2013.

[14] M. Bolhassani, A. A. Hamid, A. C. Lau, and F. Moon, "Simplified micro modeling of partially grouted masonry assemblages," *Construction and Building Materials*, vol. 83, pp. 159–173, 2015.

[15] J. Manchego and S. Pari, "Análisis experimental de muros de albañilería confinada en viviendas de baja altura en Lima, Perú," Master's thesis, Pontificia Universidad Católica del Perú, 2016.

[16] Y. Goto, G. P. Kumar, and N. Kawanishi, "Nonlinear finite-element analysis for hysteretic behavior of thin-walled circular steel columns with in-filled concrete," *Journal of Structural Engineering*, vol. 136, no. 11, pp. 1413–1422, 2010.

[17] J. Lee and G. Fenves, "Plastic-damage model for cyclic loading of concrete structures," *Journal of Engineering Mechanics*, vol. 124, no. 8, pp. 892–900, 1998.

[18] T. Jankowiak and T. Lodygowski, "Identification of parameters of concrete damage plasticity constitutive model," *Foundations of Civil and Environmental Engineering*, vol. 6, no. 1, pp. 53–69, 2005.

[19] Abaqus, "Ver. 6.14 Documentation," *Dassault Systemes Simulia Corporation*, 2014.

[20] S. Michał and W. Andrzej, "Calibration of the CDP model parameters in ABAQUS," 2015.

[21] A. T, *Fracture Mechanics: Fundamental and Applications*. Taylor and Francis, 2005.

[22] CEB-FIP, "Model code 2010," *London: Thomas Telford*, 2010.

[23] W. B. Krätzig and R. Pölling, "An elasto-plastic damage model for reinforced concrete with minimum number of material parameters," *Computers & Structures*, vol. 82, no. 15-16, pp. 1201–1215, 2004.

[24] B. Alfarah, F. López-Almansa, and S. Oller, "New methodology for calculating damage variables evolution in Plastic Damage Model for RC structures," *Engineering Structures*, vol. 132, pp. 70–86, 2017.

[25] P. Agnihotri, V. Singhal, and D. C. Rai, "Effect of in-plane damage on out-of-plane strength of unreinforced masonry walls," *Engineering Structures*, vol. 57, pp. 1–11, 2013.

[26] D. A. Hordijk, "Tensile and tensile fatigue behaviour of concrete; Experiments, modelling and analyses," *Heron*, vol. 37, no. 1, 1992.

[27] S. Oller, "A continuous damage model for frictional materials," Ph.D. dissertation, Doctoral Dissertation, Technical University of Catalonia, 1988.

[28] H. B. Kaushik, D. C. Rai, and S. K. Jain, "Stress–strain characteristics of clay brick masonry under uniaxial compression," *Journal of Materials in Civil Engineering*, vol. 19, no. 9, pp. 728–739, 2007.

[29] A. Hillerborg, M. Modéer, and P.-E. Petersson, "Analysis of crack formation and crack growth in concrete by means of fracture mechanics and finite elements," *Cement and Concrete Research*, vol. 6, no. 6, pp. 773–781, 1976.

[30] M. Dehestani and S. Mousavi, "Modified steel bar model incorporating bond-slip effects for embedded element method," *Construction and Building Materials*, vol. 81, pp. 284–290, 2015.

[31] Y. J. Park, A. M. Reinhorn, and S. K. Kunnath, "IDARC: Inelastic damage analysis of reinforced concrete frame-shear-wall structures," 1987.

[32] R. Abdullah, V. Paton-Cole, W. Easterling, and F. ASCE, "Quasi-Static Analysis of Composite Slab," *Malaysian Journal of Civil Engineering*, vol. 19, no. 2, pp. 1–13, 2007.

[33] L. Karapitta, H. Mouzakis, and P. Carydis, "Explicit finite-element analysis for the in-plane cyclic behavior of unreinforced masonry structures," *Earthquake Engineering & Structural Dynamics*, vol. 40, no. 2, pp. 175–193, 2011.
[34] P. Medeiros, G. Vasconcelos, P. B. Lourenço, and J. Gouveia, "Numerical modelling of non-confined and confined masonry walls," *Construction and Building Materials*, vol. 41, pp. 968–976, 2013.
[35] J. J. Pérez Gavilán, L. Flores, and S. Alcocer, "Efecto de la esbeltez en la resistencia de muros de mampostería confinada," *Ingeniería Sísmica*, no. 89, pp. 55–76, 2013.

Capítulo V

Comparación de alternativas de refuerzo sísmico

5.1. Multi-Criteria Analysis of Five Reinforcement Alternatives for Peruvian Confined Masonry Walls

Multi-Criteria Analysis of Five Reinforcement Alternatives for Peruvian Confined Masonry Walls

Nicola Tarque[1a], Jhoselyn Salsavilca[1b], Jhair Yacila[1c] and Guido Camata[2d]

[1]*Pontificia Universidad Católica del Perú. Department of Civil Engineering. San Miguel 15088, Lima, Peru.*
[2]*University "G.d'Annunzio" of Chieti and Pescara. Department of Engineering and Geology. Pescara 65127, Italy*

(Received keep as black, Revised keep as black, Accepted keep as black)

Abstract. In Peru, construction using confined masonry (CM) has a high percentage of acceptance within many sectors of the population. It is estimated that only in Lima, 80% of the constructions use CM and at least 70% of these are informal constructions. That is, they are executed without proper technical advice and generally have a high degree of seismic vulnerability. One way to reduce this vulnerability is by reinforcing the walls. However, despite the existence of diverse reinforcement methods in the market, not all of them can be applied massively given that there is another important factor. This is the population's ability to afford the reinforcement. Therefore, this paper studies five reinforcement techniques (welded mesh, GFRP, CFRP, steel bar wire mesh, SRG) in terms of seismic improvement, economy, among others criteria that may conflict each other. The Multi-Criteria Decision Making (MCDM) method can be employed to evaluate multiple conflicting criteria in decision making of the most optimal strengthening technique for a fast, effective and massive use plan in Peru. The results using MCDM with 10 criteria indicate that the Carbon Fiber Reinforced Polymer (CFRP) and Steel Reinforced Grout (SRG) methods are the most appealing.

Keywords: strengthening techniques, confined masonry, MCDM

1. Introduction

Confined masonry constructions are considered one of the most popular worldwide because of their easy and quick execution, and for their low costs (Alcocer *et al.* 2003). Specifically, its use is common in Central and South America, Southeast Europe, India and other parts of Asia (Bhattacharya *et al.* 2013). For example, this type of construction has been used in Chile and Colombia since the 1930's and in Mexico since the 1940's (Brzev and Perez 2014). According to Alcocer *et al.* (2003), until 2003, over 70% of Mexico's constructions made use of masonry. In Pakistan, 62.38% of all its buildings were constructed with masonry (Lodi *et al.* 2012). Peru is another case whose statistics

*Corresponding author, Ph.D. Nicola Tarque, E-mail: sntarque@pucp.edu.pe
[a]Ph.D.,E-mail: sntarque@pucp.edu.pe
[b]Eng., E-mail: jsalsavilcap@pucp.pe
[c]Eng., E-mail: jhair.yacila@pucp.edu.pe
[d]Ph.D., E-mail: g.camata@unich.it

(Fig. 1) show that the predominant type of housing is independent houses with an 86%, and confined masonry, made of fired clay units, has been identified as the preferred material for building these houses (Yepes-Estrada *et al.* 2017).
Considering many of these countries, such as Peru, are located in high seismic activity zones (Fig. 2), different seismic events have shown poor seismic performance of existing masonry structures built informally. Moreover, depending on the formality of the construction, quality of technical personnel, characteristics of the structure itself and other parameters; the seismic vulnerability associated with these constructions is higher, which results in higher risk. Obviously, the studied area's geological characteristics cannot vary in order to reduce seismic activity, however, vulnerability can be reduced since it is associated with the intrinsic properties of the edification.
Therefore, the need arose to pose the steps that should be taken in order to reduce seismic vulnerability of informal masonry constructions. These steps consist of carrying out constant investigations about the possible repair and reinforcement systems for Peruvian confined masonry walls in order to enhance the seismic performance (Popa *et al.* 2016, Remki *et al.* 2016, Smyrou 2015, Srechai *et al.* 2017). Several studies in this field have already been carried out by different universities, in this paper are presented the studies carried out in the Pontifical Catholic University of Peru.
Some studies carried out in Peru about the most relevant reinforcement techniques use welded wire mesh reinforcement (San Bartolomé and Castro 2002), glass rod reinforced polymer (San Bartolomé and Loayza 2004), carbon fiber reinforced polymer (San Bartolomé and Coronel 2009), steel bar wire mesh (Luján and Tarque 2016), and galvanized steel fiber with natural lime mortar (SRG) (Yacila *et al.* 2019, Salsavilca *et al.* 2019). Each of these reinforcements was applied to confined masonry walls on a natural scale, previously tested to their break strength or repair limit in the Structural Laboratory of the Pontifical Catholic University of Peru.
Although these techniques were already studied, the identification of a unique technique that allows for a fast, effective and massive application constitutes one of the main challenges faced by the academy. The decision making process becomes more complicated if many criteria are considered. For a fast application, it should be considered criteria as duration and difficulty of application. For a massive use, the technique should meet cost-effectiveness requirements. For an effective technique, the seismic performance in terms of stiffness, load capacity and ductility must be evaluated. The efficacy of a reinforcing system depends also on its durability and compatibility with the strengthened substrate. The durability is crucial for the long-term effectiveness of the reinforcement (De Santis *et al.* 2017) under varying temperature, moisture and other environmental factors (Cabral *et al.* 2018). The compatibility property measures the effectiveness of two materials to work together. In case of strengthening techniques, there should be compatibility with thermal expansion coefficient and elastic modulus of substrate. It could be said that Lime-based mortars which belong to SRG are mainly used for applications to historic substrates, needing relatively low Young's modulus to meet mechanical compatibility requirements(De Santis *et al.* 2017).
This work presents a summary of the previously mentioned investigations and identifies a reinforcement method through multi-criteria analysis using the MCDM TOPSIS method (Hwang and Yoon 1981). To identify the most suitable method, each reinforcement's characteristics and application process have been described. In addition, the improvement of earthquake-resistance properties of the walls such as stiffness, seismic capacity, and ductility, presented by each reinforcement method has been studied. The economic aspect is discussed in terms of labor and materials since this paper

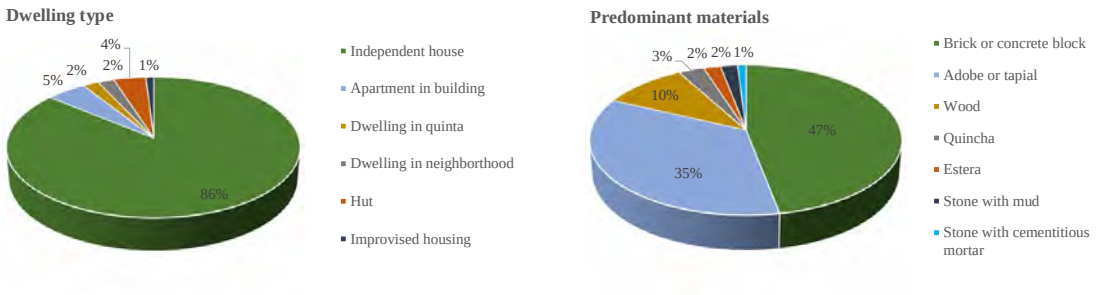

(a) (b)

Fig. 1 Population of Peru and description of the type of building: (a) Type of building, (b) main material in the houses' outer walls INEI (1981)

pretends to decide for one technique among the five ones in order to accomplish a massive use plan. It is worth mentioning that a mechanical ratio was taken account as a main criteria in MCDM due to the different quantity of retrofitting material placed to each wall and different mechanical characteristic of the masonry panels and reinforcement material. Furthermore, aspects such as the duration of application, durability, compatibility, aesthetics, and initial test conditions are also considered. According to the MCDM TOPSIS method, the best solutions for a fast, effective and massive application in Peru turn out to be the Carbon Fiber Reinforced Polymer (CFRP) and Steel Reinforced Grout (SRG).

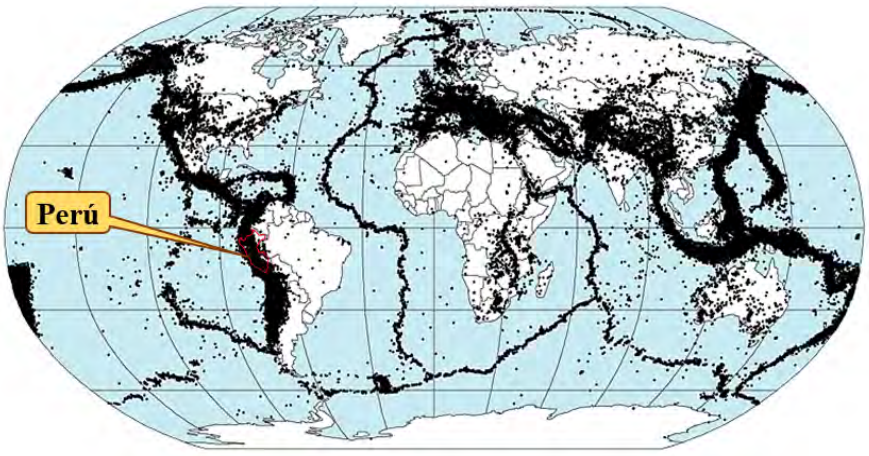

Fig. 2 Seismic activity around the world since 1973 (Lowman and Montgomery 1998)

2. Description of the four reinforcement alternatives

2.1 Steel as reinforcement material: welded wire mesh and steel bar wire mesh

For a long time, in the area of the most studied reinforcement techniques, steel has been considered as a reinforcement material capable of solving the damage in existing masonry structures. It has appeared as the main material in several reinforcement systems such as cladding, welded wire mesh, cable system, and steel bar wire mesh. The welded wire mesh technique (WM) basically consists of a set of corrugated steel rods with a 4.5 *mm* diameter and spaced every 150 *mm*. This set is placed on both sides of the walls interconnecting them with #8 wires through previous perforations in the wall section. Then, the surface is plastered with mortar obtaining 25 *mm* of additional thickness on each side of the wall. On the other hand, the steel bar wire mesh technique (CSM) consists of preparing a mesh of steel rods with 4.7 *mm* diameter. The meshes are connected through previous perforations in the wall with #8 wire and are tied against the knots of the meshes on both sides with #16 wire. Same as the previous technique, the wall is plastered so that it does not exceed 25 *mm* on each side. The difference between both procedures lies in the making of the meshes, while the welded wire mesh is a prefabricated reinforcement, the steel bar wire mesh is made in-situ.
In theory, the use of welded wire mesh (WM) should be evaluated in structures that require ductility (dissipation of energy), since the wires that make up the mesh are subjected to a cold drawing process. Thus, they tend to be fragile with an elongation at break between 1 and 3%. The tensile test performed on three samples extracted from the mesh gave an average ultimate resistance of 600 MPa. On the other hand, the steel bar wire meshes (CSM) were made with grade 60 rebar, which is characterized by having an elongation at break between 7 and 9% and an ultimate resistance of 618 MPa. This greater elongation would give a first indication of a bigger ductility contribution to the structures.

2.2 FRP as a reinforcement system: carbon and glass fiber

This reinforcement system consists of high strength fibers impregnated in a polymer matrix (two component epoxy resin). It is recommended because of the excellent properties of its components such as glass, carbon, basalt fibers among others (Buchan and Chen 2007). This section presents the CFRP and GFRP (carbon fiber reinforced polymer and glass fiber reinforced polymer) as reinforcement techniques with higher tensile mechanical characteristics due to them being discontinuous phase materials (Corradi *et al.* 2002).
Both CFRP and GFRP are easy and quick to apply. The first method is made up of a light and high resistance unidirectional carbon fiber sheet (surface density = $3\times10^{-10}\ tonne/mm^2$) that is embedded in three types of resins. The CFRP system consists of applying the first epoxy compound (that works as a primer to seal the pores) on the masonry surface and another epoxy paste (putty) to level the surface. Then, the carbon fiber is placed so that it is finally coated by the third type of epoxy resin (saturant) that encapsulates the fibers. The second method is made up of glass fibers impregnated with vinyl ester resin. They are corrugated and covered with a layer of fine sand. They are not electrically conductive and are very light ($\gamma = 2.26\times10^{-9}\ tonne/mm^3$). This GFRP system basically consists of installing the glass fiber rods as interior horizontal reinforcement every 2 rows of bricks, interspersed alternately on both sides of the wall in order to avoid weakening the cross section of the reinforced wall.
Table 1 lists characteristic values for the fibers used in the past experimental investigations.

Table 1 Mechanical properties of the carbon and glass fiber used

		Carbon fiber	Glass fiber rods
Tensile Strength	$[MPa]$	3800	827
Young's Modulus	$[GPa]$	227	40.7
Elongation at failure	[%]	1.67	0.16
Equivalent thickness/Diameter	$[mm]$	0.165	6.25

2.3 SRG as a reinforcement system: galvanized steel fiber

Currently, other reinforcement options such as the Fabric Reinforced Cementitious Matrix (FRCM), Fiber Reinforced Matrix (FRM), Steel Reinforced Grout (SRG) have arisen to compete against the previous ones, given the advantages offered by the inorganic matrix that composes them. This results in a high resistance to fire and UV rays protection. Moreover, the use of inorganic mortars allows a better adhesion to a non-uniform surface such as masonry (Gattesco and Boem 2017). Consequently, FRMs draw attention due to their application to historical structures (Ghiassi *et al.* 2016).

Specifically, the SRG (Steel Reinforced Grout) system is made up of UHTSS (Ultra High Tensile Strength Steel) and natural lime mortar. The fiber used was galvanized steel coated with zinc. This mesh is unidirectional and consists of strings that are obtained by twisting two wires around three rectilinear ones. In addition, the mortar that works as binding is made of lime with type M15 resistance according to the EN 998-2 and type R1 according to EN 1504-3. Previous researches (Salsavilca *et al.* 2019, Carloni 2017) have conducted an experimental campaign to characterize the materials of SRG and Table 2 shows the characteristic values of the materials that were used.

This technique is quite easy to install, so it does not need to be applied by experts. Before applying SRG, several aspects must be taken into consideration, such as wall clearance, strip clearance, mortar preparation, compound application and curing. Thus, after treating the surface by removing the dust and dampening it, a first layer of mortar 5 *mm* thick is applied. Then, the mesh is placed manually and pressed on the fresh mortar in order to then apply a second layer of mortar 5 mm thick. In this way, it is obtained 10 *mm* of additional thickness on each side of the wall. Finally, unlike other type of reinforcements, it is cured for 7 days.

The good performance of SRG system has turned out to be substantially dependent on the bond behavior between the composite layer and the substrate. Salsavilca *et al.* (2019) evaluated the bond behavior between SRG and masonry, and the average ultimate stress was equal to 1738 MPa. Additionally, De Santis *et al.* (2017), by means of experimental tests on SRG, pointed out an average tensile strength equal to 2838 MPa.

Table 2 Mechanical properties of used Steel Fiber and Mortar

		Galvanized Steel	Lime-based Mortar
Tensile Strength	$[MPa]$	2861	2.92
Compressive Strength	$[MPa]$	–	22
Young's Modulus	$[GPa]$	157	9.1
Failure Deformation	[%]	2.44	–
Equivalent thickness	$[mm]$	0.084	–

3. Experimental Campaign

3.1 Characteristics of specimens

The walls that were tested in each investigation were in natural scale, their outline and dimensions are shown in Fig. 3 and Table 3. All the studies sited presented the CM walls with a stretcher bond. The column-masonry joint used by San Bartolomé and Loayza (2004) and San Bartolomé and Coronel (2009) was flush, while the rest of investigations (3) presented a toothed connection.

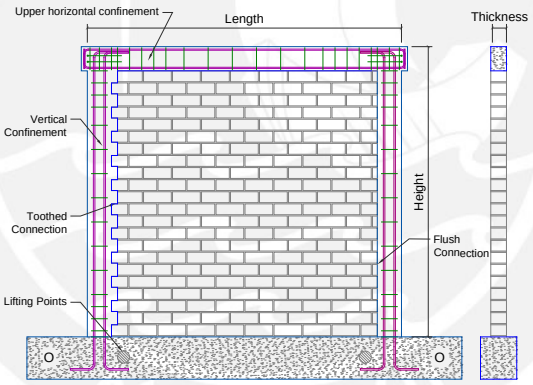

Fig. 3 Sketch of tested walls

The masonry unit used in each investigation was solid (percentage of void less than or equal to 30%) or hollow (percentage of voids greater than 30%), which directly influences the masonry axial compressive strength ($f'm$) and shear resistance ($v'm$) as shown in Table 3. The properties of the masonry such as compressive strength ($f'm$) and modulus of elasticity ($E'm$) were obtained by performing an axial compression test, and the shear strength ($v'm$) was obtained by performing the diagonal compression test. Both control tests were performed on piles and walls, respectively. Table 3 shows the mechanical properties extracted from cited investigations, except for the first three values of E(*) that were calculated according to the NTP E.070 (2006) that estimates $E = 500 f_m$.
It is worth mentioning the configuration adopted for each wall during the strengthening process since the quantity of reinforcement material influences on the final load-displacement response. In case of the welded mesh technique, it was used a mesh that covered both sides of the wall. This grid was comprised of bars (diameter 4.5 mm) spaced 150 mm vertically and horizontally. In the GFRP strengthened wall, five glass rods were place on each side with a spacing equal to 400 mm. For CFRP

Table 3 Mechanical and geometric properties of walls studied

Strengthening Technique	Masonry Unit (voids %)	f'm $[MPa]$	E'm $[GPa]$	v'm $[MPa]$	Length (L) $[mm]$	Height (H) $[mm]$	Thickness (t) $[mm]$	H/L
Welded Mesh (WM)	Solid(30)	8.6	4555*	1.70	2600	2400	130	0.92
Fiber Glass Rod (GFRP)	Hollow(45)	12.7	6726*	1.60	2400	2600	130	1.08
Carbon Fiber Mesh (CFRP)	solid(32)	8.8	4661*	0.94	2400	2600	130	1.08
Corrugated Steel Mesh (CSM)	Hollow(48)	9.46	5010	1.25	2600	2400	130	0.92
Steel Reinforced Grout (SRG)	Hollow(48)	9.46	5010	1.25	2600	2400	130	0.92

technique, it was computed that seven strips with a width of 100 *mm* will carry the load imposed during the cyclic test. Four strips were place on one side and the remaining in the other side with an approximated spacing of 600 *mm*. The wall reinforced with CSM had a configuration similar to WM since the bars (diameter 4.7 *mm*) were spaced 150 *mm* vertically and horizontally. Finally, the sketch of the wall strengthened with SRG comprised of five strips around all the wall. The strips width was 100 *mm* and the space between strips was approximated 400 *mm*.
Similarly, it should be pointed out the additional thickness that each strengthening technique provides to the wall since it is an aspect that influences on the stiffness recovering besides the reparation process which is so important too. Traditional techniques as WM and CSM add 25 *mm* to each entire side of the wall. Innovative techniques as GFRP do not add thickness since fiberglass rods are inside every 2 bed mortar joints, CFRP adds around 4 *mm* considering the epoxy resin and fiber, and SRG adds approximated 10 *mm* to each strengthened strip of the wall.

3.2 Test Protocol

The test carried out on the walls was a lateral cyclic loading test with controlled horizontal displacement (pseudo-static test) with no vertical load. The lateral load was applied at a rate of 1 cycle in 4 minutes. Fig. 4 Shows the typical test scheme for all the studied walls. The instrumentation of the tests consists of the following equipment: (1) dynamic actuator, (2) hydraulic jack and (3) steel beam.
The displacements were imposed by the dynamic actuator that had an internal LVDT for proper displacement control. This actuator was attached to the reaction frame, which was assumed to be a fixed structure. Thus, the idea was to obtain the relative displacements of the walls with respect to a point of the reaction frame. The objective of the tests was to determine the improvement of seismic behavior in reinforced walls and measure its resistance, stiffness and ductility variation.
In the case of the welded wire mesh (WM), the wall without reinforcement was subjected to 7 phases until a maximum lateral displacement of 12.5 mm was reached. The reinforced wall was subjected to 9 phases until a maximum lateral displacement of 17.5 *mm* was reached. For the glass fiber reinforced polymer (GFRP), the wall with and without reinforcement was subjected to 10 phases until a maximum lateral displacement of 20.0 *mm* was reached. For the carbon fiber reinforced polymer (CFRP), the wall without reinforcement was subjected to 8 phases until a maximum lateral displacement of 15.0 mm was reached. The reinforced wall was subjected to 11 phases until a maximum lateral displacement of 25.0 *mm* was reached. The displacement history for the last two

CSM and SRG studies complied with the guidelines of FEMA 461 (2009), which establishes that the displacements for each superior phase must be the result of increasing the immediate inferior displacement by a factor of 1.4 times. Then, for the corrugated steel mesh (CSM), the wall without reinforcement was subjected to 11 phases until a maximum lateral displacement of 20.0 *mm* was reached. The reinforced wall was subjected to 12 phases until a maximum lateral displacement of 25.0 *mm* was reached. Finally, for the galvanized steel fiber reinforced wall (SRG), the wall without reinforcement was subjected to 11 phases until a maximum lateral displacement of 20.0 *mm* was reached. The reinforced wall was subjected to 12 phases until a maximum lateral displacement of 30.0 *mm* was reached. Table 4 shows the displacement history according to each type of reinforcement studied.

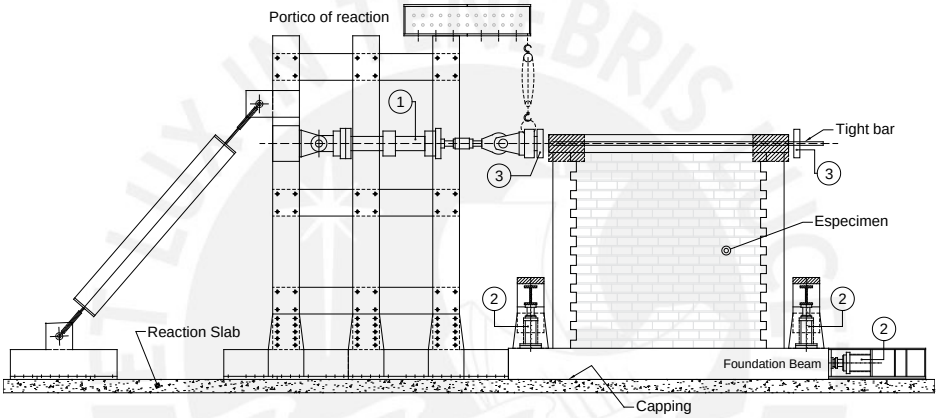

Fig. 4 Assembly for tests of confined masonry walls

3.3 Results for walls with and without reinforcement

3.3.1 Welded Wire Mesh (WM)

The original wall failed due to shear stress, while the reinforced wall failed due to bending stress. This is because the welded wire mesh was able to restraint, to a large extent, the opening of the repaired fissures. The first fissures due to bending appeared in the base of the columns at a 0.04% drift. Then, at a 0.21% drift, occurred the first failure due to shear stress, characterized by a diagonal crack in the masonry panel. Later, at a 0.42% drift, the bricks in the lower corners of the walls were crushed. Finally, at a 0.52% drift, the beam-confined column joints failed. Fig. 5 shows the failure pattern for original and reinforced walls, where it can be seen that generally, the reinforced wall tends to open the repaired fissures with a possibility of generating new fissures.

In terms of the reinforced wall, at a 0.04% drift, the first fissures due to bending appeared in the lower zones of the columns. Then, at a 0.10% drift, diagonal fissures due to shear stress were observed. These fissures were very thin because the welded wire mesh controlled the thickness. Later, for a 0.31% drift, new fissures appeared at the base of the columns. At a 0.52% drift, a split failure started to develop in the base of the wall. In addition, a vertical fissure was generated in the lower part of the masonry-column joint because the mesh was not connected to the columns.
The initial stiffness of the reinforced wall reached 89% of the initial stiffness of the wall. Likewise,

Table 4 Phases of quasi–static test for walls with and without reinforce

Technique	Concept	Displacements											
WM	Phase	1	2	3	4	5	6	7	8	9			
	Disp. [*mm*]	0.5	1.0	2.5	5.0	7.5	10.0	12.5	15.0	17.5			
	Cycles	1	1	2	2	2	2	2	3	3			
GFRP	Phase	1	2	3	4	5	6	7	8	9	10		
	Disp. [*mm*]	0.5	1.0	2.5	5.0	7.5	10.0	12.5	15.0	17.5	20.0		
	Cycles	1	1	2	2	2	2	2	3	3	3		
CFRP	Phase	1	2	3	4	5	6	7	8	9	10	11	
	Disp. [*mm*]	0.5	1.0	2.5	5.0	7.5	10.0	12.5	15.0	17.5	20.0	25.0	
	Cycles	2	1	2	3	3	3	3	3	3	3	1	
CSM	Phase	1	2	3	4	5	6	7	8	9	10	11	12
	Disp. [*mm*]	0.5	1.0	1.4	2.0	2.8	3.9	5.5	7.7	10.8	15.0	20.0	26.0
	Cycles	2	2	2	2	2	2	2	2	2	2	2	2
SRG	Phase	1	2	3	4	5	6	7	8	9	10	11	12
	Disp. [*mm*]	0.5	1.0	1.4	2.0	2.8	3.9	5.5	7.7	10.8	15.0	20.0	30.0
	Cycles	2	2	2	2	2	2	2	2	2	2	2	1

the initial stiffness of the reinforced wall resulted in an increase of 8 times the final stiffness of the original wall. Fig. 6 shows the comparison in the hysteresis loops envelopes of both walls, original and reinforced. From Fig. 6, it can be seen that the welded wire mesh reinforcement was able to increase the load capacity of the original wall by a 38% and the ductility by a 40% as well.

3.3.2 Glass Fiber Reinforced Polymer (GFRP)

At a 0.10% drift, the first fissure due to bending tensile stress appeared in the tie-column, while at a 0.19% drift, the existing fissures in the tie-columns spread to the interior of the masonry panel diagonally. Then, at a 0.29% drift, new diagonal fissures formed in the panel. In phases 6, 7 and 8 (drift=0.38%, 0.48% and 0.58%, respectively), these diagonal fissures intensified with the presence of the crushing of 2 bricks in the central part of the wall. Finally, at a 0.77% drift, the diagonal fissures spread towards the tie-columns. Fig. 7 shows the failure pattern for both walls, original and reinforced.

In the case of the reinforced wall, the first fissures in the masonry panel were observed at a 0.04% drift. At a 0.10% drift, the first fissures due to bending stress appeared in both tie- columns. At a 0.19% drift, very fin diagonal fissures appeared. For a 0.29% drift, the fixed fissures started opening. For a 0.38% drift, the thickness of the fissures due to shear stress (i.e. diagonal fissures) was controlled by the GFRP rods. For a 0.48% drift, fissures additional to those of the original wall were formed, and at a 0.58% drift, the central GFRP rod was exposed in its middle part. For a 0.67% drift, the GFRP rods started to buckle in several areas of the wall. Finally, at a 0.77% drift, the central part of the wall was crushed and the GFRP rods started losing adhesion with the masonry.
The initial stiffness of the reinforced wall reached 57% of the initial stiffness of the original wall. Likewise, the initial stiffness of the reinforced wall resulted in an increase of 5.8 times the final stiffness of the original wall. Fig. 8 shows the comparison in the envelopes of hysteresis loops of both

(a) Original (b) Reinforced

Fig. 5 Strengthening with welded mesh WM

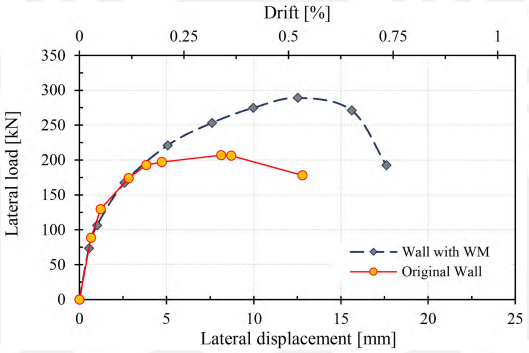

Fig. 6 Envelopes of hysteretic loops on walls with and without reinforcement WM

walls, original and reinforced. From Fig. 8, it can be inferred that the glass fiber reinforcement was able to increase the loading capacity of the original wall only by 3% and was not able to increase the ductility of the system.

3.3.3 Carbon fiber reinforced polymer (CFRP)

During the test on the original wall, there were no fissures up until a 0.10% drift, when the first diagonal fissure appeared in the lower half of the masonry. Similarly, there were bending stress fissures in both tie-columns. At a 0.19% drift, 2 diagonal fissures appeared throughout the wall. At a 0.48% drift, the masonry in the intersection of the diagonal fissures started being crushed. Finally, at a 0.58% drift, the lower edge of one of the tie-columns was completely crushed. Fig. 9 shows the failure pattern for original and reinforced walls.

In the reinforced wall, the diagonal fissures started in the upper center of the wall, at a 0.10% drift. During phases 4, 5, 6 and 7 (drift = 0.19%, 0.29%, 0.38% and 0.48%, respectively), the diagonal fissures continued to extend throughout the masonry panel. At a 0.58% drift, one of the bands located in the center of the wall suffered a small rupture. At a 0.67% drift, the band finished breaking. At a 0.77% drift, rupture and partial detachment of other bands occurred. Finally, at a 0.96%, the reinforced wall failed with rupture and partial detachment of other bands. The upper bands remained in good condition.

(a) Original (b) Reinforced

Fig. 7 Strengthening with GFRP

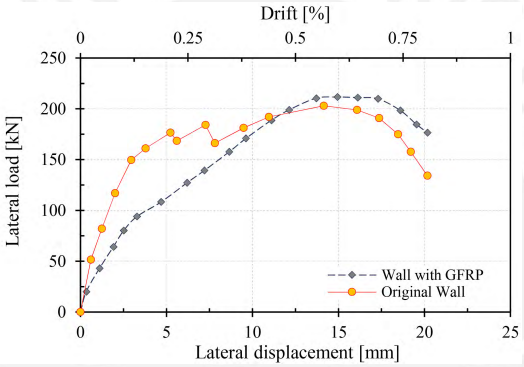

Fig. 8 Envelopes of hysteretic loops on walls with and without reinforcement GFRP

The initial stiffness of the reinforced wall reached 53% of the initial stiffness of the original wall. Similarly, the initial stiffness of the reinforced wall resulted in an increase of 12.4 times the final stiffness of the original wall. Fig. 10 shows the comparison in the envelopes of hysteresis loops of both walls, original and reinforced. From Fig. 10, it is inferred that the carbon fiber reinforcement was able to increase the loading capacity of the original wall by 20% and the ductility by 67%.

3.3.4 Corrugated steel mesh (CSM)

The first fissures, on the original wall, occurred at a 0.04% drift and were due to bending stress in the tie-columns. In phase 3 and 4 (drift = 0.06% and 0.08%, respectively) fine fissures started to appear in the masonry panel. At a 0.12% drift, stepped fissures appeared on the lower part of the panel. In phase 6 and 7 (drift = 0.16% and 0.23%, respectively), new fissures started to form in the upper corners of the wall. During phase 8 and 9 (drift = 0.32% and 0.45%, respectively), the first diagonal fissures started to appear in the panel. Finally, in phases 10 and 11 (drift = 0.63% and 0.83%, respectively), some masonry areas were detached due to crushing, while the diagonal fissures intensified. Fig. 11 shows the failure pattern for both walls, original and reinforced.

For the reinforced wall, the first fissures appeared at a 0.04% drift and were due to bending stress in the tie-columns. At a 0.16% drift, the first diagonal, stepped, fissures appeared on the masonry panel. At a 0.23% drift, quite a few fissures appeared from the corners of the wall. At a 0.45% drift, two

(a) Original (b) Reinforced

Fig. 9 Strengthening with CFRP

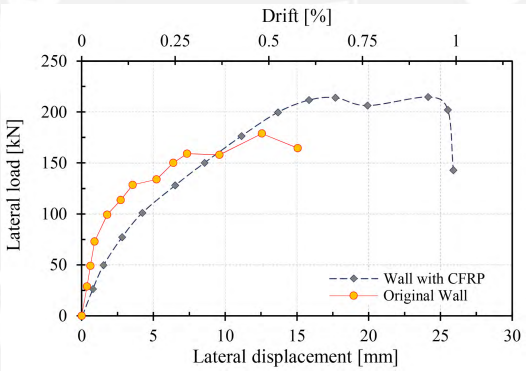

Fig. 10 Envelopes of hysteretic loops on walls with and without reinforcement CFRP

diagonal v-shaped fissures formed up to the lower part of the wall. During phases 10 and 11 (drift = 0.63% and 0.83%, respectively), the number of fissures was not increased, but rather the existing ones became more pronounced.

The stiffness of the reinforced wall reached 86% of the initial stiffness of the original wall. Similarly, the initial stiffness of the reinforced wall resulted in an increase of 6.5 times the final stiffness of the original wall. Fig. 12 shows the comparison of envelopes of hysteresis loops for both walls, original and reinforced. From Fig. 12 can be inferred that the corrugated steel mesh reinforcement was able to increase the loading capacity of the original wall by 21% and the ductility by 25%.

3.3.5 Galvanized steel fiber (SRG)

The first fissures, on the original wall, occurred at a 0.04% drift and were due to bending stress in the tie-columns. At a 0.08% drift, some of the fissures generated by bending stress in the lower part of the columns started to spread diagonally on the masonry panel. At a 0.12% drift, a horizontal fissure appeared in the lower part of the masonry panel. At a 0.16% drift, new diagonal fissures started forming from the upper corners of the wall. At a 0.23% drift, two of the diagonal fissures were intercepted in the lower part of the wall forming a V shape. In phases 8, 9 and 10 (drift = 0.32%,

(a) Original (b) Reinforced

Fig. 11 Strengthening with CSM

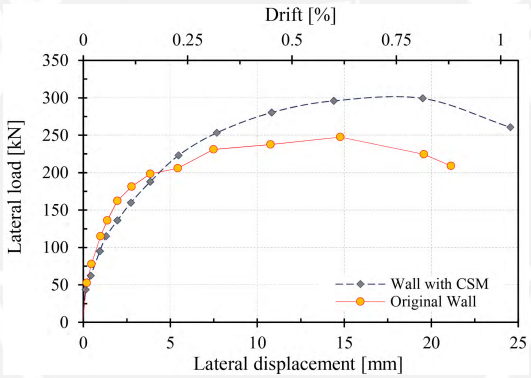

Fig. 12 Envelopes of hysteretic loops on walls with and without reinforcement CSM

0.45% and 0.63%, respectively), no new fissures appeared, but the existing ones intensified. Finally, at a 0.83% drift, a new fissure, not very long, appeared in the lower part of the wall. According to the evolution of fissures, although there were diagonal fissures, these were the result of the spreading of smaller fissures produced in previous phases, which is not typical of a failure by shear stress. Therefore, a failure of the wall by bending tress was predominant. Fig. 13 shows the failure pattern for both walls, original and reinforced.

The first fissures of the reinforced wall occurred at a 0.04% drift and were due to bending stress in the tie-columns. In phases 4 and 5 (drift = 0.08% and 0.12%, respectively) diagonal fissures started to appear on the masonry panel, at low and high heights, from the joint of the columns with the masonry towards the center of the wall. Some of them corresponded to the opening of repaired fissures of the original wall. At a 0.16% drift, no new fissures appeared, but the already existing ones intensified. At a 0.23% drift, two of the diagonal fissures intercepted on the lower part of the masonry panel, forming a V shape. Like the original wall, this is due to a generalized failure by bending stress in the reinforced wall. In phase 8, at a 0.32% drift, a new, not very long, diagonal fissure appeared on the masonry panel from the upper corner towards the center of the wall. From phase 9 (drift =

(a) Original (b) Reinforced

Fig. 13 Strengthening with SRG

0.45%), the opening of fissures started causing the surface detachment of the masonry. In phase 11, at a 0.83% drift, a new diagonal fissure appeared in the opposite direction to the one mentioned in phase 8. This fissure was indeed generated along one of the diagonals of the wall, so it is associated to a failure by shear stress. Finally, at a 1.25% drift, the diagonal fissures, generated in phases 8 and 11, intercepted forming an X shape.

The stiffness of the reinforced wall reached 55% of the initial stiffness of the original wall. Similarly, the stiffness of the reinforced wall resulted in an increase of 8.4 times the final stiffness of the original wall. Fig. 14 shows the comparison of envelopes of hysteresis loops of both walls, original and reinforced. From Fig. 14 can be inferred that the corrugated steel mesh reinforcement was able to increase loading capacity of the wall only by 4% and the ductility by 50%.

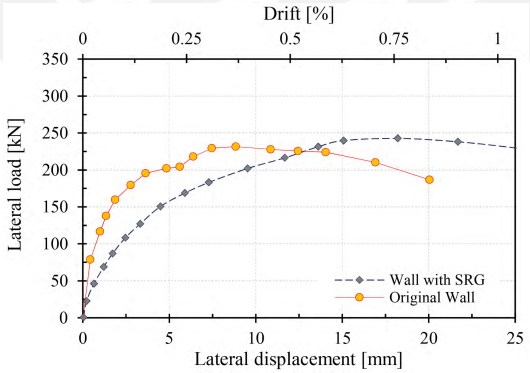

Fig. 14 Envelopes of hysteretic loops on walls with and without reinforcement SRG

4. Seismic Performance of the alternatives

The idea of reinforcing a structural element comes from trying to restore o increase some of its seismic resistance parameters. As shown in the item before, the more relevant effects of using a

reinforcing technique can be to restore the initial stiffness, or a good percentage of the same, to regain the load capacity or gain a greater one, to show a greater ductility, or just develop a combination of these.To restore the initial stiffness will help the wall receive once again the same seismic load that led to its collapse. A greater load capacity will allow the wall to have a greater resistance to the displacements imposed by an earthquake. A greater ductility will help the wall dissipate larger seismic energy, which in turn will help reduce the damage in vulnerable structural elements. It is important to ascertain the right combination of parameters for each building.

There are several factors that can influence the response of the wall, some of them have been shown in Table 3, such as the type of unit employed in the construction of the walls, the axial compression resistance $f'm$ in masonry, as well as the resistance to shear stress $v'm$. Also, another factor that directly influences the response of the wall is the H/L ratio. It was observed that all the walls show almost the same geometry, therefore, this factor does not imply that there exists a high level of dispersion in the responses of the walls tested. Additionally, each wall presented different methods to connect confinement elements and masonry panel, and presented different quantity of reinforcement as was mentioned in Section 3.1. Moreover, in this same section, the reinforcement configuration of each technique which leads to different quantity of reinforcement material and the additional thickness that each technique provides to the wall were also discussed as wall's characteristics that influence on its final behavior. Finally, it is worth highlighting that the initial condition of the reinforced walls testing, i.e. not all original walls were tested until the same drift, affects the final response of each wall favoring some and others not. For instance, SRG wall was tested until the failure (drift=0.833%) while WM wall was tested until a drift equal to 0.521%.

The aforementioned characteristics of the walls imply that the strengthening techniques showed in this work can not be compared directly. Hence, a multi-criteria decision making (MCDM) for a massive seismic retrofitting of masonry walls was done in Section 6. Within MCDM approach, a technical effectiveness was taken account thus Table 5 shows the improvement in terms of initial stiffness (K_0), load capacity (P_{max}), ductility in terms of maximum displacement (δ) for each reinforcement technique. It is worth pointing out that the initial stiffness was computed in the third phase for each case in order to have a representative value due to a possible adjustment of instrumentation during the first phases. From Table 5, it is noted that WM and CSM techniques recovered approximated an 87% of the initial stiffness but much of this is due to the reparation process and the remaining is due to these techniques which increase 5 cm the total thickness of the wall. Techniques as GFRP, CFRP and SRG recovered approximated 55% of the initial stiffness, which can be attributed almost in total to the reparation process since these technique almost does not increase wall's thickness.

Since the quantity of reinforcement is different, it is crucial to understand the influence that it may entail in the final load-response considering maximum strength of the strengthened element and of the reinforcing material. Hereafter, a mechanical ratio can be calculated as follows:

$$\omega = \frac{A_s \,.\, f_s}{f_m \,.\, b \,.\, s} \tag{1}$$

where A_s represents the area of the strengthening material, f_s is the experimental tensile strength of the reinforcement system, f_m is equal to the experimental shear strength of masonry, s is the space between reinforcing materials of width b . Table 6 lists the mechanical ratios. It is observed that CFRP and SRG have lower values than WM, GFRP and CSM which means that even with less

Table 5 Comparison of earthquake–resistant parameters of walls with and without reinforcement

Technique	Parameter	Original [O]	Reinforced [R]	Ratio [R/O]
WM	K_0 $[kN/mm]$	96.94	86.31	89%
	P_{max} $[kN]$	208.40	286.90	138%
	δ $[mm]$	12.50	17.50	140%
GFRP	K_0 $[kN/mm]$	63.24	35.92	57%
	P_{max} $[kN]$	203.10	209.90	103%
	δ $[mm]$	20.00	20.00	100%
CFRP	K_0 $[kN/mm]$	62.48	32.94	53%
	P_{max} $[kN]$	177.80	213.60	120%
	δ $[mm]$	15.00	25.00	167%
CSM	K_0 $[kN/mm]$	96.79	83.57	86%
	P_{max} $[kN]$	246.60	298.00	121%
	δ $[mm]$	20.00	25.00	125%
SRG	K_0 $[kN/mm]$	98.27	54.11	55%
	P_{max} $[kN]$	230.62	240.87	104%
	δ $[mm]$	20.00	30.00	150%

Table 6 Mechanical ratio for strengthening techniques

	WM	GFRP	CFRP	CSM	SRG
A_s $[mm^2]$	44.98	61.36	33.00	49.07	16.08
f_s $[MPa]$	600	827	3800	618	2838
f_m $[MPa]$	1.67	1.57	0.92	1.25	1.25
b $[mm]$	4.5	6.25	100	4.70	100
s $[mm]$	150	400	600	150	400
ω	23.94	12.93	2.27	34.41	0.95

quantity of material of a certain tensile strength, CFRP and SRG provide good results in terms seismic parameters as shown Table 5. Thus a technically effective reinforcing system with a low value of ω is the best option.

5. Cost-effectiveness of the alternatives

The economical aspect was made taking into account the cost of construction, repair and reinforcement of a typical CM wall. Even though the construction and repair cost is independent from the reinforcing technique, they are being considered in order to have an idea of ratio of the repair and reinforcement cost against the construction. In addition, economical aspect is important since this paper pretends to recommend a strengthening technique able to be applied massively. Each process includes the cost of materials and labor.

The cost of materials was calculated taking into account the actual Peruvian market. Among the most

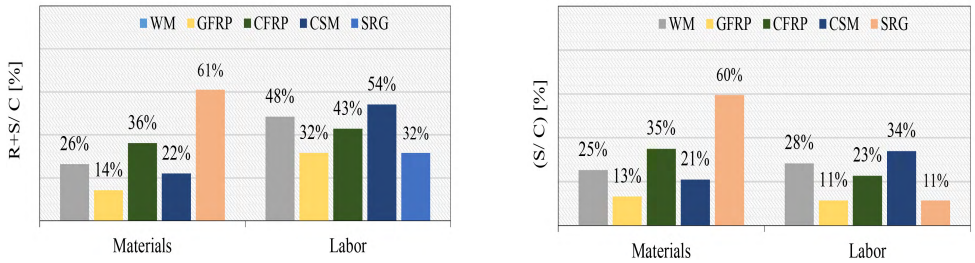

Fig. 15 Incidence of reinforcing costs: (a) failed walls and (b) new walls

used materials there is the type I portland cement with a cost per $[ft^3]$ of \$/.6.50, fine sand with a cost per $[m^3]$ of \$/.14.00, coarse sand with a cost per $[m^3]$ of \$/.15.50, wire # 8 and wire # 16 both with a cost per $[kg]$ of \$/.1.50. The cost of the reinforcement with ME was governed by the cost of the welded mesh that was \$/.61.50, of the GFRP for the fiberglass with a cost per unit of \$/.12.00. The CFRP was composed of 4 components: carbon fiber with a cost per $[m^2]$ of \$/.82.50, a Primer component with a cost per $[kg]$ of \$/.24.50, a Putty component with a cost per $[kg]$ of \$/.10.00 and a Saturant component with a cost per $[kg]$ of \$/.12.50. The SRG was composed of two components: the galvanized steel fiber with a cost per meter of mesh of \$/.17.00 and a natural lime mortar with a cost per bag of 25 $[kg]$ of \$/.22.00 .

For the cost of labor, in all reinforcement process, a crew of an operator and one assistant has been used. The base cost of an 8 hour day for an operator is \$31.00 and an assistant, \$22.00. The total time depends of the type of reinforcement. For example, using welded wire mesh, it was 2.5 days, with glass fiber 1 day, with carbon fiber 2 days, with corrugated steel mesh 3 days, and with SRG 1 day.

From Table 7, we can establish the incidence percentage that repairing and reinforcing a wall has against the cost of building it. This may be required in case of evaluating the reinforcement of a wall already cracked wall (Fig. 15(a)). If we add the incidence percentages of materials and labor, we observe that repair and reinforcement with WM represents 74%, GFRP 45%, CFRP 79%, CSM 76% and SRG 92% of what it can cost to build the same wall. It is also possible to establish incidence percentages of the reinforcement against the cost of construction. This may be required in case of reinforcement a new or an intact wall (Fig. 15(b)). In this case, if we add the incidence percentage of materials and labor, we see that reinforcing with WM represents 53%, GFRP 24%, CFRP 58%, CSM 55% and SRG 71% of what it cost to build the wall.

It must be noted that before reinforcing new walls, it is required a technical evaluation of the most vulnerable walls against a seismic event. It is not necessary to reinforce all the walls of a building. Additionally, the reinforcement techniques have shown an improvement in the seismic-resistant parameters of the CM walls, however, they must be properly applied. Therefore, the personnel in charge of reinforcement should have been properly trained.

Table 7 Costs summary for each technique (price in $ at Nov 2018)

Technique	Construction [C]	Reparation [RP]	Reinforcement [RF]
WM	**462.00**	**98.00**	**248.00**
Materials	277.00	5.00	117.00
Labor	185.00	93.00	131.00
GFRP	**462.00**	**98.00**	**114.00**
Materials	277.00	5.00	61.00
Labor	185.00	93.00	53.00
CFRP	**462.00**	**98.00**	**267.00**
Materials	277.00	5.00	162.00
Labor	185.00	93.00	105.00
CSM	**462.00**	**98.00**	**254.00**
Materials	277.00	5.00	97.00
Labor	185.00	93.00	157.00
SRG	**462.00**	**98.00**	**328.00**
Materials	277.00	5.00	275.00
Labor	185.00	93.00	53.00

6. Multicriteria decision analysis

In Section 4 and 5, it was presented a technical and economical evaluation for each strengthening technique, however, based on the results, it is not easy to decide which alternative is the best for a massive use in Peru. Multi-Criteria Decision Making (MCDM) methods are commonly employed to solve similar problems occurring in several fields (i.e. natural resources management, medical treatment choices, resources allocation planning) (Caterino *et al.* 2006). MCDM evaluates multiple conflicting criteria in decision making. In the following of the paper the application of the MCDM TOPSIS (Technique for Order Preference by Similarity to Ideal Solution) method (Hwang and Yoon 1981) for the reinforcement of Peruvian confined masonry is discussed.
The criteria taken into account are stiffness (C_1), strength (C_2), ductility (C_3), mechanical ratio (C_4), installation cost (C_5), total cost (C_6), duration of application (C_7), aesthetics (C_8), durability (C_9), compatibility (C_{10}), and the initial test condition in regards of drift (C_{11}). The last parameter C_{10} follows the criterion of considering that not all the walls were brought to a reparability limit before being repaired and reinforced.

6.1 Importance of each criterion

In order to take into account the relative importance of each criterion, the definition of the weight w_i is needed, which references to the criterion C_i. The method used here is based in eigenvalue's theory (Saaty 1994) and allows to calculate the weight, starting with the matrix A, in which each element a_{ij} is the relative importance of the C_i criteria in regards to C_j expressed in a scale of 1 to 9 degrees (Table 8). In that scale, the values 1, 3, 5, 7, 9 mean equal, moderate, essential, demonstrated, extreme importance of one criterion with respect to another. The values 2,4,6,8 are of intermediate

Table 8 Scale of relative importance Saaty (1994)

Intensity of Importance	Definition	Explanation
1	Equal importance.	Two activities contribute equally to the objective.
3	Moderate importance of one to another	Experience and judgment slightly favour one activity over another
5	Essential or strong importance	Experience or judgment strongly favours one activity over another
7	Demonstrated importance	An activity is strongly favoured and its dominance is demonstrated in practice
9	Extreme importance	The evidence favouring one activity over another is of the highest possible order of affirmation
2, 4, 6, 8	Intermediate values between the two adjacent judgments	When compromise is needed
Reciprocal of above	If criterion i compared to j gives one of the above then j, when compared to i gives its reciprocal	

importance between the two adjacent judgments.

The values of the resulting matrix A shown in Eq. 2 obey the scale of Saaty (Saaty 1994) and the values are based on personal judgment. For instance, it is assumed that the installation cost (C_5) is as important as the time of application (C_7) since both are directly related.
As a_{ij} depends on the relation w_i/w_j (w_i and w_j real weights of importance of the criteria C_i y C_j, respectively), the eigenvector W of A is formed by the sought weights w_1, w_2, ..., w_{11}, which are shown in Eq. 3. From Eq. 3 results that the C_4 (mechanical ratio) and C_{11} (initial test condition) criterion are more important with weight equal to 0.196; the criterion less important is C_8 (aesthetics) with weight $w_8 = 0.017$.

$$A = \begin{bmatrix} a_{11} & a_{12} & \cdots & a_{1\,11} \\ a_{21} & a_{22} & \cdots & a_{2\,11} \\ \vdots & \vdots & \ddots & \vdots \\ a_{11\,1} & a_{11\,2} & \cdots & a_{11\,11} \end{bmatrix} = \begin{bmatrix} 1 & 1 & 1 & 1/2 & 4 & 5 & 4 & 6 & 3 & 3 & 1/2 \\ 1 & 1 & 1 & 1/2 & 4 & 5 & 4 & 6 & 3 & 3 & 1/2 \\ 1 & 1 & 1 & 1/2 & 4 & 5 & 4 & 6 & 3 & 3 & 1/2 \\ 2 & 2 & 2 & 1 & 5 & 6 & 5 & 7 & 4 & 4 & 1 \\ 1/4 & 1/4 & 1/4 & 1/5 & 1 & 2 & 1 & 3 & 1/3 & 1/3 & 1/5 \\ 1/5 & 1/5 & 1/5 & 1/6 & 1/2 & 1 & 1/2 & 2 & 1/4 & 1/4 & 1/6 \\ 1/4 & 1/4 & 1/4 & 1/5 & 1 & 2 & 1 & 3 & 1/3 & 1/3 & 1/5 \\ 1/6 & 1/6 & 1/6 & 1/7 & 1/3 & 1/2 & 1/3 & 1 & 1/5 & 1/5 & 1/7 \\ 1/3 & 1/3 & 1/3 & 1/4 & 3 & 4 & 3 & 5 & 1 & 1 & 1/4 \\ 1/3 & 1/3 & 1/3 & 1/4 & 3 & 4 & 3 & 5 & 1 & 1 & 1/4 \\ 2 & 2 & 2 & 1 & 5 & 6 & 5 & 7 & 4 & 4 & 1 \end{bmatrix} \tag{2}$$

$$W = \{w_1, w_2, ..., w_{10}\} = \{0.125, 0.125, 0.125, 0.196, 0.033, 0.023, 0.033, 0.017, 0.063, 0.063, 0.196\} \tag{3}$$

Table 9 Decision Matrix

	C_1 [%]	C_2 [%]	C_3 [%]	C_4 [unit]	C_5 [%]	C_6 [%]	C_7 [days]	C_8 [mm]	C_9 [unit]	C_{10} [unit]	C_{11} [%]
WM	89	38	40	23.94	48	74	2.5	25	0.5	0.6	0.521
GFRP	57	3	0	12.93	32	46	1	0	0.7	0.7	0.769
CFRP	53	20	67	2.27	43	79	2	4	0.9	0.5	0.577
CSM	86	21	25	34.41	54	76	3	25	0.5	0.7	0.450
SRG	55	4	50	0.95	32	93	1	10	0.85	0.9	0.833

6.2 Ranking of the reinforcement alternatives

On the other hand, it must also take into account the yield x_{ij} of the i-th alternative (i = 1, 2, 3, 4, 5) in terms of the j-th criteria (j = 1, 2, ... , 10), which together make up the so-called decision matrix D = $[x_{ij}]$ (Table 9). For C_1 the percentage of stiffness recovered was evaluated, for C_2 and C_3 the increase in strength and ductility was evaluated against the original wall (see Section 4). C_4 points out the mechanical ratio presented in Section 4 as well. For C_5 and C_6 it was considered the percentage representing the cost of repairing and reinforcing a failed wall with against its construction cost (see Section 5). For C_7, indicates the days of delay in applying each technique (Section 5), for C_8 it was quantified the aesthetics, as the additional thickness that each technique adds to one side of the wall (Section 3.1). The durability to external agents C_9 and compatibility C_{10} were quantified by experts. For instance, SRG is more durable in alkaline environment due to the lime-based mortar and steel cords that are galvanized. CFRP presents also a good performance in terms of durability (Gattesco and Boem 2017). SRG is more compatible with the masonry for its lime-based mortar with a low elastic modulus which matches that of the substrate. Conversely, the epoxy resin of CFRP is not compatible with the masonry. Finally C_{10} indicates the final drift in tests of the non-reinforced wall (Section 3.3).

The first step of the ranking procedure is to normalize all x_{ij} values that have a different dimension. This normalization is carried out according to Eq. 4. The next step is to give weights to this matrix R (formed by r_{ij}) by multiplying each i-th column by the weight w_i of the i-th criterion, obtaining the matrix (5).

$$r_{ij} = \frac{x_{ij}}{\sqrt{\sum_{k=1}^{5} x_{kj}^2}} \tag{4}$$

$$A = \left[v_{ij}\right] = \left[w_j r_{ij}\right] = \begin{bmatrix} 0.071 & 0.099 & 0.052 & 0.107 & 0.017 & 0.010 & 0.018 & 0.012 & 0.020 & 0.025 & 0.071 \\ 0.046 & 0.008 & 0.000 & 0.058 & 0.011 & 0.006 & 0.007 & 0.000 & 0.028 & 0.029 & 0.104 \\ 0.043 & 0.052 & 0.088 & 0.010 & 0.015 & 0.011 & 0.014 & 0.002 & 0.034 & 0.021 & 0.078 \\ 0.069 & 0.055 & 0.033 & 0.153 & 0.019 & 0.010 & 0.022 & 0.012 & 0.020 & 0.029 & 0.061 \\ 0.044 & 0.010 & 0.065 & 0.004 & 0.011 & 0.013 & 0.007 & 0.005 & 0.036 & 0.037 & 0.113 \end{bmatrix} \tag{5}$$

The TOPSIS method indicates that the best alternative is the one that has the least distance to the ideal solution A^* and the greater distance to the ideal negative solution y A^-. The vector A^* is

Table 10 Relative closeness C_{i^*} of each alternative

WM	A_1	0.500
GFRP	A_2	0.434
CFRP	A_3	0.720
CSM	A_4	0.267
SRG	A_5	0.644

obtained by taking for each criterion the best performance value among A_1,.., A_5; the ideal negative solution A^- is composed of the worst performances.

$$A^* = \{0.071, 0.099, 0.088, 0.004, 0.011, 0.006, 0.007, 0.000, 0.036, 0.037, 0.113\} \tag{6}$$

$$A^- = \{0.043, 0.008, 0.000, 0.153, 0.019, 0.013, 0.022, 0.012, 0.020, 0.021, 0.061\} \tag{7}$$

If S_{i^*} and S_{i^-} are the Euclidean distances of the i-th alternative A_i from the ideal solutions and negative ideals A^* and A^-, respectively, the relative closeness C_{i^*} $(0 \leq C_{i^*} \leq 1)$ of A_i with respect to the A^* it is defined as:

$$C_{i^*} = \frac{S_{i^-}}{S_{i^*} + S_{i^-}} \tag{8}$$

The final results are listed in Table 10. According to the TOPSIS method, the best alternative is the one with the greater C_{i*} value. In this way, CFRP and SRG are the most appealing techniques, and it seems to be that the criteria C_4 and C_{11} strongly influences on these results. Both techniques have a low value of mechanical ratio and provided good results in terms of seismic parameters. In addition, it is evident that despite original SRG wall was failed (drift=0.833%) before the reinforcement process, this technique continues improving seismic parameters. Likewise, advantages related to SRG as durability and compatibility with masonry have led to rank SRG as a one of the most appealing.

7. Conclusions

Due to Peru is a high seismic zone and it is prone to be struck by an earthquake which can cause human and material loses, in this paper different systems have been studied for Peruvian confined masonry structures with the aim of recommending one technique that complies with many aspects such as economical, technical, among others for a mass use plan. The reinforcing techniques were the welded mesh system (WM), Glass and Carbon Fiber Reinforced Polymer(GFRP and CFRP), corrugated steel meshes (CSM) and Steel Reinforced Grout (SRG). The strengthening of Peruvian confined masonry through traditional (WM, CSM) or innovative (GFRP, CFRP, SRG) techniques presented interesting aspects and results have been pointed out.

Each of these technique have shown different effects on the seismic parameters (stiffness, load capacity and ductility). It has been highlighted that traditional techniques as WM and CSM recovered approximated an 87% of the initial stiffness but a part of this is due to the reparation process and the remaining is due to the increasing of the wall's thickness in 5 cm that is provided by both techniques. In case of GFRP, CFRP and SRG, a stiffness recovering of approximated 55% was computed, which

can be attributed almost in total to the reparation process since these technique almost does not increase wall's thickness. In terms of load capacity and ductility, all techniques developed a good performance increasing both parameters.

The economy of the population have been taken account in order to propose a type of reinforcement among the five aforementioned for a mass use plan, this study is an effort towards it and presents how the MCDM method is effective for the decision making. The applied TOPSIS method allowed the qualification of the performance of each alternative through 10 criteria, which are not only related to the improvement of seismic-resistant parameters but also cost-effectiveness. Another criteria were also taken into account as the reinforcement configuration by means of mechanical ratio, the duration of application, aesthetics, durability, compatibility, and the initial test condition.

Among the five presented alternatives and the indicated criteria, the best solutions turn out to be the Carbon Fiber Reinforced Polymer (CFRP) and Steel Reinforced Grout (SRG). Hence, CFRP and SRG are the reinforcements of massive, fast and effective application. Likewise, it is important to mention that it is not necessary to reinforce all the walls of a building. In case of cracked walls, it is evident that they were major structural elements so they must be repaired and reinforced without doubt. In case of new buildings or without structural damage, a technical evaluation must be carried out in order to identify the main structural elements. However, the proper training of the people in charge of the application of these reinforcement systems is recommended.

References

Alcocer, S., Arias, J. and Vazquez, A. (2003), "The new Mexico City building code requirements for design and construction of masonry structures", *Proc Ninth North American Masonry Conference, Clemson, South Carolina*, 656-667.

Bhattacharya, S., Nayak, S. and Chandra, S. (2013), "A critical review of retrofitting methods for unreinforced masonry structures", *International Journal of Disaster Risk Reduction*, 51-67.

Brzev, S. and Perez, J. (2014), "Masonry Construction around the world: an overview", *Short Course on Seismic Design of Reinforced and Confined Masonry Buildings*.

Buchan, P. and Chen, J. (2007), "Blast resistance of FRP composites and polymer strengthened concrete and masonry structures: A state of the art review", *Composites Part B: Engineering*, **38**, 509-522.

Cabral-Fonseca, S., Correia, J.R., Custódio, J., Silva, H.M., Machado, A.M. and Sousa, J. (2018), "Durability of FRP - concrete bonded joints in structural rehabilitation: A review", *International Journal of Adhesion and Adhesives*, **83**, 153 - 167.

Carloni, C. (2017), "Prove di compressione diagonale per la valutazione dell'efficacia di rinforzi strutturali applicati su pannelli murari di laterizio e malta di calce. Convenzione di ricerca con kerakoll spa rapporto di prova", *Universita di Bologna*.

Caterino, N., Iervolino, I., Manfredi, G. and Cosenza, E. (2006), "MULTI-CRITERIA DECISION MAKING FOR SEISMIC RETROFITTING OF AN UNDERDESIGNED RC STRUCTURE", *First European Conference on Earthquake Engineering and Seismology (a joint event of the 13th ECEE 30th General Assembly of the ESC), Geneva, Switzerland*.

Corradi, M., Borri, A. and Vignoli, A. (2002), "Strengthening techniques tested on masonry structures struck by the Umbria–Marche earthquake of 1997–1998", *Composites Part B: Engineering*, **16**, 229–239.

De Santis, S., Ceroni, F.G., De Felice, G., Fagone, M., Ghiassi, B., Kwiecie, A., Lignola, G.P., Morganti, M., Santandrea, M., Valluzzi, M.R. and Viskovic, A. (2017), "Round Robin Test on tensile and bond behaviour

of Steel Reinforced Grout systems", *Composites Part B: Engineering*, **127**, 100 - 120.

FEMA. (2009), "Unreinforced Masonry Buildings and Earthquakes: Developing Successful Risk Reduction Programs", *Federal Emergency Management Agency*.

Gattesco, N. and Boem, I. (2017), "Characterization tests of GFRM coating as a strengthening technique for masonry buildings", *Composite Structures*, **165**, 209–222.

Ghiassi, B., Oliveira, D., Marques, V., Soares, E. and Maljaee, H. (2016), "Multi-level characterization of steel reinforced mortars for strengthening of masonry structures", *Journal Materials Design*.

Hwang, C.L. and Yoon, K. (1981), "Multiple Attribute Decision Making", *Lecture Notes in Economics and Mathematical Systems*.

INEI (1981), "Perfil sociodemográfico del Perú: Censos Nacionales 2007: XI de población y VI de vivienda".

Lodi, S., Alam, N. and Ahmed, M. (2014), "Seismic Vulnerability Assessment of Existing Buildings of Pakistan, Earthquake Model for Middle East Region (EMME)", *Department of Civil Engineering, NED University of Engineering & Technology, Karachi, Pakistan*.

Lowman, P. and Montgomery, B. (1998), "Preliminary determination of epicentres (of) 358,214 events (between) 1963 and 1998", *NASA image obtained from http://denali.gsfc.nasa.gov/dtam/ seismic/*.

Lujan, M. and Tarque, N. (2016), "Refuerzo de muros de albañilería confinada con mallas de acero", *Fondo Editorial PUCP, Lima*.

NTP E.070. (2006), "Reglamento Nacional de Edificaciones: Albañilería", *Ministerio de Vivienda, Construcción y Saneamiento - SENCICO*.

Popa, V., Pascu, R., Papurcu, A. and Albota, E. (2016), "Retrofitting of squat masonry walls by FRP grids bonded by cement-based mortar", *Earthquakes and Structures*, **10**(1), 125-139.

Remki, M., kehila, F., Bechtoula, H. and Bourzam, A. (2016), "Seismic vulnerability assessment of composite reinforced concrete-masonry building", *Earthquakes and Structures*, **11**(2), 371-386.

Salsavilca, J., Yacila, J., Tarque, N. and Camata, G. (2019), "Experimental and Analytical Bond Behavior of Masonry Strengthened with Steel Reinforced Grout (SRG)", *sent manuscript*.

San Bartolomé, A. and Castro, A. (2002), "Reparación de un muro de albañilería confinada mediante malla electrosoldada", *Fondo Editorial PUCP, Lima*.

San Bartolomé, A. and Loayza, J. (2004), "Reparación y reforzamiento con varillas de fibra de vidrio en un muro de albañilería confinada", *Fondo Editorial PUCP, Lima*.

San Bartolomé, A. and Coronel, C. (2009), "Reparación y y reforzamiento de un muro de albañilería confinada mediante fibra de carbono", *Fondo Editorial PUCP, Lima*.

Saaty, T. (1994), "How to Make a Decision: The Analytic Hierarchy Process", *INTERFACES*, **24**(6), 19–43.

Smyrou, E. (2015), "FRP versus traditional strengthening on a typical mid-rise Turkish RC building", *Earthquakes and Structures*, **9**(5), 1069-1089.

Srechai, J., Leelataviwat, S., Wongkaew, A. and Lukkunaprasit, P.(2017), "Experimental and analytical evaluation of a low-cost seismic retrofitting method for masonry-infilled non-ductile RC frames", *Earthquakes and Structures*, **12**(6), 699-712.

Yacila, J., Salsavilca, J., Tarque, N. and Camata, G. (2019), "Experimental assessment of confined masonry walls retrofitted with SRG under lateral cyclic loads", *sent manuscript*.

Yepes-Estrada, C., Silva, V., Valcárcel, J., Acevedo, A., Tarque, N., Hube, M.A., Coronel, G. and María, H.S. (2017), "Modeling the residential building inventory in South America for seismic risk assessment", *Earthquake Spectra*, **33**(1), 299-322.

ANEXOS

Anexo A

Análisis del uso de 4 alternativas de refuerzo sísmico en muros de albañilería confinada

XXXVIII Jornadas Sudamericanas de Ingeniería Estructural Lima 2018

La Ingeniería Estructural: puente para el desarrollo e integración de América y el mundo

Id: XXXVIIIJSIE-03-015

ANÁLISIS DEL USO DE 4 ALTERNATIVAS DE REFUERZO SÍSMICO EN MUROS DE ABAÑILERÍA CONFINADA

ANALYSIS OF THE USE OF 4 SEISMIC REINFORCEMENT ALTERNATIVES IN CONFINED MASONRY WALLS

Jhoselyn Salsavilca (1); Jhair Yacila (2); Nicola Tarque (3) (P); Alfredo Manchego (4)

(1) Est. Maestría de Ing. Civil, Asistente de investigación, Pontificia Universidad Católica del Perú, Lima, Perú.
(2) Est. Maestría de Ing. Civil, Asistente de investigación, Pontificia Universidad Católica del Perú, Lima, Perú.
(3) Prof., Pontificia Universidad Católica del Perú, Lima, Perú.
(4) Msc. Ing. Civil, Pontificia Universidad Católica del Perú, Lima, Perú
Dirección para correspondencia: sntarque@pucp.edu.pe; (P) Presentador

Área Temática: Área 3 Reparación y reforzamiento

Resumen

En Perú, la construcción con albañilería confinada (AC) tiene un alto porcentaje en muchos sectores de la población. Se estima que solo en Lima el 75% de las construcciones son de AC y al menos el 70% de estas son informales. Es decir que son hechas sin asesoramiento técnico y por lo general tienen un alto grado de vulnerabilidad sísmica. Una forma de reducir esta vulnerabilidad es mediante el reforzamiento de los muros. Sin embargo, y a pesar de existir en el mercado diversas metodologías de reforzamiento, no todas pueden ser de aplicación masiva ya que hay otro factor importante: la posibilidad de que la población pueda pagar por este reforzamiento. Por ello, en este trabajo se hace un análisis del uso de cuatro metodologías de reforzamiento (fibra de vidrio, malla electrosoldada, fibra de carbono, malla de acero) estudiadas en Perú. Se recopiló información de los ensayos de los muros de AC con y sin refuerzo a escala natural ante cargas cíclicas en su plano. Se discute el aporte de cada sistema en términos de rigidez, capacidad de carga y ductilidad, y sobre todo cuál es el costo de influencia para la ejecución del reforzamiento. Los primeros resultados indican que el acero y fibra de carbono como material de refuerzo brinda mejores resultados técnicos, sin embargo, su costo es elevado a comparación del sistema de fibra de vidrio. De este modo, aún resulta dificultoso identificar un solo sistema de reforzamiento que cumpla los requisitos de factibilidad técnica y económica, para que pueda ser aplicado masivamente.

Palabras-clave: Albañilería confinada, reforzamiento, factibilidad técnica, factibilidad económica

Abstract

In Peru, the construction based on confined masonry (CM) has a high percentage in many sectors of the population. Around 75% of constructions in Lima are of this typology, which is not a problem, but at least 70% of them are informal. In other words, these constructions are built without technical advices; hence, they have a high seismic vulnerability. One way to reduce this vulnerability is by reinforcing the walls. In fact, different reinforcement methodologies with a good performance to stand loads have been developed and studied in previous researches. However, not all can be of massive application due to the possibility of the population to pay for these reinforcements. Therefore, this work presents an analysis of four reinforcement methodologies (glass fiber, welded mesh, carbon fiber, steel mesh) studied in Perú. Technical information about the response of unreinforced and reinforced wall is gathered subjected to lateral loads. For each system, its contribution is discussed in terms of rigidity, load capacity and ductility, and above all, what is the influence cost for its application. Preliminary results indicate that the steel and carbon fiber as reinforcement material provides better technical results; however, its cost is higher than the glass fiber system. In this way, it is still difficult to identify a unique reinforcement system that meets the requirements of technical and economic feasibility to be applied massively.

Keywords: Confined masonry, reinforcement system, technical feasibility, economical feasibility

1. INTRODUCCION

Las construcciones de albañilería confinada son consideradas una de las más populares a nivel mundial por su fácil y rápida construcción. Específicamente, su uso es común en el centro y sur de América, sureste de Europa, India y otras partes de Asia (Bhattacharya et al. 2013). Según Alcocer et al. (2003), en México hasta el año 2003, más del 70% de sus construcciones eran de albañilería. En Pakistán, el 62.38% de las edificaciones totales son de albañilería (Lodi et al. 2012). Otro caso es Perú cuyas estadísticas muestran que el tipo de vivienda predominante es la casa independiente en un 86%, y se ha identificado que la albañilería confinada, hecha con unidades de arcilla cocida (ladrillo), es el material preferido para construir sus viviendas (Yepes-Estrada et al. 2017).

Dependiendo de la formalidad en obra, calidad del personal técnico, características propias de la estructura y otros parámetros, la vulnerabilidad sísmica asociada a estas construcciones es mayor, lo que se traduce en mayor riesgo. Evidentemente, las características geológicas no se pueden variar para reducir la actividad sísmica de la zona de estudio, pero la vulnerabilidad sí se puede disminuir pues se asocia a las propiedades intrínsecas de la edificación. Por lo tanto, nace la necesidad de plantear qué medidas deberían optarse para reducir esta vulnerabilidad sísmica en las construcciones de albañilería informal. Una medida consiste en realizar constantes investigaciones sobre los posibles sistemas de reparación y reforzamiento para muros de albañilería confinada con el objetivo de mejorar el desempeño sismorresistente. Varios estudios en este campo ya han sido realizados en distintas universidades, y en este trabajo se presenta un análisis del uso de 4 alternativas de reforzamiento.

Las 4 técnicas de reforzamiento que se presentan en este trabajo son algunas de las más relevantes realizadas en el Perú. Estas técnicas utilizan el refuerzo con el polímero reforzado con varillas de vidrio (San Bartolomé and Loayza, 2004), la malla electrosoldada (San Bartolomé and Castro, 2002), el polímero reforzado con fibra de carbono (San Bartolomé and Coronel, 2009) y las mallas de acero (Lujan, 2016). Cada uno de estos refuerzos fue aplicado a muros de albañilería confinada a escala natural, previamente ensayados hasta derivas cercanas al límite de reparabilidad en el laboratorio de estructuras de la Pontifica Universidad Católica del Perú. Se ha descrito las características de cada refuerzo y su proceso de aplicación. Además, el aspecto técnico se discute analizando la envolvente de las curvas histeréticas. Es así que se ha estudiado la mejora que presenta cada sistema de reforzamiento en las propiedades sismorresistentes como rigidez, capacidad de carga o resistencia y ductilidad en los muros. Por otro lado, el aspecto económico se discute en términos de mano de obra y materiales para cada sistema. Además para estandarizar el impacto que significa reforzar con una determinada técnica, se evaluó el costo que implica reforzar respecto a la construcción de un muro. Los precios se cotizaron en base al mercado peruano.

2. DESCRIPCIÓN DE LAS 4 ALTERNATIVAS DE REFUERZO

2.1. Acero como material de refuerzo: malla electrosoldada (ME) y malla de acero (MAC)

En el área de las técnicas de reforzamiento más estudiadas por mucho tiempo, el acero ha sido considerado como un tipo de material de refuerzo que resuelve los daños en estructuras de albañilería existentes. Este ha aparecido como material principal en distintos sistemas de refuerzo como encamisado, malla electrosoldada, sistema de cables, malla de acero. La técnica de malla electrosoldada consiste básicamente en un arreglo de varillas de acero corrugado con diámetro de 4,5mm y espaciadas cada 150mm. Este arreglo se coloca a ambas caras de los muros interconectándolas con alambres #8 a través de perforaciones previas en la sección de los muros. Luego se enluce la superficie con mortero hasta obtener 25mm de espesor adicional. Por otro lado,

la técnica de mallas de acero consiste en preparar una malla de varillas de acero con diámetro de 4.7mm. Las mallas se interconectan a través de perforaciones hechas en la sección del muro con alambre # 8 y se amarran contra los nudos de las mallas a ambos lados con alambre #16. Así como para la técnica anterior, se enluce el muro de modo que no exceda 25 mm de espesor en cada lado. La diferencia entre ambos procedimientos radica en la elaboración de las mallas, mientras la malla electrosoldada es un refuerzo prefabricado, la malla de acero se elabora in situ.

2.2. FRP como sistema de refuerzo: fibra de carbono (CFRP) y vidrio (GFRP)

Los sistemas CFRP y GFRP (polímeros reforzados con fibra de carbono y vidrio) consisten en fibras de alta resistencia impregnadas en una matriz polimérica (resina epóxica de dos componentes). Es recomendada por las excelentes propiedades de los compuestos como la fibra de vidrio, carbono, basalto entre otros.

Tanto CFRP y GFRP son de fácil y rápida aplicación. El primer método está compuesto por una lámina de fibra de carbono unidireccional de muy alta resistencia y liviana (densidad superficial = 0.3 kg/m^2) que se embebe en tres tipos de resinas. El sistema CFRP consiste en aplicar el primer compuesto epóxico (Primer) sobre la superficie de mampostería que funciona como imprimante para sellar los poros y otra pasta epóxica (Putty) para nivelar la superficie. Luego, la fibra de carbono se coloca para que finalmente sea revestida por el tercer tipo de resina epóxica (Saturant) que encapsula las fibras. El segundo método está compuesto por fibras de vidrio impregnadas con resina vinilester. Son corrugadas y están recubiertas con una capa de arena fina. No son conductoras de electricidad y son muy livianas (γ = 2260 kg/m^3). Este sistema GFRP consiste básicamente en instalar las varillas de fibra de vidrio como refuerzo horizontal cada 2 hiladas de ladrillos, intercalándolas alternadamente en ambas caras del muro con el fin de no debilitar la sección transversal del muro reforzado.

3. CAMPAÑA EXPERIMENTAL

3.1. Características de los especímenes

Los muros de AC que se ensayaron en cada investigación fueron construidos a escala natural con un aparejo de soga. La conexión columna- albañilería es al ras para los estudios de ME y CFRP y dentada para GFRP y MAC (Fig. 1). La Tabla 1 lista el tipo de unidad empleado, la resistencia a la compresión ($f'm$) y al corte diagonal ($v'm$) de pilas de albañilería, y propiedades geométricas de longitud (L) y altura (H). El espesor es de 130 mm en todos los muros.

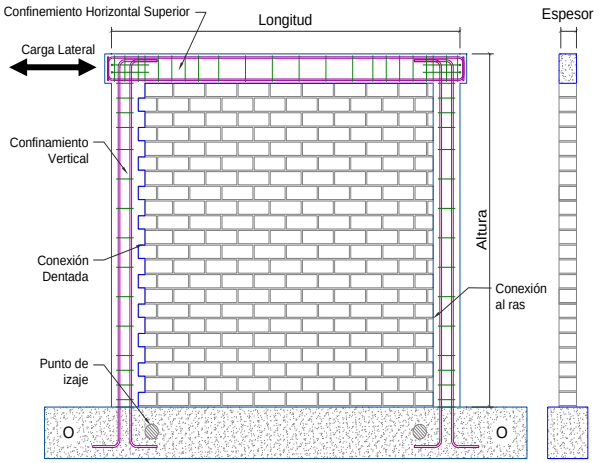

Figura 1. Esquema de muros ensayados

Tabla 1. Propiedades mecánicas y geométricas

	Unidad de albañilería (% vacíos)	$f'm$ [Mpa]	$v'm$ [Mpa]	L [mm]	H [mm]
GFRP	Hueco (45)	12.7	1.6	2400	2680
ME	Sólido (30)	8.6	1.7	2600	2400
CFRP	Sólido (32)	8.8	0.94	2400	2600
MAC	Hueco (48)	9.46	1.25	2600	2400

En los cuatro casos se empleó un mortero de junta con dosificación 1:4 (cemento: arena). Se obtuvo información de los muros MAC, la primera y segunda jornada de la extracción de muestras indican una resistencia promedio a la compresión de 21 y 15 MPa, respectivamente. Finalmente, la resistencia a la compresión característica del concreto para los elementos de confinamiento es igual a 21, 28, 19 y 17 MPa para GFRP, ME, CFRP y MAC, respectivamente.

3.2. Protocolo de ensayo

El ensayo realizado en los muros fue de carga lateral cíclica con desplazamiento horizontal controlado (ensayo cuasi estático) y sin carga vertical. El desplazamiento lateral superior fue registrado por LVDTs. El objetivo de los ensayos fue conocer el mejoramiento del comportamiento sísmico de los muros reforzados.

Las cuatro investigaciones ensayaron los muros hasta derivas cercanas al límite de reparabilidad (GFRP= 0.52%, ME= 0.77%, CFRP= 0.58%, MAC= 0.45%), por lo que no fueron ensayos destructivos. Sin embargo, los esfuerzos llevaron a los muros a experimentar un comportamiento no lineal. Luego de reforzar los muros, se realizaron ensayos hasta la rotura o hasta que la capacidad disminuya y ponga en peligro de inestabilidad del sistema.

Las Fig. 2 muestra la historia de desplazamientos a la que los muros se sometieron. El primer protocolo (GFRP, ME, CFRP) se hizo bajo el criterio del investigador y el segundo (MAC) siguiendo lineamientos del FEMA 461 (2009). Según Fig. 2a, en el estudio GFRP se ensayaron los muros sin y con refuerzo hasta 10 fases. En las demás investigaciones, el número de fases para muros originales y reforzados fue diferente, siendo los muros reforzados ensayados hasta la falla con mayor cantidad de fases. En el estudio ME, se ensayaron los muros originales hasta 7 fases y los reforzados hasta 9 fases. A diferencia del estudio GFRP, el número de ciclos de la fase 5 es dos. Finalmente, en el estudio CFRP, se ensayaron los muros originales hasta 8 fases y los reforzados hasta 11 fases, y el número de ciclos de las fases 6 y 7 es de 3. Según la Fig. 2b, en la investigación MAC, los muros originales y reforzados se ensayaron hasta 9 y 12 fases, respectivamente. Para todos los estudios, la velocidad de ensayo fue de 1 ciclo en 4 minutos.

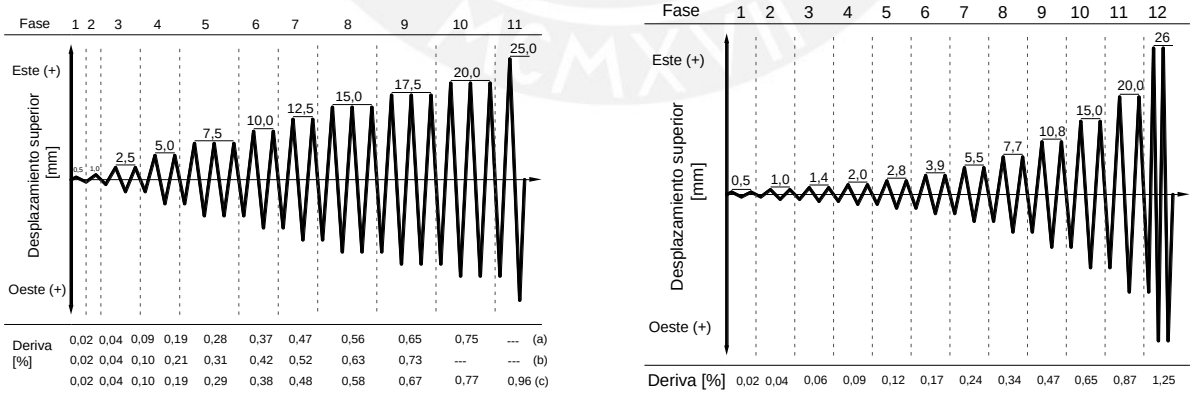

(a) (b)

Figura 2. Protocolo de ensayo para: (a) GFRP, ME, CFRP; (b) MAC

3.3. Comportamiento de los muros con y sin refuerzo

3.3.1. Muros sin refuerzo

Durante el ensayo cíclico, se fue observando cuál era el comportamiento del muro hasta el fin del ensayo (aparición y progreso de grietas, grosor de grieta). Para poder caracterizar el grosor de

grieta, se tomó la medición cuando el desplazamiento lateral inducido es máximo; es decir, cuando el muro se mueve hacia la derecha, el grosor se medirá por el lado izquierdo.
De forma general, se puede decir que los muros de AC tienen un comportamiento elástico hasta una deriva de 0,04%- 0,06%. Luego con una deriva ≈ 0.1%, los muros originales experimentan fisuras de tracción que se originan en la base de las columnas de confinamiento; las fisuras se van propagando en toda la altura de las columnas. Asimismo, aparece la primera grieta por tracción diagonal en el panel de albañilería. Con una deriva mayor entre 0,2 – 0,24%, las grietas existentes en las columnas de confinamiento se extienden hacia el panel de albañilería. Grietas diagonales finas en el panel de albañilería aparecen para una deriva entre 0,29% - 0,34% (Fig. 3a). También se observa que mientras la deriva varía entre 0,38% a 0,65% las grietas diagonales se intensifican y hay trituración de los ladrillos en las esquinas y por la parte central del muro. Finalmente, las grietas diagonales se extienden hacia las columnas de confinamiento (Fig. 3a) y se trituraban sus bordes inferiores (Fig. 3 c,d,e). Los muros fallaron por corte, la Fig. 3 muestra las grietas que se formaron, y las que resaltan son en forma de aspa lo que evidencia el tipo de falla mencionado.

(a) (b) (c) (d)

Figura 3. Comportamiento del muro original (a) GFRP (b) ME (c) CFRP (d) MAC

3.3.2. Muros con refuerzo

En todos los casos, los muros permanecieron en el rango elástico hasta una deriva de 0,04%. Luego, para una deriva entre 0,06-0,09% empezaron aparecer fisuras por flexión en los bordes libres de las columnas de confinamiento. Para el mismo rango de deriva, también aparecieron fisuras diagonales muy finas en la parte superior del panel de albañilería a excepción de los muros MAC. Las grietas en las columnas de confinamiento y grietas diagonales siguieron propagándose cuando los muros GFRP, ME, y CFRP experimentaban una deriva de 0,19%. La primera grieta diagonal en los muros MAC apareció hasta una deriva de 0,24%. Hasta los límites anteriores, ninguna técnica de refuerzo había fallado. A partir de este punto, comienza haber un comportamiento diferente en cada sistema de refuerzo.
Para el sistema GFRP, ME, CFRP en un rango de deriva ≈ 0,28% - 0,37%, las fisuras se siguen propagando y las grietas resanadas empiezan a notarse claramente. En caso del sistema GFRP, el mortero que cubre las varillas se desprende cuando la deriva = 0,56%, y las varillas se pandean cuando la deriva= 0,65%. El muro GFRP termina de fallar con trituración de ladrillos centrales y con la pérdida de adherencia de varillas- albañilería (deriva = 0,75%). El muro ME con una deriva = 0,47% experimenta el origen por falla de deslizamiento y con una deriva= 0,65% el muro se desliza 10 mm. El muro falla y se observa el deterioro en la base de las columnas y el deslizamiento del muro respecto a la viga de cimentación. El muro CFRP experimenta el primer desprendimiento de las bandas de fibra con una deriva = 0,56%, y la primera rotura de las bandas de fibra con una deriva = 0,65%. Cuando la deriva fue 0,96%, fallaron todas las bandas menos dos superiores.

Los muros MAC, en un rango de deriva ≈ 0,56% a 0,75%, presentan grietas que se van acercando a la parte inferior del muro hasta que cruzan las diagonales formando una "V" en el panel. El grosor de grietas es bastante bien controlado por la malla de acero. Finalmente, para una deriva de 1,08%, el muro MAC presenta la "V" bien remarcada. La Fig. 4 muestra el estado final de los muros reforzados.

(a) (b) (c) (d)

Figura 4. Comportamiento del muro reforzado: (a) GFRP (b) ME (c) CFRP (d) MAC

4. RESULTADOS TÉCNICOS DE LOS MUROS SIN Y CON REFUERZO

Los efectos más relevantes de emplear una técnica de reforzamiento pueden ser recuperar la rigidez inicial o un buen porcentaje de la misma, recuperar la capacidad de carga o ganar una mayor, presentar mayor ductilidad, o simplemente desarrollar una combinación de las mismas.

Del ensayo se obtiene los lazos histeréticos, cuya envolvente es la curva carga lateral vs deformación lateral que se muestran en la Fig. 5 para cada tipo de refuerzo. De la Fig. 5 se desprende que los muros reforzados con malla electrosoldada (ME) y mallas de acero (MAC) recuperan casi en su totalidad la rigidez inicial del muro sin refuerzo (85% del original). Los muros reforzados con ME logran incrementar la capacidad de carga y ductilidad en un 40%, mientras que los muros con MAC incrementan estos parámetros en un 25% aproximadamente. El muro reforzado con fibra de vidrio (GFRP) logra recuperar regular porcentaje de la rigidez inicial (70% de la inicial), pero no aumenta ductilidad y apenas logra incrementar la capacidad de carga (3% más). Finalmente, el muro reforzado con fibra de carbono (CFRP) logra recuperar solo el 40% de la rigidez inicial, incrementa la ductilidad en un 65% y su capacidad de carga en un 22%, respecto del muro original.

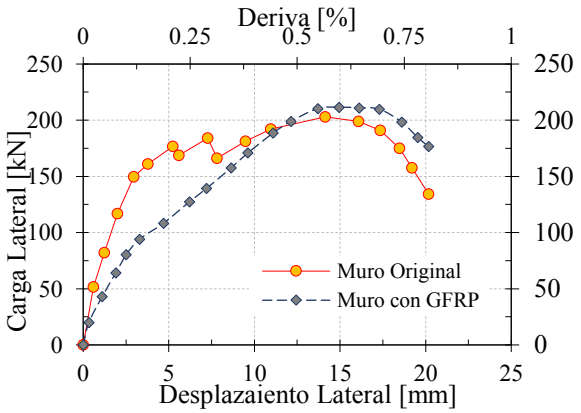

(a)

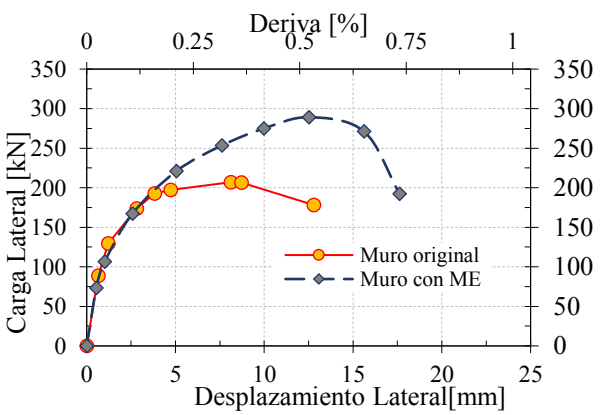

(b)

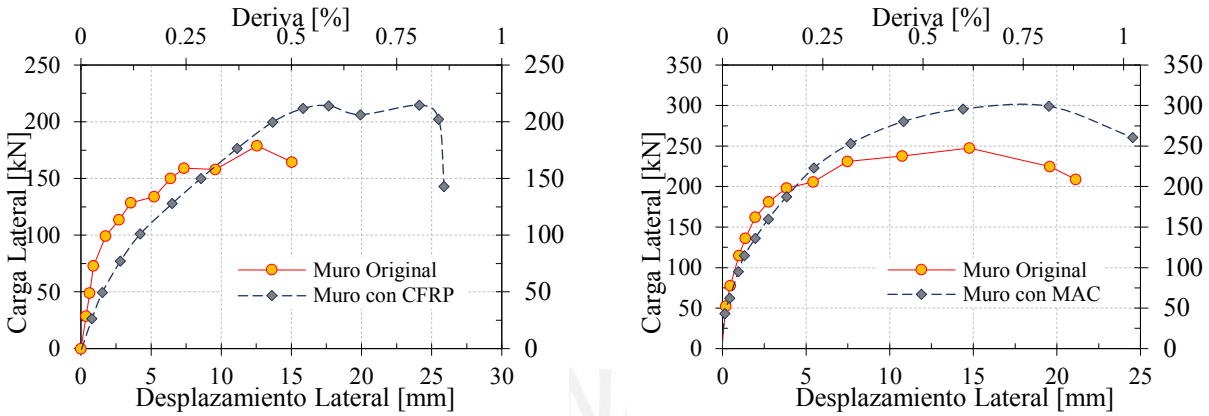

(c) (d)

Figura 5. Carga vs. desplazamiento lateral: (a) GFRP (b) ME (c) CFRP (d) MAC.

5. EFECTIVIDAD ECONÓMICA DE LAS 4 ALTERNATIVAS

La evaluación económica se hizo tomando en cuenta el costo del proceso de construcción y reforzamiento de un muro de AC típico. Debido a que todos los muros tienen una geometría similar si no es idéntica, el costo de construcción es igual en los 4 casos. Y dependiendo de la facilidad o complejidad de aplicación del sistema de refuerzo el costo de mano de obra puede bajar o subir.
Para el costo de mano de obra, en todos los procesos de reforzamiento se asume una cuadrilla conformada por un operario (s/. 100) y un ayudante (s/. 70). El tiempo de ejecución depende del tipo de refuerzo. Por ejemplo, reforzar con malla electrosoldada demandó 2,5 días, con fibra de vidrio 1 día, con fibra de carbono 2 días y con malla de acero corrugado 3 días.
La Tabla 2 muestra un comparativo de costos entre las diferentes alternativas analizadas señalando el porcentaje de incidencia que tiene reforzar un muro respecto al costo de construirlo. Se señala que el costo de reforzar un muro con el sistema GFRP, ME, CFRP y MAC representan el 25%, 53%, 58%, 55% del costo de construcción del muro respectivamente. Es así que el sistema GFRP es el más económico y CFRP es el más caro.

Tabla 1. Costo para reforzar un muro de AC

Técnica de Reforzamiento	Const. (CM) [$]	Reforzamiento (RM) [$]	RM/CM
GFRP	460	113	25%
ME	460	246	53%
CFRP	460	265	58%
MAC	460	252	55%

6. CONCLUSIONES

El reforzamiento de muros de albañilería confinada con técnicas novedosas como GFRP y CFRP o tradicionales como ME y MAC presentan interesantes resultados al someterlos a ensayos de carga cíclica lateral con desplazamientos controlados. Las cuatro investigaciones ensayaron los muros originales hasta derivas cercanas al límite de reparabilidad (deriva = 0.5%), por lo que es posible comparar directamente el comportamiento de estos muros sin y con refuerzo.
Entre los ensayos cualitativos se tiene el comportamiento del muro sin y con refuerzo de acuerdo al patrón de grietas mostrado. Los resultados del ensayo cíclico sin refuerzo muestran que los muros de AC tienen un comportamiento similar a lo largo del ensayo hasta la falla que en todos los casos fue de corte. En caso de los muros reforzados, el comportamiento fue similar hasta una deriva de 0,19%- 0,24%. Luego el comportamiento fue diferente de acuerdo al tipo de refuerzo.

Por otro lado, entre los resultados cuantitativos, se tiene la gráfica carga – desplazamiento lateral que resulta de la envolvente de los lazos histeréticos de cada ensayo. Los resultados muestran que las técnicas tradicionales ME y MAC recuperan cerca del 85% de la rigidez inicial. Los muros reforzados con ME incrementan su desempeño estructural en términos de capacidad de carga y ductilidad en un 40%, mientras que los muros con MAC aumentan estos parámetros sismorresistentes en un 25%. La técnica CFRP logra recuperar el 40% de la rigidez inicial e incrementar la resistencia y ductilidad en 22% y 65% respectivamente. En caso del sistema GFRP se recupera el 70% de la rigidez inicial, pero no incrementa ductilidad, ni capacidad de carga. Sin embargo, el análisis económico arroja que el sistema GFRP es el más conveniente pues representa el 25% de la construcción de un muro.

Ante los resultados, se reconoce que aún no es posible seleccionar un solo tipo de refuerzo, ya que mientras el sistema CFRP resulta ventajoso técnicamente (incremento notable de ductilidad), económicamente no; y mientras el sistema GFRP resulta desfavorable técnicamente, económicamente es el mejor. Por lo que se recomienda realizar un análisis multicriterio para seleccionar adecuadamente un tipo de refuerzo.

7. AGRADECIMIENTOS

Los autores agradecen al personal del Laboratorio de Estructuras de la PUCP y SENCICO por la información brindada. Asimismo, se agradece a CONCYTEC por el CONVENIO DE GESTIÓN N° 232-2015 FONDECYT que otorgó becas a los estudiantes de maestría en ingeniería civil.

8. REFERENCIAS

Alcocer, S; Arias, J. and Vazquez, A. (2003). The New Mexico city building code requirements for design and construction of masonry structures. Proceeding Ninth North American Masonry Conference, Clemson, South Carolina, p. 656–667.

Bhattacharya, S.; Nayak, S. and Chandra, S. (2013). A critical review of retrofitting methods for unreinforced masonry structures. International Journal of Disaster Risk Reduction, p. 51–67.

FEMA (2009). Unreinforced Masonry Buildings and Earthquakes: Developing Successful Risk Reduction Programs. Federal Emergency Management Agency.

Lodi, S; Alam, N. and Ahmed, M. (2012). Seismic Vulnerability Assessment of Existing Buildings of Pakistan. Earthquake Model for Middle East Region (EMME), Department of Civil Engineering, NED University of Engineering & Technology, Karachi, Pakistan.

Lujan, M. (2016). Refuerzo de muros de albañilería confinada con mallas de acero. Tesis para optar el título de Ingeniero Civil, PUCP, Lima.

San Bartolomé, A. and Castro, A. (2002). Reparación de un muro de albañilería confinada mediante malla electrosoldada. Fondo editorial, Pontificia Universidad Católica del Perú.

San Bartolomé, A. and Coronel, C. (2009). Reparación y reforzamiento de un muro de albañilería confinada mediante fibra de carbono. Fondo editorial, Pontificia Universidad Católica del Perú.

San Bartolomé, A. and Loayza, J. (2004). Reparación y reforzamiento con varillas de fibra de vidrio en un muro de albañilería confinada. Fondo editorial, Pontificia Universidad Católica del Perú.

Yepes-Estrada, C.; Silva, V.; Valcarcel, J.; Acevedo, A. B.; Tarque, N.; Hube, M. A.; Coronel, G. and Santa María, H. (2017). Modeling the residential building inventory in South America for seismic risk assessment, Earthquake Spectra, v. 33, n. 1, p. 299–322.

Anexo B

The use of SRG to improve the lateral displacement ductility of confined masonry walls

Please fill out the following information and leave the rest of the first page blank. Manuscript text should begin on the second page. **Revisions to the title, abstract, and author information must be made online in CATALYST**. This page will be used for reference by the editorial staff and reviewers only and will not be included in the final conference proceedings. Please see the *First Page* section in the manuscript guidelines for more information.

Manuscript title:	The use of SRG to improve the lateral displacement ductility of confined masonry walls
Author 1 name:	Jhair Yacila
Author 2 name:	Jhoselyn Salsavilca
Author 3 name:	Nicola Tarque
Author 4 name:	Paolo Casadei
Author 5 name:	Guido Camata
Author 6 name:	
Author 7 name:	
Author 8 name:	
Author 9 name:	
Abstract: (300-word limit)	The construction of confined masonry dwellings has become an attractive alternative for people who build their houses on their own. This means no engineering or technical intervention, therefore, there is an intrinsic high seismic vulnerability related to the dwelling's quality. If this fact is added to the disorderly growth of the Peruvian population, an undesirable increase of informal constructions becomes important. Just in Lima, it is registered that at least 70% of the total dwellings are informal and are located in hills. Additionally, seismologic information has revealed that the asperity between Nazca and South American plates are so concentrated, which means that they already have enough energy to cause a big earthquake in the southern and central coast of Peru. Thus, there is no doubt that a big disaster will occur if these buildings are not properly reinforced as soon as possible. Following this line, this study contributes with the reduction of the seismic vulnerability of these kinds of buildings and opens a research line for controlling damage to an acceptable limit state. For this purpose, an experimental campaign of a new strengthening technique based on steel reinforced grout (SRG) has been conducted. In this campaign, three confined masonry walls that were previously tested until a collapse state, were repaired and strengthened with SRG to be retested under in-plane lateral cyclic loads. The results showed the benefits of strengthening with SRG for improving the lateral displacement ductility. It is pretended that SRG could be widely used to reduce seismic risk on confined masonry dwellings of developing countries, due to its easy and fast installation and its ability to improve the ductility of walls and controlling damage in different limit states.
Keywords:	SRG, confined masonry, informal dwellings, cyclic test

Please ensure that the body of the manuscript starts at the top of the second page. *(rev. 9/10/18)*

INTRODUCTION

Confined masonry constitutes about 84% of all low-rise constructions in Peru. Unfortunately, many of these constructions are built in an improper manner. According to statistics information (INEI, 2007), just in Lima 70% of the total dwellings were built informally without any technical or engineering intervention (Fig. 1). This issue, added to the fact that Peru belongs to the Fire Belt, one of the most active subduction zones in the world, gives these constructions a high seismic vulnerability.

(a) (b)

Figure 1. Informal and disorderly construction of confined masonry dwellings in Lima-Peru (Sato, 2018)

Past seismic events around the world, have revealed the poor seismic response of the informal confined masonry dwellings, which in a huge scale becomes a catastrophic event. For this reason, seismologists and engineers are studying different ways to mitigate this natural disaster. For instance, Villegas-Lanza et al. (2016), conducted a study intended to assess the asperities between both Nazca and South American plates to predict the expected earthquake in Peru. For this purpose, they split the Peruvian coast into three: northern, central and southern segment, and proposed a large-scale heterogeneous inter-seismic coupling model along the Peruvian coast by using a large amount of updated geophysical observations. They conclude that the central and southern Peru segments could now be whipped by a big ($M_w \geq 8.5$) and ($M_w = 8.2$) earthquake, respectively.

Thus, an improvement of the seismic performance of masonry constructions through strengthening is needed. Following this line, different strengthening techniques applied such as external reinforcement have been studied in the last decades. One of the most studied technique is the Fiber Reinforced Polymer (FRP) system, which is composed of different kind of fibers such as carbon, glass, steel, basalt, among other, and an organic binder such as epoxy resin. This strengthening alternative has some advantages related to the fact that they do not add mass to the structure, they are easy to install, and has an excellent performance in terms of tensile strength and durability (Gattesco & Boem, 2017; Quagliarini, Monni, Greco, & Lenci, 2017). Nevertheless, it also has some disadvantages related to the uniform and dry surface they need to be properly applied, the poor behavior at high temperatures and alkaline environments, and some others related to the organic nature of its binder. On the other hand, overcoming these disadvantages, Fiber Reinforced Mortar (FRM) came up as a new strengthening technique. This alternative can also use the fibers aforementioned with the difference that they are embedded in an inorganic mortar. A particular case is given when FRM uses steel fiber because it is known more as Steel Reinforced Grout (SRG) which is mainly studied due to its mechanical properties and bond efficiency. On the other hand, even when SRG has already

shown its effectiveness for strengthening reinforced concrete beams, masonry arches and walls, there is still a lack of knowledge on the durability field, which in fact is of vital interest for the knowledge of its long-term performance (De Santis et al., 2017).

This work presents a novel strengthening technique based on SRG which seeks to improve the in-plane seismic behavior of confined masonry walls (CMW). For this purpose, three full-scale failed walls that were part of a study conducted by Manchego & Pari (2016), were repaired and strengthened with SRG to be retested under quasi-static lateral cyclic motions. The results are discussed in terms of lateral deformation, stiffness degradation, energy dissipation and hysteretic damping.

EXPERIMENTAL CAMPAIGN

Description of tested walls

As a previous research, Manchego & Pari (2016) conducted an experimental campaign involving nine tests of full-scale walls under lateral cyclic loading. Three of them were led up to a repairable limit state which corresponds to a drift of 0.5% according to Peruvian code (E070, 2006), and the others six walls until a collapse state. From these last, three of them had a constant vertical load of 170 kN during the test. The geometry as well as the reinforcing detail of a typical wall are shown in Figure 2. It is worth commenting that in a real work, reinforced concrete foundations are not employed to build confined masonry walls. It was built just to anchor the wall to the laboratory's slab reaction (Fig. 7).

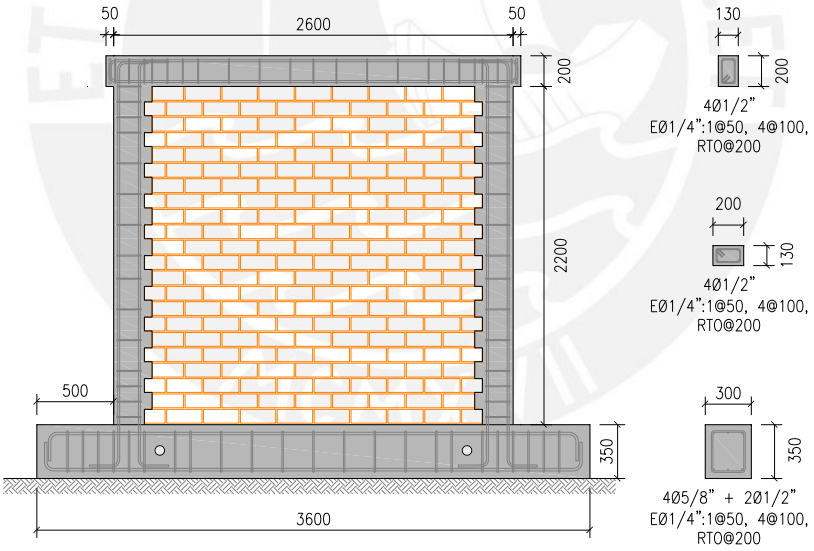

Figure 2. Geometry and reinforcing detail of a typical wall - Dimensions in millimeters

In this study, a total of three failed walls (CMW-01, 02 and 03) were selected from the preliminary experimental campaign to be repaired and strengthened with SRG, and to be retested under lateral cyclic loading. From these selected walls (Figure 3) only one had the vertical load aforementioned during the test before and after strengthening, CMW-01 and R-CMW-01 respectively.

(a) CMW-01, with vertical load (b) CMW-02 (c) CMW-03

Figure 3. Damage state of selected walls from the previous research (Manchego & Pari, 2016)

Repairment and Strengthening

A properly repairment of walls is necessary to recover a great percentage of the initial stiffness before strengthening. In this work, cracks greater than 8 mm thickness were opened by means of manual tools to avoid excessive vibrations out-of-plane. Wherever there were completely crushed bricks, these were removed and replaced by new ones. The wall corners were seriously damaged due to the excessive stress's concentration produced by the incremental bending effects. All crushed concrete was also removed and replaced by a repairment mortar, previous application of an adhesion bridge based on epoxy resin to join the oldest concrete with the new one. Finally, the openings were filled with repairment mortar. To guarantee a good strength of repairment mortar, a proper curing process of at least 28 days must be carried out. Nevertheless, being reasonable of what would be done in a real application, the walls were moistened three times a day for 7 days. Figure 4 shows the main stages of repairing process.

(a) Opening of cracks (b) Filled with repairment mortar (c) Repairing finished

Figure 4. Main stages for repairing confined masonry walls

Regarding the design, the shear strength contribution of the confined masonry as well as reinforcement must be considered. In this work, the masonry contribution was computed in accordance with Peruvian code (for other applications local code should be used), whereas the second one was computed in accordance with CNR-DT and AC434 (CNR, 2013; ICC, 2016). As a result, 5 SRG horizontal strips of 100 mm wide and 10 mm thickness were applied. Each SRG strip was made-up of ultra-high tensile strength steel fibers 0.084 mm thickness, and a natural lime mortar. These fibers were presented as cords that turned out from twisting two wires around three straight wires. Furthermore, they were protected against corrosion by a zinc coating, which helps to their long-term performance.

The strengthening process started with the surface preparation where SRG strips are located. A rough surface is recommended to ensure a better adhesion between SRG and substrate. For this reason, bricks were previously punched lightly by means of a pointed tool. It is necessary to moisten the involved bricks to clean them of possible solid residues and to avoid the absorption of mortar's water.

SRG application can be summarizes in four main steps: (1) delimitation of the work area by means of scotch tape and application of a first layer of mortar of 5 mm thickness (Figure 5a), (2) light embedding of the steel fiber into first layer of mortar (Figure 5b), (3) application of a second layer of mortar of 5 mm thickness (Figure 5c), and (4) removal of scotch tapes (Figure 5d). In order to ensure a proper stress transmission between masonry wall and SRG strips, a proper anchorage of steel fibers must be provided. In this work, overlaps of 250 mm were provided interspersed at each column ending. For other applications, it is recommended to follow the manufacturer recommendations to give a proper anchorage of the SRG system (KERAKOLL, 2018).

(a) First layer of mortar (b) Placed of steel fiber mesh

(c) Second layer of mortar (d) Strengthened wall

Figure 5. Main stages for strengthening CMW with SRG

Instrumentation and cyclic testing setup

Preceding the test, each specimen was fixed to a reaction slab by means of hydraulic jacks. Two linear variable differential transformers (LVDTs) (LVDT 1 and 2) were located along both diagonals of the masonry panel to measure the idealized strut and tie deformations. Another two LVDTs (LVDT 3 and 4) were located along confinement columns to measure their compression and tensile deformations produced by bending effects as well as vertical load. Finally, one LVDT (LVDT 5) was located between the geometric center of the confinement beam and a reference frame to control the lateral displacements induced to the wall.

The cyclic test consisted in lateral displacements applied at the top beam level through of a dynamic actuator. The loading velocity for the quasi-static test was 0.25 cycles/minute. Following the recommendations

of FEMA 461 (Applied Technology Council et al., 2007), two cycles were defined for each displacement phase, and each displacement was defined as the result of increasing by 1.4 times the displacement of the previous phase. It is worth commenting that Manchego and Pari only considered 11 phases with a maximum displacement level of 20 mm, whereas in this work, 12 phases with a maximum level displacement of 30 mm, were considered. The instrumentation and the whole experimental setup are shown in Figure 6.

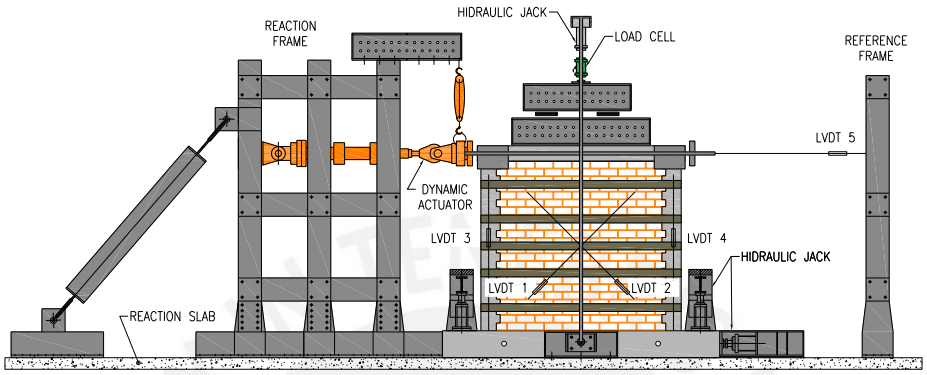

Figure 6. Experimental setup and instrumentation for cyclic testing. Adapted from Manchego & Pari (2016)

RESULTS

The first visible cracking in R-CMW-01 appeared at the lower part of the wall due to bending effects. This occurred during the fifth loading phase (drift = 0.12%). The first diagonal cracking produced by traction of the compressed strut occurred during the seventh phase (drift = 0.23%). It is worth noting that after this diagonal cracking, subsequent diagonal cracks were produced as displacements increased. The total capacity of the SRG composite could be explored during the twelfth phase (drift = 1.25%) by observing the rupture of two SRG strips located in the mid-height of the wall where the highest tensile stresses are located. According to the aforementioned, it is possible to assure that this wall had a predominant shear failure.

Regarding to R-CMW-02 and R-CMW-03, the first cracks, located at the lower third of the wall height, were produced by bending effects during the fourth loading phase (drift = 0.083%). The first diagonal cracking produced by traction of the compressed strut occurred during the eleventh (drift = 0.833%) and ninth (drift = 0.45%) loading phase, respectively. A horizontal crack at the wall base was adverted in both cases. This allowed to have a sort of rocking effect, which can be seen also at the Figure 8. According to the aforementioned, it is possible to assure that these walls had a mix of shear and bending failure. Table 1 summarizes the results related to the first cracking and maximum load capacity of the tested walls. Figure 7 shows the cracking pattern of all the tested walls.

In general terms the bonding between SRG and masonry substrate was very good, since no debonding failure could be seen in none of the cases. In some localized regions at mid-height of R-CMW-01, it was possible to see plastic elongations of the steel fiber which caused the rupture of the second layer of mortar. In case of R-CMW-02 and 03, it was no possible to explore the total capacity of SRG and the collapse state was related to the instability of the wall and its abrupt loss in load capacity either in the first or second cycle of the last phase.

Table 1. Experimental results of tested walls

Specimen	Direction	First cracking		Maximum load	
		Load [kN]	Drift [%]	Load [kN]	Drift [%]
R-CMW-01	Push	195	0.116	340	0.833
	Pull	-180	-0.116	-340	-0.833
R-CMW-02	Push	90	0.083	235	0.833
	Pull	-110	-0.116	-285	-0.833
R-CMW-03	Push	95	0.083	255	0.625
	Pull	-125	-0.116	-205	-0.625

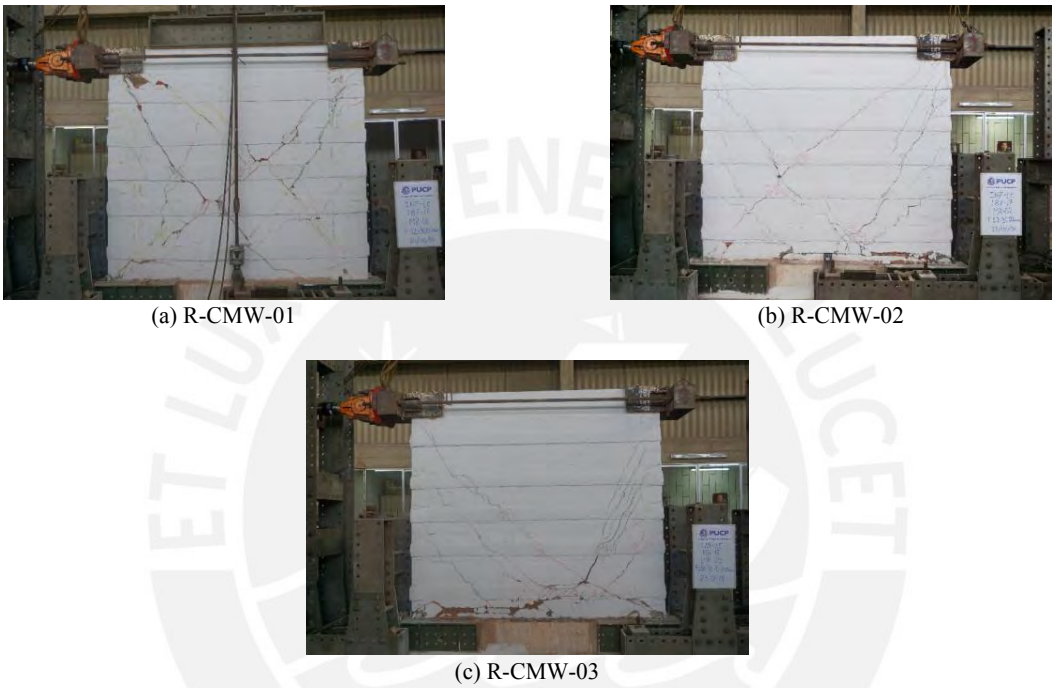

(a) R-CMW-01 (b) R-CMW-02

(c) R-CMW-03

Figure 7. Cracking pattern of tested walls

A typical characteristic of confined masonry dwellings is to have a short fundamental period, which means higher oscillation frequencies of these kind of structures. Peruvian earthquakes are characterized by a high content of frequencies where high frequencies predominate. This fact could bring the structure closer to a resonance state, which could mean an early failure of bearing walls and a subsequent building collapse. Therefore, it is necessary to increase the capacity of these buildings to deform laterally without reaching collapse, which means giving them more ductility. In this study, the lateral displacement ductility, μ, is evaluated as follow:

$$\mu = \frac{\delta_u}{\delta_y} \tag{1}$$

where δ_u is the maximum displacement reached by each wall, and δ_y is the yielding displacement of each CMW related to the first cracking.

Regarding improvement in terms of ductility, the wall's ultimate displacement of R-CMW-01 was 30 mm, as opposed to 15 mm from CMW-01. This corresponded to a 100% increase in the lateral displacement ductility of the wall. In case of R-CMW-02 and 03, the ultimate displacements were 30 mm for both cases,

as opposed to 20 mm from CMW-02 and 03. This corresponded to a 50% increase in the lateral displacement ductility of these walls. Table 2 summarizes the calculus of the increment in ductility caused by SRG. Figure 8 shows the hysteretic curves for un-strengthened and strengthened walls.

Table 2. Improved ductility calculation of tested walls

Specimen	δ_y	CMW		R-CMW		Increment
CMW / R-CMW	[mm]	δ_u [mm]	μ	δ_u [mm]	μ	[%]
01	2.8	15.0	5.35	30.0	10.7	100
02	2.0	20.0	10.0	30.0	15.0	50
03	2.0	20.0	10.0	30.0	15.0	50

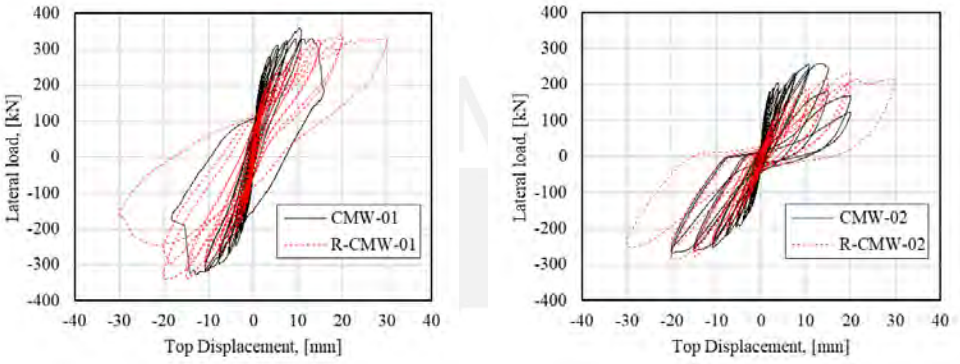

(a) CMW-01 & R-CMW-01 (b) CMW-02 & R-CMW-02

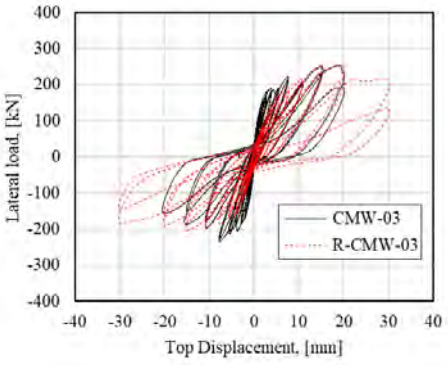

(c) CMW-03 & R-CMW-03

Figure 8. Hysteresis curves for tested walls

Energy dissipation and damping ratio

The seismic response of a building involves the absorption and dissipation of energy. This work was focused on energy dissipation, which is of main interest since it can decrease the maximum seismic response which indeed would reduce the ductility demand on a structure (Shing et al., 1990). Moreover, it is known that energy dissipation is due to viscous damping and material hysteresis and occurs throughout inelastic deformations, which in turn could be understood as damage on structural components. For this reason, it is important to assess if the proposed strengthening technique is able to improve both viscous damping and energy dissipation capabilities in order to provide better seismic performance to the walls. In this study, the energy dissipation, E_d, is evaluated such as the area enclosed for each hysteretic loop, whereas the hysteretic

viscous damping, ξ_{hyst}, is calculated as a ratio between energy dissipated and elastic strain energy as is shown in figure 9.

At initial cycles, it is known that equipment such as dynamic actuator needs short displacements for calibrating. It causes loops under small displacements that are unrealistic due to the fact they have and should not have area within the loop because they are expected to have linear-elastic behavior. For this reason, in this study, the first two loading cycles were not considered in calculating average viscous damping.

Figure 10 shows that in all cases strengthened walls were able to dissipate more energy than original walls. And it is worth noting that it was possible without losing a huge quantity of capacity load (Figure 8). Regarding the hysteretic viscous damping, R-CMW-01 showed a particular phenomenon in its final loading phase because of the abrupt loss in capacity load which meant a large amount of dissipated energy (Figure 8(a)), which in turn meant an undesirable state of instability of the wall. For this reason, the calculated value of viscous damping for this final stage was also despised. With this assumption, R-CMW-01 showed an average viscous damping of 9.65% contrary to 7.90% of CMW-01, which meant an increment of 20%. R-CMW-02 showed an average viscous damping of 12.00% contrary to 10.50% of CMW-02, which meant an increment of 14%. Finally, R-CMW-03 showed an average viscous damping of 12.45% contrary to 9.90% of CMW-03, which meant an increment of 26% (Figure 11).

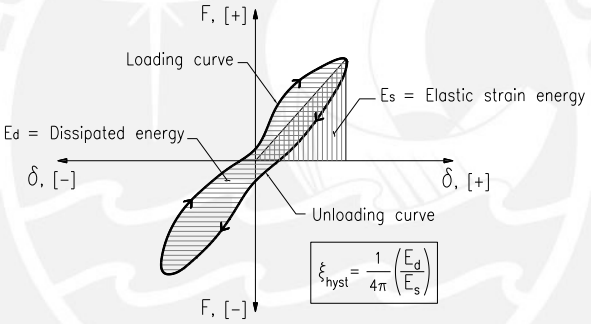

Figure 9. Calculus of energy dissipation and damping ratio

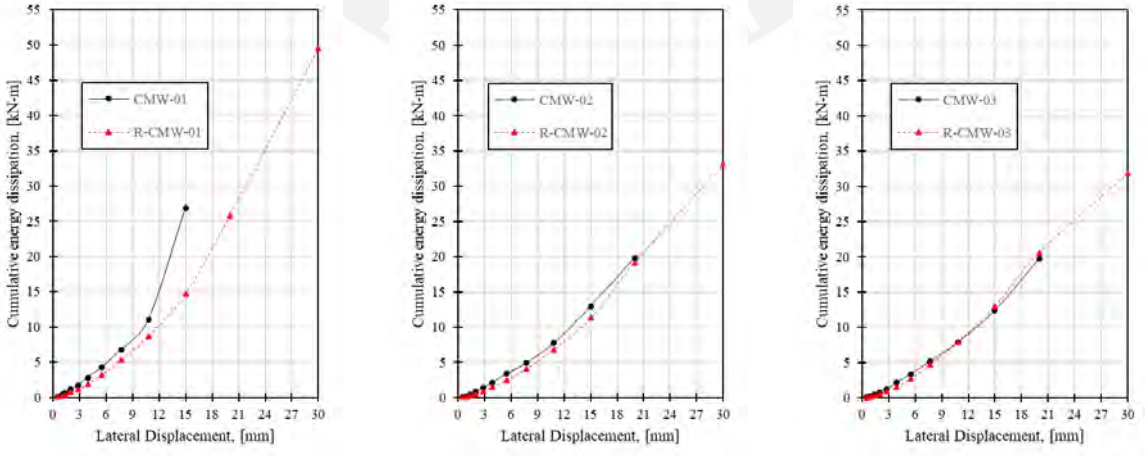

(a) CMW-01 & R-CMW-01 (b) CMW-02 & R-CMW-02 (c) CMW-03 & R-CMW-03

Figure 10. Cumulative energy dissipation of tested walls

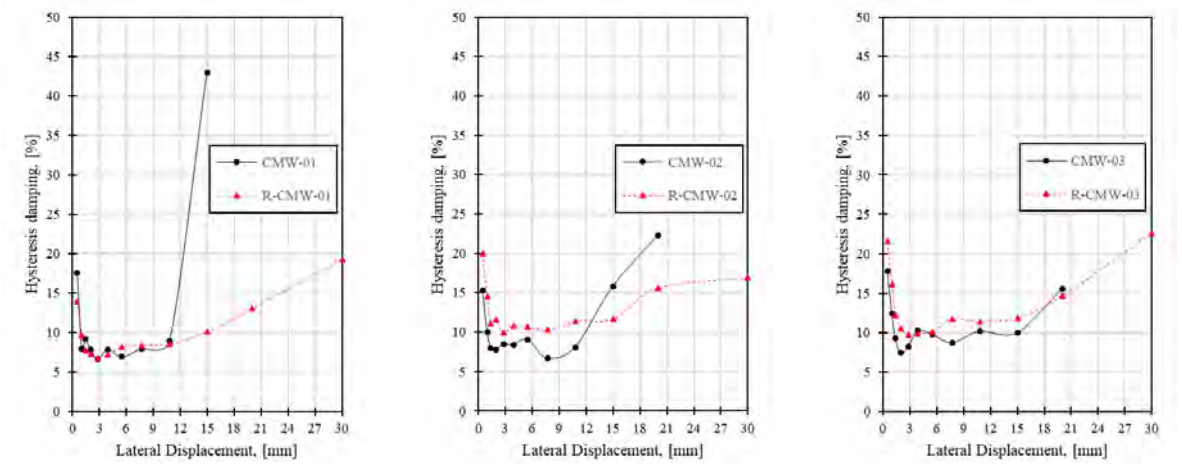

(a) CMW-01 & R-CMW-01 (b) CMW-02 & R-CMW-02 (c) CMW-03 & R-CMW-03

Figure 11. Equivalent hysteretic damping ratio of tested walls

Initial Stiffness and stiffness degradation

The recovery of initial stiffness is mainly due to the repairment of the wall. Therefore, as good as the repairing of the walls will be the recovery of initial stiffness. An ideal repairment would mean to replace cracked masonry blocks by new ones. This would help to recover a major percentage of the initial stiffness of the original walls. However, the cost associated to this ideal job does not make it attractive. For that reason, this study tried to reproduce a real repairment by repairing cracks greater than 8 mm thickness, by replacing bricks totally crushed by new ones and by applying repairing mortar to damaged concrete.

Another important parameter to assess is the stiffness degradation of confined masonry walls since this helps to design codes to provide drifts according different damage levels. For instance, Peruvian code stipulates that buildings are expected to have a linear-elastic behavior until a drift of 0.125% in case of moderate earthquakes, whereas they are expected to reach a reparable state for a drift of 0.5% in case of severe earthquakes (E070, 2006). Stiffness degradation can be the result of cracking, crushing, rebar buckling, crack opening and closing, among others. The level of stiffness degradation is related to the characteristics of the structure (e.g., material properties, geometry, connection type), as well as on the loading history (e.g., level of displacement in each cycle, number of cycles, increment ratio of displacements) (FEMA P440A, 2009).

Like the assumption done with hysteretic viscous damping, the first two loading phases were not considered in computing the initial stiffness. Figure 12 shows the normalized stiffness degradation respect to the initial stiffness of both un-strengthened and strengthened walls. It is possible to note that repairing was able to recover a 75% of initial stiffness in case of R-CMW-01 and 50% in case of R-CMW-02 and 03. According the stiffness reached for each wall in the limit state for moderate earthquake (drift = 0.125%), CMW-01 showed a decay of 35% as opposed to 30% from R-CMW-01; CMW-02 showed a decay of 40% as opposed to 30% from R-CMW-02; and, CMW-03 showed a decay of 35% as opposed to 20% from R-CMW-03. Regarding the stiffness reached for each wall in the limit state for severe earthquake (drift = 0.5%), CMW-01 showed a decay of 80% as opposed to 70% from R-CMW-01; CMW-02 and 03 showed a decay of 80% as opposed to 65% from R-CMW-02 and 03. As a summary, it was noted that in all cases strengthened

walls showed a lower decay of the initial stiffness compared with un-strengthened ones, which means that SRG allowed strengthened walls to have a stiffness degradation softer than un-strengthened ones.

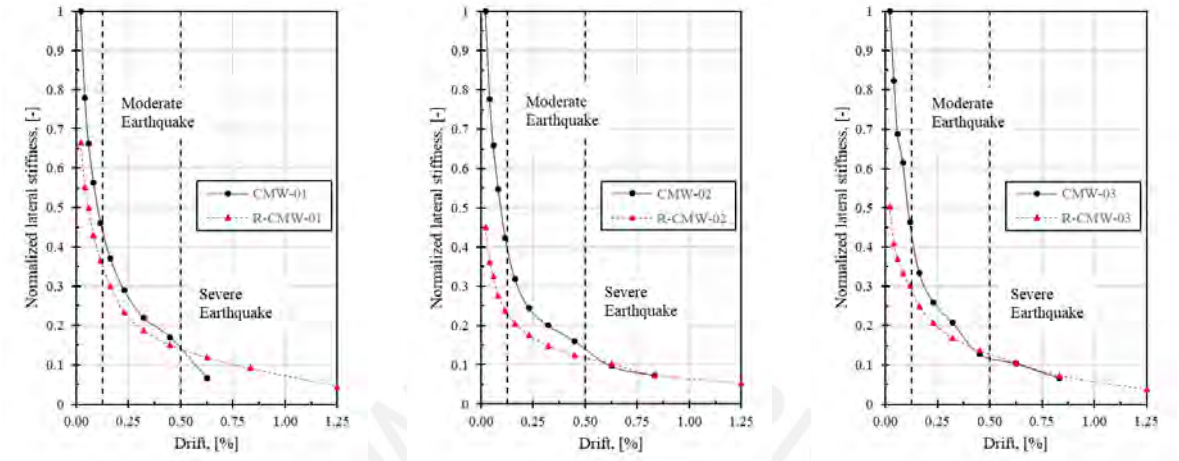

(a) CMW-01 & R-CMW-01 (b) CMW-02 & R-CMW-02 (c) CMW-03 & R-CMW-03

Figure 12. Stiffness degradation for tested walls

CONCLUSIONS

A new strengthening technique based on steel reinforced grout (SRG) was studied to improve the seismic performance of fully cracked confined masonry walls. This technique consisted in bonding externally 5 horizontal strips of 100 mm wide and 10 mm thick mortar. The procedure of strengthening was explained in detail and could be considered as one of the easiest strengthening techniques to apply.

The study involved experimental in-plane cyclic tests of three strengthened full-scale confined masonry walls previously recovered from a collapse state. These tests permitted to evaluate the displacement ductility, energy dissipation capacity, the hysteretic viscous damping, and stiffness degradation of both un-strengthened and strengthened walls. Assessing displacement ductility, it could be seen a considerable increment of 100% in case of the wall with vertical load and 50% in case of walls without vertical load. Regarding to energy dissipation, strengthened walls were able to dissipative more seismic energy, through of greater values of viscous damping, than un-strengthened walls. Furthermore, strengthened walls showed a softer stiffness degrading compared to un-strengthened walls, which means that SRG helps to maintain the integrity of the wall. It is worth highlighting the easy application of this strengthening technique compared to the advantages it has to improve seismic performance of confined masonry walls.

The strengthening technique herein proposed also allows to control damage in different limit states. This is very important because when dealing with the reducing of the seismic vulnerability of constructions, engineers need to guarantee a certain structural behavior (i.e. limiting damage) considering different limit states and not only focusing on the collapse prevention. Nevertheless, more tests comparing un-strengthened and strengthened walls must be performed to draw more deeply conclusions regarding the controlling damage states.

ACKNOWLEDGEMENTS

The authors wish to acknowledge the economic support provided by CONCYTEC within the framework of the N° 232-2015-FONDECYT Agreement, as well as the industrial company KERAKOLL, for providing the necessary materials for strengthening.

REFERENCES

Applied Technology Council, Mid-America Earthquake Center, (US), M. C. for E. E. R., Center, P. E. E. R., (US), & Program, N. E. H. R. Interim Testing Protocols for Determining the Seismic Performance Characteristics of Structural and Nonstructural Components (2007).

Construction, C.-A. C. on T. R. for. Guide for the Design and Construction of Externally Bonded FRP Systems for Strengthening Existing Structures (2013).

De Santis, S., Ceroni, F., de Felice, G., Fagone, M., Ghiassi, B., Kwiecień, A., … Viskovic, A. (2017). Round Robin Test on tensile and bond behaviour of Steel Reinforced Grout systems. *Composites Part B: Engineering*, *127*, 100–120. https://doi.org/10.1016/j.compositesb.2017.03.052

E070. Reglamento nacional de edificaciones: Albañilería. Ministerio de Vivienda, Construcción y Saneamiento - SENCICO (2006).

FEMA P440A. Effects of strength and stiffness degradation on seismic response (2009).

Gattesco, N., & Boem, I. (2017). Characterization tests of GFRM coating as a strengthening technique for masonry buildings. *Composite Structures*, *165*, 209–222. https://doi.org/10.1016/j.compstruct.2017.01.043

INEI. (2007). *Censos Nacionales 2007: XI de Población y VI de Vivienda*.

KERAKOLL. Directrices para la consolidación, refuerzo estructural y seguridad sísmica con nuevas tecnologías green (2018).

Manchego, J., & Pari, S. (2016). *Análisis experimental de muros de albañilería confinada en viviendas de baja altura en Lima, Perú*. Pontificia Universidad Católica del Perú.

Quagliarini, E., Monni, F., Greco, F., & Lenci, S. (2017). Flexible repointing of historical facing-masonry column-type specimens with basalt fibers: A first insight. *Journal of Cultural Heritage*, *24*, 165–170. https://doi.org/10.1016/j.culher.2016.11.003

Sato, J. (2018). *Reducción del riesgo en áreas vulnerables del distrito de Independencia*.

Service, I. E. Accptance Criteria for Masonry and Concrete Strengthening using Fabric-Reinforced Cementitious Matrix (FRCM) and Steel Reinforced Grout (SRG) Composite Systems (2016).

Shing, B. P. B., Member, A., Noland, J. L., Klamerus, E., & Spaeh, H. (1990). Inelastic Behavior of Concrete Masonry Shear Walls, *115*(9), 2204–2225.

Villegas-Lanza, J. C., Chlieh, M., Cavalié, O., Tavera, H., Baby, P., Chire-Chira, J., & Nocquet, J. M. (2016). Active tectonics of Peru: Heterogeneous interseismic coupling along the Nazca megathrust, rigid motion of the Peruvian Sliver, and Subandean shortening accommodation. *Journal of Geophysical Research: Solid Earth*, *121*(10), 7371–7394. https://doi.org/10.1002/2016JB013080.Received

Bibliografía

Aiello, M. A., Ascione, L., Baratta, A., Bastianini, F., Battista, U., Benedetti, A., Berardi, V. P., Bilotta, A., Borri, A., Briccoli, B., et al. (2014). Guide for the design and construction of externally bonded frp systems for strengthening existing structures.

Alcocer, S., Arias, J., and Vazquez, A. (2003). The new mexico city building code requirements for design and construction of masonry structures. In *Proc Ninth North American Masonry Conference, Clemson, South Carolina*, pages 656–667.

Babaeidarabad, S., Caso, F., and Nanni, A. (2013). Out of plane behavior of URM walls strengthened with fabric-reinforced cementitious matrix composite. *Journal of Composites for Construction*, 18(4):04013057.

Basili, M., Marcari, G., and Vestroni, F. (2015). Nonlinear analysis of masonry panels strengthened with textile reinforced mortar. *Engineering Structures*.

Bhattacharya, S., Nayak, S., and Chandra, S. (2013). A critical review of retrofitting methods for unreinforced masonry structures. *International Journal of Disaster Risk Reduction*, pages 51–67.

Blondet, M. (2005). Construcción y mantenimiento de viviendas de albañilería.

Brzev, S. and Perez, J. (2014). Masonry Construction around the world: an overview. *Short Course on Seismic Design of Reinforced and Confined Masonry Buildings*.

Buchan, P. and Chen, J. (2007). Blast resistance of frp composites and polymer strengthened concrete and masonry structures: A state of the art review. *Elsevier*, pages 509–522.

Carozzi, F. and Poggi, C. (2015). Mechanical properties and debonding strength of fabric reinforced cementitious matrix (FRCM) systems for masonry strengthening. *Composites Part B*.

Chuang, Zhuge, and McBeam (2004). Seismic retrofitting of unreinforced masonry walls by cable system. *In: proc. 13th World Conference on Earthquake Engineering*.

De Santis, S., Giulia, F., De Felice, G., and Poggi, C. (2017). Test methods for textile reinforced mortar systems. *Composites Part B*.

El-Diasity, M., Okail, H., Kamal, O., and Said, M. (2015). Structural performance of confined masonry walls retrofitted using ferrocement and GFRP under in-plane cyclic loading. pages 54–69.

FEMA (2009). *Unreinforced Masonry Buildings and Earthquakes: Developing Successful Risk Reduction Programs*. Federal Emergency Management Agency.

Garofano, A., Ceroni, F., and Pecce, M. (2015). Modelling of the in-plane behaviour of masonry walls strengthened with polymeric grids embedded in cementitious mortar layers. *Composites Part B*.

Gattesco, N. and Boem, I. (2017). Characterization tests of GFRM coating as a strengthening technique for masonry buildings. *Composite Structures*, 165:209–222.

Ghiassi, B., Oliveira, D., Marques, V., Soares, E., and Maljaee, H. (2016). Multi-level characterization of steel reinforced mortars for strengthening of masonry structures. *Journal Materials Design*.

Grande, E., Milani, G., and Sacco, E. (2008). Modelling and analysis of frp-strengthened masonry panels. *Engineering Structures*.

INEI (2008). Perfil sociodemográfico del Perú: Censos nacionales 2007: XI de población y VI de vivienda.

Kaplan, H., Yilmaz, S., Nohutcu, H., Cetinkaya, N., and Binici, H. (2008). Experimental study on the use of old tyres for seismic strengthening of masonry structures. In *The 14th World Conference on Earthquake Engineering, Beijing, China*, pages 12–17.

Kassem, N., Atta, A., and Etman, E. (2016). Structural behavior of strengthening masonry in-filled frames subjected to lateral load using bonded and un-bonded CFRP. *KSCE Journal of Civil Engineering*, 21(3):818–828.

Kuroiwa, J. and Salas, J. (2009). Manual para la reparación y reforzamiento de viviendas de albañilería confinada dañadas por sismos.

Lourenço, P. J. B. B. (1997). Computational strategies for masonry structures.

Luján, M. (2016). Refuerzo de muros de albañilería confinada con mallas de acero.

Marcari, G., Basili, M., and Vestron, F. (2016). Experimental investigation of tuff masonry panels reinforced with surface bonded basalt textile-reinforced mortar. *Composite Part B*, pages 131–142.

Martins, A., Vasconcelos, G., Fangueiro, R., and Cunha, F. (2015). Experimental assessment of an innovative strengthening material for brick masonry infills. *Composites Part B: Engineering*, 80:328–342.

Muñoz, A. (2011). Apuntes del curso de ingeniería sismorresistente.

Nanni, A. (2001). Guides and specifications for the use of composites in concrete and masonry construction in north america. In *Composites in Construction: A Reality*, pages 9–18.

Okail, H., Abdelrahman, A., Abdelkhalik, A., and Metwaly, M. (2014). Experimental and analytical investigation of the lateral load response of confined masonry walls. *Housing and Building National Reasearch Center-HBRC Journal*.

Papanicolau, C., Triantafillou, T., Papathanasiou, M., and Karlos, K. (2008). Textile reinforced mortar (trm) versus frp as strengthening material of urm walls: Out-of-plane cyclic loading. *Materials and structures*, 41(1):143–157.

Parisi, F., Iovinella, A., Balsamo, A., Augenti, N., and Prota, A. (2013). In-plane behavior of tuff masonry strengthened with inorganic matrix?grid composites. *Composite Part B*, 45(1):1657–1666.

Prota, A., Marcari, G., Fabbrocino, G., Manfredi, G., and Aldea, C. (2006). Experimental in-plane behavior of tuff masonry strengthened with cementitious matrix-grid composites. *Journal of Composites for Construction*, 10(3):223–233.

Quagliarini, E., Monni, F., Greco, F., and Lenci, S. (2016). Flexible repointing of historical facing-masonry column-type specimens with basalt fibers: A first insight. *Journal of Cultural Heritage*.

Rafi, M., Lodi, S., Varum, H., Alam, N., Ahmed, M., and Silveira, D. (2012). Assessment of seismic performance of adobe structures in pakistan and portugal. In *15th WCEE, World Conference on Earthquake Engineering*.

Rai, D. et al. (2005). Draft guidelines for structural use of reinforced masonry. *IITK-GSDMA, IIT, Kanpur Google Scholar*.

Salinas, R. and Lazares, F. (2007). La albañilería tubular y su uso en viviendas en zonas sísmicas.

San Bartolomé, A. and Castro, A. (2002). Reparación de un muro de albañilería confinada mediante malla electrosoldada.

San Bartolomé, A. and Coronel, C. (2009). Reparación y reforzamiento de un muro de albañilería confinada mediante fibra de carbono.

San Bartolomé, A. and Loayza, J. (2004). Reparación y reforzamiento con varillas de fibra de vidrio en un muro de albañilería confinada.

San Bartolomé, A., Quiun, D., and Silva, W. (2011). Diseño y construcción de estructuras sismorresistentes de albañilería.

Santa María, H., Duarte, G., and Garib, A. (2004). Experimental investigation of masonry panels externally strengthened with cfrp laminates and fabric subjected to in-plane shear loads. In *Proc 13th World Conference on Earthquake Engineering, Vancouver-Canada*.

Torrealva, D. (2007). Refuerzo de muros y tabiques de albañilería con mallas de polímero.

Triantafillou, T. and Papanicolaou, C. (2006). Shear strengthening of reinforced concrete members with textile reinforced mortar (trm) jackets. *Materials and structures*, 39(1):93–103.

Tumialán, G., San Bartolomé, A., and Nanni, A. (2004). Comportamiento sísmico de tabiques reforzados con varillas de fibra de vidrio.

Ueno, K. and Van Straaten, R. (2011). Recommended approaches to the retrofit of masonry wall assemblies: Final expert meeting report. *Building Technologies Program*.

Wang, X., Ghiassi, B., Oliveira, D., and Lam, C. (2016). Modelling the nonlinear behavior of masonry walls strengthened with textile reinforced mortars. *Engineering Structures*.

Yardim, Y. and Lalaj, O. (2016). Shear strengthening of unreinforced masonry wall with different fiber reinforced mortar jacketing. *Composite Part B*.

Zhang, D., Yang, Y., Sheng, S., and Garrity, L. (2017). Numerical modelling of FRP-reinforced masonry walls under in-plane seismic loading. *Construction and Building Materials*, 134:649–663.

Zijl, V. and Vries, P. (2005). Masonry wall crack control with carbon fiber reinforced polymer. *Journal of Composites for Construction*, 9(1):84–89.